Citation for published version:
Lunt, AJG 2016, 'Mechanical microscopy of the interface between yttria-partially-stabilised zirconia and porcelain in dental prostheses', Ph.D., University of Oxford.

Publication date:
2016

Document Version
Publisher's PDF, also known as Version of record

Mechanical Microscopy of the Interface Between Yttria-Partially-Stabilised Zirconia and Porcelain in Dental Prostheses

Alexander James George Lunt

Christ Church

Supervised by

Professor Alexander M Korsunsky

A thesis submitted for the degree of

Doctor of Philosophy

Hilary 2016

Abstract

In recent decades, the high strength, high toughness and appealing aesthetics of Yttria-Partially-Stabilised Zirconia (YPSZ) has made this ceramic the material of choice for dental prostheses. During manufacture YPSZ copings are veneered with porcelain to match the appearance of natural teeth and to reduce wear. However, near-interface chipping of the veneer is observed as a persistent primary failure mode. Recent studies suggest that failure is associated with the mechanical and microstructural state within a few microns of the interface. This insight has provided the motivating driver for this study: to develop and implement new characterisation techniques to improve the understanding of the YPSZ-porcelain interface and thereby reduce failure rates.

Microscale characterisation of the interface was performed using energy dispersive X-ray spectroscopy, Raman spectroscopy, X-ray Diffraction (XRD) and transmission electron microscopy. These studies indicated that YPSZ phase variation, elemental composition gradients and distinct microstructural features are present within 10 μm of the interface. Porcelain nanoscale voiding was found at the interface, and small angle neutron scattering confirmed that this is induced by tensile creep.

High resolution (microscale) residual stress analysis was performed in YPSZ using XRD and Raman spectroscopy, and in porcelain using a new pair distribution function analysis technique. Cross-validation of these results was performed using improved implementations of the ring-core focused ion beam milling and digital image correlation technique. The variation of Young's modulus, yield strength and fracture toughness were determined using spatially resolved micropillar compression and splitting. Improved evaluation of the single-crystal stiffness of YPSZ was also performed using a new neutron diffraction based technique.

The results of this analysis indicate a complex interaction within the first 50 μm of the YPSZ-porcelain interface which leads to a significant reduction in porcelain toughness and an increased propensity to fail at this location.

Contents

Acknowledgements

My thanks must first go to Alexander Korsunsky for the amazing opportunities he has given me over the past four and a half years. He has consistently encouraged my scientific endeavour, challenged my perceptions and pushed me beyond the limits of what I thought I could achieve. I am continually astounded by his creativity, exceptional knowledge, patience and quick wit. During both my Master’s and DPhil projects he has been the most incredible mentor, supervisor and friend, and has provided invaluable help, guidance and care whenever needed. The trust he has placed in me has helped to define me both as a scientist and as a person, and I owe him a great deal. He has my utmost respect, and I look forward to working with him in the future.

I would also like to express my gratitude to my long term girlfriend Natasha Butters, for her love, care and unwavering support. She has been my rock when times were tough, and her patience with me has been beyond measure. I am lucky to have such an amazing person to call my partner.

My deepest appreciation goes to my parents, Jane and George Lunt for their consistent guidance, support and encouragement. Words cannot express the gratitude that I have for all that you have given to me. I know that none of this would have been possible without your continual belief in my potential. What I have done, I have done to make you proud.

I would also like to acknowledge the support of my family and friends, of which (I am lucky to say) there are far too many to mention by name. I feel honoured to live my life surround by such an exciting, caring and loyal group of people.

I would also like to send my thanks to Christ Church which I have had the pleasure of living, studying and working at for almost one third of my life. I have made some amazing friends, met some incredible people and have been provided with some exceptional opportunities during my time in Oxford. I would particularly like to thank David Nowell, my college supervisor for his continual support and guidance, as well as Malcolm McCulloch for his faith in my teaching abilities. I feel very privileged to have been awarded and have fully enjoyed my role as Stipendiary Lecturer, and would like to thank my students for their passion and challenging questions. I am, and forever will be, a member of ‘The House’.

In addition, I would like to extend my thanks to my tutors and teachers who have helped guide and shape my academic interests over many years. The support and belief of these people have enabled me to reach places and experience things I would never have dreamt possible.

Thanks must also go to my colleagues and friends who have helped me so much over the past few years. It has been my pleasure to feel part of this exceptional and international community, whether it be sharing sleepless nights on beamtime, collaborating together to tackle daunting scientific problems or simply sharing a drink after a hard week at work. In particular I would like to thank Nikolaos Baimpas, Tan Sui, Mengyin Xie, Gaurav Mohanty, Enrico Salvati, Siqi Ying, Marco Sebastiani, Jiří Dluhoš, Bohang Song, Honjia Zhang and all members of the Department of Engineering Science. Special thanks go to Richard Duffin and his team of technicians who have been exceptionally helpful.

I would also like to acknowledge EPSRC for funding this project, as well as Diamond Light Source and ISIS Neutron and Spallation Source for their beamtime allocations. The support I have received at these institutions has been outstanding and I would specifically like to extend my thanks to Igor Dolbnya, Philip Chater, Ann Terry, Shu-Yan Zhang, Andrew Malandain, Saurabh Kabra, Joe Kelleher, Annette Kleppe, Dominik Daisenberger and Stephen King.

My thanks also go to Dr Neo Tee Khin and the dental technicians at the Specialist Dental Group Singapore, who have provided the necessary samples, dental support and the initial motivation to try to improve understanding of the relatively high failure rates observed at the YPSZ-porcelain interface.

Finally I would like to thank my examiners, Professor Robert McMeeking and Professor John Huber for taking the time to read my thesis. I feel that my work has been greatly improved by the constructive criticism you provided during my viva.

Selected Publications

Journal articles:

1. **A. J. G. Lunt,** et al., “Microscale residual stress and phase quantification at the yttria-partially stabilised-zirconia porcelain interface in dental prostheses,” Biomaterials. 2016 *Under review*.
2. **A. J. G. Lunt,** et al., “Residual Strain Mapping Using Atomic Pair Distribution Function Analysis of Porcelain in Dental Prostheses”, Biomaterials. 2016. *Under review*.
3. **A. J. G. Lunt,** et al., “Characterisation of nanovoiding in dental porcelain using small angle neutron scattering and transmission electron microscopy”, Acta Materialia. 2016. *Under review*.
4. **A. J. G. Lunt,** et al., “Full In-plane Strain Tensor Analysis using the Microscale Ring-core FIB milling and DIC Approach,” Journal of the Mechanics and Physics of Solids. 2015. *In Press*.
5. **A. J. G. Lunt** and A. M. Korsunsky, "A review of micro-scale focused ion beam milling and digital image correlation analysis for residual stress evaluation and error estimation," Surface and Coatings Technology. vol. 283, p. 373-388. 2015.
6. **A. J. G. Lunt,** et al., "A comparative transmission electron microscopy, energy dispersive x-ray spectroscopy and spatially resolved micropillar compression study of the yttria partially stabilised zirconia-porcelain interface in dental prosthesis," Thin Solid Films. vol. 596, p. 222-232. 2015.
7. **A. J. G. Lunt,** et al., "Tensile secondary creep rate analysis of a dental veneering porcelain," Thin Solid Films. vol. 596, p. 269-276. 2015.
8. **A. J. G. Lunt,** et al., "A state-of-the-art review of micron-scale spatially resolved residual stress analysis by FIB-DIC ring-core milling and other techniques," The Journal of Strain Analysis for Engineering Design. p. 0309324715596700. 2015.
9. N. Baimpas, **A. J. G. Lunt,** I. P. Dolbnya, J. Dluhos, and A. M. Korsunsky, "Nano-scale mapping of lattice strain and orientation inside carbon core SiC fibres by synchrotron X-ray diffraction," Carbon. vol. 79, p. 85-92. 2014
10. **A. J. G. Lunt,** et al., "Calculations of single crystal elastic constants for yttria partially stabilised zirconia from powder diffraction data," Journal of Applied Physics. vol. 116 (5) p. 053509. 2014.

Conference Proceedings:

1. **A. J. G. Lunt,** et al., “Microscale resolution fracture toughness profiling at the zirconia-porcelain interface in dental prostheses,” Proceedings of SPIE 9668, Micro+Nano Materials, Devices, and Systems, 96685S, 2015.
2. **A. J. G. Lunt,** T. K. Neo, and A. M. Korsunsky, "An electron microscopy study of sintering in three dental porcelains," Proceedings of the World Congress on Engineering. vol. 3, 2015. – **Best Paper Award.**
3. E. Salvati, **A. J. G. Lunt,** T. Sui, and A. M. Korsunsky, "An investigation of residual stress gradient effects in FIB-DIC micro-ring-core analysis," Proceedings of the International Multi Conference of Engineers and Computer Scientists. vol. 2, 2015.
4. **A. J. G. Lunt** and A. M. Korsunsky. “Intragranular Residual Stress Evaluation Using the Semi-Destructive FIB-DIC Ring-Core Drilling Method”. Advanced Materials Research. 2014.
5. O. Roberts, **A. J. G. Lunt**, et al., "A Study of Phase Transformation at the Surface of a Zirconia Ceramic," Proceedings of the World Congress on Engineering. vol. 2, 2014.

Acronyms

BSE – Backscattered Electron

CAD – Computer Aided Design

CAM – Computer Aided Manufacture

CTE – Coefficient of Thermal Expansion

DIC – Digital Image Correlation

EDXS – Energy Dispersive X-ray Spectroscopy

ER – Elastic Response

FD – Finite Difference

FE – Finite Element

FIB – Focused Ion Beam

FIST – Full In-plane Strain Tensor

KB - Kirkpatrick Baez

LDA – Local Density Approximation

MD – Molecular Dynamics

PDF – Pair Distribution Function

RMS – Root Mean Square

ROI – Region Of Interest

RVE – Representative Volume Element

RVH – Reuss-Voigt-Hill

SANS – Small Angle Neutron Scattering

SE – Secondary Electron

SEM – Scanning Electron Microscopy/Microscope

SNR – Signal to Noise Ratio

TEM – Transmission Electron Microscopy/Microscope

XRD – X-ray Diffraction

YPSZ – Yttria-Partially-Stabilised Zirconia

1. Introduction

Despite having exceptional reliability, manufacturability and biocompatibility, recent decades have seen a significant reduction in the popularity of metal dental implants [1]. The driving force behind this change has been the advent of ceramic copings, which are able to provide an aesthetic appearance more closely resembling natural teeth, and are therefore more popular with patients and dental clinicians alike. This shift has presented significant challenges in the quest to manufacture reliable, high performance dental prosthesis from what is generally perceived to be a brittle class of materials.

One of the most promising ceramics for use in this application is Yttria-Partially-Stabilised Zirconia (YPSZ), due to its high strength, excellent biocompatibility and chemical inertness [2]. The outstanding characteristic of YPSZ is however the exceptional toughness of this material which is typically $\sim 2-3$ times greater than other conventional ceramics. The origins of this toughening behaviour were originally postulated by Garvie, Hannink & Pascoe in their seminal paper entitled “Ceramic Steel?” [3] which made reference to the room temperature martensitic phase change which can be induced in YPSZ. The mechanism behind this transformation toughening was later outlined in detail by McMeeking & Evans [4] who demonstrated that a zone of increased fracture toughness was generated by the stress induced tetragonal to monoclinic transformation at crack tips.

In dental prosthesis YPSZ lacks the pearlescent finish of natural teeth and has a hardness that is sufficient to induce excessive wear of patient’s existing teeth during occlusal contact [5]. Therefore, a multi-layered veneer of dental porcelain is applied to the YPSZ coping which is also used to tailor the shape, colour and surface finish of the completed prosthesis. Despite the many benefits of this fabrication arrangement, clinical trials have indicated that the primary failure mode of these prosthesis is near-interface chipping of the porcelain veneer, which is induced in approximately 8% of implants [6]. In these cases the high cost, technical difficultly and patient inconvenience of restorative dental surgery is significant, and therefore an improved understanding of the origins of this failure is critically required.

This thesis presents a suite of mechanical and structural characterisation techniques which have been applied and developed in order to improve understanding of the origins of failure of the near interface porcelain. An overview of the stages involved in the manufacture and surgical placement of YPSZ-porcelain dental prostheses as well as the discussion of previous studies directed at understanding the interface failure is initially provided in § 1.1 and § 1.2. This is followed by an introduction to YPSZ in § 1.3, and dental porcelain in § 1.4, with particular emphasis on the characteristics of the tetragonal to monoclinic phase change of YPSZ and the mechanical properties of these materials. A brief overview of the thesis is then presented in § 1.5, which highlights that failure is associated with localised residual stress, YPSZ phase composition, porcelain creep and the resulting variations in mechanical properties.

1.1. The Manufacture and Implantation of YPSZ-porcelain Dental Prosthesis

A schematic representation of a YPSZ-porcelain dental prosthesis is shown in Figure 1.1. The prosthesis is composed of three main sections; the implant which is inserted into the jaw bone of the patient, the abutment which is fixed to the implant and the coping which is bonded to the abutment. The materials, bonding methods, surgical techniques and success rates of each of these constituent parts has been the focus of a large number of research articles, and comprehensive overviews have been widely published [7]. Although the focus of this study is placed on the interface between YPSZ and porcelain within the coping, a brief overview of the stages of prosthesis implantation and manufacture has been provided in order to provide context to the failures observed.

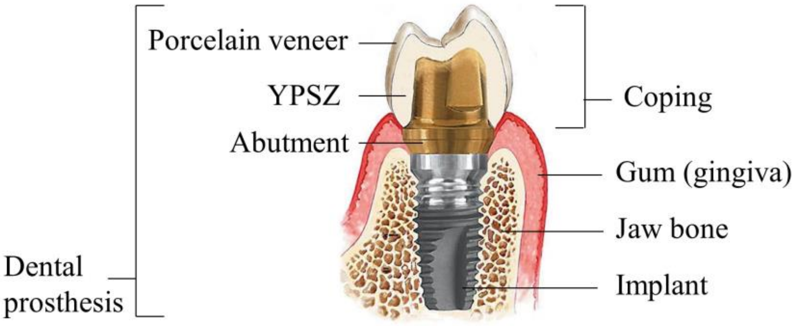

Figure 1.1. Schematic representation of a YPSZ-porcelain dental prosthesis [8].

Prosthesis implantation starts with the surgical removal of the diseased or damaged tooth, including the root and any infected gingiva or bone. Next, a hole is drilled into the jaw and the implant is screwed into place. Implants can be manufactured from ceramics such as YPSZ however metals such as titanium are more commonly used in order to provide improved bonding between the implant and bone [9]. The abutment is next attached to the implant using dental cement such as zinc phosphate or methacrylate resin. At this stage in the procedure, the implant must be given sufficient time to adhere fully to the bone before the application of the YPSZ-porcelain coping. This can take anywhere between a few weeks to several months and it is during this period that the tailor-made coping is manufactured.

Following the installation of the abutment, a dental impression or negative imprint of the neighbouring teeth and soft tissues is cast using a viscous, rapid setting polymer (Figure 1.2a). A temporary wax or polymer coping is sometimes applied to the abutment after this process in order to improve the aesthetic appearance and to minimise damage to the abutment during implant healing.

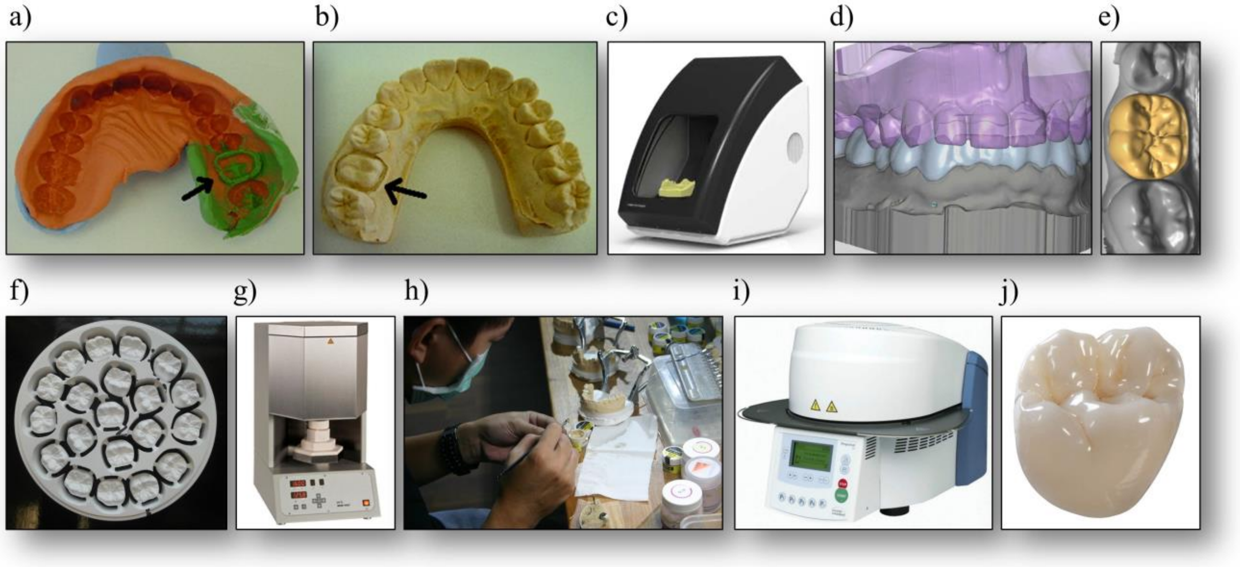

Figure 1.2. Stages in the manufacture of YPSZ-porcelain dental copings. a) Dental impression, b) cast produced, c) 3D scan of cast, d) CAD model produced, e) coping designed, f) CAM applied to the YPSZ green body, g) YPSZ sintered, h) porcelain veneer applied, i) vacuum sintering of porcelain, j) completed coping is polished after the application of multiple veneering layers [10].

Manufacture of the YPSZ-porcelain coping begins by the production of plaster cast models of the dental impressions taken (Figure 1.2b). These models are then placed into 3D scanners in order to produce a point cloud representation of the casts (Figure 1.2c). The next stage of analysis is to generate Computer Aided Design (CAD) models of both the upper and lower jaw (Figure 1.2d). The relative positions of these models are then adjusted to simulate static occlusion and to provide an indication of the required size and shape of the dental prosthesis. A tooth shape is then selected from a library of potential variants in order to match the form of the existing teeth and the required tooth profile at the implantation site, for example, molar, incisor or canine (Figure 1.2e). Computer Aided Manufacture (CAM) is next used to shape the YPSZ coping from pre-sintered blanks (Figure 1.2f). These copings are manufactured oversize, in order to accommodate for the $\approx 20\%$ linear shrinkage induced during coping sintering. The pre-sintered copings are then manually removed from the blanks and diamond polishing is used to produce a smooth, uniform exterior surface.

Many different types of YPSZ blanks are commercially available for use in the manufacture of dental copings. In this study Wieland Dental Zenotec Zr Bridge [11] has been selected as a representative YPSZ composition due its widespread and established clinical use. The composition of this material is given in Table 1.1. which closely matches that of several other widely used YPSZ variants [12].

Table 1.1. Composition of Wieland Dental Zenotec Zr Bridge [11].

Oxide	$ZrO_2 + Y_2O_3 + HfO_2$	Y_2O_3	HfO_2	Al_2O_3	Other oxides
Weight %	< 99	$4.5 - 6$	≤ 5	< 0.5	< 0.5

The recommended sintering conditions of YPSZ vary between different manufacturers however a maximum temperature of $1600°\mathrm{C}$ is typically required to minimise porosity in the component. In this study, sintering was performed in an Orotig HT-S furnace, which was used to apply a heating rate of $20°\mathrm{C}\ \mathrm{min}^{-1}$ from room temperature to $800°\mathrm{C}$. The heating rate was then changed to $10°\mathrm{C}\ \mathrm{min}^{-1}$ from $800 - 1600°\mathrm{C}$ at which point the temperature was held constant for 2 hours. The sample was then furnace cooled in order minimise the likelihood of thermal shock induced fracture.

Several recent studies have been performed to investigate the impact of further processing through sandblasting or the application of preparation liquids at this stage of manufacture [13, 14]. Although the results of these studies appear promising, in order to be representative of conventional manufacturing techniques no further processing was applied to the YPSZ coping at this stage.

The next stage of coping manufacture is the application of the porcelain veneer (Figure 1.2h). A multitude of porcelain compositions are commercially available which can be used to tailor the colour, mechanical properties and Coefficient of Thermal Expansion (CTE) of the porcelain [15]. Porcelain is supplied as a micro-to-nanoscale powder which is combined with deionised water to produce a slurry and then manually applied to the surface of the YPSZ in thin layers [16]. In this study Ivoclar Vivadent IPS e.max Ceram was selected for the veneering process due to its widespread use, suitability for multiple layers of application and absence of additional pigments [17]. This consistent porcelain composition (Table 1.2) was selected in order to minimise effects induced by elemental variation through the veneer. Sintering was performed using an Ivoclar Vivadent Programat CS2 vacuum furnace in accordance with the manufacturer's prescribed automated temperature routines (Figure 1.2i). Heating was performed at a rate of $40°\mathrm{C}\ \mathrm{min}^{-1}$ to a temperature of $750°\mathrm{C}$ which was held for 1 minute, followed by furnace cooling of the sample back to room temperature. In order to build up the shape of the completed prosthesis, two to three further layers of porcelain veneer were then applied using the same technique.

Table 1.2. Composition of incisal IPS e.max Ceram [17].

Oxide	SiO_2	Al_2O_3	Na_2O	K_2O	ZnO	CaO, F, P_2O_5	Other oxides
Weight %	$60-65$	$8-12$	$6-9$	$6-8$	$2-3$	$2-6$	$2-8.5$

The final stage of coping manufacture involves fine grit (3 μm) polishing of the veneered surfaces in order to produce a pearlescent finish (Figure 1.2j). The coping is then placed onto the abutment of the plaster cast model to check the fit suitability and contact tolerances with existing teeth.

Upon the successful healing of the dental implant, the final stage of prosthesis installation is performed. The wax or porcelain temporary crown is removed from the abutment which is then cleaned and dental cement is used to attach the inner surface of the YPSZ-porcelain coping to this component. If necessary, further diamond polishing is applied at this stage to minimise contact with neighbouring teeth.

1.2. Failure of YPSZ-porcelain Dental Prostheses

Near-interface porcelain chipping has become well-established as the primary failure mode of YPSZ-porcelain dental prostheses both through simulated mastication loading (*ex vivo*, Figure 1.3a) [18] and clinical trials (*in vivo*, Figure 1.3b) [19]. This widespread observation, in combination with the significant difficulties induced by prosthesis failure has resulted in a large number of studies being directed towards this issue, as recently overviewed by Raigrodski et al. [20]. Despite this directed and coordinated analysis, a critical assessment of the literature demonstrates that a comprehensive understanding of the origins of failure has yet to be revealed.

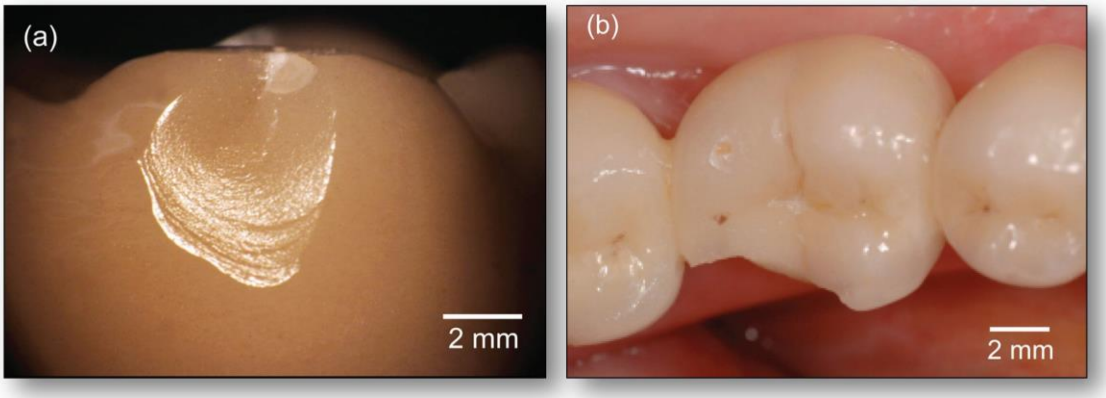

Figure 1.3 Near-interface chipping of porcelain veneers a) *ex vivo* and b) *in vivo* [21].

One of the primary reasons for this limited insight is that a significant percentage of studies are directed towards reducing the prosthesis failure rates through the development of new manufacturing techniques and methods, without attempting to understand the underlying characteristics of failure. This approach has proved highly successful in identifying manufacturing parameters which can greatly increase the bond strength and thereby reduce failure rates; from modified thermal processing routes [22], to effective porcelain compositions [23] and optimal veneering thicknesses [24]. Without the active use of studies such as these, the poor reliability of YPSZ-porcelain copings would almost certainly render them uncompetitive when compared with alternative methodologies. However, analysis of this type has resulted in a large number of literature studies which suggest the importance of a considerable number of parameters, and from which a number of conflicting conclusions are presented. It is my belief that this approach of improvement through manufacturing process trials is showing ever decreasing returns in terms of reduced prosthesis failure rates, and therefore further improvement is only possible through enhanced understanding of the underlying causes of prosthesis failure.

In order to begin to understand the origins of failure, several studies have been directed towards the characterisation of cracked and chipped YPSZ-porcelain prostheses. A broad range of techniques have been applied to examine this behaviour, from Scanning Electron Microscope (SEM) imaging (Figure 1.4) [25] to micro-tomography [26] and Energy Dispersive X-ray Spectroscopy (EDXS) [27]. The common feature in these analytical studies has been the importance of high resolution (≤ μm) characterisation, which indicates that the origins of failure are highly localised to the near-interface porcelain region.

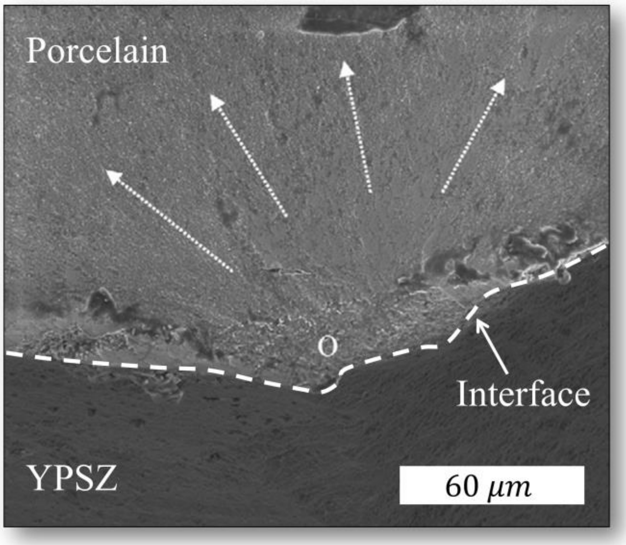

Figure 1.4. SEM image across the YPSZ-porcelain interface showing the origin (o) of porcelain chipping and the direction of crack propagation [25].

One widely presented explanation for the high frequency of near-interface chipping is the presence of localised residual stresses within the near-interface porcelain. Residual stresses are defined as the forces that remain locked within a material in the absence of an exterior load. Regions of high magnitude tensile residual stress, when combined with externally applied forces (such as mastication loading), can reach a magnitude which is sufficient to induce fracture through a weakest link type failure.

Of the two constituent materials in this system, YPSZ has a flexural strength ($1{,}200\ \pm 200$ MPa [11]) which is over ten times greater than dental porcelain (90 ± 10 MPa [17]). The brittle nature of these ceramic materials ensures that flexural failure occurs as a direct result of crack tip opening and the compressive strength of both materials has been shown to be much greater than the tensile equivalents [28]. Therefore, in order to minimise the likelihood of porcelain tensile failure, the CTE of dental porcelain ($\alpha_P = 9.5 \times 10^{-6}\mathrm{K}^{-1}$ [17]) and YPSZ ($\alpha_Z = 10.5\ \times 10^{-6}\mathrm{K}^{-1}$ [11]) have been selected to induce residual mild compression in porcelain during post-sintering cooling from 750℃ [29]. Although this approach has been widely exploited in the manufacture of YPSZ-porcelain dental prosthesis, the interaction between the two materials and resulting stress distribution have never been fully understood. Following the residual stress analysis performed in Chapter 6, a multiscale analytical model of residual stress generation at this location is presented in § 6.6 to improve understanding of this effect.

Another factor which is believed to influence the residual stress state at the YPSZ-porcelain interface is the tetragonal to monoclinic phase change of YPSZ [29]. This crystallographic transformation can be induced by tensile or shearing residual stresses and results in a 4% volumetric expansion as well as localised twinning [30], as outlined in more detail in § 1.3. This volume expansion serves to reduce the tensile residual stress within the YPSZ, however it can also induce tensile stresses in neighbouring regions [31]. Although monoclinic YPSZ has been experimentally observed within the YPSZ dental copings [14, 32], this analysis has either been performed over very small length scales or at an insufficient resolution to provide insight into the role of phase transformation in failure. Therefore as part of this study, improved characterisation of this behaviour has been performed using X-ray powder diffraction and Raman spectroscopy (in § 6.3 and § 6.4, respectively).

Several revealing studies into the residual stress variation within porcelain and YPSZ copings have been published. Mainjot et al. performed depth resolved (100 μm) hole drilling using a 2.5 mm diameter drill bit to reveal the presence of distinct gradients within the near-interface region. Nanoindentation has also been applied to determine the variation of the average residual stress in YPSZ and porcelain with an incremental step size of 50 μm between measurement points [33, 34]. These studies demonstrated fluctuations in porcelain residual stress which were closely related to the thickness of the porcelain veneer applied, that porcelain was generally in a state of tensile residual stress, and that YPSZ was largely in a state of mild near-uniform compressive stress. Despite these promising results, this nanoindentation analysis was performed by using variations in indentation hardness to characterise stress. This approach is highly dependent upon precise calibration of the unstressed hardness of the substrate, is sensitive to tip imperfections and is based on the implicit assumption that the mechanical characteristics remain constant within the measured region (which has since been shown to be invalid in Chapter 7). Therefore, further independent validation of these results is required.

More recently the ring-core Focused Ion Beam (FIB) milling and Digital Image Correlation (DIC) microscale residual stress analysis technique has been applied to a YPSZ-porcelain cross section by Sebastiani et al. [35]. This approach proved to be highly successful at resolving residual stresses within the coping and was performed within the porcelain veneer at an incremental step size of 0.5 mm. Moderate variations in residual strain (and stress) were observed using this approach, however only five measurement points were collected across the entire thickness of the porcelain veneer, severely restricting any potential insights into the localised residual stress states expected in the near-interface region. In order to overcome this limitation, higher resolution, more reliable quantification of residual stress has been performed using improved implementations of the ring-core FIB milling and DIC technique, as outlined in Chapter 6.

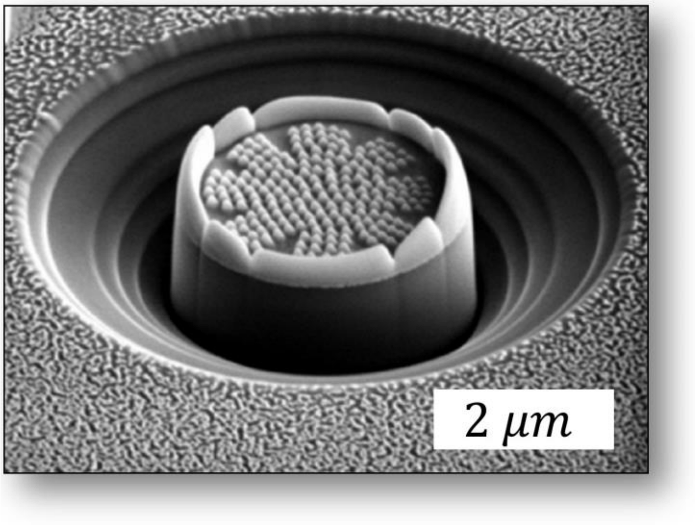

Figure 1.5 SEM image of ring-core FIB milling and DIC in dental porcelain [35].

The near-interface proximity of porcelain chipping has led to the suggestion that the failure may be influenced by elemental diffusion across this boundary. Elemental composition is known to be highly influential on the mechanical properties of both YPSZ and porcelain [36] and EDXS analysis has confirmed that the elemental diffusional distances of Zr and Si are approximately 5-10 μm [27]. Mechanical characterisation in the form of nanoindentation has previously been used to assess if elemental composition (or YPSZ phase transformation) induces localised weakness of the near-interface region [35]. Deviations were observed in Young's modulus, hardness and fracture toughness in the near-interface region, however the impact of the large variations in residual stress across the interface was not accounted for in this analysis. This severely limits the validity of any conclusions which can be drawn from this study and has served as motivation for improved characterisation of the microstructural and mechanical state of the interface region (Chapter 7).

1.3. An Introduction to YPSZ

Zirconia is a dioxide of the transition metal zirconium. In its pure form zirconia has a monoclinic crystal structure at room temperature. However, alloying with other oxides, such as CaO, MgO, CeO_2 or Y_2O_3 stabilises the tetragonal (or cubic) crystal structure to lower temperatures [2]. Yttria-Partially-Stabilised Zirconia is defined as a Zirconia alloy with a concentration of Y_2O_3 higher than 0.5 mol% however the most widely used concentrations of YPSZ are between $3 - 5$ weight % as these ceramics offer the best balance between toughness and strength [37].

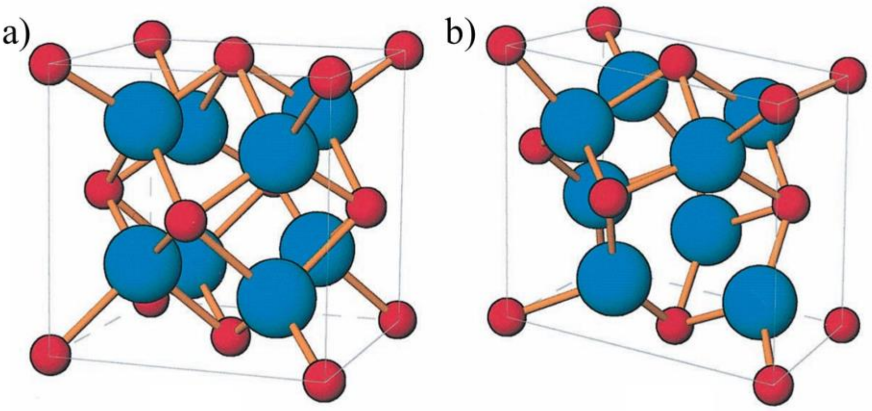

Figure 1.6. Schematic of a) tetragonal and b) monoclinic ZrO_2 (Zr-blue, O-red) [38].

The tetragonal to monoclinic phase transformation in YPSZ is diffusionless and involves a concerted movement of a large number of atoms through a shearing process. This martensitic transformation is a grain by grain phenomenon which induces a reversible crystallographic shape change and volume expansion of 4% (Figure 1.6) [30, 38]. Atomic force microscopy has been used to observe the transformation in more detail and both slip and twinning characteristics have been detected [39]. The phase transformation of in YPSZ is also dependent upon the thermal history and strain state of the material, with a critical transformation stress or strain at any given temperature. Stress-strain curves for single YPSZ crystals have been observed by Mercer et al. and these confirm the presence of a stress plateau at a critical transformation stress σ_T (Figure 1.7) [40]. The phase transformation of YPSZ has also been shown to be greatly affected by surrounding matrix constraints [2] which explains why mechanical, chemical and thermal processing of near interface regions can preferentially induce the YPSZ phase transformation at these locations [41].

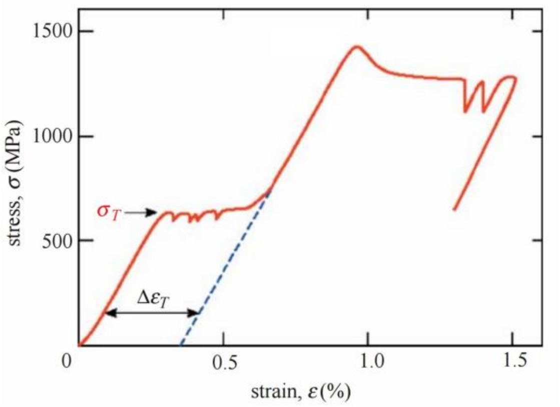

Figure 1.7. Representative compressive stress-strain response of a 3mol% YPSZ single crystal at 500℃. The transformation expansion strain is indicated by $\Delta\varepsilon_T$ [40].

The high toughness of YPSZ is an unusual property for a ceramic. This behaviour originates from the tetragonal to monoclinic transformation observed in the vicinity of crack tips. The transformation process absorbs some of the stored elastic strain energy required for crack propagation, induces a volumetric expansion that reduces the tensile stress and also acts to close the crack [42]. The high fatigue strength of YPSZ can also be explained by the reversible transformation at the crack tip. The cyclic loading of the crack tip leads to a hysteretic effect that dissipates energy via the phase transformation mechanism thereby reducing the energy available for crack propagation [40].

The sintering conditions applied to YPSZ during manufacture are highly influential on the Young's modulus, flexural strength and hardness of this material. Reductions in all three of these parameters are observed with lower sintering temperatures and increasing levels of porosity [43]. Elemental composition is also highly influential in the mechanical characteristics of YPSZ, and doping with a broad range of transition metal oxides has proven to be particularly successful at increasing the flexural strength and hardness of YPSZ [44]. Higher concentrations of yttria have been shown to increase the stabilisation of the tetragonal phase which results in a higher strength and hardness, at the expense of material toughness. Despite the severe difficulties in determining reliable single crystal stiffnesses of YPSZ (as outlined in more detail in Chapter 4), yttria content has also been shown to be influential in the elastic anisotropy of individual grains [45]. A critical examination of the literature also reveals that there is significant variation in published estimates of Poisson's ratio for YPSZ, with typical bulk averages in the range of $\nu = 0.25 - 0.30$ and single crystal stiffness estimates varying as much as $\nu = 0.02 - 1.65$ [46].

An overview of the relevant mechanical properties of Zenotec Zr Bridge is provided in Table 1.3.

Table 1.3. Mechanical properties of Zenotec Zr Bridge [11].

Fracture toughness	Flexural strength	Hardness	Young's Modulus	Poisson's ratio
$5\ \mathrm{MPam}^{0.5}$	$1{,}200 \pm 200\ \mathrm{MPa}$	$12{,}750 \pm 1{,}960\ \mathrm{MPa}$	$210\ \mathrm{GPa}$	0.30

1.4. An Introduction to Dental Porcelain

Porcelain is a class of ceramic materials which is predominantly composed of ionic and covalently bonded oxides, which are formed into a viscous slurry, shaped into the required geometry and then sintered in a kiln or furnace to produce a high strength but brittle material. The term porcelain can be used to describe a broad range of compositions including the kaolin and quartz based ceramics widely used in utilitarian wares or art. Dental porcelain is distinct from these other ceramic types as it is primarily composed of feldspar, combined with smaller amounts of quartz (Figure 1.8). Silica (SiO_2) typically accounts for over 60 weight % of dental porcelain, which is combined with various oxides to produce a biocompatible material with optimal appearance, strength and hardness [47].

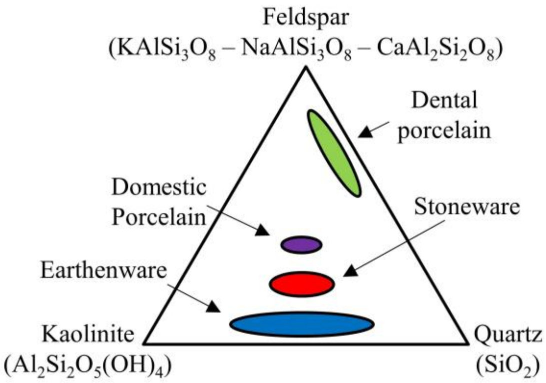

Figure 1.8 Triaxial plot indicating constituent components of porcelain classes.

Dental veneering porcelain can typically be grouped into two categories depending upon the crystalline content and glass composition of the particular ceramic. ‘Glass based ceramics’ are porcelains which are predominantly amorphous in structure and contain high concentrations of feldspar. The amount of crystalline phase in this type of ceramic is highly dependent upon the exact sintering regime applied [48] and these ceramics have proven to be highly reliable, with one of the most popular compositions being Cerec Vitablocs Mark II [49]. This kind of ceramic material forms the basis for the second category of dental porcelain; ‘glass based systems with fillers’ in which small concentrations ($<$ 1 weight %) of crystalline materials such as leucite ($KAlSi_2O_6$), lithium disilicate ($TiSi_2O_6$) or fluorapatite ($Ca_5(PO4)_3F$) are added. These crystalline phases can influence the thermal characteristics of the porcelain such as sintering temperature and CTE, and can also influence the mechanical properties of these materials [50]. IPS e.max Ceram is the most widely used dental veneering porcelain within this category [17].

Processing route can be used as an alternative method for categorising dental porcelain into either powder/liquid (Figure 1.9a) or solid bloc (Figure 1.9b) based systems [51]. Powder and liquid based systems are applied to YPSZ or metal frameworks using the conventional slurry and sinter based approach outlined in § 1.1. In contrast, recent developments in CAD and CAM have facilitated the manufacture of single phase porcelain copings. The copings benefit from the absence of the YPSZ-porcelain interface, but are weaker and currently less reliable than traditional designs [52].

Figure 1.9 Dental porcelain types [17, 49] a) powder form b) solid bloc and c) shading variation.

Another important factor in the manufacture of dental porcelain is the ability to tailor the colour and shade of the veneer (Figure 1.9c). Spectrophotometers or visual comparison with existing teeth are used to determine the required porcelain shade and small concentrations of metallic pigments then added to the porcelain powder during manufacture to tailor the colour. The following pigments are widely used: TiO_2 – amber, $CuSO_4$ – blue, Cr_2O_3 – green, Fe_3O_4 – brown and MnO – lavender.

The microstructure of dental porcelain is highly sensitive to the sintering durations and temperatures applied during manufacture [36]. Incomplete sintering leads to segregation of elemental phases and prevents full densification of the porcelain veneer [16], this microscale porosity has an unappealing ‘cloudy’ appearance and leads to a reduction in strength. Despite the presence of the these microscale voids, fractography of chipped veneers indicates that macro-scale failure does not originate at these microscale features (Figure 1.4) and that the origin of failure lies elsewhere [25].

The mechanical characteristics of dental porcelain are highly dependent upon the elemental composition, with increased fracture toughness and hardness being observed at higher concentrations of Al_2O_3 [53]. The flexural strength of porcelain can be greatly improved by the addition of crystallites [54] and Young’s modulus shows high sensitivity to porosity [55]. Few articles have been directed towards the study of Poisson’s ratio of porcelain, however typical values lie within the range of $0.20 - 0.25$.

An overview of the relevant mechanical properties of IPS e.max Ceram is provided in Table 1.4.

Table 1.4. Mechanical properties of IPS e.max Ceram [17].

Fracture toughness	Flexural strength	Hardness	Young’s Modulus	Poisson’s ratio
$2.75 \pm 0.25\ \mathrm{MPam}^{0.5}$	$90\ \pm 10\ \mathrm{MPa}$	$5{,}400\ \pm 200\ \mathrm{MPa}$	$60\ \mathrm{GPa}$	0.23

Few studies have been directed towards understanding the creep characteristics of porcelain, however a 4-point bending study by Ponraj et al. has demonstrated that domestic porcelain obeys the secondary creep rate equation at temperatures above $800°\mathrm{C}$:

$$\dot{\varepsilon} = A\sigma^{\bar{n}}e^{-Q/RT}, \tag{1.1}$$

where $\dot{\varepsilon}$ is the strain rate, A is the creep rate scaling factor, σ is the applied uniaxial stress, $\bar{n}$ is the stress rate exponent, Q is the activation energy, R is the universal gas constant and T is the absolute temperature in K. Creep-induced nanovoiding has been widely observed in the constituent phases of porcelain [56-58] which is believed to be associated with vacancy diffusion [59]. This behaviour is known to reduce the strength and fracture toughness of these materials [60] and has previously been shown to be sufficient induce component failure [61].

1.5. Thesis Overview

This thesis is directed at improving the current understanding of the relatively high frequency of porcelain chipping observed at the YPSZ-porcelain interface in dental prosthesis. The results of previous studies have indicated that the origins of this behaviour are localised to within a few hundred microns of the interface and therefore techniques capable of micro-to-nanoscale assessment have been applied. However, in order to understand better the microscale features observed, macro-scale quantification of the bulk properties of YPSZ and porcelain has been performed where relevant.

Assessment of the microstructure and mechanical properties across the YPSZ-porcelain interface has been performed using a broad range of techniques, which have been selected to provide insight into the characteristic features responsible for failure. This has included well-established techniques such as X-ray powder diffraction and Raman spectroscopy, recently developed techniques such as micropillar compression and splitting, as well as a suite of new experimental techniques. These newly developed techniques are based on improvement or modification of existing methodologies to meet the needs of this experimental study, but also offer several new characterisation tools for related investigations.

Chapter 2 provides a background to the experimental methods implemented or developed in this study. This includes characterisation techniques such as scanning and transmission electron microscopy which have been applied to visualise the structure of the YPSZ-porcelain interface. The multiple diffraction and spectroscopy based methods exploit the interaction between photons, neutrons and electrons to provide crystallographic, elemental and structural insight into the near-interface characteristics, as well as the microscale mechanical analysis methodologies applied to the near-interface region. Where relevant, the results of recent related studies have been included.

Chapter 3 presents the required development of the ring-core FIB milling and DIC approach. This has included the refinement of the DIC procedure to facilitate the complete assessment of the error bounds of the residual stress outputs from this analysis. An overview of a new analytical approach which exploits the isotropic geometry of the ring-core milling feature to quantify the Full In-plane Strain Tensor (FIST) at the milling location is also provided. Two new spatially resolved techniques are also presented which are capable of residual stress measurements in increments of between mm and tens of microns (the sequential ring-core approach), or between 1 and 10 microns (the parallel FIB milling geometry).

Chapter 4 provides an overview of a new technique which has been established to provide improved insight into the single crystal elastic stiffness parameters of YPSZ. Reliable quantification of these parameters is necessary for improved understanding the YPSZ-porcelain interface, however the micro-twinning characteristics of YPSZ ensures that conventional techniques are unsuitable. The new approach is based on *in situ* loading of YPSZ during neutron scattering, followed by the refinement of polycrystalline Finite Element (FE) simulations of the experimental arrangement.

Chapter 5 describes a new small-scale ceramic tensile creep loading arrangement which has been conceived and applied in order to improve insight into the creep response of dental porcelain. The high sintering temperatures and residual stresses within near-interface porcelain are known to be sufficient to induce creep at this location. Transmission electron microscopy and small angle neutron scattering have also been applied to assess the characteristics of creep induced nanovoiding in dental porcelain.

Chapter 6 presents the results of microscale residual stress and phase analysis across the YPSZ-porcelain interface and surrounding regions. These parameters are known to be highly influential in the near-interface porcelain chipping observed, however very few studies have been published on this topic. Microscale-resolved transmission X-ray powder diffraction and Raman spectroscopy have been used to assess the variation of phase and tetragonal strain within a cross section of the YPSZ coping. Validation has been performed using the parallel FIB milling geometry and the sequential FIST ring-core residual stress analysis technique, which was also applied across the porcelain veneer. A new method based on pair distribution function analysis for residual strain quantification in amorphous materials has also been outlined and applied to validate the strain variation observed within the amorphous porcelain.

Chapter 7 describes the microstructural and micromechanical experimental techniques applied across the YPSZ-porcelain interface. Despite the limited number of previous studies performed, the localised failure of near-interface of porcelain indicates that a structural or mechanical weakness is present at this location. Therefore energy dispersive X-ray spectroscopy has been used to assess the elemental diffusional distances across the YPSZ-porcelain interface and transmission electron microscopy has been used to assess the nanoscale structural variation at this location. Spatially resolved micropillar compression and micropillar splitting have also been used to quantify the variation in Young’s modulus, yield strength and toughness within the first 100 μm of the interface.

Chapter 8 outlines the main conclusions, combines the results obtained and provides potential explanations for the features observed. A brief overview of potential future work arising from this analysis is also provided.

2. Experimental Methods

This chapter presents an overview of the experimental techniques which have been used and refined in the course of this investigation. In § 2.1 a brief introduction is provided to the electron microscopy techniques used in the structural characterisation of the interface. The theoretical background to the multitude of diffraction and spectroscopy techniques is next outlined in § 2.2. These can be grouped into micro-focus techniques for high-resolution analysis, and macro-scale neutron diffraction for improved averaging of bulk characteristics. An overview of the recent micromechanical analysis techniques is then provided in § 2.3, including micropillar compression [62] and micropillar splitting [63] for the characterisation of elastic modulus and hardness, on the one hand, and toughness on the other. An introduction to the FIB milling and DIC technique for residual stress analysis is also provided, with particular focus on the ring-core milling geometry [64].

2.1. Microstructural Characterisation

Electron microscopy has become well-established as one of the most effective tools for micro-to-nanoscale structural characterisation in a broad range of scientific disciplines. This imaging technique is based on the generation, acceleration and electromagnetic focusing of an electron beam in order to produce a nanoscale spot size on the sample of interest. The interaction between the electron beam and the sample of interest can be detected in reflection (as in SEM analysis, Figure 2.1a) or through transmission (as is the case in Transmission Electron Microscopy (TEM) analysis, Figure 2.1b).

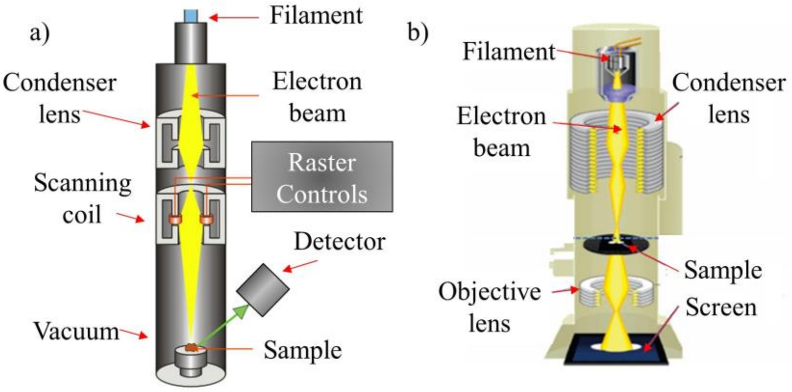

Figure 2.1. Schematic representations of a) SEM and b) TEM [65].

2.1.1.Scanning Electron Microscopy

In SEM the electron beam is deflected using a scanning coil in order to raster the beam incrementally across the sample. At each scanning position a detector is used to record the number of

Secondary Electrons (SE) or Backscattered Electrons (BSE) produced during the interaction between the sample and the incident beam. These numbers are assigned to greyscale values, which are then used to generate an image of the surface. SEM analysis is a reliable, easy and effective method for surface imaging with a typical maximum resolution of ≈ 1 nm. SEM sample suitability is only limited by the requirements of vacuum compatibility and charge conductivity, which in the case of highly insulating materials can be improved by coating the sample with a thin layer of conductive material such as Au or Pd. The SEM analysis performed during this thesis was mostly carried out using the Tescan LYRA 3XM FIB-SEM at the Multi-beam Laboratory for Engineering Microscopy (MBLEM), University of Oxford, UK.

2.1.2. Transmission Electron Microscopy

In order to facilitate effective transmission of the incoming electron beam, TEM analysis is performed on thin (< 100 nm) lamella which are extracted from the material of interest typically using a FIB milling approach (as outlined in more detail in § 5.3.1). Incident beam interaction is associated with either electron absorption (in thicker samples) or through electron modulation, in order to produce a 2D representation of the lamella with a typical maximum resolution of 0.05 nm. This high resolution can be used to provide insight into the shape, size and distribution of nanoscale features. In this study TEM analysis has been performed using the JEOL JEM-2100F TEM at the Research Complex at Harwell, Oxfordshire, UK which has been applied to study nanovoiding in porcelain in § 5.3 and the micro-to-nanoscale structural variation across YPSZ-porcelain interface in § 7.3.

2.2. Diffraction and Spectroscopy Based Techniques

The diffraction and spectroscopy based techniques used in this study have exploited the interaction between an incident beam (composed of electrons, neutrons or photons) and the atomic structure of YPSZ or porcelain to probe the mechanical, structural, elemental composition or bond characteristics of these materials. This interplay can be detected by either the scattering (change of direction) or frequency shift (change in energy) induced in the incident beam. Importantly, these techniques are able to provide high resolution characterisation, either by exploiting the micro-focus capabilities of the incident radiation to probe microscale gauge volumes or by selective examination of the scattering behaviour observed. Many of these techniques also facilitate *in situ* characterisation of the loading or thermal response of the materials, which can be critical in improving the understanding of the failures observed.

2.2.1. Synchrotron X-ray Powder Diffraction

X-Ray powder Diffraction (XRD) is an extremely effective tool for the characterisation of strain, phase and texture in crystalline materials. Although XRD can be implemented using lab-based X-ray sources, the high brilliance of the 3rd generation synchrotron X-ray sources provides increased penetration depths and improved insight into the bulk characteristics of a given specimen. Synchrotron emission is based on the acceleration and injection of a small packet of charged particles (typically electrons) into a polygonal path. The beam travels close to the speed of light and bending magnets are used to contain the beam within this closed loop. This bending process emits photonic radiation which covers a broad spectrum of wavelengths including X-rays. Alternatively insertion devices known as wigglers or undulators can be placed into the beam path to produce a sinusoidally varying magnetic field which induces constructive interference at the desired frequency.

Powder diffraction is typically performed using a monochromatic beam, which is defined as having a single characteristic wavelength and small bandwidth. Therefore a monochromator is used to select the required wavelength from the broad spectrum of incoming radiation. The choice of wavelength is highly dependent upon the capabilities of the beamline and the characteristics of the sample under investigation.

In order to facilitate high resolution analysis, the incident beam is next refined and focused. Optical methods have been developed to exploit interference (zone plate focusing) or refraction (compound refractive lenses) to focus the incident radiation. However, in the analysis that follows one of the most versatile approaches has been used: Kirkpatrick Baez (KB) mirrors which reflect and focus the incident radiation in the vertical and horizontal orientations as shown in Figure 2.2.

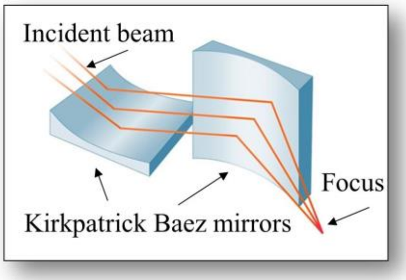

Figure 2.2 Schematic of KB mirrors [66].

In the case of XRD, the sample is next aligned to the focal spot in order to illuminate a small gauge volume of grains within the polycrystalline substrate. The regular crystallographic structure within each grain induces diffraction through a process known as Bragg scattering as originally proposed by W.H and W.L. Bragg [67]. Under these conditions the incident beam interaction with each atomic plane can be considered in a similar manner to reflection as shown in Figure 2.3. In order to generate constructive interference between incident waves, the path length difference between consecutive waves must be equal to an integer (n) multiplied by the wavelength of the incident radiation (λ). An expression for the path length difference can be determined geometrically from the lattice spacing (d_{hkl}) for a given Miller index (hkl) and the scattering angle θ, to give Bragg's law:

$$n\lambda = 2d_{hkl}\sin\theta. \tag{2.1}$$

For a given incident wavelength and lattice spacing, a characteristic diffraction peak will be therefore be observed in a direction offset 2θ from the incident radiation, and within the plane of the lattice normal $(\hat{n}_{hkl})$. For any given powder diffraction pattern, the presence of multiple peaks indicates differing lattice spacings for the various Miller indices in the crystallographic structure.

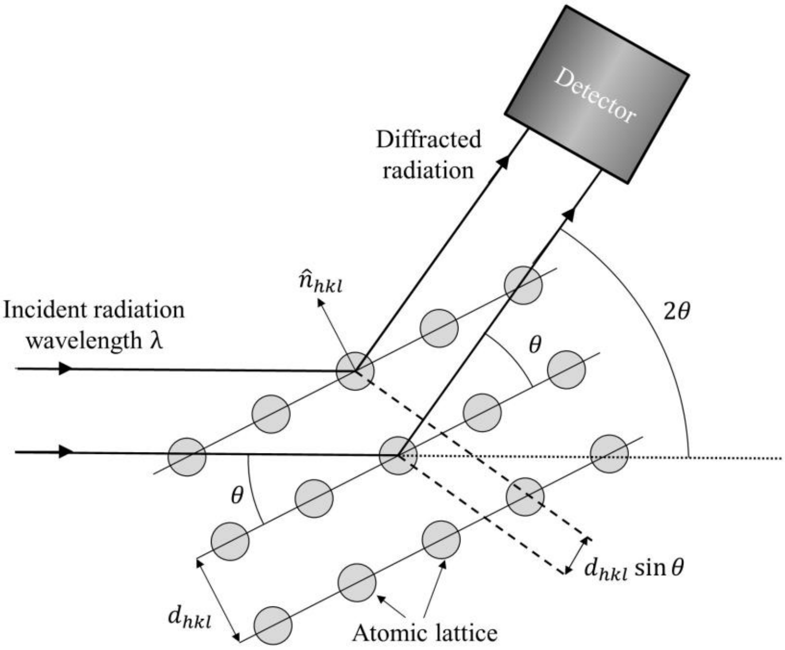

Figure 2.3 Schematic representation of Bragg scattering.

In order to perform successful collection of powder diffraction data, many thousands of crystallites need to be simultaneously illuminated within the gauge volume. This means that the average grain size of the polycrystalline substrate must be significantly smaller than the focal spot size of the incident media. Assuming that the sample is untextured i.e. has no preferred crystallographic orientation, the illuminated crystallites will be randomly orientated and therefore the Bragg condition will be met for any given azimuthal angle (φ). The resulting diffraction is observed as Debye-Scherrer cones with half opening angles $\left(2\theta_{hkl}^1, 2\theta_{hkl}^2, \ldots\right)$ corresponding to differing lattice spacings $\left(d_{hkl}^1, d_{hkl}^2, \ldots\right)$ and Miller indices as shown in Figure 2.4.

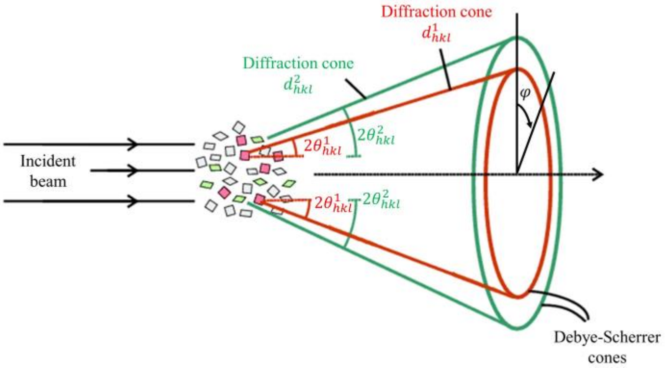

Figure 2.4. Schematic representation of Debye-Scherrer cone powder diffraction [68].

Powder diffraction is typically performed using either a grazing incidence or a transmission mode arrangement. In grazing incidence diffraction, the sample is arranged such that the incident beam is offset by $\approx 3-5°$ from the a vector within the surface of the sample [69]. This approach is highly effective in the study of thin films and coatings as it samples the near-surface characteristics of the sample, however suffers from geometric elongation of the focal spot and only provides insight into the in-plane behaviour in a single orientation. In contrast to this arrangement, in transmission X-ray diffraction the incident radiation is aligned with the sample plane normal in order to collect a through sample average. Typically, a 2D detector is placed downstream from the sample in order to record the diffraction patterns corresponding to a particular cross section of the Debye-Scherrer cones. This geometry provides insight into the in-plane structural variation, and can be used to provide insight into crystallographic preferred orientation through the variation in diffracted intensity as a function of azimuthal angle.

Processing of the 2D diffraction data is typically performed using software such as FIT2D [70]. Estimation of the sample-to-detector distance is required as an input to the processing routines, and is determined using diffraction patterns obtained from calibration samples such as silicon powder or LaB_6. Radial integration of the patterns is then performed as a function of azimuthal angle in order to provide 1D profiles of intensity against scattering angle as shown in Figure 2.5.

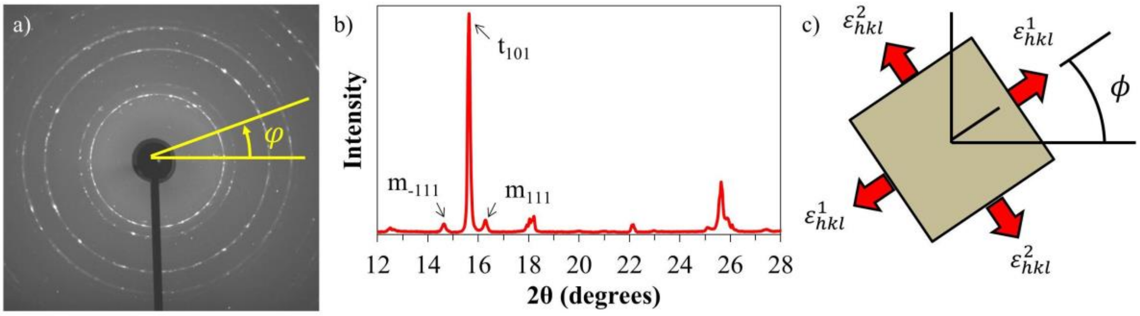

Figure 2.5. XRD of YPSZ showing a) 2D diffraction pattern and b) 1D intensity against 2θ plot. The relative angular offset (ϕ) of the principal strains ε^1_{hkl} and ε^2_{hkl} is shown in c).

In order to perform quantitative assessment of the resulting diffraction spectrum, fitting is next applied. Rietveld refinement involves the simulation, generation and incremental fitting of the spectra, starting from the crystallographic structure of the powder investigated [71]. This approach is particularly successful for the refinement of the lattice constants or determination of the average grain sizes of a given material however Rietveld refinement typically requires large numbers of approximations and can be a computationally expensive. An alternative fitting approach is based on single peak fitting in order to determine estimates for the height, standard deviation and centre of each peak. Diffraction peaks are typically best described by a convolution between the Gaussian and Lorentzian distributions, known as a Voigt function. However, a simple and effective approximation to this is the Gaussian distribution:

$$f(2\theta, \varphi) = \alpha e^{-\frac{(2\theta-\beta)^2}{2s^2}}, \tag{2.2}$$

where α is the peak height, β is the peak centre and s is the peak standard deviation. An estimate for integrated area beneath the fitted peak can then be obtained from:

$$I(\varphi) = \sqrt{2\pi}\alpha s. \tag{2.3}$$

Least squares fitting of these distributions also provides estimates of the confidence intervals of each parameter which is critical to the strain and phase analysis presented below.

Powder diffraction can be used to determine phase composition through the presence and relative intensity of diffraction peaks. In order to facilitate quantitative analysis, calibration is performed by mixing powders of known volume fraction and assessing the diffraction spectra resulting from these composite mixtures. For example, the differing crystallographic arrangements associated with monoclinic and tetragonal YPSZ result in distinct peaks in the powder diffraction patterns [72]. The Miller indices corresponding to the highest intensity peaks are the monoclinic 111 and -111 as well as the tetragonal 101 (as shown in Figure 2.5) and an expression for the amount of monoclinic phase present (X_m) has been developed based on the ratios of the integrated intensities of these peaks [73]:

$$X_m = \frac{I_{-111}^m + I_{111}^m}{I_{-111}^m + I_{111}^m + I_{101}^t}, \tag{2.4}$$

where the superscript indicates the phase of the peak and the subscript indicates the Miller index. This expression can then be used to provide estimates of the monoclinic volume fraction (V_m) from [74]:

$$V_m = \frac{1.311X_m}{1 + 0.311X_m}. \tag{2.5}$$

The confidence interval of V_m can be determined by careful propagation of the confidence intervals obtained during Gaussian fitting through Equations 2.3-2.5. It is important to point out that this analysis is typically performed on data which has been fully azimuthally integrated (from $0°$ to $360°$) in order to improve the precision of this volume fraction estimate.

X-ray powder diffraction can be used to provide insight into localised strain behaviour through variations in lattice parameter spacing. Lattice strain quantification is based on determination of the peak centre of (typically) high intensity diffraction peaks which are converted to peak centre estimates using:

$$d_{hkl}(\varphi) = \frac{\lambda}{2\sin\left(\frac{\beta(\varphi)}{2}\right)}. \tag{2.6}$$

Estimates of the lattice strain can then be determined from:

$$\varepsilon_{hkl}(\varphi) = \frac{d_{hkl}(\varphi) - d_{hkl}^{0}}{d_{hkl}^{0}}, \tag{2.7}$$

where d_{hkl}^{0} is the unstrained lattice parameter spacing. One of the main difficulties associated with lattice strain analysis is reliable quantification of d_{hkl}^{0} and a comprehensive review of methods which can overcome this limitation has recently been published [75]. These approaches are typically associated with XRD of a strain free sample, which is produced either through sample sectioning or powder based methods. However the effectiveness of these techniques can be somewhat limited due to incomplete stress relief or changes in d_{hkl}^{0} induced by local elemental variation or any processing applied to the sample. An alternative and highly successful approach is to compare the strain obtained from XRD with independent absolute residual strain analysis methods such as the ring-core FIB milling and DIC technique [76], and this approach has been successfully implemented in § 3.3, § 3.5 and § 6.5.

As well as providing insight into the lattice strain in a particular azimuthal orientation (φ), XRD can be used to characterise the in-plane strain tensor [77]. This analysis provides quantitative estimates of the principal in-plane strains (ε_{hkl}^{1} and ε_{hkl}^{2}) and angular offset from the original coordinate frame shown in Figure 2.5c (ϕ) by fitting of Mohr's circle to the azimuthal variation of lattice strain:

$$\varepsilon_{hkl}(\varphi) = \frac{\varepsilon_{hkl}^{1} + \varepsilon_{hkl}^{2}}{2} + \frac{\varepsilon_{hkl}^{1} - \varepsilon_{hkl}^{2}}{2}\cos 2(\varphi + \phi). \tag{2.8}$$

Insight into these parameters is critical in improving understanding of the principal stresses and orientations at the YPSZ-porcelain interface and the associated chipping failures observed.

2.2.2. Neutron Diffraction

Neutron diffraction offers an alternative characterisation tool to XRD, which is particularly effective in probing the bulk response of relatively large gauge volumes ($\approx \mathrm{mm}^3$) of material. The absence of charge results in weak interaction between the incident neutrons and the atomic media under investigation. Although this means that most neutrons pass through the sample, long exposures and careful collimation of scattered neutrons can be used to provide insight into the diffraction response from a region of interest within the sample.

Neutrons are produced during the fission of heavy elements such as tungsten and uranium. One approach which can be used to generate a source of neutrons is through the use of a nuclear reactor. In this arrangement, a self-sustaining fission process is induced and carefully controlled to generate a continual neutron source. An alternative approach is to accelerate bunches of protons using a synchrotron and to direct the incident beam onto a heavy metal target to induce instantaneous spallation of neutrons. This process is repeated at a high frequency in order to produce a pulsed neutron source. The neutron diffraction carried out as part of this study was performed at ISIS Pulsed Neutron Source, Harwell, UK and therefore the following introduction is devoted to this generation approach.

Following spallation, moderators such as water, liquid methane and liquid hydrogen are next used to reduce the velocity of high speed neutrons to energies most useful for material characterisation. Despite this reduction in high speed neutrons, a broad spectrum of neutron energies are still produced from the source and a chopper (or rotating neutron blanking device) can be used to select a subsection of the incident neutrons for the analysis required. Beam refinement is next performed using a series of slits and focusing optics in order to generate a millimetre sized neutron beam which is directed at the sample.

Bragg's law (Equation 2.1) can be used to describe the scattering induced by the interaction between the incident neutrons and the crystallographic lattice within the sample. However the experimental method used to record this neutron diffraction response is somewhat different to that used in XRD. In this approach, instead of fixing the wavelength of the incident radiation, the scattering angle 2θ is fixed by recording diffraction from a single orientation. This scattering angle is determined by the direction of the scattering vector within the sample of interest, $\boldsymbol{Q}$. For example, Figure 2.6 shows a schematic diagram of the experimental setup used in the neutron diffraction study in Chapter 4. In this arrangement, insight into the lattice strain response in directions parallel and perpendicular to the loading direction was performed by aligning the scattering vectors ($\boldsymbol{Q_1}$ and $\boldsymbol{Q_2}$) corresponding to diffraction (detector) banks 1 and 2 in these two orientations.

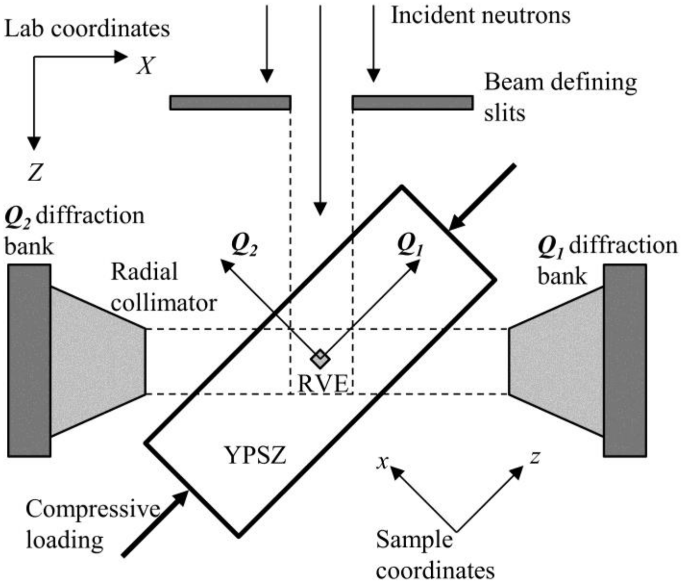

Figure 2.6. Plan view schematic diagram of the neutron diffraction experimental setup at beamline Engin-X which was implemented in Chapter 4.

The incident beam is composed of neutrons travelling at different speeds and therefore the time taken for each neutron to travel from the spallation target to the detector bank can differ. These small variations in the time of flight are carefully recorded by the detector banks in order to populate a distribution of intensity against flight time (Figure 2.7). These distributions are similar in form to the 1D intensity against 2θ plots produced by radial integration of 2D diffraction plots, with diffraction peaks corresponding to the lattice spacing at a given Miller index. Gaussian peak fitting can be used to determine the time of flight associated with each peak centre (t_{hkl}) which is related to the neutron wavelength (λ_{hkl}) corresponding to each peak centre through the de Broglie equation:

$$\lambda_{hkl} = \frac{ht_{hkl}}{m_n L_T}, \tag{2.9}$$

where L_T is the beamline specific total flight path from the neutron source to the detector, h is Planck's constant and m_n is the mass of a neutron. A rearranged version of Bragg's law can then be used to find the lattice values associated with each peak:

$$d_{hkl} = \frac{\lambda_{hkl}}{2\sin\theta}, \tag{2.10}$$

where 2θ is equal to the scattering angle (which is equal to 90° for the experimental arrangement shown in Figure 2.6). These values can then be used to provide estimates of lattice strain through Equation 2.7.

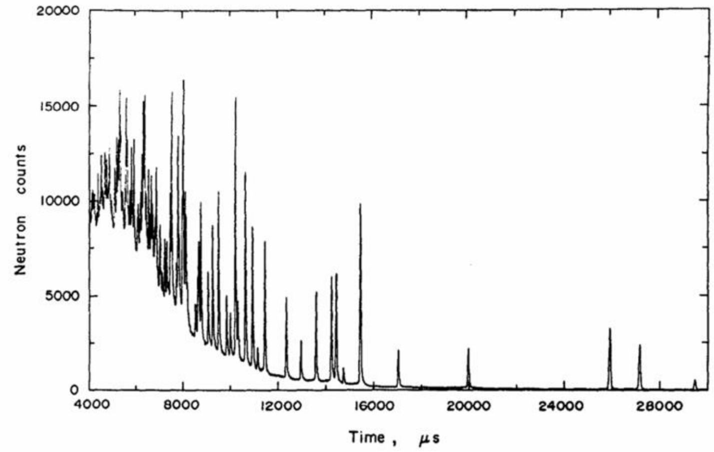

Figure 2.7. Time of flight against intensity for a zirconium alloy [78].

Neutron diffraction can also be used to provide insight into larger scale features within the range of $\approx 1 - 100$ nm through the use of Small Angle Neutron Scattering (SANS). The origins of this behaviour lie in the scattering response of an array of regular sized or regularly spaced features such as voids and grain boundaries within this nanoscale length range. The constructive interference between scattered waves results in a diffraction peak which is indicative of the length scale of these features.

Of particular importance to the field of SANS, is the relationship between the magnitude of the reciprocal space scattering vector ($|\boldsymbol{Q}| = Q$) and the spacing between scattering features (d):

$$Q = \frac{2\pi}{d}. \tag{2.11}$$

This expression demonstrates that the larger nanoscale features examined in SANS will correspond to a scattering vector which is smaller in magnitude. Bragg's law can then be used to show that for a particular neutron wavelength, the scattering angle (2θ) will be reduced. Therefore, in a typical SANS arrangement, detector banks are placed far from the sample in order to collect information at small Q. For example, the SANS analysis outlined in § 5.3 was performed at beamline LOQ at ISIS Neutron Spallation Source, which has a 2D area detector placed 4.1 m downstream of the sample and is able to collect information in the range $Q = 0.006 - 0.24$ Å^{-1}. Each pixel in the 2D array corresponds to a known scattering angle, which can be used to convert the time resolved spectra recorded into a single plot of intensity against Q through Equations 2.9-2.11 as shown in Figure 2.8. The presence of peaks within this intensity distribution can be used to provide insight into the average size (peak centre), distribution (peak width) and number density (peak magnitude) of nanoscale features [79]. Power law fitting of the underlying distribution can also be used to provide insight into the shape or interface behaviour of these features [80].

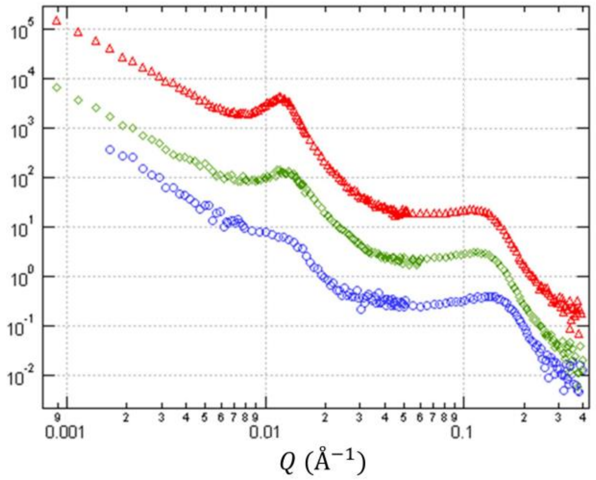

Figure 2.8. SANS intensity against Q for 3 polymers showing differing levels of crystallinity [81].

2.2.3. Pair Distribution Function Analysis

In recent decades, diffraction based techniques for high resolution structural analysis of crystalline materials have become well-established and broadly applied in order to improve understanding of localised strain in these materials. These techniques are based on the sharp diffraction peaks which occur as a result of the regular lattice structure in these materials (Figure 2.9a). In contrast, limited insight has been available into the atomistic behaviour of amorphous materials due to the diffuse scattering response associated with these materials (Figure 2.9b). This scattering behaviour is representative of the average spacing between atoms in disordered materials such as dental porcelain, however cannot be analysed for strain in the same manner as in XRD or neutron diffraction peak analysis.

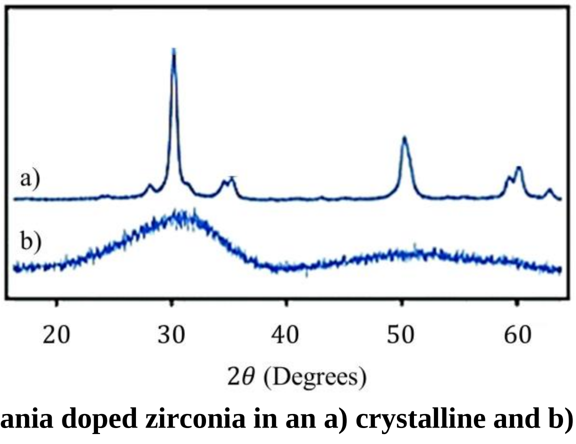

Figure 2.9. XRD of titania doped zirconia in an a) crystalline and b) amorphous state [82].

In order to extract local structure information from these amorphous diffraction spectra, a new approach has been developed which provides insight into the real space atomic spacing from the reciprocal space data collected. This relation is known as the Pair Distribution Function (PDF) $(G(r))$ which represents the probability of finding an atom at a particular radial distance (r) from any atom within the structure as shown schematically in Figure 2.10.

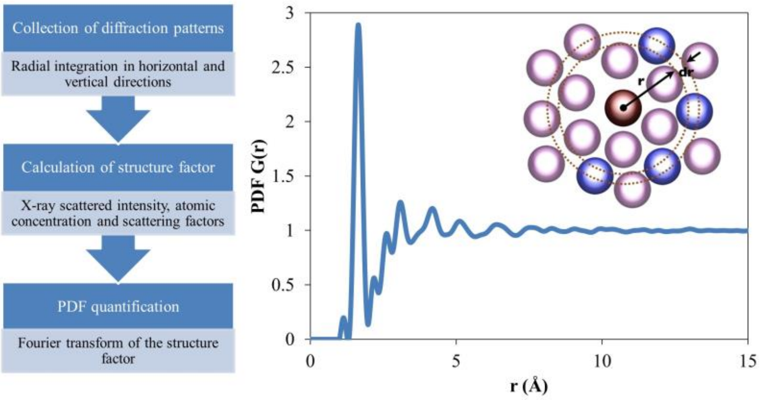

Figure 2.10. Schematic of steps involved in PDF analysis and a typical $G(r)$ for dental porcelain.

Successful implementation of this analytical method is dependent upon precise flat and dark field correction of the diffuse diffraction images collected, using the relationship:

$$C(i,j) = \frac{[R(i,j) - D(i,j)] \cdot m}{F(i,j) - D(i,j)}. \tag{2.12}$$

where i, j represents the pixel position in the matrix, C is the $I \times J$ sized matrix representing the corrected image, R is the raw image matrix, F is the flat field image matrix (with the sample removed), D is the dark field image matrix (with the shutter closed) and $m = \frac{1}{IJ}\sum_{i=1}^{I}\sum_{j=1}^{J}[F(i,j) - D(i,j)]$.

During the experimental process, care must also be taken to ensure that the scattering response at large Q values is collected. This factor is critical during the Fourier transformation of the diffraction data as it is used as a finite approximation to the infinite integral and small values of Q_{max} induce Fourier termination errors (aberrations) in the PDF. Therefore in the case of XRD, high energy incident radiation (small λ), small sample to detector distances and large detectors (large θ) are used to maximise the recorded Q space. For example, the PDF analysis outlined in § 6.2 was performed at Beamline I15 at Diamond Light Source, Harwell, UK using a monochromatic incident radiation of 76 keV and a sample to detector distance of 262 mm to capture scattering up to $Q_{max} = 25.1\ \text{Å}^{-1}$.

Following radial integration of the corrected image, the resulting intensity against Q distribution is used to quantify the normalised structure function $S(Q)$. This is a descriptor of how the material scatters incident radiation which takes into account the scattering factors associated with each constituent element and a comprehensive overview of this analytical step has previously been presented elsewhere [83]. The Fourier transform of this function can then be used to determine the $G(r)$ through [84]:

$$G(r) = \frac{2}{\pi}\int_0^{Q_{max}} Q[S(Q) - 1]\sin(Qr)\,dQ. \tag{2.13}$$

Molecular Dynamic (MD) simulations offer a powerful modelling tool which can be used to simulate the amorphous structures analysed using PDF analysis. Progressive refinement of the atomic arrangement can be performed by comparing simulated PDFs with those obtained experimentally in order to provide a much improved understanding of the atomic structure of a given material [85].

An alternative use for PDF analysis of amorphous materials was recently presented in an article by Poulsen et al. entitled “Measuring strain distributions in amorphous materials” [86]. Applied strain has recently been shown to be linearly related to PDF peak shifting in bulk metallic glasses [87]. This has served as the basis for a new strain characterisation technique which has been established and applied to a porcelain veneer in § 6.2.

2.2.4.Energy Dispersive X-ray Spectroscopy

In recent decades, EDXS has become a well-established technique for high resolution (microscale) elemental composition analysis in a broad range of materials. This experimental technique is based on excitation of the atoms within a region of interest, followed by characterisation of the resulting X-ray radiation. Atomic excitation can be induced through laser or X-ray interaction, however the combined imaging and excellent (sub-micron) focusing capabilities of SEM beams ensures that this excitation source is the most widely used. Monte Carlo simulations of EDXS have demonstrated that the gauge volume of this technique has a characteristic teardrop shape (Figure 2.11a) with dimensions that are highly dependent upon the elemental composition sample of interest [88]. For example the diameter of a typical gauge volume is expected to be ≈ 1.5 μm in dental porcelain and ≈ 1.2 μm in YPSZ.

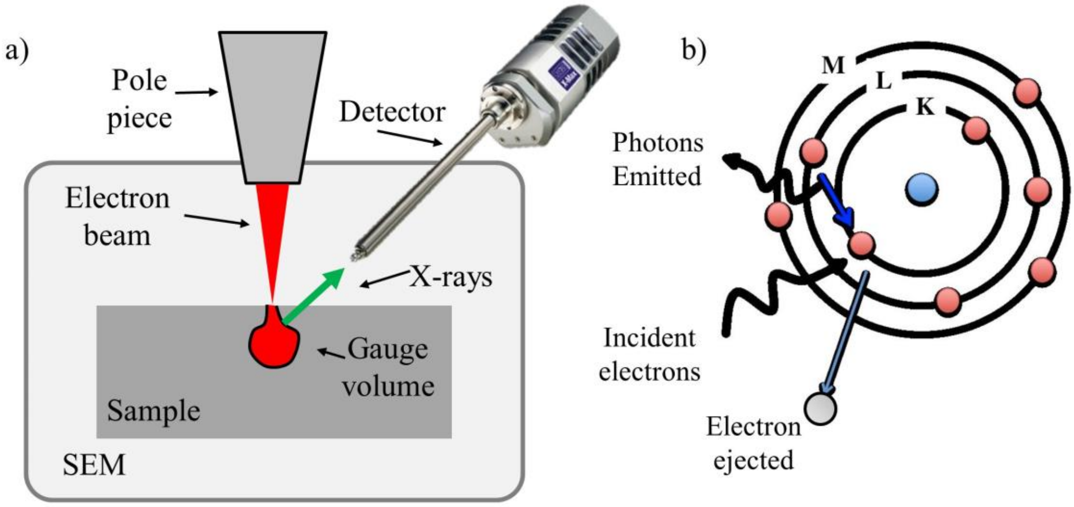

Figure 2.11. a) Schematic representation of EDXS experimental approach, b) electron orbital representation showing the origin of photon emission.

Photon emission in EDXS is induced by the interaction between incident radiation and electrons within an inner shell of the atom (Figure 2.11b). The energy transferred during this interaction results in the ejection of an electron and the creation of a hole. An electron from a higher energy shell then fills the hole and emits the excess energy as a photon. The wavelength of this radiation is dependent on the difference between the energy levels in the excited atom and therefore this characteristic signature can be used to determine the atomic species present within the gauge volume.

An energy dispersive spectrometer is next used to count the number of photons emitted at a given wavelength and within a predefined energy band (usually in the range $0 - 30$ keV for in SEM analysis). Several million photon counts are required in order to build up a representative spectrum of the type shown in Figure 2.12a. Analysis of the elemental composition can then be performed by comparing the relative intensities of the peaks associated with different atomic species. This process of peak refinement and fitting has become routine and fully automated using commercial software such as AZtecEnergy [89]. Elemental composition mapping is now also possible through rastering of the incident electron beam and recording spectra at each point as shown in Figure 2.12b.

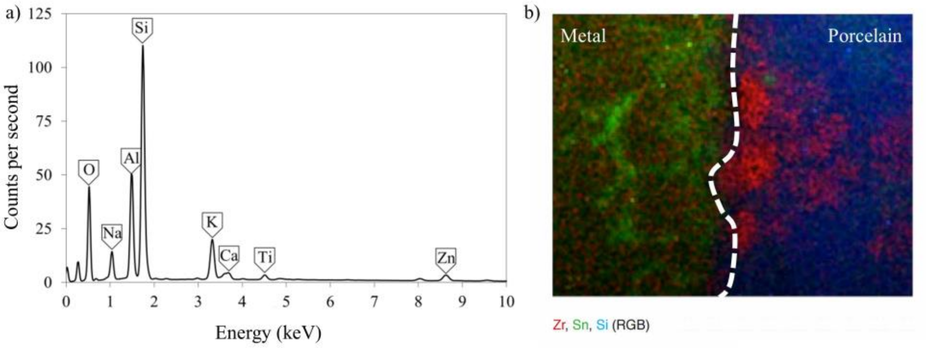

Figure 2.12. a) Typical EDXS spectra for e.max Ceram dental porcelain with annotation of the peaks corresponding to different elements. b) 2D EDXS elemental mapping of interface in a porcelain veneered metal prosthesis [90].

2.2.5.Raman Spectroscopy

Raman micro-spectroscopy offers a sensitive tool for spatially resolved (at ≈ 1 μm resolution or better) mapping using chemical bond identification. In this technique, a monochromatic laser beam (in the visible frequency range) is focused at the sample surface, the scattered light is recorded by a spectrometer, and the energy (wavelength) shift spectrum is examined. Basic interpretation of the Raman spectroscopic shift assumes that the material may be represented by balls (atoms) connected with springs (chemical bonds) that vibrate in response to an input of energy. Vibrational modes of specific molecules are functions of a number of factors such as bond orientation and length, atomic mass, etc. Whilst most incident photons undergo elastic Rayleigh scattering at the same energy as the incident photons, a small fraction (approximately 1 in 107 photons) is inelastically scattered at longer wavelengths (Stokes shift), whilst an even smaller proportion are shifted to shorter wavelengths (anti-Stokes shift). A band stop filter removes elastically scattered photons and a Raman spectrometer detects and measures the intensity of the remaining light as a function of wavelength shift. The Raman shift is calculated using:

$$\omega = \frac{1}{\lambda_i} - \frac{1}{\lambda_s}, \tag{2.14}$$

where λ_i and λ_s represent the wavelengths of the incident scattered light respectively. It is worth noting that the Raman shift represents the energy difference between levels which are characteristic of a particular material, and does not depend on the frequency of the incident radiation. Each peak therefore corresponds to a particular vibrational mode within the material.

The intensity of Raman peaks of YPSZ is directly proportional to the concentration of scattering crystallographic species, enabling quantitative microanalysis of monoclinic and tetragonal phases to be conducted (Figure 2.13a). However, at this stage it is important to note that in the context of Raman spectroscopy, peak intensity is defined as the number of counts recorded at the peak apex [91]. In the case of solid samples, the shape of Raman peaks are well approximated by the Gaussian distribution (Equation 2.2) [92] and therefore the values of α obtained through peak fitting can be used as representative estimates of Raman peak intensity. The most widely used empirical relationship which can be used to determine YPSZ monoclinic volume fraction from Raman spectroscopy data was developed by Clarke and Adar and is given as [93]:

$$V_m = \frac{\alpha_{178}^m + \alpha_{189}^m}{0.97(\alpha_{145}^t + \alpha_{260}^t) + \alpha_{178}^m + \alpha_{189}^m}, \tag{2.15}$$

where the superscript of α refers to the tetragonal and monoclinic phase of the peak and the subscript refers to the wavenumber of the peak centre in cm^{-1}.

Raman spectroscopy can also provide insight into the residual (or applied) stress within the interaction volume by exploiting the proportionality between Raman peak centre shifting and a representative average stress (Figure 2.13b). Analysis of the stress state within different crystallographic states is also possible by examination of the differing peak shifting responses associated with each phase. In the case of YPSZ, peak shifting has been shown to have the strongest correlation with the first invariant (trace) of the stress tensor [94] and a comprehensive overview of the peak shifting response of monoclinic and tetragonal peaks up to 800 cm^{-1} has recently been published [91].

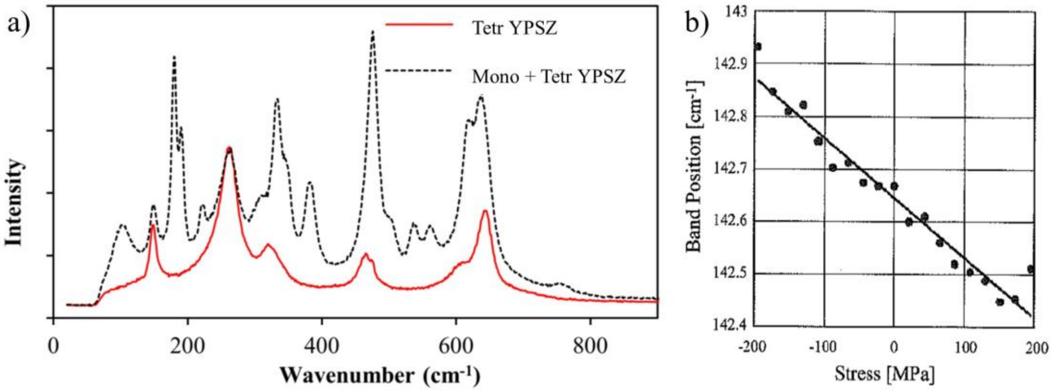

Figure 2.13. a) Raman wavenumber against intensity for tetragonal and two phase YPSZ [72]. b) Peak centre against applied stress for the tetragonal peak at nominal centre 145 cm^{-1} [91].

2.3. Microscale Mechanical Characterisation

The last decade has seen significant development in the precision, capability and use of microscale testing devices such as nanoindenters and SEM loading stages. These improvements can be directly related to the advent of reliable, high precision piezoelectric systems which have been used to manufacture microscale actuators (piezo-stages) and highly sensitive load cells (piezo-transducers). These advances have coincided with increasing access and significant improvement in the capabilities of micromachining techniques such as FIB milling and micro-lithography, which facilitate the manufacture of microscale mechanical testing specimens and loading devices. The combined capabilities of these two fields have led to the conception and development of multiple microscale mechanical testing routines which have been used to provide improved understanding of mechanical interaction at small length scales. These insights are critical in improving component design and reducing failure in a broad range of macro and microscale components [95].

Example studies include the microscale fracture toughness analysis through loading of a notched micro-beam (Figure 2.14a) [96]. Nanoindentation for microscale hardness and elastic modulus testing has become routine and can be combined with atomic force microscopy in order to assess the impact of pileup (Figure 2.14b) [33]. Micro-cantilever bending has been established as a method to resolve residual stresses within thin films (Figure 2.14c) [97] and micro-tensile loading can now be performed on FIB milled dog-bone specimens (Figure 2.15d) [98].

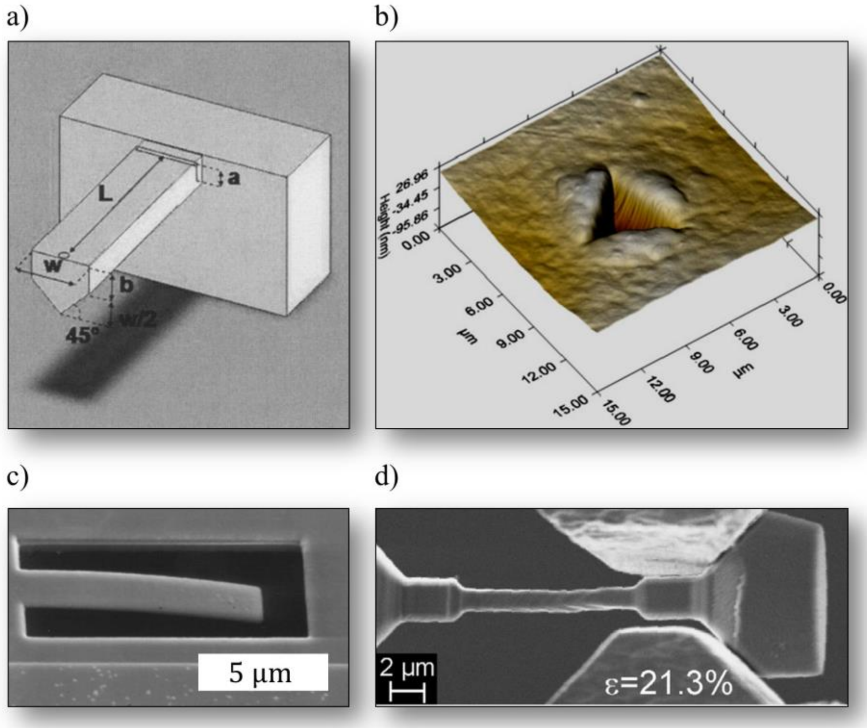

Figure 2.14. Experimental geometries of microscale mechanical testing methods. a) Micro-beam geometry for fracture toughness analysis [96], b) nanoindentation for hardness testing in YPSZ [33], c) micro-cantilever bending for residual stress analysis in thin films [97], d) micro-tensile analysis of plastic deformation in copper [98].

The micromechanical testing performed in this study has been selected to improve insight into the most important characteristics in improving the understanding of failure at the YPSZ-porcelain interface. These can be grouped into two categories; micropillar manipulation for improved characterisation of mechanical properties and FIB milling for residual stress analysis.

2.3.1.Focused Ion Beam Milling

In recent years FIB milling has become increasingly used as a micromachining tool in the preparatory stages of high resolution studies such as in the manufacture of TEM lamella, or micro-cantilevers [99]. FIB milling was originally developed as a standalone technique for use in the semiconductor industry however modern FIB systems are typically integrated into SEMs in order to facilitate simultaneous imaging and milling, as well as exploiting the vacuum conditions, sample stages and detectors required by both systems.

FIB milling is based on the generation and acceleration of ions which are directed towards the sample of interest. Ions are produced from a heated liquid source such as gallium, gold or iridium which is exposed to a potential difference sufficient to induce spontaneous ion emission. The ion beam is next refined, accelerated and focused onto the sample through a series of electromagnetic lenses in order to produce a beam with a typical energy of 30 keV and spot size of a few nanometres. Careful control of the milling current can then be used to determine the nature of beam interaction with the sample surface. High milling currents (≈ 10 nA) can be used to sputter atoms from the surface and mill features such as the trenches required during TEM lamella preparation (Figure 2.15a).

Following coarse milling, a reduced current (≈ 150 pA) is typically required to polish and refine the remaining features. This intermediate level current is also used for techniques such as FIB tomography in which serial sectioning and SEM imaging are used to produce 3D representations of a particular gauge volume (Figure 2.15b). Reduced currents are also suitable for FIB deposition, which involves gas injection of hydrocarbon precursors containing heavy metal atoms such as platinum onto the surface of the sample. Ion beam interaction with these molecules results in the removal of the organic ligands leaving the heavy metal ions bonded to the sample surface. Further reductions of the ion beam current (≈ 1 pA) facilitates ion beam imaging which is based on the emission and detection of secondary electrons during raster scans of the sample surface, as used in SEM imaging.

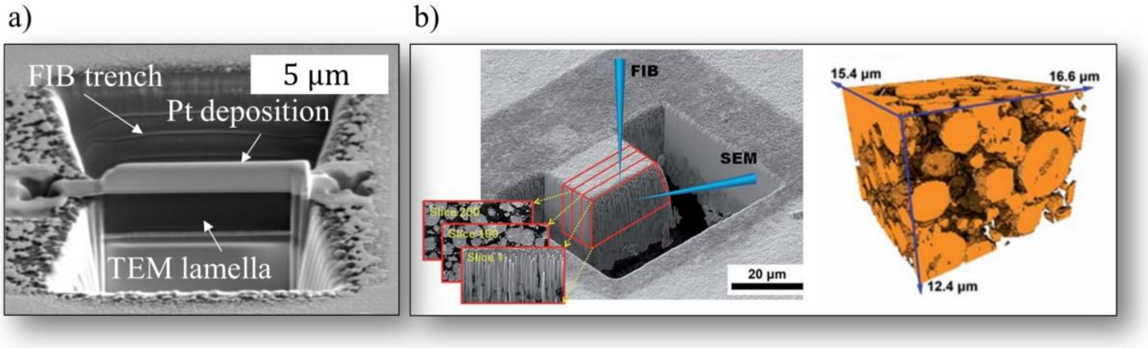

Figure 2.15 FIB techniques a) TEM lamella preparation in an organic light emitting diode, [100] b) FIB tomography of a Li battery cathode [101].

2.3.2.Micropillar Compression and Splitting

In the past ten to fifteen years the new field of micropillar mechanical microscopy has been established to provide improved insight into the elastic behaviour, deformation response and fracture characteristics of a broad range of materials. Micropillar manufacture is based on FIB milling of an annular trench to produce a micropillar. A reduced milling current is then used to refine the pillar in order to produce a smooth and well defined cross sectional shape (Figure 2.16a). SEM imaging of the pillars is necessary in order to determine reliable estimates of both pillar height and cross sectional areas.

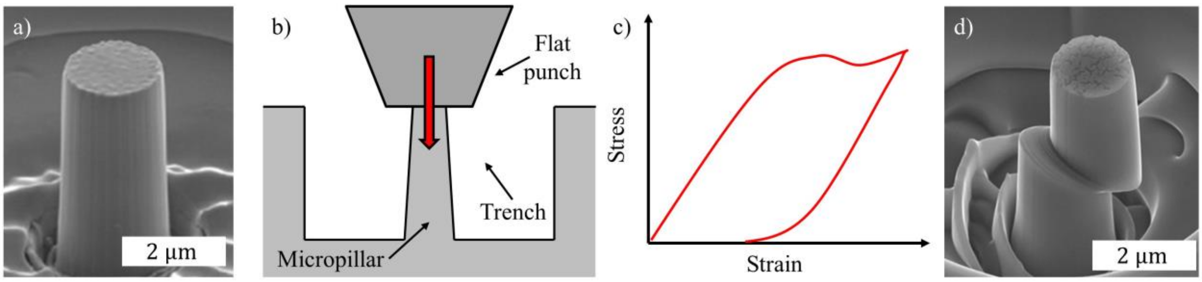

Figure 2.16. a) FIB milled micropillar, b) Flat punch compression, c) Characteristic stress-strain response, d) Pillar after loading [102].

As well as facilitating measurements from a small ($\approx 1 - 5$ µm diameter) gauge volume, micropillar testing benefits from complete residual stress relief in the pillar. This relaxation is critical in facilitating reliable mechanical characterisation and is known to have significant impact on alternative mechanical characterisation techniques such as nanoindentation [33]. The compact geometry associated with micropillar mechanical microscopy also facilitates high resolution ($\approx 10 - 15$ µm) incremental spatially resolved characterisation through FIB milling of pillar arrays.

In micropillar compression, square or circular cross section pillars are milled with a height to diameter aspect ratio of between 2.5 and 5 (Figure 2.16a). A flat punch nanoindenter tip is then aligned with the pillar using SEM imaging and the force-displacement response of the pillar is recorded during compression (Figure 2.16b). Normalisation of this loading response is then performed using the pillar cross sectional area and height in order to determine the stress-strain response of the pillar (Figure 2.16c). This distribution can be used to quantify the elastic modulus and yield strength behaviour of the microscale gauge volume. Further insight into the brittle or ductile deformation mode of the pillar can be obtained by imaging or post-compression characterisation of the pillar (Figure 2.16d) [103].

Micropillar splitting for high resolution fracture toughness quantification is a new approach which was first published by Sebastiani et al. in 2014 [63, 104]. This new technique was established to overcome some of the limitations associated with existing microscale fracture toughness techniques; the approach has a well-defined micro-scale gauge volume, requires a comparatively short and simple milling routine and induces fracture at the pillar centre (far from the FIB influenced region). In this approach a microscale pillar is milled with a height to diameter aspect ratio of 1 (Figure 2.17a) and indentation is performed in the pillar centre using a sharp nanoindentation tip (Figure 2.17b). Pillar fracture is observed as a load drop in the force-displacement curve at a critical load P_c (Figure 2.17c). The fracture toughness within the pillar (K_B) can then be determined from the expression [63]:

$$K_B = \gamma_B \frac{P_c}{R^{1.5}}, \tag{2.16}$$

where R is the pillar radius and γ_B is a dimensionless parameter dependent upon the ratio between Young's modulus and hardness in the substrate. Examination of the split pillar also provides insight into the type of fracture, as well as any preferred orientations in the fracture response (Figure 2.17d).

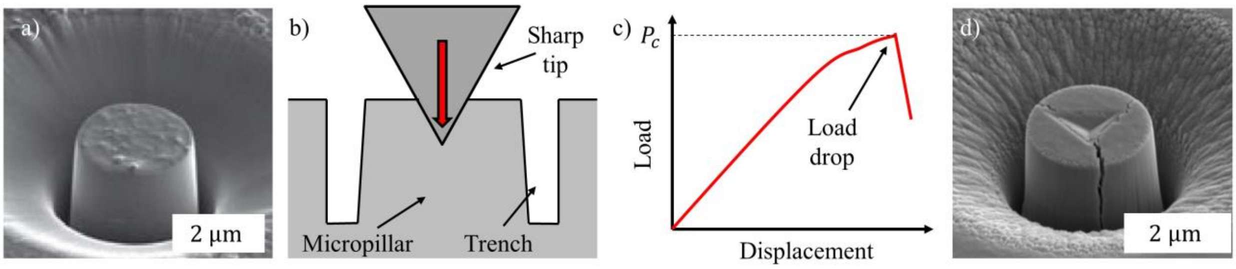

Figure 2.17. a) FIB milled micropillar, b) Pillar indentation, c) Characteristic load-displacement response showing load drop at fracture, d) Pillar after fracture[63].

Although micropillar splitting has a number of distinct advantages, this approach has been shown to be only suitable for brittle materials such as ceramics. Another difficulty associated with the current experimental approach is associated with precisely aligning a Berkovich indentation tip to the pillar centre. In order to overcome this limitation an approach using pillar centre markers and cube corner indentation has been developed and is outlined in § 7.5.

2.3.3.FIB Milling and DIC for Residual Stress Analysis

Quantification of residual stress through the introduction of traction (stress) free surfaces has become well-established at millimetre length scales through techniques such as hole drilling, ring-core milling and slitting [105]. In order to facilitate the miniaturisation of these techniques, material removal can instead be performed using FIB milling, which results in stress re-equilibration within microscale gauge volumes. In these cases, instead of using surface mounted strain gauges, quantification of the resulting strain change (relaxation) can be performed using DIC of SEM images of the sample surface.

DIC is based on the allocation of image subsets (or markers) within the region of interest which are tracked in subsequent images. In order to facilitate effective marker tracking, distinct features are required within the marker subsets and therefore several methods have been developed to increase SEM imaging contrast (Figure 2.18). In the case of rough surfaces, the intrinsic contrast has previously been shown to be sufficient to enable effective marker tracking (Figure 2.18a) [106], however for smooth heterogeneous substrates surface patterning is required. FIB deposition can be used to generate an array of high contrast features (Figure 2.18b) [107], however this approach is prone to aliasing during DIC and the influence of marker deposition of the underlying residual stress state is unclear. An alternative approach based on sputtering a thin film (≈ 5 nm thick) and applying a single pass of the FIB has been shown to produce a stable, high contrast and random surface pattern which is particularly effective, and which has minimal impact on pre-existing residual stress state in the sample surface (Figure 2.18c).

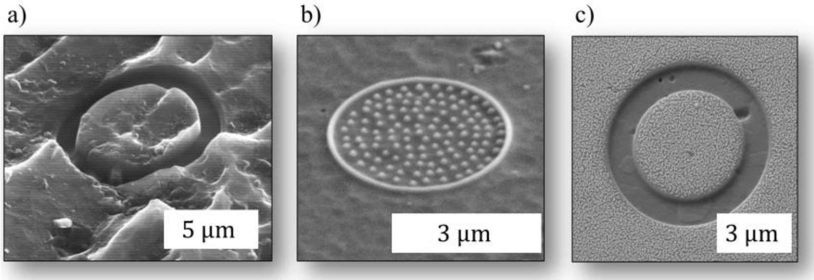

Figure 2.18. Methodologies for the generation of SEM imaging contrast. a) Intrinsic surface roughness [108], b) FIB deposition [107], c) sputter coating followed by a single FIB pass.

Commercially available DIC software such as LaVision DaVis [109] have been widely used to provide estimates of the relaxation induced by FIB milling, however many authors have chosen to adapt and develop open source software [110]. These modified routines can be tailored to meet the requirements of specific milling geometries and have resulted in vast improvements in the precision and reliability of strain quantification, as outlined in § 3.2.

Following the quantification of surface strain estimates, comparison with representative FE models of the milling approach is next required. Typically, these simulations are based on isotropic and homogenous material approximations and therefore care must be taken to determine the model suitability, for example in the case of large grained or anisotropic substrates [111]. Least squares fitting can then be used to match the experimentally observed relief with the FE simulations and to provide estimates of the pre-existing in-plane residual stress.

Residual stress analysis using FIB milling and DIC offers a number of distinct advantages over comparable microscale diffraction or spectroscopy based methods. Firstly, although focusing can be used to generate micro-to-nanoscale beam cross sections, diffraction and spectroscopy have potentially large gauge volumes in the direction of the incident beam. Beam alignment to the location of interest is also often challenging. In contrast, FIB milling and DIC based techniques have well defined microscale 3D gauge volumes, and can exploit SEM imaging to offer gauge volume alignment to nanoscale precision.

The second limitation is associated with the need for reliable estimates of unstrained reference samples, or lattice constants in radiation based analysis. Although relative variations in lattice parameter can be determined without this insight, it is not possible to carry out absolute residual stress determination. In comparison, FIB milling and DIC based measurements provide absolute measures through comparison with the stress-free surfaces induced by milling.

Diffraction based techniques also rely upon the interaction between the incident radiation and crystal lattices. Therefore, non-crystalline materials or materials in which severe deformation has resulted in large amounts of lattice distortion cannot be analysed using these techniques. In contrast, FIB milling and DIC can be applied equally well to amorphous or polymeric substrates [112, 113].

Apart from possessing demonstrable tangible benefits in terms of experimental capability, FIB milling and DIC techniques are also highly practical: the decreasing cost of SEM and FIB microscopy systems have resulted in widespread use of these systems. This increased access, in combination with the relatively short experiment durations (typically 10-50 measurements per day) has vastly reduced the nominal cost per stress measurement, making the approach highly competitive, especially when compared to synchrotron or other large facility based techniques.

Despite offering many advantages, care must be taken when performing FIB milling and DIC analysis in order to ensure that the residual stress estimate is representative. Typically, the origin of error can be grouped into three main categories; intrinsic limitations, imaging and sample preparation.

The main intrinsic limitation of FIB milling and DIC analysis is associated with the process of ion beam milling which involves bombarding the surface of the sample with high energy ions. Although on the macro-scale this approach is very gentle, highly localised (nanoscale) residual stresses are generated in these regions [114]. This phenomenon introduces a resolution limit for FIB milling and DIC based methods, below which ion milling itself begins to affect the residual stress state perceived.

SEM imaging is based on the acceleration and focusing of incident electrons and therefore, in the case of a highly insulating sample, charge build up can cause image distortion and drift in the milling position. In order to overcome this difficulty, the sample can be sputter coated with a conductive metal such Au or Pd, or conductive paint can be applied around the region of interest. Drift correction by tracking of a fiducial marker can also be successful for small amounts of drift.

Another effect widely known to influence the SEM imaging quality is the re-deposition of sputtered material onto the DIC tracking regions. In order to reduce this effect FIB milling can be performed at reduced milling rates or the amount of milled material can be reduced, for example by using a thinner trench. An alternative approach involves applying a deposition barrier between the DIC region and the milling location, although this approach may influence the residual stress state measured [35].

A third imaging difficulty is associated with the angular offset between FIB and SEM columns, and the fact that at any given time the plane normal of the sample can only be aligned with one of the two. One approach to overcome this difficulty is to rotate the sample between each milling and imaging step, however this approach is reliant upon the precision of stage rotation and has been shown to induce large amounts of drift. The alternative approach is based on correcting for the tilt of the SEM image by artificially changing the increment between points in the pixel array. This approach has been shown to minimise the error induced and has therefore become the most widely used technique [106].

In terms of sample preparation, the main limitation of the FIB milling and DIC residual stress analysis approach is associated with the near-surface nature of the technique. In many cases the residual stress analysis location lies below the surface and therefore sample sectioning has to be performed. This sectioning process modifies the residual stress state in the area of interest both through the introduction of a new traction free surface and through the machining applied. The relationship between the stress state before and after sectioning can be determined based on some simple approximations as outlined in more detail in Appendix A, and gentle removal techniques can also be used to minimise the impact of machining, for example through the use of electrical discharge machining, diamond wafering or grinding. These processes are typically followed by fine grain or electro-polishing in order to reduce further the impact of any induced residual stress.

Advances in FIB software and hardware have in recent years greatly expanded the range of geometries that can be milled using ion beams. This flexibility has enabled a wide range of FIB milling and DIC residual stress analysis techniques to be developed, each having particular advantages and limitations when compared to others.

Surface Slotting

FIB micro surface slotting was first published by Kang et al. in 2003 [115] and is based on the miniaturisation of the macro-scale crack compliance method. The approach is based on milling a single narrow rectangular slot into the material surface (Figure 2.19a) followed by DIC of the regions on either side of the slot. The simple milling regime and speed of analysis are the main benefits associated with this technique.

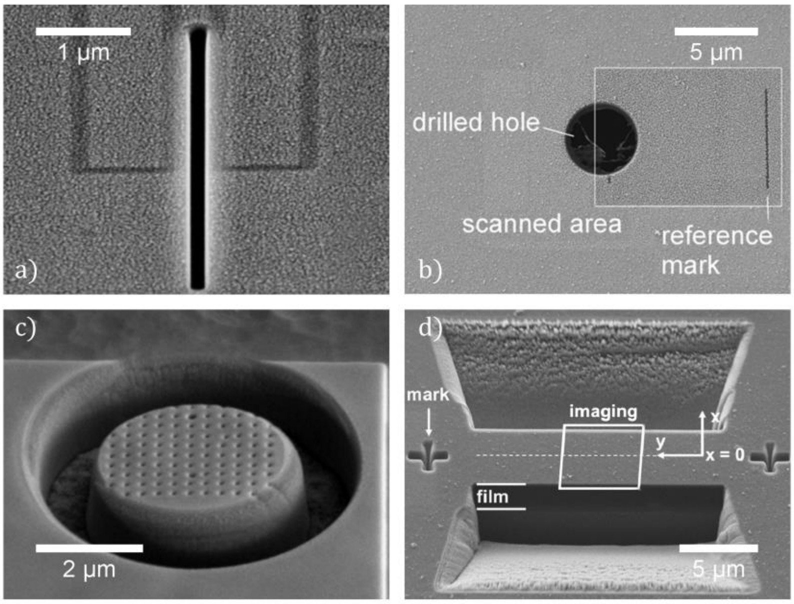

Figure 2.19. FIB milling and DIC residual stress analysis geometries. a) Micro-slotting [115], b) micro-hole drilling [116], c) ring-core milling [64] and d) the H-bar geometry [117].

As well as the limitation of only providing a single component measure of residual stress, micro-slotting relies on performing DIC on a region outside the 'nominal' gauge volume. This greatly reduces the precision of the gauge volume definition both in terms of size and position. The geometry also limits how close subsequent markers can be placed, severely restricting spatially resolved analysis.

Hole Drilling

FIB micro hole drilling was originally published by Sabaté et al. in 2007 [116] and is based on the miniaturisation of the simple and fast classical hole drilling technique [118]. This approach provides a measure of the 2D stress state in the surface of interest by milling a small circular hole and performing DIC of the surrounding region (Figure 2.19b).

Similar to micro-slotting, the use of external strain field analysis in micro hole drilling limits the gauge volume precision and suitability of this technique for spatially resolved analysis. Another difficulty is associated with the limited amounts of strain relief induced by milling. This increases the impact of noise on the residual stress estimates and requires regularisation in order to overcome the resulting unrealistic variations in residual stress, thereby limiting the sensitivity of the technique [119].

Ring-core Milling

The micro-scale ring-core FIB milling and DIC approach was originally proposed by Korsunsky et al. in 2009 [64] and is based on the miniaturisation of the macroscopic ring-core method. In this experimental method, an annular milling pattern is used to obtain full strain relief of a core of material lying at the sample surface (Figure 2.19c). This approach ensures that the gauge volume is well defined both in terms of position and size. The isotropic nature of this milling geometry also facilitates strain quantification in different orientations in order to determine the complete 2D in-plane stress state in the sample of interest. Other advantages include the large, near uniform strain relief induced in the core [120], which facilitates effective averaging and provides stress estimates which are robust to noise. Finally, the use of a central core, rather than a reliance upon surrounding region means that markers can be placed close together for high resolution spatially resolved analysis [121]. Depth resolved analysis has also recently been demonstrated using this technique [107].

The principal difficulty associated with the micro-scale ring-core FIB milling approach is the small region over which DIC analysis can be performed. In order to overcome this limitation, an approach based on incremental milling and repeated SEM imaging has been developed [64, 106, 122]. This approach provides a record of the average strain relief within the micro-pillar island (or core) as a function of milling depth which is then compared with the results of FE modelling.

H-bar Milling

The H-bar FIB milling geometry was originally proposed by Krottenthaler et al. in 2012 [117]. This approach is based on milling two trenches on either side of the gauge volume in order to quantify the residual stress component in a direction perpendicular to the long axis of the trench (Figure 2.19d). This method has a well-defined gauge volume and benefits from a large uniform strain relief within the central bar. DIC analysis is performed within this relatively large region in order to provide improved strain averaging when compared to other techniques.

The main limitation of the H-bar geometry is the fact that only one strain component can be detected. However a recent publication has demonstrated that the subsequent addition of a second set of trenches (in a direction perpendicular to the first) can be used to provide insight into the residual stress state in a direction perpendicular to the first measurement [123].

3. Refinement of the Ring-core FIB Milling and DIC Residual Stress Analysis Technique

3.1. Introduction and Motivation

The ring-core geometry has become well-established as one of the most versatile and powerful FIB milling and DIC milling routines due to the high magnitude near-uniform strain relief induced in the core during milling [120] and the corresponding increased noise robustness and residual stress estimate precision. Despite these advantages, as outlined in § 3.2, the existing implementation of this method had not released the full potential of this analytical technique. Therefore, in order to facilitate the residual stress analysis required to improve the understanding of the YPSZ-porcelain interface characteristics, refinement of the ring-core FIB milling and DIC technique has been performed.

Precise and consistent estimation of the confidence interval of any quantitative measurement is necessary in order to draw reliable conclusions from the data captured. A new analytical routine for complete error assessment, automated outlier removal and confidence interval propagation has been established, as outlined in § 3.3. This approach has recently been published in my review article [106].

The isotropic nature of the ring-core milling geometry ensures that strain relief can be determined in any given in-plane orientation. However existing techniques could not be used to take advantage of this aspect of the technique. Therefore I have established a new analytical method which is capable of resolving the angular variation of strain in order to evaluate the Full In-plane Strain Tensor (FIST) at each milling location, as outlined in § 3.4. An article validating this technique by comparison with XRD has recently been published in the Journal of Mechanics and Physics of Solids [124].

The ring-core geometry benefits from a precisely defined gauge volume and is not reliant upon strain analysis in neighbouring regions. This makes the approach eminently suitable for spatially resolved residual stress analysis. In this regard two new techniques have been conceived to facilitate residual stress analysis in the incremental range of mm to tens of microns (the sequential ring-core milling approach in §3.5) and between $10 - 1$ μm (the parallel FIB milling approach in §3.6). These approaches have facilitated the spatially resolved analysis necessary to improve insight into the YPSZ-porcelain interface, and have recently been published in my other journal review article [121].

3.2. Existing Capabilities of the Ring-core FIB Milling and DIC Geometry

Prior to widespread acceptance, the conception of a new experimental method is typically associated with simplifications and approximations which are gradually refined to provide a reliable and useful characterisation tool. Despite the many benefits of the ring-core FIB milling and DIC approach, at the start of this project this technique was still in the developmental stages and there were therefore a number of limitations which meant that it could not be used to provide the required insight into the residual stress state at the YPSZ-porcelain interface. This served as the motivation for the technique refinement outlined in § 3.3-3.5. However, in order to explain the origins of the work presented in these sections, an overview of the existing capabilities of the ring-core technique is provided in § 3.2.1, along with a brief overview of the required refinement in § 3.2.2.

3.2.1.Ring-core FIB Milling and DIC Technique Overview

The methodology underlying the ring-core FIB milling and DIC technique has previously been presented in detail in the literature [64], however in order to identify the existing limitations of the technique, a brief overview of the main stages in this analysis are presented here. A schematic representation of the main steps involved in this process is shown in Figure 3.1.

After placing the sample into the FIB-SEM chamber, the first stage of analysis involves aligning the FIB (red) and SEM (blue) incident beams onto the same location as shown in Figure 3.1a. The sample is then rotated to align the surface normal with the FIB beam. As outlined in § 2.3.3, SEM imaging can be performed either by using tilt correction (changing the ratio between horizontal and vertical pixel increments) or by tilting the sample to align the SEM column to the surface normal. Later studies have shown that the error associated with the tilt correction is far smaller than those induced by stage tilting, and therefore this approach has become the most widely used [106]. Following the collection of the first SEM image, a shallow (nanoscale depth) annual feature is FIB milled into the surface. Repeated SEM imaging and shallow incremental FIB milling is then performed until the core has become fully stress relieved. This occurs at a milling depth (H) approximately equal the core diameter, d (as shown by the strain relief profile in Figure 3.1f).

At this point in the discussion it is important to point out that the original implementations of the ring-core FIB milling and DIC approach were based on residual stress analysis at a single location within a thin film which was in a state of isotropic stress [64, 107, 125]. Firstly, this stress state ensured that

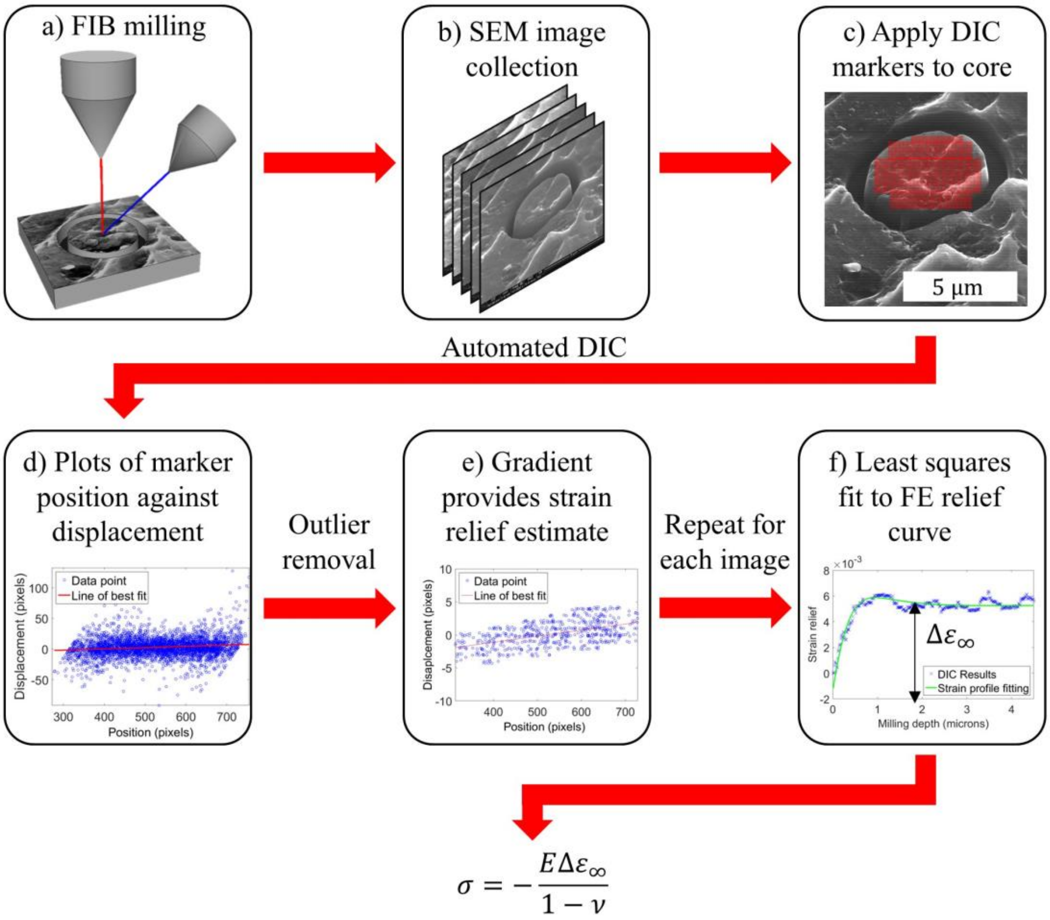

Figure 3.1. Schematic representation of the existing ring-core FIB milling and DIC approach. a) FIB milling and b) SEM image collection form the experimental stage. c) Marker placement and automated DIC is then performed on the images collected to produce d) plots of position against displacement. e) Following outlier removal the gradients of these plots are used to determine the strain relief estimate associated with each image. f) Least squares fitting of FE relief profiles are then used to quantify $\Delta\varepsilon_\infty$, which can be used to determine residual stress.

residual stress analysis was equivalent in any direction and secondly no spatially resolved analysis was performed. In the case where multiple measurements were made (to gain insight into the scatter of the localised stress state) the milling positions were selected to be at large distances from each other in order to ensure that there was no interaction.

Following the collection of the SEM images (Figure 3.1b), quantification of the strain relief can be performed using DIC of the SEM images collected (Figure 3.1c). DIC is an image processing technique which is used to determine the relative displacement field between two or more images. This technique is well established and the fundamental principles [126, 127], coding implementations [110, 128] and potential applications [129, 130] have been discussed at length elsewhere.

For a given example, the displacement field can be composed of image shift, distortion, rotation or magnification. Analysis is typically performed using one of two approaches: full field DIC [131, 132] involves applying an unknown displacement field to the entire original image to estimate the average global change, or subset DIC [133, 134], which is associated with placing markers (“seeds”) onto the original image, each of which is associated with a particular correlation subset window. The displacement field of each of these subset windows can typically be determined in a computationally efficient and fast fashion compared to full field DIC. The flexibility associated with subset DIC, in terms of marker placement, size and overlap, along with the ability to assess and eliminate poorly tracked markers, has meant that this DIC approach has become increasingly robust, reliable and efficient.

Although it is theoretically possible to determine the full displacement and distortion field at each marker, subset DIC is typically based on the approximation that the displacement field can be represented purely by a vector shift between the two data sets. For this approximation to be valid, image distortion and rotation need to be small in the limited subset window. This approach enables precise and rapid estimation of the relative displacement through the use of 2D normalised cross-correlation $C(u,v)$ [135]. In the case of a subset window ($\mathcal{S}$) half-width of n pixels (total size of $(2n+1)\times(2n+1)$ pixels) and an image $\mathcal{I}$, the cross-correlation surface at a position u,v is given by:

$$C(u,v)=\frac{\sum_{i=-n}^{n}\sum_{j=-n}^{n}[\,\mathcal{S}(i,j)-\overline{\mathcal{S}}\,]\cdot[\,\mathcal{I}(u+i,v+j)-\overline{\mathcal{I}_{uv}}\,]}{D(u,v)}, \tag{3.1}$$

where

$$D(u,v)=\sqrt{\sum_{i=-n}^{n}\sum_{j=-n}^{n}[\,\mathcal{S}(i,j)-\overline{\mathcal{S}}\,]^2\cdot\sum_{i=-n}^{n}\sum_{j=-n}^{n}[\,\mathcal{I}(u+i,v+j)-\overline{\mathcal{I}_{uv}}\,]^2}, \tag{3.2}$$

$\overline{\mathcal{S}}$ is the mean intensity value of the subset, and $\overline{\mathcal{I}_{uv}}$ is the mean intensity value within a $(2n+1)\times(2n+1)$ window within $\mathcal{I}$ that is centred at u,v. This expression can be repeatedly applied across the region to determine the profile of the cross-correlation function over the given range of u and v displacements as shown in Figure 3.2. The peak position on this surface corresponds to the u,v combination that achieves the most similarity between the subset windows chosen within the reference and deformed images. The magnitude of the peak is the correlation coefficient, r. It is a measure of similarity between the subset windows in the reference and deformed image, with the value of unity indicating that the two subset windows are identical.

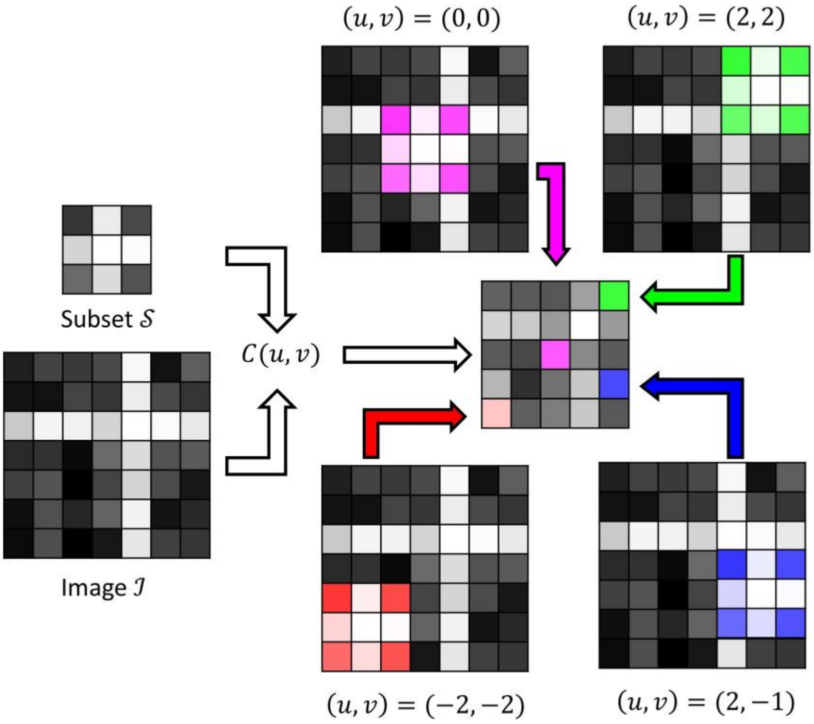

Figure 3.2. Schematic of normalised 2D cross-correlation, $C(u,v)$, between subset $\mathcal{S}$ and image $\mathcal{J}$. Each pixel value on the cross-correlation surface is associated with a different relative offset (u,v) between the $\mathcal{S}$ and $\mathcal{J}$ as shown on the right side of the figure.

Post-processing of the shifts determined at each marker location can then be used to quantify global displacement fields between the initial and subsequent images. Typically in FIB residual stress analysis, the DIC strain resolution sought is 10^{-4} or better; this corresponds to 1 pixel displacement over 10,000 pixels. This lack of high precision has previously served as the main limitation in the use of DIC to quantify strain relaxation. Despite this, the combination of four approaches has recently facilitated this precision:

1. *Sub-pixel resolution DIC.* Vector shift is typically calculated using integer pixel displacement values of u and v. In order to improve the precision of shift determination, the estimation of the peak position can be obtained by functional fitting of the cross-correlation surface, e.g. using a polynomial fit to describe the region closest to the peak. As well as providing a more statistically rigorous estimate (through the use of multiple data points), this approach can be used to determine the peak centre to sub-pixel resolution, typically to better than 0.05 pixels.
2. *DIC marker averaging.* The displacement of markers within the FIB milled core has been shown to vary linearly with position as shown in Figure 3.1e. Least squares fitting of the linear relationship between these displacement measurements and the results of FE analysis can be

used to provide the final estimate of strain relief [136]. The average displacement of many thousands of markers can therefore be used to improve further the precision of the strain relief.

3. *High magnification SEM imaging.* In order to optimise the accuracy of converting displacements determined by DIC into strain, high magnification and high pixel matrix SEM imaging is necessary. Typically, DIC analysis is performed on SEM images of the size greater than 1024×1024 pixels, with the nominal pixel size of 5 nm or less.
4. *High imaging contrast.* In order to optimise 2D image correlation, high contrast imaging is necessary. This ensures that the cross-correlation surface peak is sharp, so that sub-pixel peak displacement measurement is valid (as outlined in detail in § 2.3.3).

In order to determine quantitative estimates of the strain relief within the core at each milling depth, plots of the change of marker position (Δx) against position (x) are used (Figure 3.1d). The gradient of this plot is equal to the strain relief at a given image number ($\Delta\varepsilon = \Delta x/x$) however care must be taken when performing this analysis in order to effectively remove outliers. Prior to the refinement outlined in § 3.3, two outlier removal techniques were typically used at this stage of the analysis:

1. *Markers moving relative to neighbours.* The vector displacement field associated with each of the markers can be post processed to assess if any markers appear to undergo large displacement relative to their neighbours, and thereby remove those erroneous points. Typically in the case of ring-core FIB milling and DIC, the displacement fields observed within the material are approximately uniform, or at most approximately linear over small regions. Therefore, a normalised dot product between each vector and the average shift of several of its neighbours is used to determine outliers within the data set as shown in Figure 3.3. In the case of a uniform displacement field this normalised dot product (c) will be equal to unity (Figure 3.3a). If the markers move in opposite or different directions this value will be less than unity (Figures 3.3b and 3.3c), and if the shift of the chosen point is in the same direction as its neighbours, but has a larger magnitude, then this value exceeds unity (Figure 3.3d). Thresholds can therefore be applied to leave only markers with c values within a certain range, for example between 0.5 and 1.5. Marker removal is also usually performed iteratively by removing markers showing the largest discrepancies and recalculating the relative shift of all other markers.

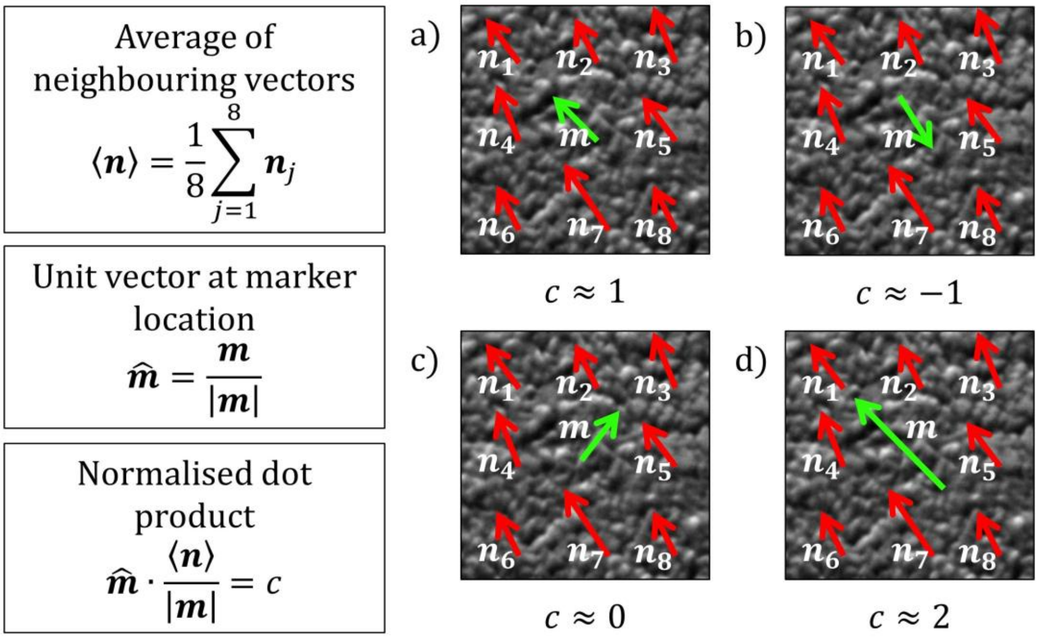

Figure 3.3. Schematic showing the value of the normalised dot product c between the average of 8 neighbouring vectors and a unit vector in four different cases. Thresholding is typically used to exclude poorly tracked markers in which the magnitude of c is greater than 1.5 or less than 0.5.

2. *Manual marker removal.* Manual examination of the strain or displacement fields produced by DIC serves is an alternative approach to reveal outliers and poorly tracked markers. Typically, a peak in the strain or displacement field is indicative of a poorly mapped region or marker and can therefore be manually removed from the data set. Despite the advantages of this outlier removal technique, this approach is highly subjective and results in a strain measure which is operator dependent. Therefore the formulation of new automated outlier detection and removal methods is critical to the repeatability of residual stress quantification, as outlined in § 3.3.

Following outlier removal, least squares fitting can be used to determine estimates of $\Delta\varepsilon$ as a function of image number (Figure 3.1e). The nominal milling increment can then be used to obtain the strain relief distribution as a function of milling depth as shown in Figure 3.1f. This relief curve has a characteristic form which has been determined through FE simulations of the ring-core milling geometry and has been characterised by the so called ‘relief master curve’ [64]:

$$f(\Delta\varepsilon_\infty, z) = 1.12\Delta\varepsilon_\infty \times \frac{z}{1+z}\left[1 + \frac{2}{(1+z^2)}\right], \qquad 0 < z < 2 \tag{3.3}$$

where $z = H/0.42d$, H is the milled depth, d is the core diameter and $\Delta\varepsilon_\infty$ is the full strain relief at an infinite milling depth. For large milling depths the value of the relief curve tends towards a plateau at $\Delta\varepsilon_\infty$ as shown in Figure 3.1f. This parameter describes the strain change induced in the core by complete relief of the residual stresses contained within the gauge volume and is therefore the critical parameter in the determination of the residual stress estimates. At this stage in the analysis it is also important to highlight that a positive strain change indicates that the island has increased in size during relaxation and therefore that the residual stress state within the core was originally compressive. Equivalently, relaxation of a tensile residual stress will lead to a reduction in core size which will result in a negative $\Delta\varepsilon_\infty$.

In the case of an isotropic in-plane stress state, analysis can be performed to determine $\Delta\varepsilon_\infty$ in any orientation and the residual stress estimate (σ) can then be quantified using:

$$\sigma = -\frac{E\Delta\varepsilon_\infty}{1-\nu}, \tag{3.4}$$

where E and ν are representative values for Young's modulus and Poisson's ratio within the gauge volume, respectively. The original ring-core FIB milling and DIC strain to stress conversion was based on bulk parameter approximations, which can provide reliable estimates of microscale behaviour in small grained untextured or elastically isotropic substrates [64]. However recent technique refinement has facilitated improved stress estimation in anisotropic conditions [111] and is outlined in § 3.3.5.

In order to provide useful estimates of residual stress, precise and well defined confidence intervals are needed. Despite this being an evident requirement, stress estimates from preliminary ring-core FIB milling and DIC have previously been published without the declaration of error bounds [107]. More recent analysis has provided simplistic error bounds based on the scatter associated with repeat implementations of the experimental technique [137]. This lack of, or very simplistic treatment of error severely limit the utility of the residual stress values obtained, thereby providing the motivation for the improved error estimation techniques outlined in § 3.3.

3.2.2.Refinement Required

A critical assessment of the overview of the existing capabilities of the ring-core FIB milling and DIC approach (in § 3.2.1) reveals that there are three main aspects which need refinement in order to facilitate improved understanding of the YPSZ-porcelain interface residual stress state. The first of these is associated with outlier removal, error analysis and propagation in order to provide well characterised error bounds of residual stress (in § 3.3.1 - § 3.3.3). Improvement of the relief profile fitting is also required in order to accommodate for uncertainties in milling rate and surface roughness (in § 3.3.4).

Finally the uncertainties in elastic modulus and Poisson’s ratio need be taken into consideration when converting these strain estimates to residual stress (in § 3.3.5).

The second developmental process is associated with the isotropic ring-core milling geometry and the potential insights into the in-plane residual stress state offered by this axisymmetric arrangement (in § 3.4). Most residual stress states cannot be approximated by isotropic conditions and therefore a new technique has been developed to determine the angular variation of residual stress within the core, and thereby estimate the in-plane principal strain magnitudes and orientations. These values can then be used to provide estimates of the principal in-plane residual stress state originally present in the core. Experimental validation of this technique has been performed by comparison with FIST XRD.

Thirdly, the ring-core FIB milling and DIC approach has been refined in order to facilitate microscale mechanical microscopy, i.e. residual strain profiling or mapping in the sample of interest. In the case of the sequential ring-core milling approach (in § 3.5), this has involved assessing the interaction between incremental milling locations and quantification of the minimal increment between successive measurements. The parallel FIB milling and DIC residual stress analysis technique (in § 3.6) has also been established in order to overcome the limitation associated with this incremental spacing between measurement points. Cross-validation of both approaches has been performed using XRD.

3.3. Outlier Removal, Error Analysis and Propagation

3.3.1. DIC Error analysis of SEM images

Accurate residual stress error quantification in FIB milling and DIC techniques depends upon the quality of the SEM images collected during the experimental process. The precision of the resulting DIC analysis is highly sensitive to the image noise, beam focus and contrast, and therefore error estimation must start from this stage of the analysis. As stated previously, the most widely used correlation approach is subset DIC. Therefore this new analytical routine has been established using the errors associated with the normalised 2D cross-correlation approach.

When sharp, high contrast, low noise images are captured, the cross-correlation surface typically takes the form of a single, sharp and well defined peak as shown in Figure 3.4a. The peak correlation coefficient is this case is close to unity, and the peak sharpness results in a precise estimate of the relative offset.

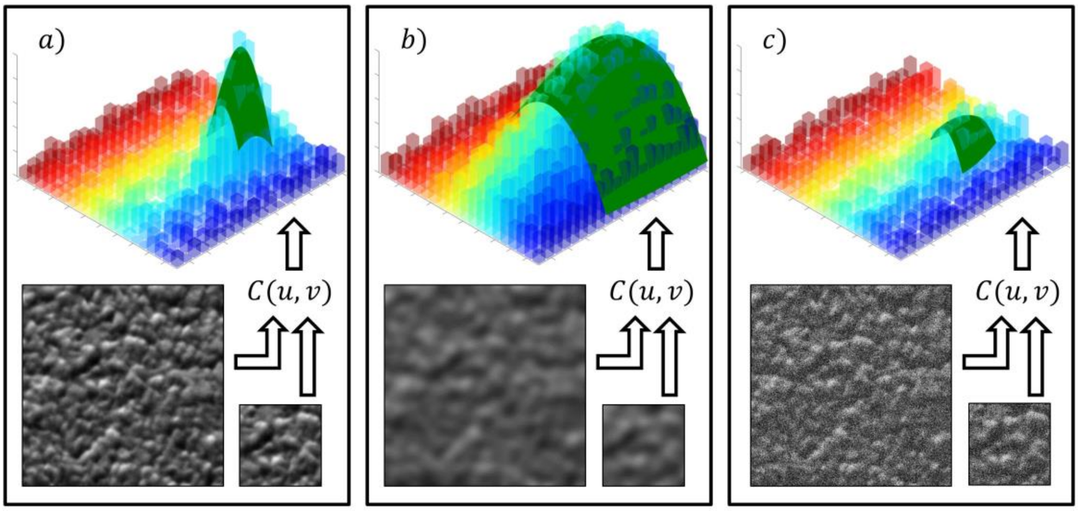

Figure 3.4. The normalised cross-correlation surface (bar plots) and polynomial peak fitting (green surfaces) associated with three different image types. a) Sharp, low noise images result in a single well defined peak with a correlation coefficient ~1 and precise estimates of the relative offset between images. b) Poorly focused, blurry or low contrast images result in a broad peak with a correlation coefficient ~1 but imprecise estimates of the relative offset between images. c) Noisy images result in a low correlation coefficient and a high roughness cross-correlation surface which leads to imprecise estimates of the relative offset between images.

In the case of a poorly focused, blurred or low contrast image, significant peak broadening is observed in the cross-correlation surface illustrated in Figure 3.4b. Even though the correlation coefficient in this case may also be close to unity, the precision of the displacement vector between the two images is much reduced.

Cross-correlation of images containing large amounts of noise will result in a high roughness cross-correlation surfaces as shown in Figure 3.4c. Noise also produces random differences between the reference and deformed image subsets, thereby reducing the magnitude of the correlation coefficient at the peak. These two effects lead to a large decrease in the signal to noise ratio, and a reduction in the precision of the displacement vector between the two images.

Examination of the three image cases outlined in Figure 3.4 demonstrates that the correlation coefficient on its own does not provide a good measure of the precision of displacement vector. Despite this, this parameter is a useful thresholding measure to remove noisy data points (§ 3.3.2).

An alternative and more reliable measure of the displacement vector precision is the standard deviation of the peak fit applied to the cross correlation surface. This parameter is critical for error estimation and the removal of poorly tracked markers and therefore a new approach for quantification of this parameter has been implemented.

The large number of markers used in DIC analysis means that the computational cost associated with tracking each marker needs to be carefully considered. Depending upon the DIC precision required, the complexity of this peak fitting process can be tailored using two main approaches. Firstly, a subset of the cross-correlation surface can be selected for analysis, rather than fitting the entire surface. Secondly, the 2D function used in the fitting process can be selected depending on the level of precision required. For example, a 2D Gaussian function typically provides a good match to the peaks observed in the cross-correlation surface, however the computational cost associated with fitting this function is higher than a polynomial peak fit.

In the case of the micro-scale ring core FIB milling and DIC approach it was decided that 2D polynomial peak fitting of a 3×3 window around the highest magnitude point in the cross-correlation surface would be most effective. Least squares fitting was therefore implemented using matrix multiplication in order to determine a peak profile of the form:

$$C_P(u,v) = A_1 + A_2u + A_3v + A_4uv + A_5u^2 + A_6v^2, \tag{3.5}$$

where A_i for $i = 1{:}\,6$ are the variables to be determined, u is the horizontal displacement and v is the vertical displacement. Differentiation of this function gives the expressions for the peak position:

$$u_P = \frac{2A_6A_2 - A_3A_4}{A_4^2 - 4A_5A_6}\ , \quad v_P = \frac{2A_5A_3 - A_4A_2}{A_4^2 - 4A_5A_6}\,. \tag{3.6}$$

Rounding is then used to determine this figure to a resolution of 1/1000th of a pixel. An estimate of the covariance matrix can also be obtained using further matrix multiplication and the residuals at each data point [138]. The diagonal terms in this matrix represent the variance σ_{Ai}^2 of each of the variables A_i for $i = 1{:}\,6$. Examination of the off-diagonal terms reveals that the five variables (A_i for $i = 2{:}\,6$) used in the calculation of u_P and v_P can be approximated as statistically independent. The propagation of these errors can then be used to estimate σ_{up} and σ_{vp}, the standard deviations of u_P and v_P, respectively:

$$\sigma_{up} = \sqrt{u_p^2\left[\frac{4(A_2^2\sigma_{A6}^2 + A_6^2\sigma_{A2}^2)^2 + (A_4^2\sigma_{A3}^2 + A_3^2\sigma_{A4}^2)^2}{(2A_6A_2 - A_3A_4)^2} + \frac{16(A_5^2\sigma_{A6}^2 + A_6^2\sigma_{A5}^2)^2 + 2A_4^4\sigma_{A4}^4}{(A_4^2 - 4A_5A_6)^2}\right]}, \tag{3.7}$$

$$\sigma_{vp} = \sqrt{v_p^2\left[\frac{4(A_5^2\sigma_{A3}^2 + A_3^2\sigma_{A5}^2)^2 + (A_4^2\sigma_{A2}^2 + A_2^2\sigma_{A4}^2)^2}{(2A_5A_3 - A_4A_2)^2} + \frac{16(A_5^2\sigma_{A6}^2 + A_6^2\sigma_{A5}^2)^2 + 2A_4^4\sigma_{A4}^4}{(A_4^2 - 4A_5A_6)^2}\right]}. \tag{3.8}$$

Although several approximations are necessary in the use of the above expressions, the simplicity of these calculations ensures that the peak centre position and associated standard deviations can be computed with a minor increase in processing time. These estimates of confidence can then be used in the removal of outliers as outlined in § 3.3.2.

3.3.2. Outlier Removal

In order to improve the accuracy and precision of residual stress estimates, the removal of poorly tracked DIC markers (or outliers) is a necessary step in reliable estimation of the resultant displacement field. Ineffective tracking can be caused by a variety of different effects including aliasing, re-deposition of FIB milled material onto the sample surface, noisy imaging or changes to surface appearance near milling locations [139]. One important requirement of the newly developed outlier detection and removal techniques has been technique automation which is required to reduce the operator dependence of the results obtained. The approach based on the identification and removal of markers moving relative to neighbours (outlined in § 3.2.1) has also been integrated into the automated outlier removal process which includes three new analytical stages (as shown schematically in Figure 3.5):

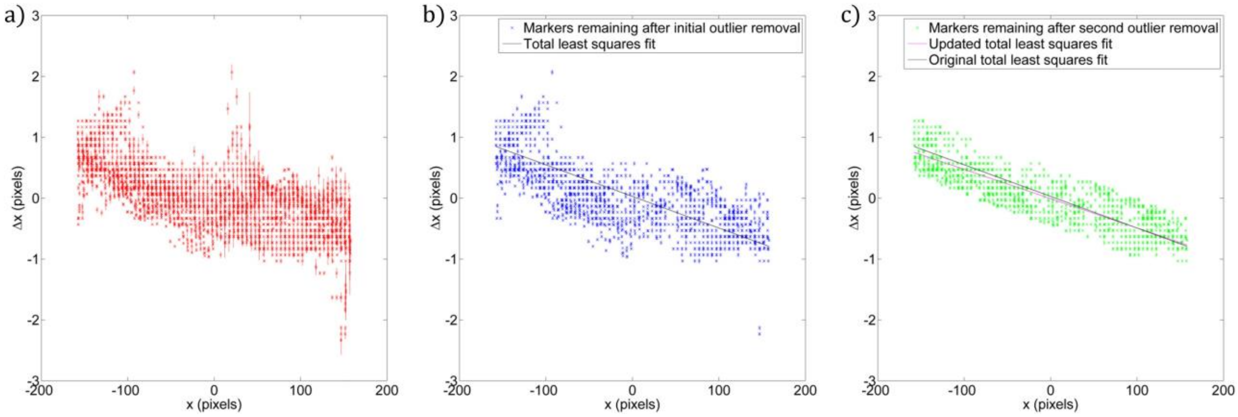

Figure 3.5. A typical example of automated outlier removal on plots of displacement Δx against position x. a) Markers remaining after correlation coefficient thresholding of 0.5 to leave a noisy profile. b) Markers remaining after σ_{up} and σ_{vp} thresholding, along with the removal of markers moving relative to each other. c) Markers remaining after thresholding of the distance from the original least squares fit.

1. *Correlation coefficient thresholding.* As stated in § 3.2.1, the maximum correlation coefficient, r, can be used as a threshold to remove markers for which there is a large difference between the reference image and deformed image, for example through the addition of large amounts of

noise (Figure 3.4c). An effective threshold for the correlation coefficient has been found to be 0.5, which can be used to leave only markers with a high magnitude peak in the cross-correlation surface as shown in Figure 3.5a.

2. *Peak position standard deviation thresholding.* The standard deviations of the estimates of peak position (σ_{up} and σ_{vp}) provide estimates of the sharpness of the peak in the cross-correlation surface. Relatively high standard deviations in either u or v direction indicate a poorly tracked marker, and therefore thresholding can be used to leave only those markers with precise peak estimation. A typical histogram of peak position standard deviation is shown in Figure 3.6. Care must be taken when choosing a threshold as the optimal value will depend highly upon the particular dataset under consideration. For example, the application of noise will result in an increase in the standard deviation of all markers. An effective approach is therefore to threshold values based on a parameter descriptor of the set, for example 1.5 times the average. This thresholding approach has been applied to the displacement against position plot in Figure 3.5a to leave only the well tracked markers in Figure 3.5b.

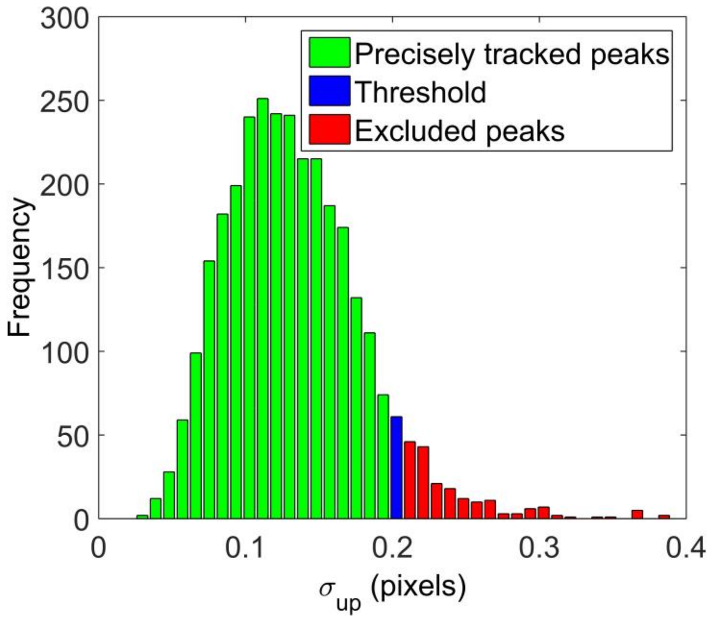

Figure 3.6. A typical histogram of σ_{up} obtained during the DIC analysis. Thresholding has been performed at 1.5 times the average value of σ_{up} to leave only the precisely tracked markers.

3. *Outliers to the linear displacement field.* FE modelling simulations of the ring-core geometry indicate that the strain relief within the core is expected to be near-uniform [120]. Therefore markers which do not correspond closely with this behaviour are likely to be indicative of

poorly tracked locations. In order to quantify this nominal distance from the linear distribution, least squares fitting can be initially applied to the noisy data set as shown in Figure 3.5b. The closest distance between each point and this linear fit can then be determined using the dot product and a typical histogram is shown in Figure 3.7. As previously highlighted, care must be taken when selecting a suitable threshold for this type of exclusion, however a value equal to 1.5 times the average distance has been found to be a robust displacement limit for the ring-core FIB milling and DIC approach (as implemented in Figure 3.5c and 3.7). This technique has been shown to be effective in removing outliers but care must be taken to ensure that the initial fit is representative of the behaviour observed. This process must therefore only be performed after other outlier removal techniques have been implemented.

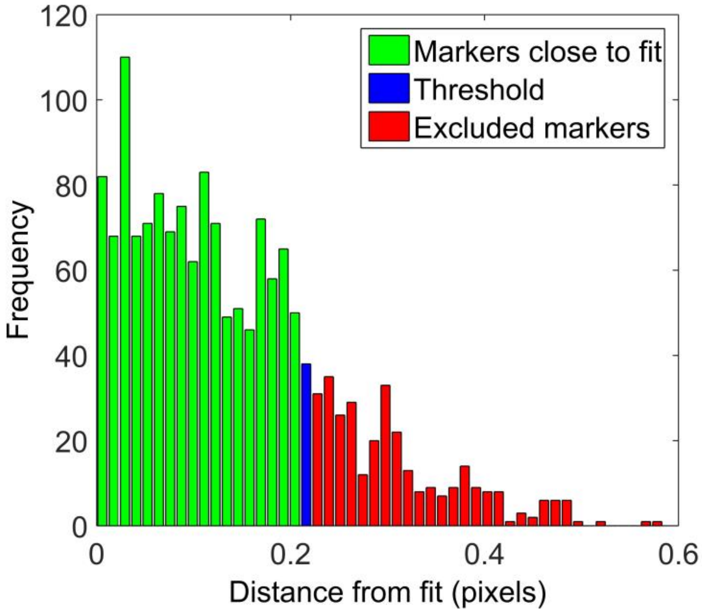

Figure 3.7. A typical histogram of marker distances from the linear least square fit obtained during the DIC analysis of the ring-core FIB milling and DIC approach. Thresholding has been performed at 1.5 times the average value in order to remove outliers.

At this stage in the analysis it is important to highlight that although the three new outlier removal techniques are fully automated, the thresholding criterion is based on a scaling value applied to a parameter descriptor of the data set. This flexibility enables the outlier removal techniques to be tailored to meet the needs of a specific experimental dataset in a reliable and repeatable manner, without introducing the uncertainty associated with manual removal.

3.3.3. Strain Quantification

In the ring-core FIB milling and DIC technique, repeated SEM imaging of the core is used to provide a record of relaxation at different milling depths. The strain relief observed on the surface of the core has previously been shown to be approximately uniform [140], corresponding to a linear variation in the displacement of DIC markers with position in the central region (Figure 3.5) [121]. The incremental changes in strain relief also ensure that the marker shift between subsequent images is reduced and therefore that DIC marker tracking is more effective.

This linear fit to the variation of tracking point displacement (Δx) with its position (x) provides insight into the strain relief in the core. The nature of DIC processing results in equal confidence bounds on both the dependent variable Δx and the independent variable x and therefore total least squares fitting [141] is necessary to account for both of these uncertainties. Estimates of the weighting of each data point are provided by the inverse of the standard deviation of the DIC marker peak (σ_{up} and σ_{vp}). The resulting gradient provides estimates for the magnitude ($\Delta\varepsilon$) and standard deviation ($\sigma_{\Delta\varepsilon}$) of the strain relief in the core as a function of image number.

3.3.4. Relief Profile Fitting

The next stage of analysis is associated with weighted least squares fitting of the FE 'master curve' (Equation 3.3) to the plot of strain relief ($\Delta\varepsilon$) as a function of image number. The weighting parameters for this analysis are given by the inverse of the standard deviation of the strain relief ($\sigma_{\Delta\varepsilon}$) at each image and the covariance matrix produced can be used to estimate the standard deviation of $\Delta\varepsilon_{\infty}$ ($\sigma_{\Delta\varepsilon_{\infty}}$).

As highlighted in § 3.2, only nominal estimates of the milling depth are known for a given image number and this can present difficulties when performing least squares fitting of the 'master curve'. In order to overcome this difficulty an extra parameter (η) can be introduced in the least squares fitting process to relate the milling depth to the image number (I), such that $H = \eta I$. Setting this parameter to a constant implies that the milling rate remains constant throughout the process. Although this is true in the near-surface region, this approximation becomes increasingly invalidated at large depths.

Another factor which is known to influence the strain relief profiles induced during FIB milling is the impact of surface roughness [108]. Milling of rough surfaces can result in limited amounts of relief during the first few milling increments as shown in Figure 3.8. This behaviour is indicative of the milling of the peaks and troughs in the sample surface, without inducing relief within the core. In order to accommodate for this behaviour, another parameter (δ_{Start}) can be introduced into the 'master curve' least squares fitting routine. The modified version of the z parameter in Equation 3.3 therefore becomes:

$$z = \frac{I\eta}{0.42d} - \delta_{Start}. \tag{3.9}$$

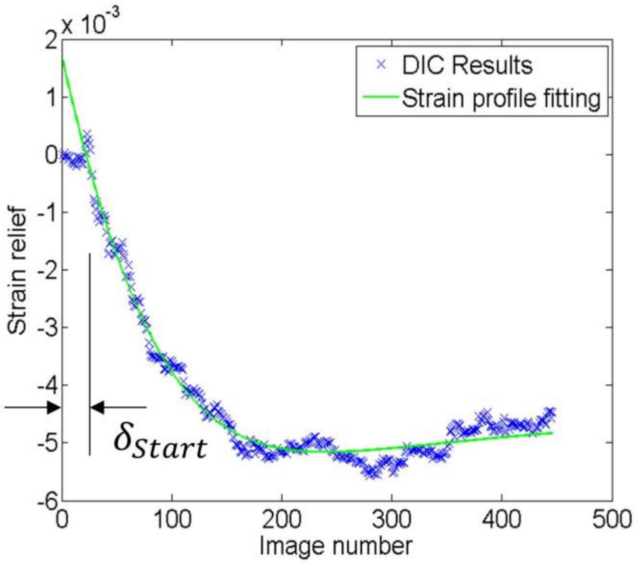

Figure 3.8. Strain relief against image number showing master curve fitting for a core originally in a state of tension. Surface roughness results in limited relief and offsets the profile by $\boldsymbol{\delta_{Start}}$.

It is at this stage in the analytical routine that the angular variation of strain relief is characterised during FIST (as outlined in detail in § 3.4). This approach is used to determine the principal strain relief orientation and magnitudes ($\Delta\varepsilon_\infty^1$ and $\Delta\varepsilon_\infty^2$), and associated confidence intervals ($\sigma_{\Delta\varepsilon_\infty^1}$ and $\sigma_{\Delta\varepsilon_\infty^2}$) through weighted least squares fitting. These parameters form the basis of residual stress quantification and determination of the associated confidence intervals, as outlined in § 3.3.5.

3.3.5. Calculation of Residual Stress

The relationship between surface strain relief and the residual stresses originally present in the surface forms the fundamental basis of FIB milling and DIC experimental techniques. In all techniques, this relationship is based on the elastic stiffness constants of the substrate material, which follows from the assumption that no reverse inelastic deformation occurs during FIB milling. In the case of ring-core geometry, this assumption is well-justified, since material removal causes unloading towards the unstressed state. In order to calculate reliable estimates of the confidence bounds on residual stress, the uncertainties of both the surface relief estimate and the elastic stiffnesses must be taken into account.

Typically there are two principal origins of elastic modulus uncertainty. The first is the underlying uncertainties in material composition, processing history and characterisation. Elemental doping [142], microstructure [143], thermal processing history [144], manufacturing route [145] and thermodynamic phase [146] are all known to have a large impact on the elastic behaviour. For example, the bulk elastic modulus of steel can vary in the range $190 - 220$ GPa depending on the elemental doping and thermal history. For this reason an accurate record of processing history or precise materials characterisation is necessary to reduce the uncertainty of description of the elastic response.

The other origin of elastic stiffness uncertainty is relevant to the study of anisotropic materials, in which stiffness is also dependent upon orientation. Elastic anisotropy can be as a result of underlying crystallinity [147], preferred grain orientation (or texture) [148] or a composite structure [149]. For example, in Chapter 4 the directional stiffness of YPSZ has been shown to vary by a factor of 2.6 depending upon the orientation in which load is applied. As outlined in more detail below, the impact of this uncertainty depends upon the relative size of the gauge volume and the anisotropic region. In the case where the anisotropic region is approximately equal to or greater than the gauge volume, orientation uncertainty may have a significant impact on the confidence intervals of the elastic modulus.

As highlighted in § 2.3, in recent years a suite of analytical techniques have been developed in order to quantify elastic behaviour at the microscale. These techniques provide insight into mechanical behaviour at the same length scales as those probed using FIB milling and DIC residual stress analysis, and therefore typically provide estimates of the material stiffness which are more representative than bulk analysis. Importantly, many of these techniques also provide parameter uncertainty estimates which are required in residual stress error estimation.

In contrast to this microscale analysis, for the case of isotropic or untextured nanocrystalline materials, reliable values of continuum material elastic constants are available and can be used in the calculation of residual stress. Inside a typical FIB milling and DIC micro-scale gauge volume, many thousands of grains will be present in a nanocrystalline substrate material, so that the different elastic responses of each grain are averaged out, producing a response representative of the global behaviour.

Assuming that homogeneous and isotropic assumptions can be applied at the length scales under consideration, expressions for the non-equi-biaxial principal stresses in the surface ($\sigma_1$and σ_2) can be determined as:

$$\sigma_1 = -\frac{E}{(1-\nu^2)}[\Delta\varepsilon_\infty^1 + \nu\Delta\varepsilon_\infty^2], \tag{3.10}$$

$$\sigma_2 = -\frac{E}{(1-\nu^2)}[\Delta\varepsilon_\infty^2 + \nu\Delta\varepsilon_\infty^1], \tag{3.11}$$

where E and ν are the Young's modulus and Poisson's ratio, respectively. By making the approximation that these terms are statistically independent, estimates for the standard deviation of the principal stresses (σ_{σ_1} and σ_{σ_2}) can be obtained from the standard deviation of Young's modulus (σ_E), Poisson's ratio (σ_ν) and the strain relief values obtained through DIC ($\sigma_{\Delta\varepsilon_\infty^1}$ and $\sigma_{\Delta\varepsilon_\infty^2}$):

$$\sigma_{\sigma_1} = \frac{E}{(1-\nu^2)}\sqrt{\left[\left(\frac{\sigma_E}{E}\right)^2 + 2\left(\frac{\nu\sigma_\nu}{1-\nu^2}\right)^2\right](\Delta\varepsilon_\infty^1 + \nu\Delta\varepsilon_\infty^2)^2 + \sigma_{\Delta\varepsilon_\infty^1}^2 + \left(\nu\sigma_{\Delta\varepsilon_\infty^2}\right)^2 + (\Delta\varepsilon_\infty^2\sigma_\nu)^2}, \tag{3.12}$$

$$\sigma_{\sigma_2} = \frac{E}{(1-\nu^2)}\sqrt{\left[\left(\frac{\sigma_E}{E}\right)^2 + 2\left(\frac{\nu\sigma_\nu}{1-\nu^2}\right)^2\right](\Delta\varepsilon_\infty^2 + \nu\Delta\varepsilon_\infty^1)^2 + \sigma_{\Delta\varepsilon_\infty^2}^2 + \left(\nu\sigma_{\Delta\varepsilon_\infty^1}\right)^2 + (\Delta\varepsilon_\infty^1\sigma_\nu)^2}. \tag{3.13}$$

It is important to note that the existing FE simulations of FIB milling and the resulting relaxation are based on the assumptions of material isotropy and homogeneity. In the case of single crystal or large grained materials (relative to the gauge volume size) these predictions will no longer be representative of the relief observed, and modified simulations are required.

3.4. Full In-Plane Strain Tensor Analysis

High resolution (microscale) residual stress analysis is critical in understanding the failure of a broad range of mechanical components; from carbon fibre composite systems [112], to silicon nanowires for microelectronic devices [150] and thin film solar cell applications [151]. In some studies, the determination of an average stress component is sufficient to provide the answers required. However, the improved insight offered by the full quantification of residual stress variation with orientation is often necessary [152, 153].

In recent years, strain tensor determination and stress calculation based on neutron [154] and X-Ray Diffraction (XRD) [77, 155-157] measurements have become well-established techniques. Despite the many benefits of these approaches, there are a number of well-known limitations. Firstly, precise estimates of unstrained lattice parameters are required; this is particularly difficult in the case of high resolution studies where local variations in elemental composition may also induce 'chemical' changes of this parameter over similar length scales. Secondly, these high precision techniques can only be applied to crystalline materials and therefore equivalent analysis cannot be performed in amorphous materials. Another difficulty is associated with the limited 3D resolution that can be obtained. This is due to the large penetration depths of the neutron and high energy X-ray beams typically required in these studies. Approaches involving tomographic [158] and grazing angle [69] methods have been developed to overcome this limitation at the expense of increased processing complexity, time and reduced precision. Finally, these methods typically require access to synchrotron or neutron source facilities which severely restricts the number of applications that can be studied.

The ring-core FIB milling and DIC approach is based on milling an isotropic annular feature at a location of interest in order to perform high resolution residual stress (or strain) analysis. Despite the potential capabilities of this technique, previous studies have only characterised residual stress in at most two independent directions [108]. Other orientations have not been attempted due to a lack of automation in the DIC and outlier removal methods required to quantify strain. These manual stages have previously been labour intensive and have therefore severely limited the number of repeated strain quantification procedures which could be performed in a given timescale. However, the advances in outlier removal, error evaluation and propagation in § 3.3 can now facilitate rapid, precise and fully automated strain quantification. Using this automated approach, this sub-section demonstrates the experimental and analytical steps necessary to evaluate the strain relief variation as a function of orientation angle, thereby enabling FIST analysis. Provided that the elastic constants of the system under consideration are known fully, the corresponding residual stress variation can then be determined from this in-plane strain tensor.

In order to validate this new experimental technique, the results of FIST ring-core analysis of a single location has been compared with those obtained using high energy transmission XRD of a dental prosthesis sample. The stress states associated with these two experimental approaches are known to be different: in the case of surface ring-core milling the stress condition is close to plane stress, while XRD analysis provides an average of both the near surface (plane stress) and bulk (which is closer to conditions of plane strain). Therefore in order to provide comparisons between these two techniques the analytical relationships between the two states have been determined using analytical methods and FE simulations have been used to validate these relationships. This comparative approach also provides the upper and lower bounding limits of the lattice spacing of YPSZ.

3.4.1. Materials and Methods

The sample selected for this experimental validation was a YPSZ dental prosthesis manufactured using the approach outlined in § 1.1 by dental technicians at the Specialist Dental Group, Singapore. The location selected for strain tensor analysis was a distance of 50 μm from the porcelain interface within the YPSZ. This position is known to have moderate levels of residual stress but is sufficiently far from the interface that the YPSZ phase transformation and elemental diffusion effects are not present (as outlined in Chapter 6 and 7, respectively). This ensures that the unstrained lattice spacing (d_{hkl}^{0}) is not influenced by these two factors and is therefore representative of the bulk YPSZ.

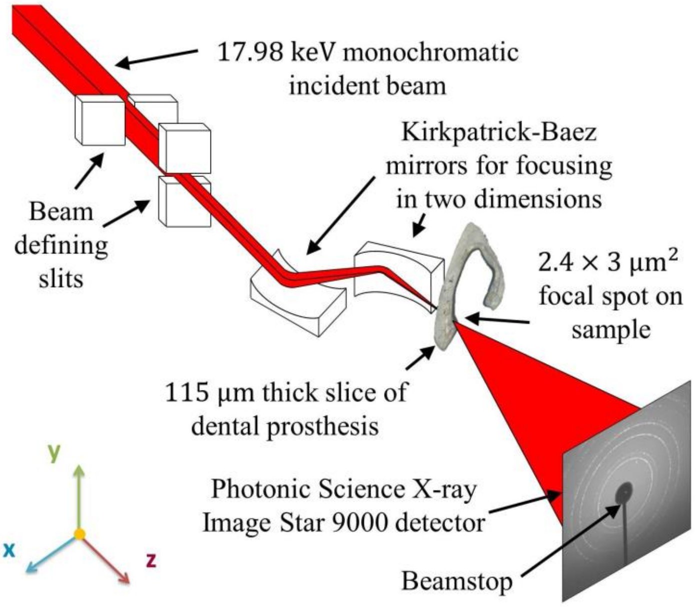

Figure 3.9. Schematic of the synchrotron XRD experiment showing beam defining and focusing setup, sample oriented in a transmission geometry and a typical diffraction pattern.

In order to facilitate access to the near-interface region, the sample was mounted in epoxy and a cross section of the YPSZ prosthesis was obtained using a Buehler Isomet Diamond Saw (Figure 3.9). A slow rotational cutting speed of 25 rpm (on a 127 mm diameter blade) was selected to minimise the residual stresses induced during sample preparation. A metallurgical incremental grinding and polishing process was then used to minimise the influence of sample preparation on the residual stress state. The final sample thickness was selected to be 115 μm in order to maximise the intensity of the diffraction patterns collected during the synchrotron XRD experiment.

Micro Focus XRD

Transmission powder XRD was performed at Beamline B16 (Diamond Light Source, UK) using the set up shown in the schematic in Figure 3.9. A 17.98 keV monochromatic incident beam (just below the K-edge of zirconium) was selected in order to minimise absorption by the sample and a micro-focusing KB mirror pair arrangement was used to reduce the beam spot on the sample to $2.4 \times 3\ \mu\mathrm{m}^2$. A Photonic Science X-ray Image Star 9000 detector placed in the transmitted beam was used to collect complete 360° Debye-Scherrer diffraction patterns at 170 mm downstream from the sample.

A combination of optical alignment, X-ray imaging and identification of the interface through the differences in the scattering patterns of YPSZ and porcelain were used to determine the incident location of the beam on the sample to nanoscale precision. Diffraction patterns were then collected at a position $50\ \mu\text{m}$ from the interface in the form of a 3×3 array covering an area of $7.2\ \times 9\ \mu\text{m}^2$ as shown in Figure 3.10. At each position a 5 minute exposure was used to capture a high quality diffraction pattern.

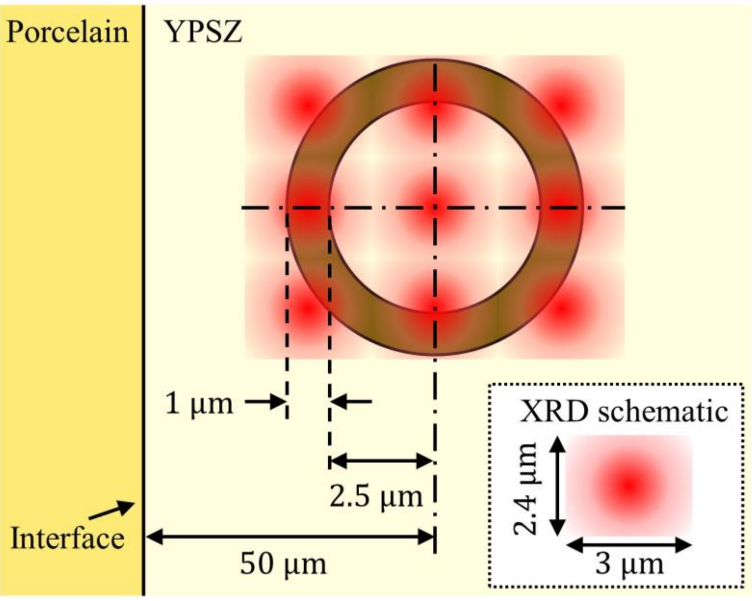

Figure 3.10. Schematic of residual stress analysis locations. The 3 × 3 array of XRD mapping points is shown superimposed over the 5 μm diameter ring-core milling geometry at a distance of 50 μm from the YPSZ-porcelain interface.

Each diffraction pattern was then radially binned as a function of the azimuthal angle φ (as illustrated in Figure 3.11) to give line plots of scattered beam intensity against Q position averaged over 10° regions between 0° and 360°. For example, the 0° distribution was obtained from integrating between -5° and 5°. Beamstop shadowing was found to influence the profile obtained at $\varphi = 270°$ and therefore the line profile obtained at 90° was used for this orientation.

Gaussian peak fitting was then performed on the (101) peak of tetragonal zirconia. The high intensity of this peak ensured that the peak centres could be determined at the precision necessary to perform reliable strain tensor quantification. For example, the peak centres for the 0°, 10° and 20° positions have been highlighted by markers in Figure 3.11. Bragg's law was then used to convert the peak centre estimates to the lattice spacing in the (101) direction (d_{101}). This analysis was performed on all 9 diffraction patterns and the fitting confidence of each peak was used to determine a weighted average and the associated confidence interval for d_{101}at each angle φ.

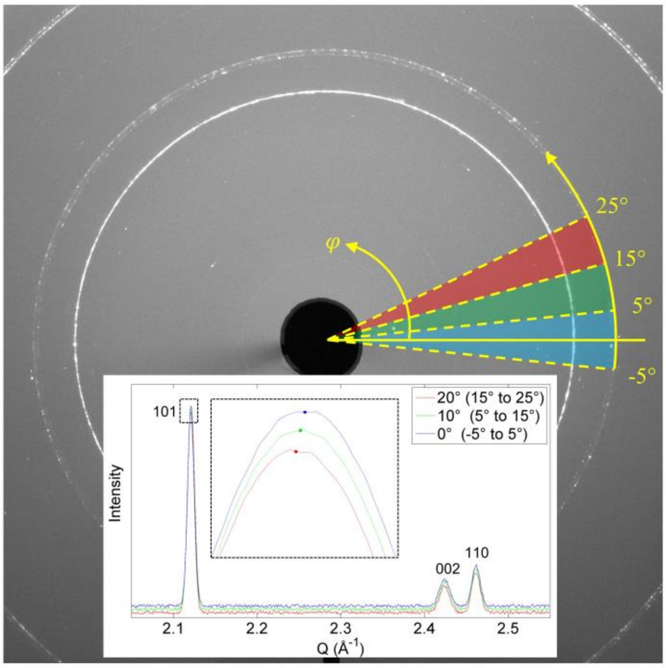

Figure 3.11. Radial integration of 2D diffraction pattern to produce 1D intensity distributions (insert). Gaussian peak fitting was performed on the tetragonal 101 diffraction peak in order to determine the peak centre position (indicated by markers) as a function of φ.

X-ray diffraction was also used to determine independent measurements of the unstrained 101 lattice parameter of the YPSZ (d_{101}^{0}) using the Brucker D8 Lab Source Diffractometer at the High Energy X-ray (HEX) laboratory, Oxford UK. In the first sample, representative nanocrystalline powder was obtained from the same batch of Zenotec Zr bridge which had been used in the manufacture of the YPSZ coping. The remains of the YPSZ coping were also ground into a micro-scale powder using a diamond sintered burr cone. Both powders were loaded into 1 mm diameter quartz capillaries and Cu K-alpha emission (with a spot size ≈ 0.3 mm) was directed towards the samples. The 2D diffraction patterns of the samples were collected and radially integrated to give 1D profiles of intensity against scattering angle. Gaussian peak fitting was performed on the tetragonal 101 diffraction peak and Bragg's law was used to provide an estimate of d_{101}^{0} for both powders.

In the case of the ground YPSZ coping, large amounts of monoclinic YPSZ were found to have been induced in the YPSZ by the grinding process applied. Phase changes are known to induce errors in the estimation of unstrained lattice parameters [75] and therefore the inconsistencies between the d_{hkl}^{0} estimate of 2.9674 ± 0.0012 obtained from this analysis and those determined in § 3.4.2 was expected.

The results from the Zenotec Zr powder sample provided an unstrained lattice parameter estimate of 2.9567 ± 0.0006. This result also indicated distinct differences with the analysis performed in §

3.4.2. This is most likely as a result of minor changes in composition, combined with the grain growth known to be induced in YPSZ during sintering [159]. Both of these effects are known to induce significant changes to the unstrained lattice parameter estimates of nanocrystalline materials [75, 160]. Therefore the comparison between XRD and ring-core analysis was selected as the most reliable unstrained lattice parameter approach for this system [112, 121].

FIB Milling and DIC

Ring-core FIB milling was performed on the sample using the Tescan Lyra 3 FIB-SEM at MBLEM, Oxford, UK [161]. The prosthesis cross section was mounted on an SEM stub using silver paint and was sputter coated with 5 nm of gold-palladium in order to reduce sample charging. Applying a single fast pass of the focused ion beam across the surface of the sample causes the formation of a surface pattern that generates high imaging contrast, as shown in Figure 3.12a. As outlined in § 2.3.3, these patterns have previously been shown to facilitate effective DIC marker tracking during ring-core milling, without inducing stress state modification in the sample [106].

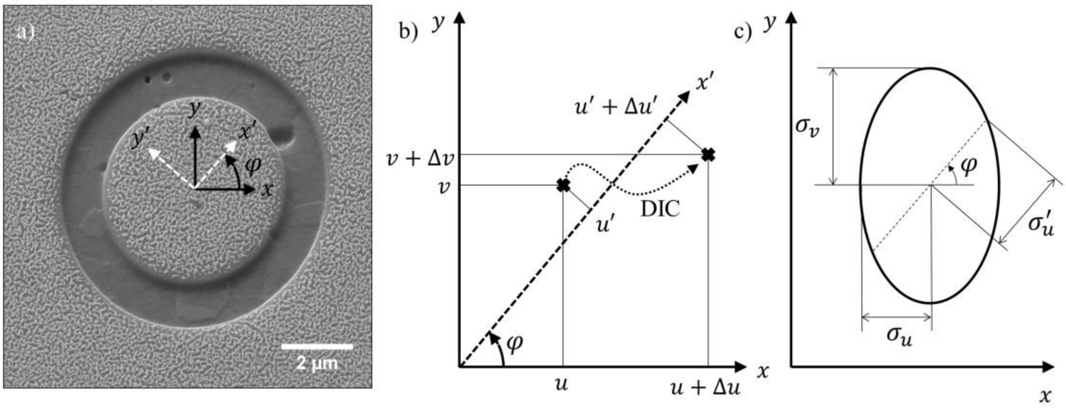

Figure 3.12. a) Secondary electron SEM image of the ring-core milling showing original (x, y) and rotated (x', y') coordinate systems for a given angle φ. b) Schematic showing a DIC marker shift of $(\Delta u, \Delta v)$ from starting position (u, v) and the corresponding position (u') and shift $(\Delta u')$ in the (x', y') coordinate frame. c) Schematic ellipse of DIC shift uncertainty showing the relationship between the standard deviations in the original (σ_u, σ_v) and the rotated coordinate system (σ'_u).

A single 5 µm diameter core was fabricated in the YPSZ by milling a 1 µm wide circular trench at a distance of 50 µm from the YPSZ-porcelain interface as shown in Figure 3.12a. This milling location was aligned with the location of XRD analysis to a microscale precision using multiple characteristic features of the prosthesis cross section. This level of alignment was necessary to ensure that the same location (and residual stress state) was examined using both experimental techniques.

A nominal milling depth of 125 nm was selected for each increment of the FIB milling process, and a 2048×2048 pixel secondary electron SEM image of the surface was captured at each step. In total 48 images were captured as a record of the core relaxation during FIB milling to a nominal depth of 6 μm in a time of ≈ 30 minutes.

A modified version of the DIC code produced by Eberl et al. [110] was used to determine the strain relief at the surface of the core as a function of milling depth. Small amounts of drift were observed between each of the recorded images (with a maximum of ≈ 30 nm between subsequent images) and low resolution DIC (drift correction) was performed on the exterior surface regions to correct for this effect. Subset DIC was performed on the island by placing several thousand markers over the core centre where uniform strain relief is expected. Marker tracking was then performed using the approach outlined in § 3.3 in order to obtain the marker shift $(\Delta u, \Delta v)$ relative to the start positions (u, v) in the (x, y) coordinate frame, along with the standard deviations of these shifts (σ_u and σ_v).

In-plane strain tensor quantification relies upon the precise determination of the strain magnitude variation as a function of angle φ. In the case of the ring-core milling approach this requires the determination of the core strain relief as a function of φ, and therefore the quantification of the DIC marker shift along an axis x' as shown in Figures 3.12a and 3.12b. For a given angle φ and marker starting position (u, v) the expression for the starting position along the x' direction is given as:

$$u' = u\,cos\,\varphi + v\,sin\,\varphi. \tag{3.14}$$

Following automated marker tracking in the (x, y) coordinate frame, the shifts along the x' direction can be determined as:

$$\Delta u' = \Delta u\,cos\,\varphi + \Delta v\,sin\,\varphi. \tag{3.15}$$

Quantification of the peak shift standard deviation in the direction parallel to the x' axis (σ_u') is also necessary in order to determine strain uncertainty in a given direction. An elliptical representation of the uncertainty field in which the principal axes are aligned with the x and y directions (Figure 3.12c) can be used to estimate this value as:

$$\sigma_u' = \sqrt{\frac{\sigma_u^2 \sigma_v^2}{\sigma_v^2 cos^2\varphi + \sigma_u^2 sin^2\varphi}}. \tag{3.16}$$

The rotated standard deviation estimates and marker shifts can then be used as inputs into the strain relief quantification routine outlined in § 3.3.3. In this approach, linear fitting of the relationship between

u' and $\Delta u'$ can be used to obtain the strain relief estimates associated with each milling depth ($\Delta\varepsilon$), as well as the corresponding standard deviations ($\sigma_{\Delta\varepsilon}$). Outlier removal is necessary at this stage in order to remove poorly tracked markers and the automated multi-stage marker filtering routine outlined in § 3.3.2 was implemented. Thresholding was performed to remove DIC markers which showed low levels (< 0.5) of correlation. The standard deviation of each marker position (σ_u') was also used to threshold markers with a standard deviation greater than 1.5 times the average value. Finally, the removal of markers moving relative to the expected displacement field was performed. Thresholding based on 1.5 times the average value of this relative offset was also found to be effective.

The relationship for the strain relief ($\Delta\varepsilon$) against milling depth was then fitted using the ring-core strain relief 'master function' outlined in § 3.3.4 (Figure 3.13) in order to determine quantitative estimates of magnitude and standard deviation of the plateaus observed in the strain relief curves ($\Delta\varepsilon_\infty$). As previously highlighted, the negative of this fitted parameter provides the estimate of the gauge-volume average residual strain in a given direction. For example, a positive core relief strain indicates that the original residual strain in the core was compressive.

This analysis was implemented for φ values ranging from 0° to 360° in 10° steps in order to determine $\Delta\varepsilon_\infty$ and $\sigma_{\Delta\varepsilon_\infty}$ as a function of angle. As expected, it was found that the strain relief values and standard deviations obtained in opposite directions were equal, i.e. $\Delta\varepsilon_\infty^{0°}$=$\Delta\varepsilon_\infty^{180°}$ and $\sigma_{\Delta\varepsilon_\infty^{0°}} = \sigma_{\Delta\varepsilon_\infty^{180°}}$. This distribution of absolute strain was next used to determine estimates for the residual strain principal orientations and principal values as outlined in § 3.4.2.

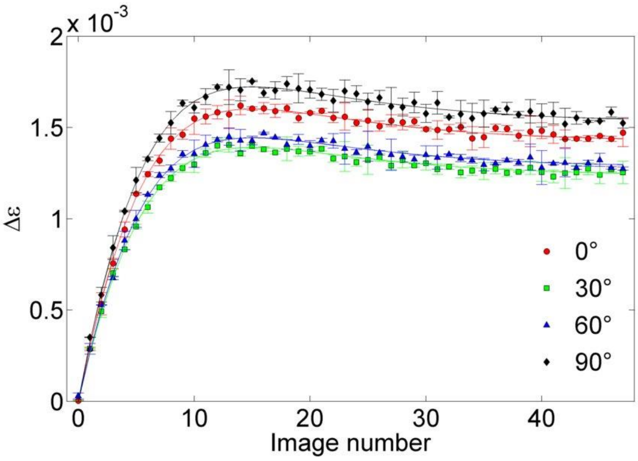

Figure 3.13. Strain relief against image number for data oriented at differing angles of φ. The original data and the 95% confidence error bars have been plotted with the 'master curve' fitting.

3.4.2. Theory and Calculation

The tetragonal (101) lattice spacing estimates (d_{101}) obtained through XRD were used to quantify the lattice strain variation (ε_{101}) as a function of φ using the Equation 2.7. Initially an estimate for this value ($d_{hkl}^0 = 2.9582$ Å) was obtained from the short ($a = 3.605$ Å) and long ($c = 5.177$ Å) lattice constants of YPSZ provided in the literature [162], using the expression:

$$\left(\frac{1}{d_{hkl}^0}\right)^2 = \frac{h^2 + k^2}{a^2} + \frac{l^2}{c^2}, \tag{3.17}$$

where $hkl = 101$.

A value for the standard deviation of the (101) unstrained lattice spacing ($\sigma_{d_{hkl}^0} = 0.0015$ Å) was also calculated based on the standard deviations of the short ($\sigma_a = 0.0010$ Å) and long ($\sigma_c = 0.0020$ Å) lattice constants provided in the literature:

$$\sigma_{d_{hkl}^0} = \frac{d_{hkl}^0}{2(c + a)} \sqrt{a^2\sigma_c^2 + c^2\sigma_a^2} \tag{3.18}$$

The standard deviation of the peak centre values $\left(\sigma_{d_{hkl}^0}(\varphi)\right)$ were then used in combination with the standard deviation of the unstrained lattice spacing in order to obtain estimates of the standard deviation of the lattice strain $\left(\sigma_{\varepsilon_{101}}(\varphi)\right)$:

$$\sigma_{\varepsilon_{101}}(\varphi) = \left(\frac{1}{\varepsilon_{101}}\right)^2 \sqrt{\left(\sigma_{d_{101}}(\varphi) d_{hkl}^0\right)^2 + \left(\sigma_{d_{hkl}^0}\, d_{101}(\varphi)\right)^2}. \tag{3.19}$$

Full In-plane Strain Tensor Quantification

The next stage of analysis required quantification of the strain tensors obtained through ring-core FIB milling and DIC ($-\Delta\varepsilon_\infty(\varphi)$) and the preliminary distributions of the (101) interplanar lattice strain $\left(\varepsilon_{101}(\varphi)\right)$ obtained using literature values of d_{101}^0. The generic expression for in-plane residual strain variation ($\varepsilon(\varphi)$) has been outlined in Equation 2.8. Least squares fitting was performed on the strain distributions obtained through XRD and ring core milling using the inverse square of the standard deviation of each term as a weighting factor. This analysis provides estimates of the principal strains (ε_1 and ε_2) and the angular offset between the original and principal coordinate systems (ϕ), as well as the standard deviation of these terms (σ_{ε_1}, σ_{ε_2} and σ_ϕ).

It is important to note that the use of the literature value of d^0_{101} has little or no effect on the magnitude of principal axis orientation angle ϕ obtained from this fitting procedure (as shown in Table 3.1), although it does affect the magnitude of the principal strains. It was found that the values obtained for the angular offset were 52.1° and 53.4° using the ring-core and XRD techniques respectively. This 1.3° difference is likely to have arisen from small misalignment during sample positioning in the two experiments and therefore the approximation that the ring-core and XRD principal stress and strain orientations were aligned was used in the remainder of the analysis.

Table 3.1. Table showing fitted estimates and standard deviations of the principal strains, stresses and orientations for the ring-core and XRD stress/strain tensor analysis. The lattice parameters obtained from the literature and through least squares fitting (in both plane stress and plane strain) have been included for the XRD analysis.

Technique	d^0_{101} (Å)	ε_1 (millistrain)	ε_2 (millistrain)	σ_1 (MPa)	σ_2 (MPa)	ϕ (degrees)
Ring-core	-	1.73 ± 0.007	1.26 ± 0.007	499 ± 1.81	424 ± 1.81	52.1 ± 1.26
XRD literature d^0_{101} [a]	2.9582 ± 0.0015	1.80 ± 0.007	1.44 ± 0.007	-	-	53.3 ± 0.99
XRD fitted d^0_{101} (Plane stress)	2.9586 ± 0.0004	1.67 ± 0.006	1.31 ± 0.007	489 ± 1.72	432 ± 1.65	53.2 ± 0.97
XRD fitted d^0_{101} (Plane strain)	2.9596 ± 0.0003	1.36 ± 0.006	0.96 ± 0.007	546 ± 2.50	482 ± 2.38	53.4 ± 0.96

[a] Calculated using lattice parameters published by Shah et al. [162].

Careful consideration of the gauge volumes associated with the two techniques reveals that ring-core technique provides an estimate of the average strain in a 5 μm tall, 5 μm diameter near-interface cylinder, whereas the through sample penetration of the incident X-ray beam probes a $7.2 \times 9 \times 115\ \mu\text{m}^3$ volume. Although these gauge volumes are both centred at the same location in the plane of the sample, the average out of plane conditions are different. In order to derive the relationship between these two stress states, new notation is required to distinguish the stress and strain states associated with these two conditions. In the analysis that follows, a circumflex accent (^) indicates conditions of plane stress and a tilde accent (˜) is indicative of plane strain conditions.

In the case of the near-surface ring-core technique, the mechanical state can best be described as a state of plane stress. Therefore the principal stresses $(\widehat{\sigma_1}, \widehat{\sigma_2})$ and the associated standard deviations $(\sigma_{\widehat{\sigma_1}}, \sigma_{\widehat{\sigma_2}})$ can be determined using expressions adapted from Equations 3.10-3.13:

$$\widehat{\sigma_1} = \frac{E}{1-\nu^2}(\varepsilon_1 + \nu\varepsilon_2), \tag{3.20}$$

$$\widehat{\sigma_2} = \frac{E}{1-\nu^2}(\varepsilon_2 + \nu\varepsilon_1), \tag{3.21}$$

$$\sigma_{\widehat{\sigma_1}} = \frac{E}{1-\nu^2}\sqrt{\left(\sigma_{\varepsilon_1}^2 + \nu^2\sigma_{\varepsilon_2}^2\right)}, \tag{3.22}$$

$$\sigma_{\widehat{\sigma_2}} = \frac{E}{1-\nu^2}\sqrt{\left(\sigma_{\varepsilon_2}^2 + \nu^2\sigma_{\varepsilon_1}^2\right)}. \tag{3.23}$$

Estimates of E and ν were obtained from the literature and were given as 210 GPa [11] and 0.32 [163], respectively. No information was available on the likely distributions of these values and therefore they were treated as error-free measures. This approximation will artificially increase the precision of principal stress value determination (Table 3.1), but experimental errors are likely to dominate.

In the case of the XRD analysis the gauge volume can no longer be simply described as a simple planar mechanical state. In reality the X-ray beam samples both the near surface regions (in conditions close to plane stress) as well as bulk material (which can be approximated by generalised plane strain). A review of the literature reveals that no agreement has yet been reached on the most representative plane state approximation in the case of transmission X-ray analysis [164, 165], although the solutions of a few generalised cases have been published [166, 167]. The most suitable approximation is dependent upon the particular sample geometry (i.e. if the aspect ratio of the sample is large in the through beam direction then plain strain conditions are typically more suitable) and the average length scale of any structural/microstructural phenomena (i.e. in the case of a fibre composite system, the ratio between sample thickness and fibre diameter will dictate the most suitable approximation). For all practical purposes it can be noted however that the plane strain and plain stress assumptions can be considered as the upper and lower bound for the stress state within the region sampled by transmission XRD.

The YPSZ-porcelain prosthesis slice has a cross sectional area of approximately $10 \times 10\ \text{mm}^2$ and a thickness of 115 μm. The aspect ratio of the sample is therefore sufficiently large as to approximate the system as a thin plate in a state of plane stress. On the other hand, in terms of structural/microstructural features the only representative length scale is the nano-scale average grain size present in YPSZ. In this respect the sample thickness is far greater than the local feature length scales and the system may be better represented as a state of plane strain. In reality the XRD state sampled will be a weighted average of these two mechanical states and analysis was performed to determine the response for both conditions.

The Relationship between Plane Strain and Plane Stress

To compare the estimates of the residual stress state from XRD and FIB milling, the relationship between plane strain and plane stress conditions for the same sample needs to be determined. Derivation of the relationships between these conditions using stress state decomposition is provided in Appendix A along with numerical validation through FE simulations. The results of this analysis are provided by expressions for the plane stress tensor in terms of $\tilde{\sigma}_x$ and $\tilde{\sigma}_y$:

$$\widehat{\sigma_x} = (1 - \nu^2)\tilde{\sigma}_x, \tag{3.24}$$

$$\widehat{\sigma_y} = (1 - \nu^2)\tilde{\sigma}_y, \tag{3.25}$$

$$\widehat{\varepsilon_x} = \frac{1 - \nu^2}{E}\left[\tilde{\sigma}_x - \nu\tilde{\sigma}_y\right], \tag{3.26}$$

$$\widehat{\varepsilon_y} = \frac{1 - \nu^2}{E}\left[\tilde{\sigma}_y - \nu\tilde{\sigma}_x\right], \tag{3.27}$$

$$\widehat{\varepsilon_z} = -\frac{(1 - \nu^2)\nu}{E}\left[\tilde{\sigma}_x + \tilde{\sigma}_y\right]. \tag{3.28}$$

These expressions demonstrate the $(1 - \nu^2)$ factor which relates the existing in-plane stresses (under conditions of plane strain) to those modified by the introduction of the free surface (plane stress). This model is based on treating the system as a free surface which is a good approximation in this case.

3.4.3.Results

Following the establishment of the relationship between the residual stress state according to plane stress or plane strain approximations (Equations 3.24 and 3.25), these expressions were used to estimate d_{101}^{0} in the case of plane strain. Beginning with the plane stress elastic field solution, the in-plane residual stress determined by ring-core FIB milling were transformed into the corresponding estimates of plane strain. The interpretation of XRD strain measurements was then adjusted by varying the unstrained lattice parameter, and estimates of the corresponding stress components were calculated using plane strain relationships between strains and stresses:

$$\tilde{\sigma}_1 = \frac{E}{(1 + \nu)(1 - 2\nu)}\left((1 - \nu)\varepsilon_1 + \nu\varepsilon_2\right), \tag{3.29}$$

$$\tilde{\sigma}_2 = \frac{E}{(1 + \nu)(1 - 2\nu)}\left((1 - \nu)\varepsilon_2 + \nu\varepsilon_1\right), \tag{3.30}$$

$$\sigma_{\tilde{\sigma}_1} = \frac{E}{(1 + \nu)(1 - 2\nu)}\sqrt{\left((1 - \nu)^2\sigma_{\varepsilon_1}^2 + \nu^2\sigma_{\varepsilon_2}^2\right)}, \tag{3.31}$$

$$\sigma_{\tilde{\sigma}_2} = \frac{E}{(1 + \nu)(1 - 2\nu)}\sqrt{\left((1 - \nu)^2\sigma_{\varepsilon_2}^2 + \nu^2\sigma_{\varepsilon_1}^2\right)}, \tag{3.32}$$

where $(\sigma_{\tilde{\sigma}_1}, \sigma_{\tilde{\sigma}_2})$ are the standard deviations of the principal strains. The lack of confidence intervals in E and ν prevented full quantification of this error and therefore these variables were treated as error-free in Equations 3.31 and 3.32. The optimum value of the (101) lattice parameter was found to be 2.9596 Å, which corresponded to the principal stresses of 546 MPa and 482 MPa.

For the plane stress approximation, the refinement of d_{101}^0 was performed by comparing the XRD principal strain values with the absolute values obtained through ring-core FIB milling (1.73×10^{-3} and 1.26×10^{-3}). The optimised magnitude of $d_{101}^0$was found to be 2.9586 Å, which corresponded to the principal strains of 1.67×10^{-3} and 1.31×10^{-3}. Equations 3.20-3.23 were then used to obtain the estimates of principal stresses and associated standard deviations included in Table 3.1.

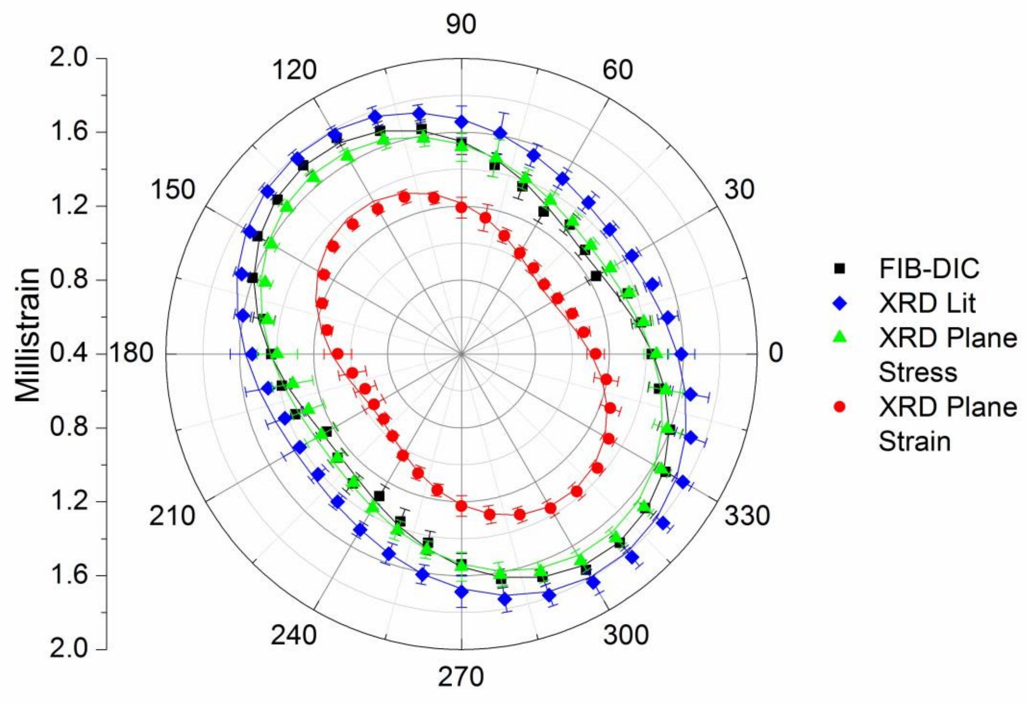

Figure 3.14. Polar plot of millistrain against angle φ showing strains obtained using the ring-core FIB milling and DIC technique and XRD using the literature, plane stress and plane strain refined values of d_{101}^0. The error bars correspond to the 95% confidence intervals of each data point.

A polar plot of strain variation with angle φ is provided in Figure 3.14 showing the results obtained from the ring-core FIB milling and DIC approach along with the XRD results. The strain distributions obtained with the literature, plane strain and plane stress values of d_{101}^0 have been included, along with the results of least squares fitting of Equation 2.8. The variation of residual stress with angle φ for the ring-core FIB milling and XRD approaches are shown in Figure 3.15.

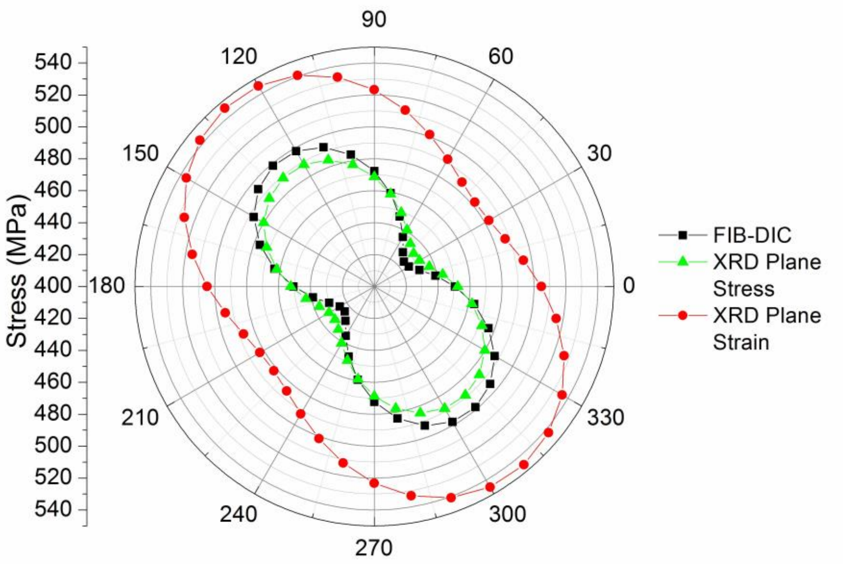

Figure 3.15. Polar plot of stress against angle φ showing the variations obtained using the ring-core FIB milling and DIC technique and XRD assuming plane stress and plane strain conditions.

3.4.4. Discussion

A critical examination of the angular variation of strain obtained from XRD shown in Figure 3.14 reveals that it follows the required $\cos(2\varphi)$ functional form. This suggests that the lattice spacing captured during this analysis is representative of the full in-plane strain state present within the sample.

The sensitivity of strain calculation to the precise quantification of lattice spacing is also demonstrated in Figure 3.15. The use of the literature value of $d_{101}^{0} = 2.9582$ Å produces a strain state which does not agree with the observations of the ring-core FIB milling and DIC approach. The refinement of this parameter assuming conditions of plane strain provides an upper bound value of $d_{101}^{0} = 2.9596$ Å, a change of 0.0014 Å which is sufficient to decrease the principal strains by 0.45 millistrain on average. A lower bound for d_{101}^{0} can also be obtained by considering the situation where the XRD gauge volume conforms to plane stress conditions, leading to $d_{101}^{0} = 2.9586$ Å.

As previously discussed, the through thickness XRD gauge volume spans regions under the conditions of plane stress and plane strain. Therefore, the strain distribution determined through XRD interpretation corresponds to a convolution between the two states. This means that the plane strain and plane stress conditions serve as upper and lower bounds respectively.

A review of the literature was performed to assess the d_{0}^{101} estimates obtained. No quantitative information on the expected lattice parameters of Zenotec Zr Bridge [11] was identified however a range of YPSZ compositions were obtained and the results of the comparison are given in Table 3.2.

Table 3.2. Table of YPSZ lattice parameters and the associated d^0_{101} values for different wt. % of yttria (along with the associated standard deviations).

Ref.	Manufacturer / Product Name	wt. % yttria	a (Å)	c (Å)	d^0_{101} (Å)
[162]	Tosoh / TZ-3YE	3.0	3.605 $\pm$ 0.001	5.177 $\pm$ 0.002	2.9582 $\pm$ 0.0015
[168]	Z-Tech LLC / EF-Premium	5.3	3.6055 $\pm$ 0.0004	5.1797 $\pm$ 0.0002	2.9592 $\pm$ 0.0002
[11] [a]	Wieland Dental / Zenotec Zr Bridge	4.5 $-$ 6.0	-	-	2.9586 $\pm$ 0.0004
[11] [b]			-	-	2.9596 $\pm$ 0.0003
[169]	Synthesised in house using: Merck / zirconium oxychloride Riedel-de Haën / yttrium oxide	6.8	3.6162 $\pm$ 0.0004	5.1576 $\pm$ 0.0006	2.6909 $\pm$ 0.0005
		9.3	3.6251 $\pm$ 0.0005	5.1401 $\pm$ 0.0008	2.9625 $\pm$ 0.0007
		14.1	3.6297 $\pm$ 0.0007	5.1394 $\pm$ 0.0010	2.9648 $\pm$ 0.0009
		15.4	3.6325 $\pm$ 0.0009	5.1426 $\pm$ 0.002	2.9670 $\pm$ 0.0015

[a] This work – XRD plane stress approximation.
[b] This work – XRD plane strain approximation.

Figure 3.16 provides a pictorial representation of the lattice spacing variation with wt. % of yttria and reveals that this variation appears to correspond to a linear relationship. The Region Of Interest (ROI) associated with this study has also been included in this figure. It is bounded by the plane strain and plane stress estimates of d^0_{101} and the manufacturer's tolerances for yttria wt. % [11]. It can be seen that the lattice parameters published by Howard et al. [168] and the linear relationship predicted by the literature values fall within this ROI. This suggests that the bounding values of d^0_{101} calculated using the plane stress and plane strain approximations in this study are likely to be reliable.

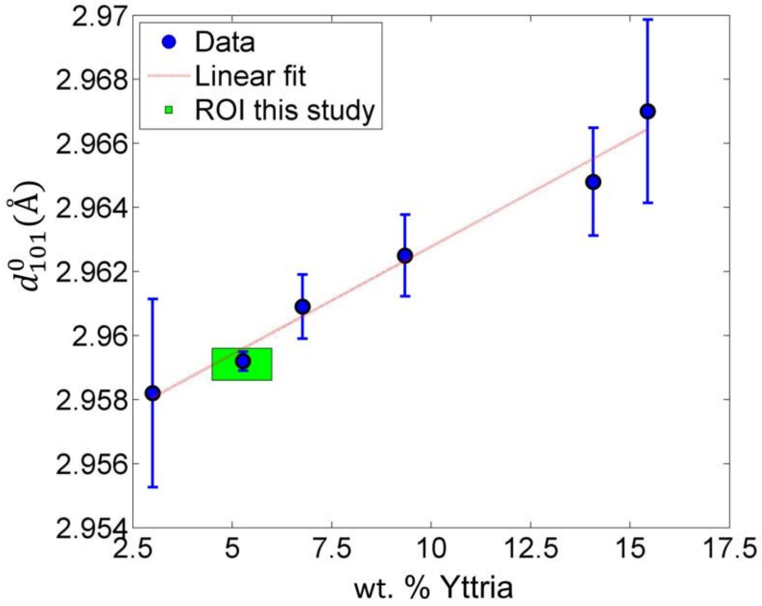

Figure 3.16. Plot of d^0_{101} against wt. % yttria. The ROI of this study is bounded by the plane strain and plane stress estimates of d^0_{101} and the yttria wt. % in Zenotec Zr Bridge [11].

FIST Ring-core FIB Milling and DIC

Stress and strain tensor quantification using XRD is a well-established technique [155, 157] which can be used as a reference to assess and validate the quality of stress and strain evaluation using ring-core FIB milling and DIC. Examination of the angular strain variation shown in Figure 3.14 (and Table 3.1) reveals that the required $\cos(2\varphi)$ relationship is also observed in the data sets obtained using ring-core FIB milling and DIC. The angular offset between the XRD and ring-core profiles is on average 1.2°, which is comparable to the sample mounting orientation error. This demonstrates that the two techniques are aligned with each other to a level of precision that is better that the scatter and experimental error that arises due to external factors.

The least squares fitting that has been performed between the plane stress XRD and ring-core analyses ensures that care must be taken when comparing the magnitudes of the principal strain values obtained. For example, if only one of the principal values were taken into consideration, optimisation of the interplanar spacing (d_{101}^{0}) could be used to exactly match the XRD and ring-core strain estimates in that direction. In contrast to this approach, optimisation of the interplanar spacing was instead performed simultaneously on both principal strain component values using a single parameter (d_{101}^{0}). In this situation, the underlying lattice parameter variation is critical to the quality of fit observed. The optimised error between the two values was found to be ± 0.06 millistrain or approximately 4% of the strain value. This level of precision demonstrates that the principal strain relationships for the XRD and ring-core FIB milling techniques are very similar.

The excellent matching observed between the principal strain values also translates to the stress estimates determined. In the case of plane stress the difference between the XRD and ring-core principal stress estimates were 10 MPa (2%) and -8 MPa (1.9%) for the 1 and 2 values respectively. Similar comparisons can be drawn with the plane strain results by dividing the stress estimates by $(1-\nu^2)$. In this case the offsets were 9 MPa (1.8%) and -9 MPa (2.1%) for the 1 and 2 values respectively.

A critical examination of the final stress state reveals that at 50 µm from the YPSZ-porcelain interface the YPSZ is in a tensile state (average plane stress value = 461 MPa, average plane strain value = 514 MPa) with a relatively small shear component (plane stress value $\tau_{max} = 37.5$ MPa, plane strain value $\tau_{max} = 31$ MPa). As outlined in § 1.2, limited numbers of studies have been performed on the residual stress state in near-interface YPSZ and therefore only one nanoindentation study by Zhang et al.

[33] has quantified the stress magnitude at a resolution comparable to this study. This analysis revealed that at 50 μm from the interface the average plane stress residual stress value in the YPSZ was between 475 and 511 MPa for porcelain coatings of comparable thickness to that applied in this study. The intrinsic variation between samples, and differing experimental techniques used to quantify the residual stress states in each case mean that some discrepancy is expected between these two sets of results. However, it can and should be noted that in general the plane stress ring-core FIB milling and DIC approach shows good agreement with XRD measurements and other results.

3.5. The Sequential FIB Milling and DIC Approach

Spatially resolved residual stress analysis offers obvious advantages over single point measurements, through their capacity to reveal stress gradients. This lateral resolution is necessary to improve understanding of the interactions between microstructure, processing route and stress state in a range of materials and assemblies [170-172]. In order to ensure precise knowledge of the stress analysis location and to ensure a consistent gauge volume, a combination of microscopy and measurement is necessary in spatially resolved techniques. For these reasons the ring-core FIB milling and DIC technique has excellent potential for sequential (i.e. incremental) spatially resolved analysis.

Direct comparison between the initial (undisturbed and residually stressed) and final (milled and strain relieved) states is needed for reliable semi-destructive stress analysis. Therefore care needs to be taken to ensure that successive measurements do not influence each other. In the case of the ring-core FIB milling and DIC geometry, the annular traction-free surfaces induces stress (and therefore strain) relief in the surrounding region and care must be taken to quantify the distance over which this variation becomes negligible. This places a lower limit on the distance between successive milled features.

To obtain an estimate of this lower limit, calculations on the basis of the classical Lamé thick-walled cylinder solution can be used. Consider the outer surface of the trench r_T as the inner surface of an infinitely thick cylinder in a state of equi-biaxial, uniform in-plane stress σ_R. The radial stress (σ_{rr}) and hoop stress ($\sigma_{\theta\theta}$) distributions can be written in a general form as[173] :

$$\sigma_{rr} = C - \frac{D}{\bar{r}^2}, \tag{3.33}$$

$$\sigma_{\theta\theta} = C + \frac{D}{\bar{r}^2}, \tag{3.34}$$

where the variable $\bar{r}$ represents the radial coordinate, and C and D are undetermined constants. The traction free surface at a radius r_T and constant residual stress σ_R state at an infinite distance are used as boundary conditions to determine C and D such that:

$$\sigma_{rr} = \sigma_R \left[1 - \left(\frac{r_T}{\bar{r}}\right)^2\right], \tag{3.35}$$

$$\sigma_{\theta\theta} = \sigma_R \left[1 + \left(\frac{r_T}{\bar{r}}\right)^2\right]. \tag{3.36}$$

This simplified stress analysis provides sufficient insight to conclude that the residual stress variation surrounding an annular feature is inversely proportional to the square of the ratio between the radial coordinate and the outer radius of the feature. By comparing the full through depth relief in a thick walled cylinder and the limited milling depth ($\sim r_T$) of the ring-core FIB milling and DIC approach, it can be seen that this approximation is an overestimate of the actual stress relief. This means that at a radius equal to five times island diameter, the induced stress change is guaranteed to fall below 1%.

In order to provide a quantitative illustration of the capabilities of the sequential ring-core approach, an example study has been selected: a material surface response to shot peening. The residual stress profile induced by shot peening has been well characterised by a wide range of previous studies [174-177] and shows a near-surface compressive stress which tends towards a tensile state within the bulk. This distribution is outlined in detail in § 3.5.2, with the exact stress magnitudes depending on the shot peening parameters applied.

3.5.1.Materials and Methods

The sample selected for the present study was cut from an aero engine compressor blade made from nickel superalloy IN718. Careful control of the processing route resulted in a microstructure of sub-micron precipitates of γ' phase $Ni_3(Al,Ti)$ within an intermetallic face-centred-cubic austenitic phase γ matrix. Despite the highly anisotropic nature of grains within Ni-based superalloys, the microstructure was sufficiently refined to approximate the material as a polycrystalline under the scale of observation ($\approx$ 5 μm). The validity of this approximation was demonstrated by the similarity between the experimental strain relief profiles and the homogenous, isotropic FE simulations [64].

To ensure a consistent interaction, shot peening was applied to the entire compressor blade in a direction aligned to the surface normal. The affected depth was known to be significantly less than 1 mm; beyond the resolution of traditional macro-scale techniques.

The sample was then sectioned using a Buehler Isomet diamond saw, in order to expose a cross-section of the blade surface. Although this sectioning process is known to be mechanically gentle, incremental grinding and polishing was used to reduce the impact of any residual stresses induced by this process. As a final sample preparation stage, the polished cross-section was etched with Kalling's No. 1 reagent for 60 s. This revealed the γ and γ' distribution in the microstructure of underlying material and greatly increased the contrast of the SEM images of the surface. In turn, this improved the precision with which DIC marker tracking could be performed on the images collected.

The Sequential FIB Milling and DIC Approach

The ring-core FIB milling and DIC approach was performed in the Tescan Lyra 3XM FIB-SEM at MBLEM, Oxford, UK. Optimisation of the SEM parameters was used to generate a spot size of 6.9 nm and an automated contrast and brightness routine was used to maximise the dynamic range of the captured images. An image size of 2001×2001 pixels was selected as a compromise between high resolution imaging and experiment duration (and the associated potential for sample drift). Optimisation of FIB parameters was then performed to generate an effective spot size of 7.5 nm at a beam current of 100pA which was selected to reduce ion irradiation in the core.

An island diameter of 5 µm was chosen as a balance between milling time (longer for larger diameters) and the precision of stress evaluation (better for larger diameters). A trench width of 1.5 µm was selected to minimise the impact of re-deposited material onto the island surface and a nominal milling step of 100 nm was then used as an input into the automated incremental FIB milling script. Between each increment, tilt corrected SEM imaging of the core region was performed at an oblique angle of $55°$. Milling was performed to a nominal depth of 5.3 µm in order to ensure that complete stress relief was obtained in the central island. The entire process took approximately 45 minutes and generated a total of 54 images.

The ring-core FIB milling and DIC approach was sequentially implemented to form a line of milled annular features extending from the blade surface to approximately 520 µm into the bulk. Due to edge rounding, the first milling feature was placed approximately 20 µm from the edge. This process was then repeated 10 times along a line perpendicular to the surface in steps of approximately 50 µm. This spacing was chosen to ensure negligible marker interaction, while providing sufficient resolution to resolve the impact of shot peening. Difficulties in alignment and beam drift meant that some stress analysis points were unsuccessful. For this reason some features were placed closer together and others further apart as shown in Figure 3.17. The closest markers were placed 25 μm apart which corresponds to a maximum potential residual stress deviation of 2.5%.

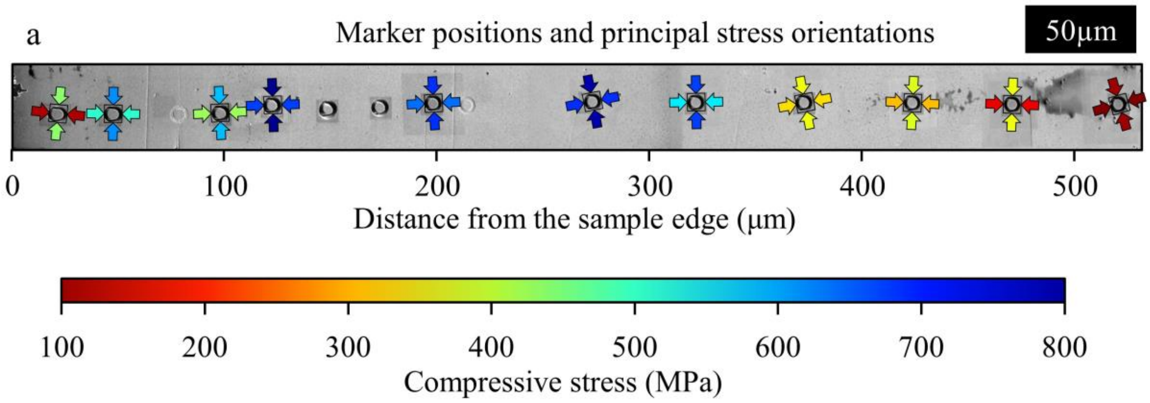

Figure 3.17. Diagrammatic representation of the magnitude (arrow colour) and orientation (arrow rotation) of the principal stresses over an SEM image of the final milling positions.

After SEM image collection, strain relief quantification was performed using the routines outlined in § 3.3 and 3.4. Outlier removal was performed using correlation coefficient thresholding, to leave only well tracked markers with coefficients > 0.5. DIC standard deviation thresholding was implemented to remove markers with a standard deviation greater than 1.5 times the average value, and automated removal of outliers to the linear displacement field was also used to remove markers with a value greater than 1.5 times the average. Full error propagation and FIST analysis was implemented to determine the principal strain relief estimates ($\Delta\varepsilon_\infty^1$ and $\Delta\varepsilon_\infty^2$), orientations and associated confidence intervals.

Equations 3.10-3.13 were then used to convert these residual strains into estimates of residual stress. This analysis was based on the approximation that the gauge volume investigated could be considered isotropic and homogeneous, and therefore that the bulk Young's modulus (205 GPa) and Poisson's ratio (0.294) of IN718 are valid representations of the elastic behaviour. Careful examination of the microstructure of the ROI suggests that this is a valid approximation, since γ' inclusions are typically $<$ 100 nm. An average of $\approx 200{,}000$ inclusions is therefore expected within a single 5 μm core.

XRD Experimental Procedure

Following the sequential ring-core FIB milling and DIC residual stress analysis, XRD was performed at beamline I15 at Diamond light Source, UK using the experimental setup shown in Figure 3.18. A $70 \times 70\ \mu\text{m}^2$ collimation assembly was used to define a pencil beam and a photon energy of 76 keV was selected to maximise the incident flux and diffraction signal from the sample.

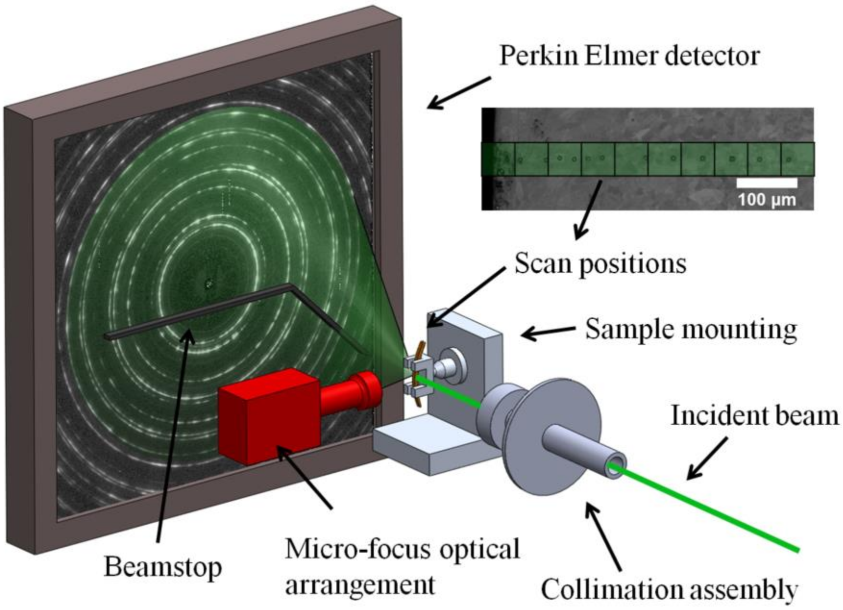

Figure 3.18. Schematic representation of the synchrotron XRD setup at beamline I15. Diffraction patterns were collected by scanning the X-ray beam across the positions shown in the inset.

The sample was placed into a specially manufactured mount and an optical alignment system was used to align the beam with the FIB milling and DIC marker locations at micro-scale precision. A raster scan was then used to collect diffraction patterns in increments of 50 μm from the edge of the sample. A Perkin Elmer flat panel 1621-EN detector (2048×2048 pixels, pixel size $0.2 \times 0.2\ \mathrm{mm}^2$) was used to record the resulting diffraction patterns.

It was found that the relatively large γ phase crystallites present within the specimen induced graininess in the diffraction patterns (Figure 3.18) and for this reason, 30° azimuthal integration was used to improve the grain sampling statistics of the resulting 1D spectra. A critical examination of the Debye-Scherrer rings revealed that sample graininess had least impact on the γ phase peak with Miller index 200. Lattice parameter quantification was therefore performed for the scattering vectors parallel and perpendicular to the edge of the sample for this peak.

3.5.2. Results

The variation in the principal stress magnitude and orientation determined by the sequential FIB milling and DIC approach is shown in Figure 3.17. In general, compressive stresses in the range $100 - 500$ MPa were observed near the sample edge. An increase in the magnitude of compressive stress is then observed towards a maximum of ≈ 800 MPa at ≈ 200 μm from the sample edge. The magnitude of the compressive stress then reduces to ≈ 100 MPa at a 520 μm from the sample surface.

In order to aid in the visualisation of the stress distribution and provide comparison with the XRD results, stresses in directions parallel and perpendicular to the interface were resolved and are shown in Figure 3.19. The variation of these resolved components follows a very similar trend, with stresses in the perpendicular direction showing a marginally smaller magnitude. In order to visualise the distributions more effectively, least squares fitting of nominal shot peened distributions was implemented [178], and the results of this analysis are shown in Figure 3.19. Although the nominal distance from the sample edge is plotted in Figure 3.19, the actual surface location was unknown and the out-of-plane traction-free condition at the sample surface was not enforced in this analysis.

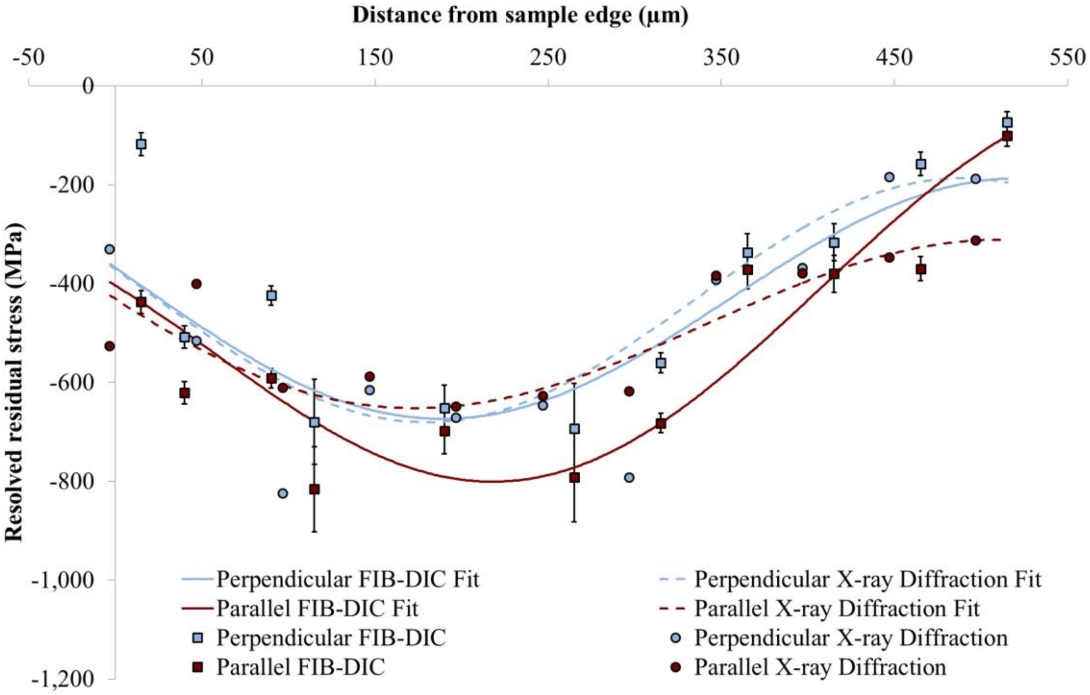

Figure 3.19. XRD and FIB milling and DIC residual stress estimates in directions parallel and perpendicular to the sample edge, against distance from the sample edge. The error bars indicate the 95% confidence intervals of each measurement.

As outlined in § 3.4, care must be taken to account for the differing stress states associated with the XRD and ring-core FIB milling and DIC. The relationships between plane strain and plane stress conditions have been determined in Appendix A and are provided in Equations 3.24-3.28. This approach also facilitates direct comparison between the absolute residual stress estimates provided by FIB milling and the relative values associated with XRD. The optimal value for the unstrained lattice parameter of face centred cubic γ phase of IN718 was found to be $a_{\gamma}^{0} = 3.59756$ Å, which corresponded well to existing literature values [179, 180].

3.5.3. Discussion

The residual stress profiles obtained from the XRD and FIB milling and DIC approaches reveal very similar distributions within the blade. This is particularly true in the case of the average behaviour, which is indicated by the fitted profiles. In the case of the perpendicular stress fitted curves, strong similarities between the range of stress (493 MPa and 486 MPa), maximum compressive stress (680 MPa and 673 MPa), and location of this maximum stress (179 μm and 189 μm from the interface) were observed for the XRD and FIB milling and DIC results, respectively. Greater differences were observed between the parallel stress distributions, however the general trends observed are still similar.

Local grain-to-grain variations in stress can be identified by the scatter around the fitted profiles. This effect is known to be highly influential in crack propagation [181], and recent studies have demonstrated that the ring-core approach is particularly effective in capturing this behaviour [108].

In summary, the sequential spatially resolved ring-core FIB milling and DIC approach has been demonstrated to be an accurate, high resolution (micron-scale), in-plane residual stress analysis technique which has the potential to be applied to a wide range of problems. The main limitation of the sequential spatially resolved ring-core FIB milling and DIC residual stress analysis technique is the spatial increment required between subsequent strain measurements. An alternative approach, the parallel spatially resolved FIB milling and DIC approach, is introduced to overcome this limitation in § 3.6.

3.6. The Parallel FIB Milling and DIC Approach

In order to increase the spatial resolution of the ring-core FIB milling and DIC approach, an alternative to the sequential approach, based on parallel milling of multiple cores, is proposed here. The parallel milling approach is based on simultaneously monitoring the strain relief in all cores during a single milling routine.

The central parameter of the ring-core FIB milling and DIC technique is the complete strain relief at an infinite milling depth ($\Delta\varepsilon_\infty$). This is the saturated value of the strain change induced in the surface of the milled island feature and is dependent only upon the residual stress state and the material parameters, and *not* on the milled feature geometry. Although the strain path between the undisturbed and fully relieved state depends on the milling process and the interactions between neighbouring features, the total strain change value $\Delta\varepsilon_\infty$ is invariant to these changes. Continuous imaging of the relief, effective DIC and the attainment of a sufficient milling depth are used to obtain the most reliable estimate of $\Delta\varepsilon_\infty$.

A recent paper by Sebastiani et al. [123], aimed at quantifying Poisson’s ratio at the micro-scale, demonstrated the impact of alternative milling process routes on the surface relief in an equi-biaxial-stressed thin film. Initially, two parallel trenches were FIB milled in the surface (Figure 3.20b). Following this, two further trenches were milled in a direction perpendicular to the first trenches in order to leave a 3 µm square ‘island’ of relieved material (Figure 3.20c). The strain relief variation in the vertical and horizontal directions was then used to estimate Poisson’s ratio.

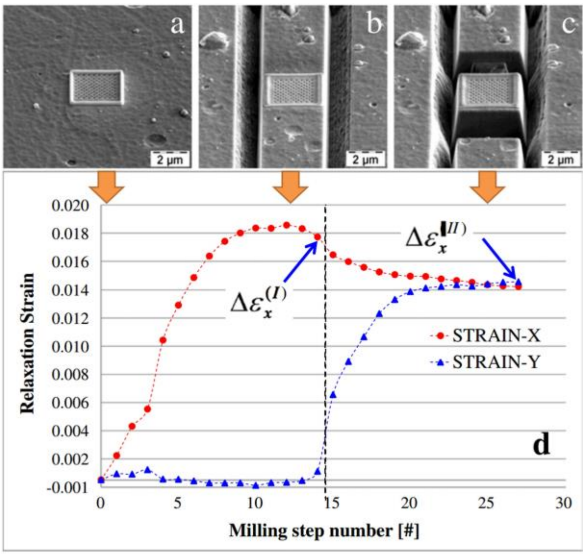

Figure 3.20. Poisson’s ratio determination at the micro-scale. a) DIC marker placement. b) Parallel vertical trench milling. c) Horizontal milling to leave a 3 µm fully relieved square island [123].

For the purposes of the present discussion I am going to use the results of Sebastiani et al. [123] to consider the strain relief profiles as a function of depth, as shown in Figure 3.20d. Although the strain relief profiles in the two directions differ, the strain values converge at large milling depths. This proves that $\Delta\varepsilon_\infty$ is *robust*, i.e. will reach a magnitude that depends only on the undisturbed residual stress. It is known that the parallel milling approach will induce smaller variations in strain relief than those demonstrated by Sebastiani et al., and therefore that a reliable estimate of $\Delta\varepsilon_\infty$, will therefore be obtained at large milling depths. This complete stress relief analysis also demonstrates equivalence between the ring-core and square-core milling geometries i.e. they both enable reliable quantification of $\Delta\varepsilon_\infty$ provided milling has been performed to a sufficient depth. Both techniques can therefore be used interchangeably depending on the specific user shape requirements.

In order to pursue parallel milling and imaging of multiple cores, a regular line of square features was implemented – the so-called ‘chocolate block’ geometry (Figure 3.21). This approach ensures that maximum lateral resolution of one marker width could be reached, with a regular step size between adjacent measurements, and is a much simpler milling regime than would be required to produce circular markers. Placing the markers close together also reduces the SEM field of view necessary to simultaneously capture all markers, thereby reducing the implementation time. The main limitation on the number of markers comes from the maximum SEM imaging resolution which can be achieved, i.e. the number of pixels that can be captured at the resolution necessary for accurate stress determination.

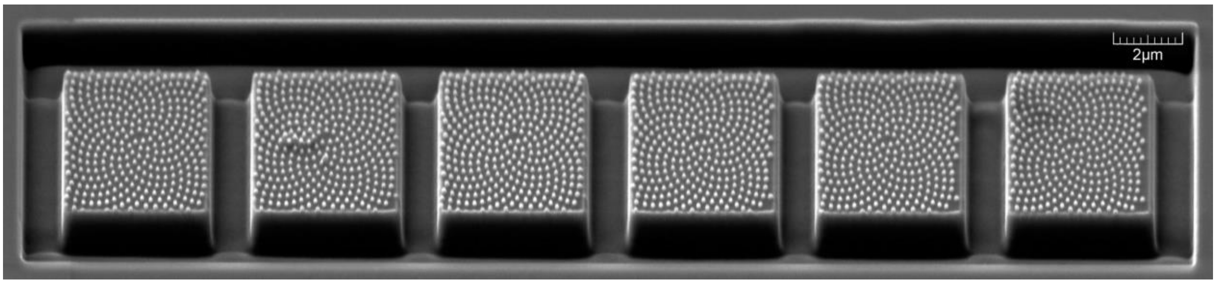

Figure 3.21. SEM image of the parallel FIB milling and DIC arrangement – the 'chocolate block' geometry. Electron deposition of markers has been used to increase the surface contrast of the cores. The average residual stress in the 4 μm cores was determined at an increment of 5 μm.

In order to guarantee reliable results, the core surface must achieve a state of complete stress relief when milled in a regular arrangement, as proposed in this technique. Synchrotron XRD mapping [76] has recently been used to demonstrate that this is valid for depth-diameter ratios greater than ≈ 0.25 and therefore all milling has been performed to depth-diameter aspect ratios greater than 1.

In terms of the DIC analytical procedure, the parallel FIB milling and DIC approach is very similar to the sequential approach at each marker. The main difference is that the strain relief profile is no longer accurately described by the isolated ring-core feature due to the influence of neighbouring markers. Nevertheless, accurate estimates of $\Delta\boldsymbol{\varepsilon}_{\infty}$ can be obtained, provided that the island is milled to a depth sufficient to induce full relief.

Experimental Validation of the Parallel FIB milling and DIC Approach

Cross-validation between the results of a new experimental technique and a well-established method is a necessary step to assess result reliability. In this regard, a recent study of the residual strain distribution inside a carbon core silicon carbide (SiC) fibre was selected for comparison [112].

During this experiment XRD was performed at beamline B16, at Diamond Light Source, Harwell, UK. High spatial resolution (400 nm) maps of lattice parameter variation were collected across the carbon core and silicon carbide regions of the uniaxially reinforced titanium alloy (Ti-6Al-4V) composite. In order to convert this lattice variation into a measure of residual strain, accurate knowledge of the unstrained lattice parameter was required. Insurmountable difficulties arise in producing strain-free powder reference samples of these materials. Therefore, without the high spatial resolution (5 μm) analysis performed using the parallel FIB milling and DIC approach, only relative information on the strain variation could be obtained.

As previously highlighted, the strain relief obtained during the parallel FIB milling and DIC approach is a measure of absolute relief in the material surface. Therefore, after performing the necessary XRD strain value averaging, the unstrained lattice parameters of the SiC and graphite core were obtained by direct comparison between the XRD and the FIB milling and DIC strain profiles. Not only did this serve to cross-validate the two experimental techniques, but it also provided the necessary insight to ensure that the nano-scale strain variation determined by XRD was a measure of absolute strain variation; the critical parameter in understanding the failure modes of these fibres.

At this point it is important to note that the back-calculation of the residual stress state must be performed with care due to the variations in amorphous content and associated anisotropy. Nevertheless, the strain profiles obtained by XRD and the FIB milling and DIC approach can be compared, and show consistent results as outlined in § 3.6.2.

3.6.1.Materials and Methods

The SiC and titanium alloy composite in this study was comprised of 35% by volume SCS-6 SiC fibres aligned in a single direction. The fibre was composed of a 30 μm diameter graphite core which was surrounded by SiC with an outer diameter of 140 μm. Within this graphite core, a distinct untextured central 13.5 μm diameter region was observed. Two different lattice parameter values were therefore obtained for carbon; one for the inner and one for outer region.

In order to minimise the residual stresses induced during preparation, sample sectioning was performed using a Buehler Isomet diamond saw. This process was followed by an incremental grinding and colloidal silica polishing procedure. A final thickness of ≈ 500 μm was selected in order to maximise the diffracted beam intensity at the energies available at beamline B16.

As part of the experimental process, tomographic reconstruction of the SiC was also performed, as discussed in more detail in the literature [112]. In order to facilitate full illumination of the sample by the X-ray beam, further sectioning was performed using a similar diamond saw and polishing process. The final sample was a $1 \times 0.5 \times 0.5$ mm^3 cuboid as shown in the insert in Figure 3.22.

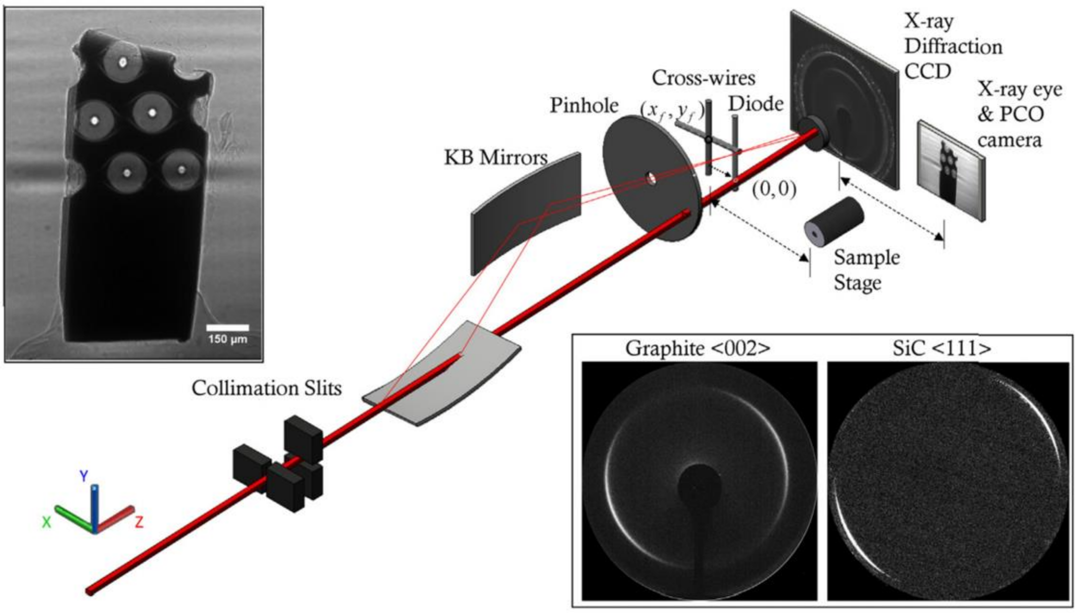

Figure 3.22. Schematic of the XRD setup showing the aligned sample and diffraction patterns from the SiC and graphite regions [112].

XRD Experimental Procedure

In order to record the highly spatially resolved variations of elastic strain, the KB mirror focusing capabilities available at B16 were exploited to produce a $0.4 \times 0.5\ \mu m^2$ beam. A 150 μm diameter pinhole was used to block the higher order reflections as shown in Figure 3.22. The sample was placed on a translation and rotation stage and an incremental beam-alignment process was then implemented to determine the location of the beam on the sample surface to nano-scale accuracy, this is outlined in detail elsewhere [112].

Piezoelectric translation stages were used to raster the sample incrementally across the beam, and diffraction patterns were recorded at each location. Six line scans were implemented in order to map a representative region of the SiC and the carbon core.

Azimuthal integration of the resulting diffraction patterns was performed, and the lattice parameter variation was determined for scattering vectors pointing in the radial and hoop directions. The lattice parameter variation in each of the different regions was determined: a in the case of face centred cubic SiC and c, the larger unit cell dimension, for the hexagonal close packed graphite. As previously noted two different lattice constants were required in the graphite; c_0 in the case of the outer textured region and c_i in the case of untextured the inner core region. The crystallographic texture associated with the SiC region limited the azimuthal angles over which a representative lattice constant could be quantified and therefore only the variation in the radial lattice constant was determined.

The Parallel FIB Milling and DIC approach

Following XRD, the sample was placed into the Tescan Lyra 3XM FIB-SEM at MBLEM, Oxford. SEM parameter optimisation was performed to give a 5.7 nm spot size and an image size of 4096×4096 pixels was selected in order to maximise the resolution of the captured images. Careful focusing, line and image averaging, as well as automated contrast and brightness selection was used to maximise the dynamic range and reduce noise in the image.

The same FIB beam parameters were implemented as those outlined in § 3.5.1. Both the SiC and carbon core were found to have similar FIB milling rates and therefore a single parallel milling process was implemented on both regions simultaneously. Six cores with dimensions of $4 \times 4\ \mu\mathrm{m}^2$ were selected as a compromise between maximising the number of stress evaluation points, and the precision of these estimates. A trench width of 1 μm was chosen in order to minimise the increment between successive points and a depth-diameter ratio of 1.27 was selected to ensure complete relaxation in the core. The stress analysis positions were located at radial distances between 2.5 μm and 27.5 μm from the fibre axial line, in increments of 5 μm, as shown in Figure 3.23.

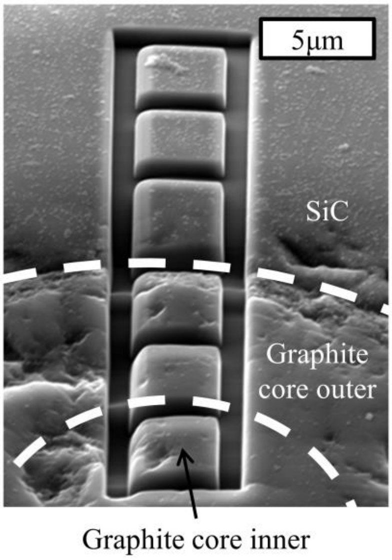

Figure 3.23. SEM image of the parallel FIB milling and DIC technique in which the interfaces between the SiC region, the graphite core outer and the graphite core inner are highlighted. The core sizes are uniform in the direction of the global surface normal. However, slight variations in topology create the illusion of size variation [112].

In order to overcome the limitations of SEM imaging, a very small FIB milling increment of 15 nm was selected. This minimises the strain change between successive measurements and increases the likelihood of effective DIC tracking. A small milling current of 100 pA was selected to reduce the amount of material redeposition on the islands (and the associated image blurring in the DIC analysis) and to minimise the residual stress induced by gallium ion implantation.

The optimised arrangement captured 340 images over a period of approximately 5 hours. Although this time period may seem long, the full 2D in plane stress state is characterised at 6 different locations during this interval. Twelve independent implementations of a 1D stress characterisation technique would be necessary to obtain comparable data, resulting in an equivalent time budget of 25 minutes per data point for the parallel FIB milling and DIC method.

DIC of the resulting images was performed using the routine outlined in § 3.3. Automated outlier removal was performed using the same variables outlined in the sequential ring-core FIB milling and DIC analysis in § 3.4.1. It was found that the residual colloidal silica provided increased surface contrast, thereby improving marker tracking effectiveness.

The use of square markers in this study, rather than the isotropic annular milling geometry associated with ring-core milling, prevented quantification of the FIST. Instead, strain relief profiles were obtained in two perpendicular directions for each of the 6 cores; the radial and hoop directions.

Relatively high levels of noise (and the associated 95% confidence intervals) were observed in the profile of strain relief against the image number. A weighted average of the strain relief ($\Delta\varepsilon$) from multiple (20) images was therefore calculated based on the inverse of the standard deviation of each relief value ($\sigma_{\Delta\varepsilon}$). Following normalisation against the full depth strain relief values, the results of this averaging are shown in Figure 3.24.

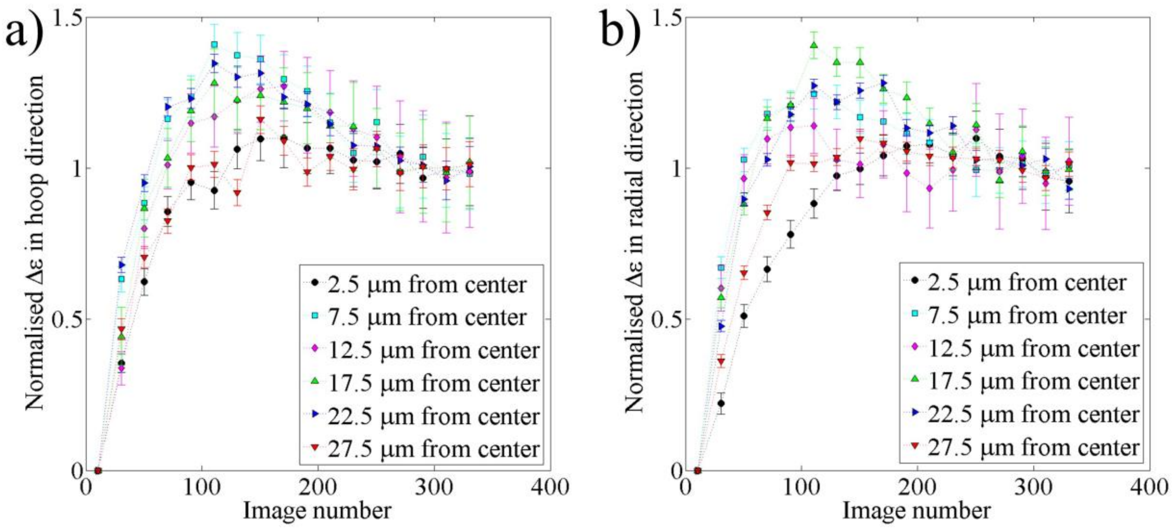

Figure 3.24. Normalised strain relief twenty point weighted average against image number for the six stress analysis locations, in the a) hoop and b) radial directions.

The first conclusion that can be drawn from this Figure 3.24 is that milling has been performed to a depth sufficient to induce full relief in the cores. This is demonstrated by plateaus in all of the strain relief profiles. The influence of neighbouring markers is also demonstrated in this figure, through the slight differences observed in the strain relief profiles. Feature symmetry suggests that the profiles at 2.5 µm and 27.5 µm, 7.5 µm and 22.5 µm, and 12.5 µm and 17.5 µm should be similar. Careful examination of the profiles demonstrates a degree of similarity between these profiles.

Despite minor variations in the strain relief profiles, the general variation is very similar to the functional form of the isotropic, single ring-core FE model in Equation 3.3. Based on this insight, careful least-squares fitting of this function was performed on the data. The close agreement observed between the XRD and parallel FIB milling and DIC results suggests that the use of this functional representation is effective in determining estimates of $\Delta\varepsilon_\infty$ for this milling geometry.

3.6.2.Results

In order to interpret the SiC and graphite XRD lattice parameter variation in terms of strain, accurate quantification of the unstrained lattice parameters was required. A least squares optimisation approach was therefore implemented starting from literature values of the unstrained lattice parameters (a^0= 4.3596 Å [182] for the face centred cubic SiC region and c^0=6.720 Å [183] for the larger unit cell dimension of the graphite region). For this analysis, averaging of the XRD strain values over the relevant gauge volume was necessary to provide comparative values. For example, the FIB milling and DIC estimate at the 2.5 µm position represents a strain average between the radii of 0.5 µm and 4.5 µm. The optimised values were found to be a^0 = 4.3982 Å, c_o^0 = 6.8353 Å and c_i^0 = 6.9980 Å where the superscript 0 refers to the unstrained lattice parameters of the SiC (a), graphite outer region (c_0) and the graphite inner region (c_i) defined in § 3.6.1.

The variations in the absolute residual strain obtained from the XRD and FIB milling and DIC approach are plotted together in Figure 3.25. The SiC region can be seen to be in a state of compressive strain which decreases in magnitude at distances further from the core. The central carbon core region is in a state of approximate hydrostatic compressive strain of $\approx$ 0.4%. The outer carbon core, on the other hand, is in a state of dilatational strain; the radial component is tensile and the hoop is compressive.

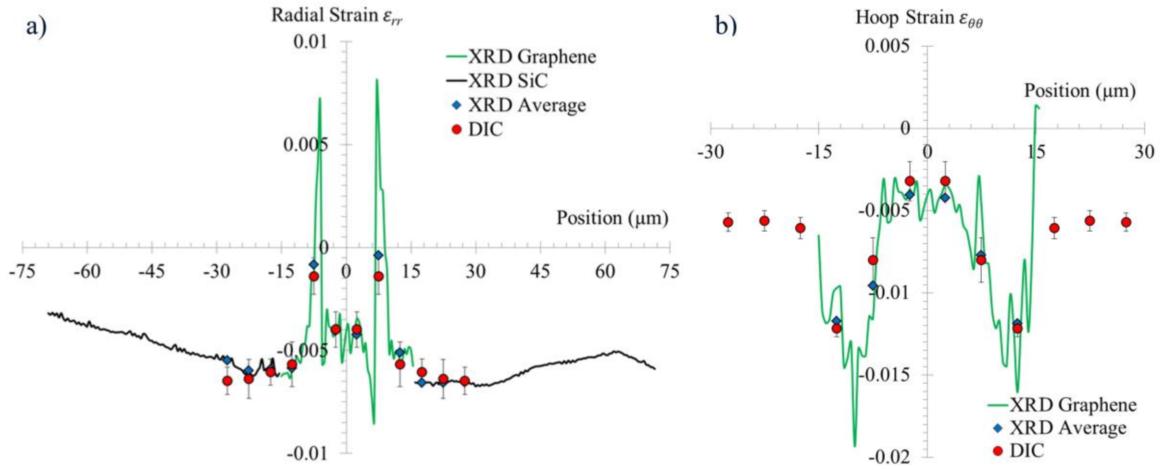

Figure 3.25. a) Radial and b) hoop strain distributions within the graphite and SiC regions of the core [112]. The results of both the XRD and parallel FIB milling and DIC are shown. The 95% confidence intervals are indicated by the error bars.

3.6.3.Discussion

A critical examination of the results of parallel FIB milling and DIC indicates that relatively large 95% confidence intervals are produced by this analysis, with an average confidence interval of $\approx \pm 20\%$. The origin of this low confidence is primarily associated with the difference between the strain relief profiles (Figure 3.24) and the functional fitting distribution implemented (Equation 3.3).

Examination of the average XRD data reveals that only three out of the eighteen data points fall outside the FIB milling and DIC 95% confidence bounds, and that the average percentile error is 13%. Taking into account the assumptions necessary to compare these two different techniques, these two data sets show strong similarities in the distributions obtained. This suggests that the parallel spatially resolved FIB milling and DIC approach is a reliable method for in-plane absolute residual distributions of strain, and of stress in well-characterised materials.

Despite the advantages of the parallel FIB milling and DIC technique its use is likely to be limited to specialised applications where micron-resolved residual stress analysis is crucial in improving current understanding. This restriction is primarily associated with the long milling times ($\approx$ 5 hours). Other restrictions on the technique include the minimum resolution and maximum region over which stress can be assessed. Very high resolution analysis ($<$ 1 μm) would likely begin to be influenced by the effects of residual stress induced by ion implantation and the reduced area over which DIC can be performed, whereas limitations on maximum high resolution SEM image size place an upper boundary on the assessment region. Finally, as highlighted in the carbon fibre example study, difficulties in obtaining precise and reliable stiffness tensor matrices at these resolutions may provide challenges in the conversion of the strain relief values to residual stress estimates.

The elastic strain distributions evaluated during this study were used as the basis for further FE simulation of the SiC and carbon core region [112]. The insights obtained provided improved understanding of the impact of the processing route on the resulting microstructure and strain distributions. Of particular interest was the relatively high tensile strains observed at the interface between the carbon outer and carbon inner regions inside this complex hierarchical structure.

3.7. Conclusions

3.7.1. Outlier Removal, Error Analysis and Propagation

Accurate and reliable estimates of the error bounds on the residual stress estimates provided by FIB milling and DIC based techniques are a pre-requisite step in assessing the reliability of such approaches. These bounds can be influenced by a wide range of potential error sources, including image noise, marker aliasing and material redeposition.

In § 3.3 a new approach capable of precise error quantification and propagation has been developed to provide confidence intervals on the residual stress estimates produced by the ring-core FIB milling and DIC approach. This analysis starts from the error associated with DIC marker tracking and uses weighted least squares fitting to propagate this error. The confidence intervals of the resulting core relaxation can then be used in combination with the errors on the elastic constants to provide precise estimates of the confidence intervals of the residual stress estimates.

Three new automated outlier detection and removal techniques have also been elucidated. These methods are based on correlation coefficient and DIC marker standard deviation thresholding, as well as the removal of outliers to the expected linear displacement field. By removing the need for manual outlier removal, these approaches have made the results of the ring-core analysis more robust, rapid and reliable. This has also facilitated the repeated implementation of this analysis required for FIST quantification.

The generic nature of the outlier removal and error propagation techniques presented here ensures that they have potential for use in the other FIB milling and DIC based techniques outlined in § 2.3.3. The relative simplicity of the new techniques also facilitates efficient coding implementation in the broad range of programming languages in which this analysis is currently being implemented.

3.7.2.FIST Analysis

The strain and stress tensors obtained using the FIST ring-core FIB milling and DIC method, and XRD show excellent agreement both in terms of angular orientation and principal strain and stress values. The realistic lattice spacing estimates and agreement with residual stress values previously published in the literature demonstrates that the results obtained using the two techniques are highly consistent with each other and with current knowledge of the YPSZ-porcelain system.

This study has demonstrated the FIST FIB milling and DIC technique which is the first experimentally validated FIB based technique capable of quantifying the full in-plane tensor in a microscale gauge volume. The short experimental durations (≈ 30 minutes), automated processing routines and well-defined confidence intervals associated with this technique ensure that this approach offers a rapid, reliable and precise solution for experimental stress analysis at the micro-scale. This method overcomes the primary limitations of XRD strain tensor analysis: it provides an absolute measure of residual strain without the need for unstrained lattice parameter estimates, interrogates a well-defined 3D gauge volume, is suitable for use on amorphous materials, and can be readily implemented at a broad range of laboratory facilities.

This experimental technique has the potential to improve current understanding in the wide range of applications for which knowledge of the strain tensor is required within a microscale gauge volume. Although this method is a semi-destructive near-surface based technique, the approach can be extended to sub-surface measurements through appropriate sample sectioning. Although sectioning is known to modify the near-interface strain state, the analytical results presented in Appendix A establish a link between the plane stress approximation of the near-surface residual stress state, and the plane strain approximation which is appropriate for the material bulk. This result enables the evaluation of the original strain state present in the sample prior to sectioning.

Alongside the validation of the FIST ring-core FIB milling and DIC technique that was the main focus of this section, a simple technique has been presented that is capable of producing bounding estimates for the unstrained lattice spacing. This methodology is particularly well suited for the case where other lattice parameter determination methods have proved unsuccessful, for example due to limited quality diffraction patterns, or the impossibility of achieving the required spatial resolution in regions of high chemical gradients.

The derivation and numerical validation of the relationship between plane strain and plane stress conditions will also be useful in a broad range of mechanical studies, e.g. for continuously processed samples that contain sources of residual stress (eigenstrains) that are uniform along the axis of extrusion, and which are examined at their cross-sections.

3.7.3.Spatially Resolved Residual Stress Analysis

Two spatially resolved FIB milling and DIC based techniques have been presented and validated in § 3.5 and 3.6. These techniques have well-defined gauge volumes, can be used to provide insight into the 2D stress state of the material and can probe two differing spatial length scales in a sample of interest.

The sequential spatially resolved ring-core FIB milling and DIC approach can be used to quantify the residual stress state at a spatial resolution between millimetres and tens of micrometres, with micro-scale averages obtained at each point. A comparison between XRD and this approach has demonstrated this technique produces reliable and consistent results. The main limitation of this approach is the interference observed when subsequent stress measurements are placed close together.

In order to overcome this limitation, the parallel FIB milling and DIC approach has been presented. This technique involves simultaneous milling of multiple compact features (squares) in order to obtain residual stress estimates with a spatial resolution at the micro-scale, both in terms of the gauge volume and step. Cross-validation between the residual strain profiles obtained by high resolution XRD and this method suggests that, despite observing larger signal to noise ratios, this approach also offers a reliable and effective technique for spatially resolved residual stress.

Overall, the two newly proposed techniques are fast, robust and reliable. They offer the potential to perform spatially resolved residual stress analysis from the millimetre down to micrometre scale with nano-scale precision. The application of these techniques can be used to improve understanding of materials failure; particularly the YPSZ-porcelain interface (as outlined in § 6.5).

3.7.4.Summary of Refined Ring-core FIB milling and DIC Residual Stress Analysis

In this chapter several refinements to the ring-core FIB milling and DIC approach have been presented. These approaches have substantially expanded the capabilities of this technique, have facilitated improved automation and provided precise estimation on the error bounds of the stress estimates. Here I provide a brief summary of the experimental and analytical stages necessary to implement residual stress analysis using these refined approaches. These steps are illustrated graphically as a flow diagram in Figure 3.26, where they are grouped into three main sections; experimental implementation, strain relief estimation and elastic stiffness estimation. The greatly increased capabilities and refinement in this diagram can be compared and contrasted with Figure 3.1, which represented the state-of-the-art capabilities of ring-core FIB milling and DIC prior to this analysis. Potential sources of error have also been included and are highlighted in white in Figure 3.26.

The ring-core approach starts with preparing the sample for FIB milling at the location of interest. This procedure can also be associated with the first sources of experimental error; relief induced by sample sectioning (in order to facilitate access to the area of interest), or with surface preparation techniques which may influence the residual stress state prior to analysis.

Next, the user must decide the type of residual stress quantification required; single point, low resolution or high resolution spatially resolved analysis. The appropriate milling geometry / sequence of milling can then be selected for the next experimental stage.

High magnification and high contrast SEM imaging is then performed to capture the starting ‘undisturbed’ surface, before incremental FIB milling and SEM imaging is applied. Errors associated with the experimental process are known to include the intrinsic noise of SEM imaging, sample drift induced by charging of the sample surface, redeposition of milled material onto the DIC surface and the residual stress induced by ion implantation.

Following FIB milling and SEM micrograph collection, DIC of selected regions within the images is implemented. At this stage, the orientation of interest needs to be considered and the DIC marker displacements need to be rotated accordingly (Equation 3.15). In the case of FIST analysis, this rotation and strain quantification process is repeated several times in order to gain insight into the in-plane angular variation. This behaviour is shown in the form of a loop in Figure 3.26 which has an exit flag at the point where all necessary orientations have been assessed.

At this stage, automated outlier removal can be performed using correlation coefficient and peak position standard deviation thresholding. An iterative outlier removal process based on the relative movement between markers can also be performed. Least squares fitting of Δx against x is then carried out to determine estimates of the core strain relief of each image ($\Delta \varepsilon$), along with the associated uncertainties of this parameter (based on the DIC marker standard deviations). Any outliers to this expected displacement field can then be removed in an incremental fitting and outlier deletion process.

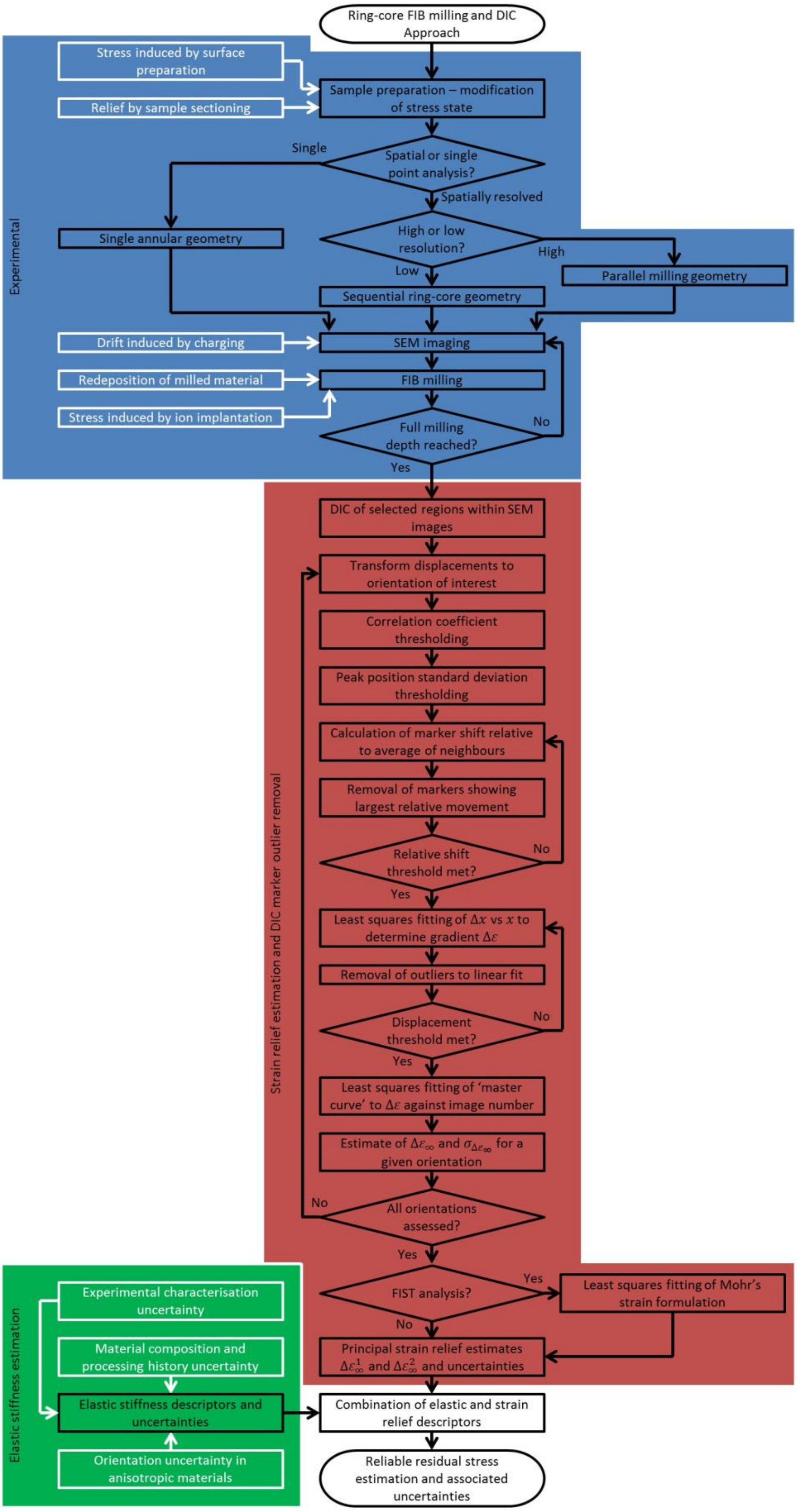

Figure 3.26. Updated flow diagram of ring-core FIB milling and DIC showing the new capabilities outlined in this study. The process has been grouped into 3 stages; experimental, strain relief estimation and elastic stiffness estimation. Potential sources of error are shown in white.

The resulting strain relief against image number distributions are then fitted with the ‘master curve’ (Equation 3.3) to provide estimates of the full strain relief at infinite milling depth ($\Delta\varepsilon_\infty$) in a given orientation. In order to quantify the confidence intervals on this parameter, each data point is weighted using the inverse of its standard deviation.

In order to determine the principal strain relief estimates two approaches can next be used. The first is based on the approximation that the principal strain orientation of the system is intrinsically known, for example in the case of an orientationally dependent substrate. Alternatively FIST can be performed using Mohr’s strain formulation, as outlined in § 3.4.

The final stage of the analysis involves the calculation of residual stress estimates and confidence bounds from the strain relief and elastic stiffness parameters, and their associated confidence intervals. Elastic stiffness estimates can be obtained from material composition and process history or from experimental characterisation. These approaches provide intrinsic confidence limits for the parameter descriptors of the material elastic response which can be combined with the uncertainty of the strain relief estimates in order to provide comprehensive estimates of the residual stress confidence intervals.

Overall, the capabilities, precision and reliability of the residual stress estimates provided by ring-core FIB milling and DIC technique have been greatly improved by the development outlined in this chapter. These improvements have been necessary to facilitate enhanced understanding of the residual stress state at the YPSZ-porcelain interface as outlined in detail in Chapter 7.

4. Calculation of the Single Crystal Stiffness Coefficients of YPSZ

4.1. Introduction and Motivation

Reliable and precise estimation of the single crystal stiffness constants of tetragonal YPSZ is necessary to improve understanding of the microscale grain-to-grain interaction induced by the tetragonal to monoclinic phase change. These insights can be used as inputs to FE models of the YPSZ-porcelain interface [184] to relate the strain tensors within the model to values of stress and to predict how the phase transformation proceeds.

Very few representative estimates of the elastic stiffness coefficients of YPSZ have been published in the literature, due to the severe difficulties associated with the application of conventional analysis techniques. Although phase velocity analysis of acoustic waves has been successfully applied to monoclinic zirconia [185], the micro twinning characteristics of YPSZ cause interference during the application of this technique. Equally, the change in frequency of light due to inelastic photon scattering (Brillouin scattering) has been successfully applied to single crystals of cubic zirconia [186], however the polycrystalline nature of YPSZ makes this approach unsuitable.

For the reasons above, I decided to invest effort in developing and applying novel methods based on neutron scattering to obtain upper and lower estimates of the single crystal stiffnesses of YPSZ [187]. This technique has been in the past performed in conjunction with Voigt or Reuss averaging to approximate the system as described by uniform stress or strain fields, respectively. In order to overcome this limitation, a new approach using multiple FE simulations has been developed so that the stress and strain fields in YPSZ could be more reliably captured [188]. The approach is based on model matching of the predictions of the average lattice strain within a selected grain group defined by the orientation of the lattice plane normal, with the experimentally recorded strains from a polycrystalline aggregate. I have recently published in the outcomes of this analysis in the Journal of Applied Physics [189].

4.2. Materials and Methods

In this study, a standard cylindrical compression test specimen of diameter 8 mm and length 22 mm was manufactured from Zenotec Zr Bridge using dry milling and the manufacturer recommended sintering conditions (as outlined in § 1.1) [11]. Neutron diffraction of these samples was performed during *in situ* compression at beamline Engin-X at ISIS Spallation Neutron Source. An Instron 100 kN uniaxial servohydraulic loading rig was used to load the sample, which was held by specially manufactured hardened grips and an MTS 632.13F-21 dynamic extensometer clip gauge was attached to the sample in order to record the macroscopic strain change.

Beamline setup similar to that outlined in detail by Daymond et al. [190] was implemented, in which simultaneous measurements of time-resolved spectra were made from the two detector banks, as shown in Figure 2.6. The centres of these banks were positioned at fixed horizontal scattering angles of +/- 90^0 to the incident beam and the loading axis was aligned horizontally at 45^0 to the incident beam. This ensured that the scattering vectors $\boldsymbol{Q_1}$ and $\boldsymbol{Q_2}$ recorded by the detector banks were parallel and perpendicular to the axial loading direction, respectively.

Beam-defining slits and radial collimators were used to define a $3 \times 3 \times 3\ \mathrm{mm}^3$ gauge volume in the centre of the sample. Disc choppers speeds were selected to define neutron pulses so as to access the time-of-flight range of $17 - 58$ ms (corresponding to a d_{hkl} range of $0.95 - 3.26$ Å). The small sample size and high neutron scattering length of zirconium meant that d_{hkl} peak fitting errors of less than 10^{-4} Å were obtained after $16\ \mu\mathrm{A} - \mathrm{hrs}$ of total integrated neutron flux. Comparison between the two diffraction spectra revealed that the signal to noise ratio associated with $\boldsymbol{Q_2}$ was approximately twice that associated with $\boldsymbol{Q_1}$. This was an intrinsic limitation of the setup and was associated with the larger path length of the diffracted beam through the loading rig for scattering in the $\boldsymbol{Q_2}$ direction.

The sample was incrementally compressed in 25 MPa steps from 8 MPa in load-control mode and a loading rate of $0.04\ \mathrm{MPa\ s^{-1}}$ was chosen to reduce time-dependent effects. The sample failed in brittle manner during the ramp to reach the compressive stress of 1408 MPa.

4.3. Results

Open Genie, a diffraction data analysis and plotting software package developed at ISIS spallation neutron source, was used to perform Gaussian peak fitting of the resulting diffraction spectra. This approach was used to calculate the time of flight (t_{hkl}) associated with the $101, 110, 102, 112$ and 200 peak centres. Equations 2.9 and 2.10 were then used to determine the neutron wavelength corresponding to each peak centre (λ_{hkl}) and the corresponding lattice spacing (d_{hkl}). The lattice strain for each peak (ε_{hkl}) was calculated using Equation 2.7 and estimates of the unstrained lattice parameters (d^0_{hkl}) which were obtained from diffraction of the unloaded sample.

This analysis technique was applied to the data associated with scattering vectors both parallel and perpendicular to the loading direction. A distinct change of lattice strain gradient was observed on several of the fitted peaks when the sample was loaded beyond 458 MPa. A typical example of this response is shown by the plot of 200 lattice strain against applied macro-stress (σ_{Macro}) in Figure 4.1. The 'apparent lattice stiffness' ($E_{App} = \sigma_{Macro} / \varepsilon_{hkl}$) for this lattice orientation was found to change from 260.6 ± 8.1 GPa for stresses below 458 MPa to 199.7 ± 2.0 GPa for stresses above 458 MPa. The characteristic 'knee' observed in this data is indicative of the onset of ferroelastic re-orientation in YPSZ [191]. In order to remove the effects of this transition, a decision was made to limit the focus of this study to the region below 458 MPa.

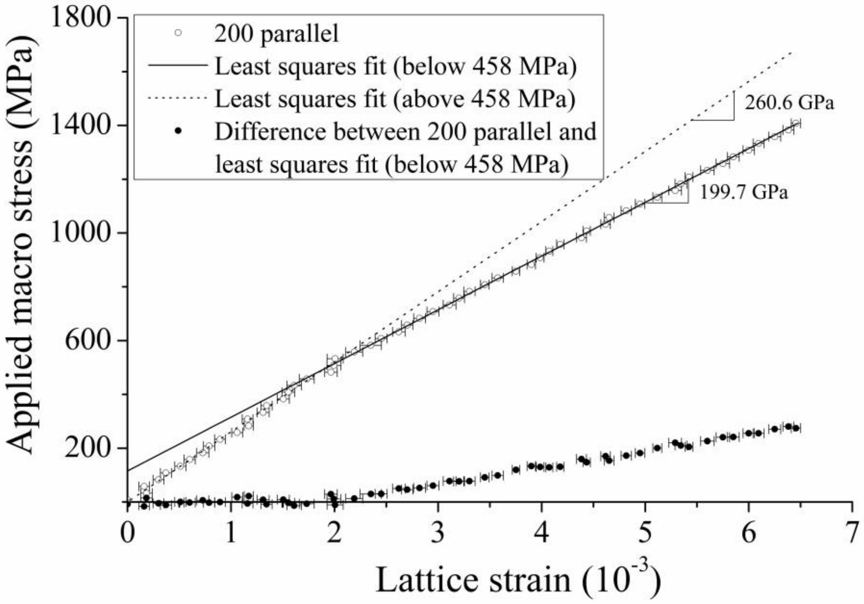

Figure 4.1. Applied macroscopic stress against the 200 lattice strain in a direction parallel to the loading axis (with associated 95% confidence intervals from peak fitting). The change in gradient at 458 MPa is indicated by the differing gradients above and below this stress.

A plot of lattice strain for all fitted peaks in directions parallel and perpendicular to the loading direction against applied macro-stress (σ_{Macro}) in the range of 8 to 458 MPa is shown in Figure 4.2. The variations in average 'apparent lattice stiffness' are illustrated by the differing gradients associated with each reflection. Following outlier identification and removal, least squares fitting was used to determine the line slopes. A 95% confidence interval (CI_{95}) was also calculated for each lattice orientation based on the combination of peak fitting error and least squares goodness of fit.

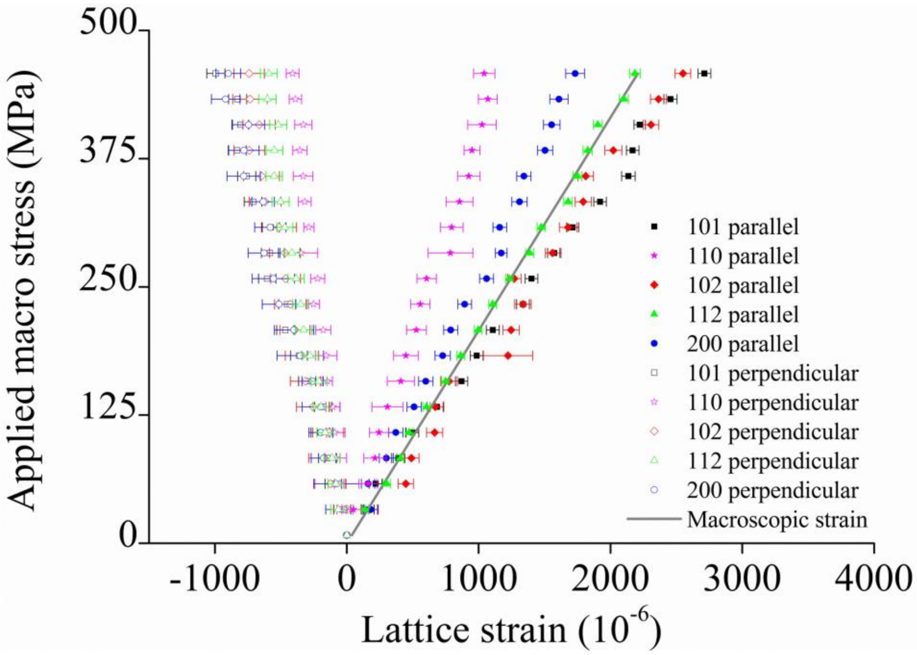

Figure 4.2. Applied macroscopic stress against lattice strains from scattering vectors parallel and perpendicular to the loading axis showing strain errors. The macroscopic strain response based on the experimentally recorded Young's modulus is included for comparison.

A comparison between the average stiffness in directions parallel and perpendicular to the axis of loading demonstrates the Poisson's ratio effect observed during macroscopic loading. For this reason the magnitudes of both E_{App} and CI_{95} in the perpendicular direction are increased by a factor equal to $1/\nu_{hkl}$, where ν_{hkl} is the effective Poisson's ratio in a given lattice orientation, as shown in Table 4.1.

Table 4.1 Apparent lattice stiffness (E_{App}) and 95% confidence interval (CI_{95}) for the lattice planes associated with the scattering vectors parallel and perpendicular to the loading axis.

	Parallel		Perpendicular	
	$E_{App}\ (GPa)$	$CI_{95}(GPa)$	$E_{App} = -E_{hkl}/\nu_{hkl}\ (GPa)$	$CI_{95}(GPa)$
101	**177.6**	**±5.4**	**−488.4**	**± 28.9**
110	**406.5**	**±15.2**	**−1094.6**	**± 69.2**
102	**184.1**	**± 6.7**	**−574.6**	**± 39.1**
112	**208.5**	**± 4.7**	**−703.5**	**± 39.0**
200	**260.6**	**± 8.1**	**−502.7**	**±32.7**

The macroscopic stress-strain response was also fitted using a least squares approach to give an estimate of Young's modulus of 207.5 GPa. This value compares favourably with the value of 210 GPa provided by the manufacturer and a representation of this macroscopic stress-strain response of YPSZ was calculated and included in Figure 4.2.

4.4. Finite Element Modelling

A cube-shaped polycrystalline Representative Volume Element (RVE) of YPSZ was defined as a model within the general purpose FE code, ABAQUS. Twenty-node quadratic brick elements (C3D20) were used to define a regular mesh in 3D, and a crystal lattice orientation was assigned to each integration point. An untextured polycrystal was defined using an algorithm implemented within a MathCAD pre-processor; a random orientation distribution was computed for grain 'seeds', each with an associated position and crystal orientation. The Voronoi tessellation approach was then implemented in order to generate a synthetic grain microstructure most closely matching those observed experimentally [192]. The RVE approach implemented in this analysis was originally developed for use in polycrystalline plasticity modelling by Song et al. [193]. However, since the region considered in this study had only elastic behaviour, the plastic response within the model was not activated.

In order to simulate the applied loading, symmetrical boundary conditions were implemented for the three perpendicular principal orientations (x, y and z in Figure 4.3). A representative uniaxial compressive stress was then applied to the model. At each loading increment the strain distributions parallel and perpendicular to the loading axis were recorded. A representative average lattice strain was then calculated for each lattice plane orientation by selectively averaging only over those grains for which the angle between the scattering vector ($\boldsymbol{Q_1}$ and $\boldsymbol{Q_2}$ in Figure 2.6) and the $101, 110, 102, 112$ or 200 plane normals was less than 5^0. This figure is equal to the angular acceptance range of the experimental detector banks at Engin-X.

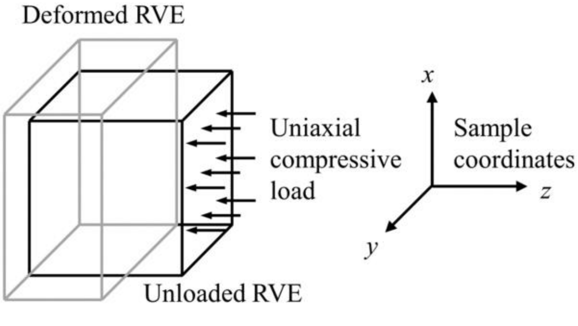

Figure 4.3. Schematic representation of RVE loading.

The final stage of the implementation was to calculate a FE average 'apparent lattice stiffness' $\left(E_{App}^{FE}\right)$ for each lattice orientation based on the average lattice strain. The resulting simulation delivered average values of apparent polycrystalline lattice moduli based on the inputs in the form elastic crystal stiffness constants. These could then be directly compared to the data recorded experimentally.

4.4.1.RVE Grain Number Analysis

For any model based on random seeding and a specific representation of a statistical ensemble, the output of the polycrystalline FE modelling approach is required to be independent of the specific model implementation. The validation of this criterion has been the focus of extensive study in a range of different materials [194] and, in general, increasing the number of grains in a simulation reduces the model dependence on a specific seeding set.

The dependence of the results on seeding was investigated by repeatedly executing the model with different numbers of grains. For each grain number, ten independent, randomly seeded distributions were implemented and the average relative standard deviation of the FE average ‘apparent lattice stiffness’ across this set of runs was calculated. The number of grains required to ensure that the model was sufficiently independent of the specific seeding implementation was determined by comparing these standard deviations with the 95% confidence interval calculated experimentally (Table 4.1). It was decided that, in order to match this confidence interval, the average relative standard deviation should be less than one quarter of the minimum normalised experimental confidence interval (in both loading orientations). This ensured that the FE modelling was sufficiently representative to capture reliably the material behaviour without overfitting experimental noise. It was found that simulations of $\approx 130{,}000$ grains were sufficient to reduce the average relative standard deviation of E_{App}^{FE} to below the experimental threshold in directions parallel and perpendicular to the loading axis (Figure 4.4).

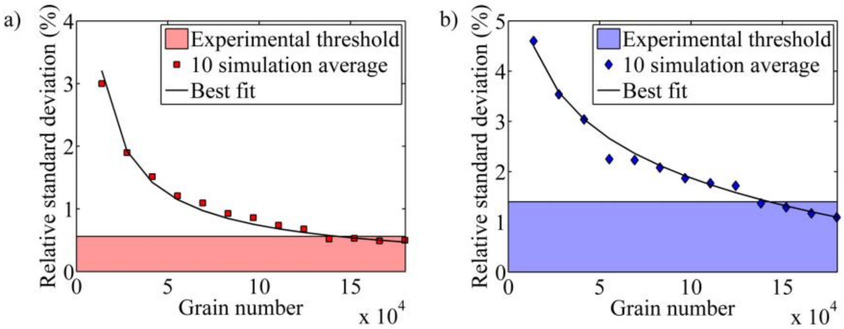

Figure 4.4. Plots of average relative standard deviation of E_{App}^{FE} as a function of the number of simulated grains in directions (a) parallel and (b) perpendicular to the loading axis.

To perform the FE-based inverse solving procedure it is necessary for the model to be implemented many thousands of times. In order to allow the increase of the number of optimisation steps (and afford the resulting improvement in the quality of fit), the FE model needs to be as time-efficient as possible. When using FE modelling to simulate a specific number of grains, two main approaches can be used:

1. Run a single FE model in which all grains are simulated. This approach minimizes the effect of local crystallographic texture by averaging over a large volume in a single model. However, the execution time of FE modelling typically increases quadratically with the number of integration points (and grain numbers) as shown in Figure 4.5.
2. Run many smaller sized FE models in which different grain distributions are simulated in each implementation. Despite using a nominally untextured grain set, small numbers of grains may result in an apparent local preferred grain orientation. Therefore the results of this analysis need to be averaged to minimize the impact of this effect. Simulating the polycrystal in this way is computationally time efficient as the execution time increases linearly with the grain number. However, in the limit of increasing model numbers, the approach tends towards a 'Taylor-type' implementation in which each grain experiences a uniform stress state. Therefore, before selecting this approach, a comparison between the output of this averaging technique and the single model is required in order to ascertain the influence of this behaviour.

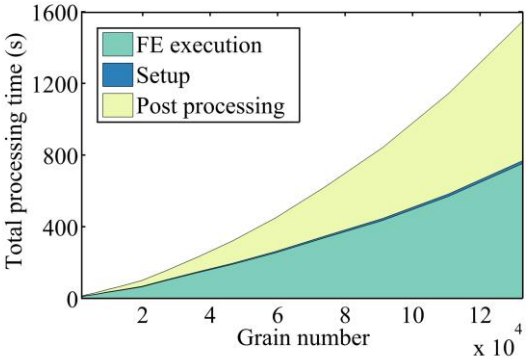

Figure 4.5. Area plot showing the contributions towards total processing time as a function of the number of grains simulated in a single model.

In order to quantify the total implementation time of the two approaches, the execution time of various FE models was recorded. Each model simulated a different number of grains, however the average number of integration points associated with each grain remained constant. The setup and execution time of each model were also recorded and the relationship between total processing time and grain number was found to be approximately quadratic as shown in Figure 4.5.

Analysis of the total processing time required by repeated implementations of smaller grain number FE models was then performed. Simulations with low grain numbers required large numbers of repeated executions and suffered from the time taken to initiate the ABAQUS subroutines. In contrast, simulations with high grain numbers (and long processing times) were prone to the time cost associated with simultaneously modelling large numbers of elements (Figure 4.5). It was found that ten implementations of the 13,824 grain model were optimal in terms of total processing time, requiring only 692 seconds to simulate over 130,000 grains (Figure 4.6).

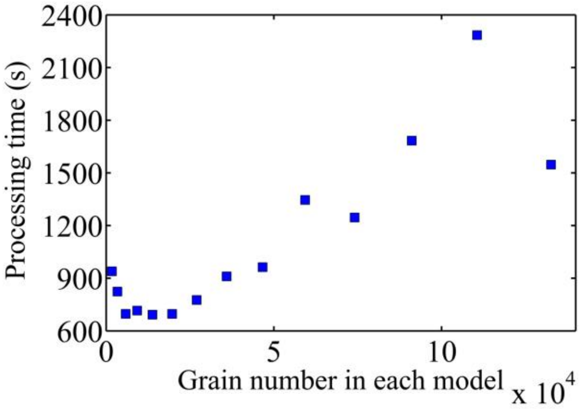

Figure 4.6. Total processing time required to simulate at least 130,000 grains using the repeated execution of models with different grain numbers.

Simulations were then performed to compare the E_{App}^{FE} results from the single 130,000 grain model and the average of the ten 13,824 grain implementations. The same grain sets were used for ten implementations of each process and the stiffness values were found to differ by 0.4%, with a corresponding 1.2% difference in the experimental cost function (see § 4.4.2). This resulted in a 2.1% increase in standard deviation between the two processes.

4.4.2. Optimisation of Elastic Stiffness Constants

Optimisation of the elastic crystal stiffness constants was then performed based on the average E_{App}^{FE} delivered by the average of the ten models of the polycrystalline FE RVE. A cost function based on the sum of squared differences between the model-derived and experimentally evaluated values was calculated and minimisation was performed by varying the six elastic crystal stiffness parameters associated with a tetragonal crystal structure. Starting values for the six constants were taken from the Reuss approximation of tetragonal 3 mol% YPSZ outlined by Ma et al. [191].

A large number of local minima were observed in this cost function and therefore an optimisation approach based on simulated annealing and steepest descent was implemented to increase the probability of finding the global minima and reduce stagnation at local minima. This hybrid optimisation technique was automated using a MATLAB shell in which run calls to ABAQUS were repeatedly executed. Many thousands of optimisations steps were implemented, and parameter convergence was verified. The optimised elastic crystal stiffness constants are shown in Table 4.2.

Table 4.2 Comparison of elastic stiffness constants (GPa) for zirconia crystallographic phases quantified using wave based, neutron diffraction and first-principle based approaches.

	Monoclinic		Cubic					Tetragonal					
	Wave based					Neutron Diffraction					First-Principle		
Method	Light	Acoustic (including ultrasonic)				RVH[a]	Reuss Averaging			This work	LDA[b]	FD[c]	ER[d]
Yttria Doping (mol%)	0.0	0.0	6.9	8.1	8.0	10.0	10 .0	0.0[e]	3.0	4.5-6.5[f]	0.0	0.0	0.0
Refs.	[186]	[185]	[45]	[195]	[196]	[197]	[197]	[187]	[191]		[198]	[46]	[46]
C_{11}	361	358	405	402	204	516	374	327	371	451	394	433	439
C_{22}	408	426											
C_{33}	258	240						264	330	302	388	258	264
C_{44}	100	99	58	56	158	42	100	59	87	39	46	10	37
C_{55}	81	79											
C_{66}	126	130						64	84	82	74	63	69
C_{12}	142	144	110	95	87	177	150	100	189	240	165	124	127
C_{13}	55	67						62	143	50	60	57	60
C_{15}	-21	-26											
C_{23}	196	127											
C_{25}	31	38											
C_{35}	-18	-23											
C_{46}	-23	39											
η_{AF}	1.02	1.03	0.36	0.47	1.05	0.22	0.83	0.42	0.12	0.89	0.90	1.65	1.09
ν_{min}		-0.62	0.11	0.09	-0.19	0.27	0.09	0.11	0.24	0.06	0.07	0.02	0.06
ν_{max}		1.30	0.59	0.60	0.51	0.34	0.74	0.51	0.44	0.62	0.61	0.89	0.66

[a] Reuss-Voigt-Hill (RVH) average
[b] Local Density Approximation (LDA)
[c] Finite-Difference (FD)
[d] Elastic-Response (ER)
[e] 12 mol% Ceria
[f] 5 mol% Hafnia

The E_{App}^{FE} values associated with the optimised elastic stiffness constants (E_{App}^{Opt}) are shown in Figure 4.7. The average error associated with these final values was less than 4% and eight out of the ten stiffness values were within the 95% confidence intervals calculated from the experimental results. The optimisation outlined above was implemented with a single seeding of 130,000 grains. Therefore, following optimisation, the relative standard deviation of ten implementations was assessed to determine the seeding sensitivity of the model. A relative standard deviation of 0.10% was found in the parallel direction and 0.35% in the perpendicular direction; these values compare favourably with one quarter of the experimental thresholds (0.15% in the parallel and 0.4% in the perpendicular direction, respectively).

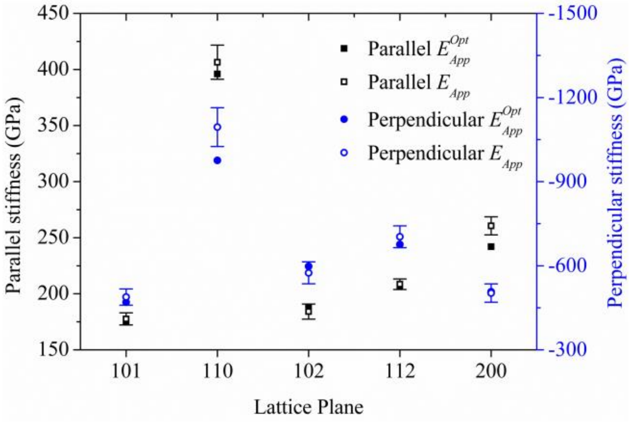

Figure 4.7. Plot showing E_{App}^{Opt} against E_{App} and the experimentally derived error bounds in directions parallel (black, left) and perpendicular (blue, right) to the loading direction.

4.5. Discussion

The approach outlined above demonstrates a RVE-based procedure for determining single crystal elastic stiffness constants from polycrystalline YPSZ neutron diffraction data. In this FE based method, the requirements of stress equilibrium and strain compatibility between grains were fully enforced. This offers distinct advantages over the simplifications associated with existing Reuss and Voigt based averaging techniques. Added to this, FE simulations also have the potential to be extended to more complex inelastic constitutive laws. Alternative methods of solving the polycrystal elasticity problem could however also be implemented using this diffraction based approach. For example, self-consistent polycrystal modelling has previously been shown as an effective technique [199].

The optimised crystal stiffness values can be used to determine the Reuss, Voigt and Reuss-Voigt-Hill averaging bounds on the macroscopic modulus; 170, 235 and 190 GPa respectively. The differences between the Young's modulus provided by the manufacturer (210 GPa) and these averages demonstrate that such approximations are unable to fully encapsulate the material response.

An overview of the published crystal stiffness constants of monoclinic, tetragonal and cubic phase zirconia based materials is given in Table 4.2. The experimental and theoretical techniques associated with each set of data were grouped into the three main approaches; wave propagation based techniques, neutron diffraction methods and first-principle calculations. A comparison between these results demonstrates a wide variation in crystal stiffness parameters for materials with almost identical compositions. This large variation may be a direct result of the different alloying additions and their concentrations. However, comparisons between identical material compositions also show large variations in parameter values depending on the exact technique implemented, even within the same publication. As an example I note the two-fold difference between the Reuss and Reuss-Voigt-Hill crystal stiffness parameters of 10 mol% YPSZ reported by Howard et al. [197].

Comparison between the results of this study and the single crystal stiffness constants reported in the literature show that, in general, the results of the optimisation lie well within the variation band of other approaches. The term that appears to show the greatest difference between the present approach and others is C_{12}. In order to quantify this effect and enable direct comparison between the anisotropy of different crystal phases, a factor based on the normalised difference between the maximum and minimum crystal elastic stiffness of a given crystal structure, E_{max} and E_{min}respectively, was computed:

$$\eta_{AF} = \frac{2(E_{max} - E_{min})}{E_{max} + E_{min}}. \tag{4.1}$$

This anisotropy factor was originally proposed by Kocks et al. [200] and the values for each of the literature results were then calculated numerically (as shown in Table 4.2). This analysis confirms that the value of the optimised C_{12} stiffness parameter corresponds to highly anisotropic behaviour. This may be indicative of the structural instability responsible for the ease of phase transformation from tetragonal to monoclinic phase in YPSZ. It is worth noting that the literature values show little consistency in the anisotropic crystal stiffness response of tetragonal or cubic YPSZ.

The addition of hafnia to this particular type of YPSZ may provide one possible explanation for the increased value of C_{12}. Unlike the other alloying oxides listed in Table 4.2, the similarities between the ionic radius of hafnium ion Hf^{4+} and zirconium ion Zr^{4+} enable direct substitution of these two cations [201]. The slight differences in ionic radii and the increased atomic mass of Hf^{4+} may lead to lattice distortion within the YPSZ single crystal resulting in an increase in these stiffness terms.

The resulting influence of this anisotropic behaviour on the distribution of Young’s modulus, Poisson’s ratio and shear modulus was examined using E1AM [202], an analytical tool for calculation and visualisation of anisotropic elastic properties. Direct comparison between the tabulated literature data and the results of this work demonstrated that Young’s modulus and shear modulus for the optimised case fall well within the range of variation of these literature stiffness values. The variation of the two moduli corresponds to the previously reported trend of increasing stiffness with yttria content [45]. The large variation in the range and magnitude of ν from the optimised case were also found to be in close agreement with the literature values for tetragonal YPSZ. Any remaining disagreement is likely to be associated with the greater tetragonal stabilisation of the $4.5 - 6$ mol% yttria present in this study. High yttria content YPSZ is in a structural state that is energetically close to the state of equilibrium between phases [203], and many crystal structures demonstrate anomalous large variations or small values of Poisson's ratio upon approaching the phase transition.

4.6. Conclusions

An RVE-based FE approach to calculate the elastic stiffness constants of polycrystalline dental YPSZ has been proposed and implemented. In this model the spatial distributions of stresses and strains that satisfy both the equilibrium and compatibility requirements have been used to compute grain group average elastic lattice strains that could be directly matched to experimental measurements using neutron diffraction. The technique relies upon the optimisation of elastic stiffness constants and model-matching to produce improved estimates of the elastic stiffness constants.

The approach associated with the new technique requires minimal calibration, simple sample preparation and can be implemented experimentally in a much shorter time than other existing methods. The generic nature of the analytical approach also means that a range of neutron or X-ray diffraction setups can be used to obtain the diffraction spectra necessary for model matching. The final optimised parameters were found to match eight out of ten experimentally measured stiffness values, and the total error was less than 4%. This suggested a 'near-global' optimum had been identified.

Direct comparisons between the optimised crystal stiffness parameters and literature values shows that in general the values obtained lie within the range of values obtained using other approaches. This improved insight into the elastic response of dental YPSZ, in combination with the polycrystalline FE modelling routine elucidated, will facilitate improved modelling of the YPSZ-porcelain interface to drive forward understanding and thereby minimise the failure rates of near-interface porcelain.

Although this approach has been developed specifically to overcome the difficulties associated with the identification of the elastic stiffness constants of YPSZ, it has significant potential for use in the study of other materials. Applications include the wide range of polycrystalline materials for which the growth of representative single crystals is not possible, or materials in which the material characteristics result in interference during the implementation of existing techniques.

5. Characterisation of the Creep Response of Dental Porcelain

5.1. Introduction and Motivation

During the manufacture of YPSZ-porcelain dental prosthesis, the near-interface porcelain is exposed to a combination of high magnitude tensile residual stresses (≥ 100 MPa) [33] and sintering temperatures in the range of $600 - 750$°C. This combination of stress and temperature has previously been shown to be sufficient to activate creep in silica (the primary constituent of porcelain) [204] and to reduce the mechanical strength of silica based ceramics [56]. An improved understanding of the creep rate behaviour and damage characteristics of dental porcelain was therefore necessary in order to determine if this phenomenon is related to the failure of near-interface porcelain.

The small sample sizes of commercially available dental porcelain ($< 20 \times 15 \times 10$ mm^3) means that the 76 mm long specimens necessary for the ASTM Standard C1291 high temperature ceramic tensile creep test method [205] cannot be manufactured from this material. A new experimental procedure for high temperature tensile creep testing of ceramics was therefore established and applied to a representative porcelain sample in order to determine the secondary creep rate exponents as outlined in § 5.2. The results of this analysis have recently been published in the form of a journal article [206].

TEM analysis of the near-interface porcelain has revealed the presence of nanovoiding at this location (as revealed in § 7.3) which were similar in form to creep induced features previously observed in silica based ceramics [57]. In order to determine if this nanovoiding behaviour is indicative of creep induced damage in dental porcelain, representative samples were crept and assessed using SANS and TEM and the results of this analysis are presented in § 5.3. A journal article on this research is currently undergoing peer review [207].

5.2. Secondary Creep Rate Quantification

The secondary creep rate analysis presented here has been performed over the temperature range $650 - 800$ °C in 50°C increments in order to be representative of the typical sintering temperatures applied to YPSZ-porcelain dental prostheses. Stresses within the range of $50 - 125$ MPa have also been applied in order to simulate stresses previously observed in porcelain at the YPSZ-porcelain interface.

As outlined in § 1.4, porcelain dental veneers such as IPS e.max Ceram [17] are typically supplied in a powder/liquid form which is applied to YPSZ using a 'slurry-sinter' type approach. This manufacturing method does not easily facilitate the production of representative tensile creep rate specimens and therefore, in order to overcome this limitation, solid blocs of porcelain of the most similar commercially available porcelain (Cerec Vitablocs Mark II) were instead used as the base material for creep specimen manufacture [49]. These two porcelain types have marginally different manufacturing techniques (automated layer build up vs manual layer by layer application) however the elemental composition of the two porcelain types are very similar (to within the manufacturer published tolerances). The addition of small amounts (< 1 weight %) of crystalline fluorapatite filler to IPS e.max Ceram may also influence the creep response of this material, however the low concentration of this phase ensures that it is unlikely to have a significant impact on the creep rate behaviour.

The brittle nature of porcelain and associated statistical likelihood of failure of this material means that there are significant challenges associated with creep loading this material in tension. A range of tensile creep rate studies have previously been successfully performed on similar brittle ceramics [208, 209] however these approaches are reliant upon relatively long sample lengths (> 50 mm). There is an increasing trend towards creep testing smaller ceramic samples, particularly in the $10 - 20$ mm range associated with dental implants. This presents the need for a miniaturised technique capable of testing small samples in order to facilitate ceramic tensile creep testing over the temperature ranges typically applied to dental porcelain (less than $850°$C). A reduction in the sample size also has the added benefit of reducing the influence of the gradients in material properties and temperatures typically observed between the bulk and surface regions in larger samples. Based on the work of Post et. al [210], a single sample testing approach was chosen for this new testing technique. This methodology ensured that, despite the relatively high sample failure rates observed, representative strain rates were obtained across the range of temperatures and stresses previously outlined.

5.2.1.Materials and Methods

As part of the preliminary testing into suitable sample preparation approaches, attempts were made to manufacture tensile creep specimens which were similar in form to those previously outlined in the literature [208, 209]. The limited sample size of the Vitablocs was found to present severe difficulties in effectively holding the sample during conventional shaping processes. This resulted in repeated fracture and brittle failure of the sample and thereby severely restricted the machining modes which could be implemented.

Following these initial trials it was found that diamond grinding of the material could effectively be used to shape the sample and therefore a procedure based on this approach was developed. Multiple tensile creep specimens were manufactured using this three stage optimised process. Firstly an 8 mm diameter, 18 mm long cylindrical section was milled from the $12 \times 14 \times 18\ \text{mm}^3$ blocks using an Eternal Tools 8 mm inner diameter diamond core drill bit. This cylinder was then mounted into a lathe using specially manufactured grips and an Eternal Tools 4 mm diameter diamond cylindrical burr (rotating on an axis perpendicular to the lathe axis) was used to profile the central section of the specimen as shown in Figure 5.1. An electronic read out was used to ensure that the positioning of the polishing tool was accurate to within 1 μm. The 'dog-bone' sample shape and gentle end radius shown in Figure 5.1 were selected in order to minimise stress concentration during loading of the sample.

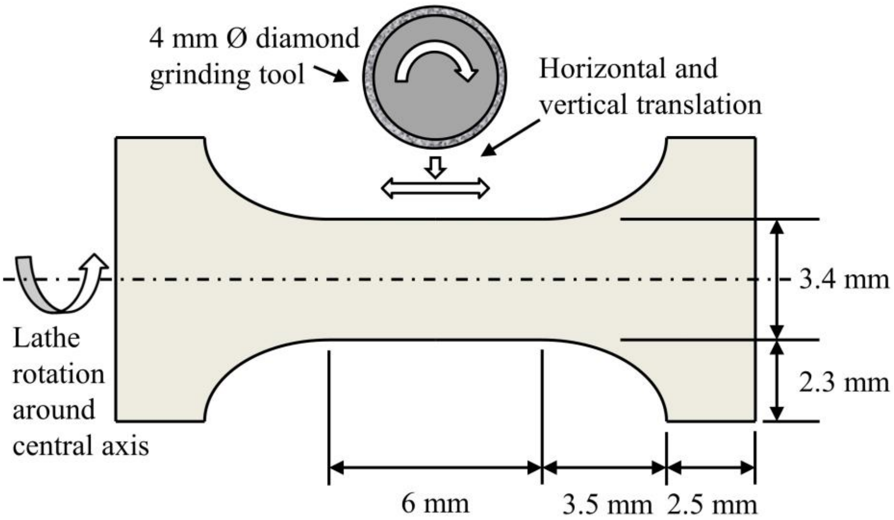

Figure 5.1. Cross section of porcelain 'dogbone' specimen and relative position of diamond grinding tool during manufacture.

Specimens of this type were initially loaded and were found to fail (through brittle fracture) at very low loads. Scanning Electron Microscopy (SEM) of the failed surfaces revealed that this failure was initiating at the sample surface at locations where relatively high roughness was observed (on the scale of ≈ 50 μm). Therefore, in order to reduce the surface roughness of later samples, a polishing stage was introduced into the manufacturing process. This involved initially holding grinding paper of decreasing grain size (down to 2500 grade) against the rotating, shaped sample. A diamond polishing paste of grit size 1 μm was then applied to the surface using a polishing cloth to further improve the surface quality.

Following this manual process, the sample length and width of each sample were measured in multiple locations using a micrometre screw gauge and vernier calliper, respectively. The gauge section of the sample used in this study was 3.381 ± 0.005 mm and the total length was 17.754 mm.

Tensile Loading Grip Development

Several differing materials, sizes and shapes of tensile clamping mechanisms were trialled during the preliminary testing stages of this analysis. One region which was found to be critical to the success of the loading rig was the curvature of the loading surfaces of the clamps. These regions were required to be as similar as possible to the sample curvature in order to reduce points of stress concentration within the porcelain. It was also found that the insertion of a small amount of aluminium foil between the sample and the loading clamp helped to distribute the load more evenly over the curved surface. At temperatures above $330^0\mathrm{C}$ the foil is sufficiently malleable to deform into the profile of both contact surfaces; this presents a larger contact area and thereby minimises localised stresses.

The optimal clamping design was based on a ‘split collet’ arrangement as shown in cross-section in Figure 5.2. The clamps were made from a high temperature nickel alloy, Inconel 817 in order to minimise high temperature creep effects. During mounting, the sample was placed between two identical collets. A loading pin was then inserted into the void between the collets and a locking pin was used to hold the components together. An alignment ring was also used to ensure that the collets remained parallel during loading. This process was repeated on both sides of the sample and the entire assembly was then mounted into the loading rig using M12 threads. The application of high temperature copper grease onto all contact surfaces minimised sticking friction and also aided in sample grip disassembly.

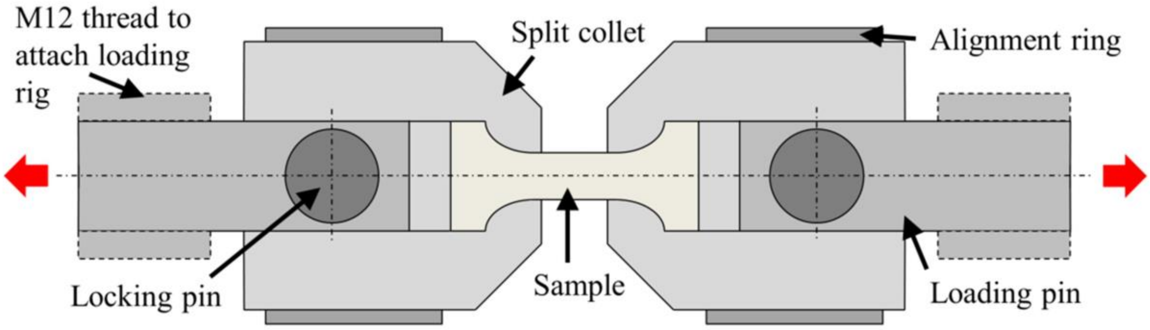

Figure 5.2. Cross section of split collet loading clamps.

The design of the sample grips ensured that, for a given load, the apparent stress at each of the contact locations was significantly lower than the stresses within the gauge section. For example at the interface between the sample and the split collet the nominal reduction in stress was a 4.5 times the gauge stress. Within the collet system itself, the maximum nominal stress location is 4.9 times less than the gauge stress and occurs at the location between the loading pin and the locking pin.

Loading Rig and Sample Heating Setup

The custom built Instron 50 kN servo-hydraulic loading rig at instrument Engin-X, ISIS Spallation Source, UK was used to apply a uniaxial load to the creep samples in this experiment. The nature of the split collet loading arrangement meant that there was insufficient room to place an extensometer onto the sample and therefore the displacement of the loading rig was used to monitor the strain rates produced. The sample displacement of the loading rig and nominal stress (based on initial sample cross section) were recorded once per second throughout the experiment. Despite providing nanometre scale readouts of the displacement, the nominal Root Mean Square (RMS) of this reading was found to be 0.281 μm when loaded to the equivalent of 125 MPa (1100 N). This reading was found to be within 1.2% of the theoretical strain estimate after holding for 1 hour. Upon holding this nominally constant stress, the RMS of the recorded stress value was found to be 1.1 N. This corresponds to a precision of 0.1% which is identical to the manufacturer's published value at the maximum 50 kN load [211].

The high temperature radiant furnace arrangement built for the 50 kN loading rig was used to heat the sample to the required temperatures. In order to ensure that the sample was heated to the correct temperature a thermocouple was attached directly to the gauge section and a feedback loop was used to control the power input to the lamps. After changing temperature and thermally equilibrating, the sample temperature was found to be constant to within 1°C at each temperature for the entire experiment.

In order to reduce the temperature of the surrounding grips and therefore minimise the effects of any creep in these regions, the 4 heating lamps were focused directly onto the sample centre. This focusing setup, and the increased surface area of the grips ensured that the maximum radiant heat flux on the grips was at least 2.94 times smaller than the flux on the sample surface, with an average flux reduction of 5.59. In order to reduce the temperature of the split collects further, two streams of cooling water (at a temperature of approximately 10°C) were also passed through metal contacts at the position where the M12 threads were connected to the loading rig. It is also important to highlight that the positions of maximum nominal stress in the loading rig were located internally and therefore were least influenced by the heat flux from the heating lamps.

Experimental Method

The brittle nature of Vitablocs Mark II porcelain resulted in a large number of sample failures at relatively low loads (corresponding to nominal stresses of 5 MPa or less). For this reason a routine based on maximising the observed secondary creep rate behavioural response from one sample was developed. This approach was based on recording the strain rate behaviour at multiple stresses and temperatures on the same sample and therefore required care to ensure that tertiary creep rate behaviour did not influence the parameters measured. For this reason, the hold time at each stress and temperature was carefully selected as a balance between clearly observing the strain rate behaviour and minimising sample deformation (and the associated impact on material characteristics and sample dimensions).

Each sample was placed into the split collet loading grip assembly and then mounted into the servo-hydraulic loading rig. The slack was then manually removed from the system and the sample was preloaded to between $0.2 - 0.7$ MPa. The temperature was then increased from $17°\text{C}$ to $800°\text{C}$ at a rate of $10°\text{C min}^{-1}$ in a load control mode. During this process the thermal expansion of the system was accommodated by changing the displacement position of the loading rig. Upon reaching $800°\text{C}$, the displacement was monitored as a function of time to ensure that no thermal expansion could be observed in the system. It was found that 3 hours were necessary for the loading rig to fully equilibrate to a point at which no discernible drift could be detected on the displacement reading.

The sample was then loaded to 50 MPa at a rate of $1\ \text{MPas}^{-1}$. This loading rate was selected as a compromise between minimising creep extension during loading and minimising loading shock. The elastic response of the loading rig, split collet and the sample (in parallel) was observed during this loading regime and the displacement point and time after this loading was recorded. The sample was then held at a constant temperature and stress until a clear deviation from the starting position was observed. A Signal to Noise Ratio (SNR) of at least 20 was selected as the criterion at which the trend could clearly be identified above the background noise (based on the nominal RMS of the displacement readout previously identified). By implementing a threshold criterion in this way, it was hoped that a sufficiently representative creep rate could be determined without inducing large amounts of creep damage.

It was found that a hold of 30 minutes was sufficient to clearly observe a linear change in displacement against time at $800°\text{C}$ and 50 MPa. Within the first two minutes some deviation from this linear trend was observed. This response was believed to be either representative of work hardening (primary creep) or ‘load settling’ in the Instron rig. This region was therefore removed from the least squares linear fitting process outlined in § 5.2.2. The sample was then incrementally loaded to 75 MPa, 100 MPa and 125 MPa at a rate of 1 MPas^{-1}. At each load the same signal to noise criterion was used to determine the hold time necessary. Minor levels of non-linear behaviour were also observed for the first few seconds at each of these loads.

Next, the sample was reduced to a nominal load of 0.5 MPa at an unloading rate of 1 MPas^{-1}. The temperature was then reduced to 750°C at a rate of 10°C min^{-1}. Careful monitoring of the displacement was used to determine the time taken to thermally equilibrate the system and in this case it was found that after approximately 1 hour the system showed no observable change in this value. The same multi-loading and holding regime was then repeated for this temperature and the hold times were recorded at each stress. It was found that, for a given stress, the hold times required at 750°C were an average of 4.1 times longer than at 800°C. Based on this insight, it was decided that the hold times for the 700°C analysis would be further increased by this factor.

The same 4.1 increase in hold time was next repeated for the 650^{0}C analysis at the same four stresses previously outlined. The increased number of data collection points at these measurements ensured that reliable least squares linear fitting could still be applied, even in the cases where the SNR was found to be marginally less than 20, as outlined in more detail in § 5.2.2.

The sample was then finally unloaded to 0.5 MPa at an unloading rate of 1 MPas^{-1} and the temperature reduced back to room temperature at a cooling rate of 10°C min^{-1}. The sample was then manually unloaded and the split collet assembly removed from the loading rig. A visual inspection of the sample gauge section revealed no obvious signs of necking and a micrometer screw gauge was used to measure the crept sample length. The new length was found to be 17.778 mm which corresponded to a sample extension of 24 μm.

5.2.2.Theory and calculation

Typically, in order to accurately quantify the strain rate and stress at every temperature and applied load, the gauge cross sectional area and length need to be determined at each position during the analysis. However, in the case of this study, careful control of the creep hold period ensured that a nominal gauge length extension of only 0.40% was applied. Based on constant volume calculations, this extension corresponds to an equivalent 0.40% reduction in cross sectional area.

The influence of differing sample cross section or sample length can be considered in more detail by examining the form of the secondary creep rate equation (Equation 1.1). Secondary, or steady state creep occurs when a constant plastic strain rate is achieved under the action of a constant nominal stress and previous studies have characterised this behaviour for a range of ceramics [212], including porcelain [57, 204]. Although the power law relationship between strain rate and stress in Equation 1.1 is phenomenologically based, the exponential relationship with temperature is based on the activation energy necessary to induce creep in a given material and the limitations of this relationship have been comprehensively discussed elsewhere [213].

Into Equation 1.1 we can substitute expressions for the nominal strain rate ($\dot{\varepsilon} = \dot{\Delta}L/L$) and nominal stress ($\sigma = F/a$); where $\dot{\Delta}L$ is the rate of change of the gauge length, L is the nominal gauge length, F is applied load and a is the nominal cross sectional area:

$$\dot{\varepsilon} = \dot{\Delta}L/L = Aa^{-\bar{n}}F^{\bar{n}}e^{-Q/RT}. \tag{5.1}$$

In the case of an increase to the nominal gauge length (δL) and a decrease in the sample cross section (δa) the expression for true strain rate ($\dot{\varepsilon}_{True}$) becomes:

$$\dot{\varepsilon}_{True} = \dot{\Delta}L/(L + \delta L) = A(a - \delta a)^{-\bar{n}}F^{\bar{n}}e^{-Q/RT}. \tag{5.2}$$

The relationship for the nominal strain rate can then be written as:

$$\dot{\varepsilon} = A(1 + \delta L/L)(1 - \delta a/a)^{-\bar{n}}\sigma^{\bar{n}}e^{-Q/RT} = A_{True}\sigma^{\bar{n}}e^{-Q/RT}, \tag{5.3}$$

where A_{True} is the true value of A for a given extension and cross sectional area reduction. Previous studies into the creep rate behaviour of porcelain containing silica and alumina have highlighted that these materials “have $\bar{n}$-values close to unity” [204] and therefore estimates for the relative % change between the value of A at the beginning of testing and the value of A_{True} can be performed. The maximum difference between these two values was found to be 0.83% at the point when the final unloading was performed. This percentage error is much smaller than the confidence intervals outlined in § 5.3 and therefore all creep rate analysis was performed using a value of 6 mm for gauge length and 8.98 mm^2 for cross sectional area.

Manual splitting of the resulting strain against time profiles was initially performed in order to select suitable regions over which to calculate the strain rate behaviour. A least squares fitting approach was used to fit a straight line through the selected regions and the gradient of this fit was used to provide an estimate of the strain rate for each stress and temperature. The error bounds associated with this fitting process also provided estimates for the standard deviation of each strain rate value. It was found that in the cases of slow strain rate behaviour, the increased number of sampling points was sufficient to reduce these error measures to suitably representative bounds as demonstrated in § 5.3.

As previously highlighted, some non-linearity was observed within the first few seconds of the constant stress and temperature hold. Typically this behaviour was representative of an increase in the strain rate, however in other cases a reduction was apparent. This lead to the suggestion that this effect was instead a characteristic response of the feedback system within the Instron and the associated minor 'overshooting' or 'undershooting' in stress. This non-linear region was therefore removed from the least squared fitting process. A critical examination of the data was also performed to ascertain if any tertiary creep rate effects could be identified. No obvious gradient increases were observed during any holding periods. This lack of tertiary creep was further confirmed by the lack of necking observed in the sample.

Following least squares fitting of the profiles, an estimate of the RMS value of the noise on the displacement reading at each loading position and temperature was performed. At higher loads the noise value was found to be marginally higher than at lower stresses. A figure for the SNR at each stress and temperature was then calculated based on these noise RMS values. The average value for this figure of merit was 20.8 with a minimum of 18.3 and a maximum of 27.9. This suggested that the increased hold time approach had been sufficient to overcome the impact of noise on the low temperature data.

5.2.3.Results

The three unknown constants in the secondary creep rate equation are the activation energy Q, the stress exponent $\bar{n}$ and the creep rate constant A. In order to determine these variables the natural logarithm form of the secondary creep rate equation can be used:

$$\ln(\dot{\varepsilon}) = \ln(A) + \bar{n}\ln(\sigma) - Q/RT. \tag{5.4}$$

From this equation it can be seen that, for a given stress, the gradient of a plot of $\ln(\dot{\varepsilon})$ against $1/T$ will be equal to $-Q/R$ as shown in Figure 5.3. Least squares fitting of these linear trends was performed using the inverse of the strain rate standard deviation as weightings for each value. Estimates of the standard deviation of the estimates of Q were also determined based on the least squares confidence limits of the fitted gradient.

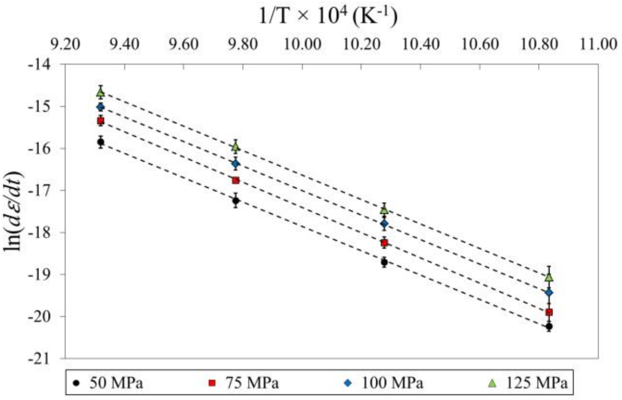

Figure 5.3. Plots of $\ln(\dot{\varepsilon})$ against $1/T$ for constant values of stress. Error bounds on each of the strain rate values have been included to demonstrate the 95% confidence intervals on these terms.

A plot of the estimates of activation energy for each of the different stresses is shown in Figure 5.4. The 95% confidence intervals associated with each value is also shown in this figure, demonstrating that the values are consistent to within this margin. The impact of reduced strain rates (and the increased impact of noise) at lower stresses can also be seen in the reduced confidence of these values. A final weighted average calculation was used to determine an overall estimate of both the activation energy and the 95% confidence interval for the entire experiment; $Q = 243.0 \pm 3.1$ kJmol^{-1}. This confidence interval represents a 2.5% margin of error and suggests that the estimate of activation energy has been quantified to a relatively high level of precision.

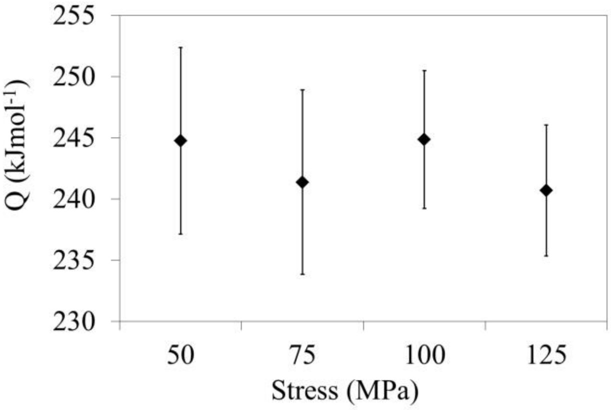

Figure 5.4. Estimates of Q for each of the different applied stresses. The 95 % confidence intervals are shown by the error bars and demonstrate that the 4 values are consistent to within this margin.

The expression given in Equation 5.4 can also be used to determine estimates for the stress rate exponent $\bar{n}$, by quantifying the gradient of plots of $\ln(\dot{\varepsilon})$ against $\ln(\sigma)$ at constant temperatures, as shown in Figure 5.5. The inverse of the standard deviation of each of the strain rate values was used as weighting inputs for the least squares fitting of this linear trend. The confidence bounds associated with this fitting were also used to provide estimates of the standard deviation of the stress exponent values.

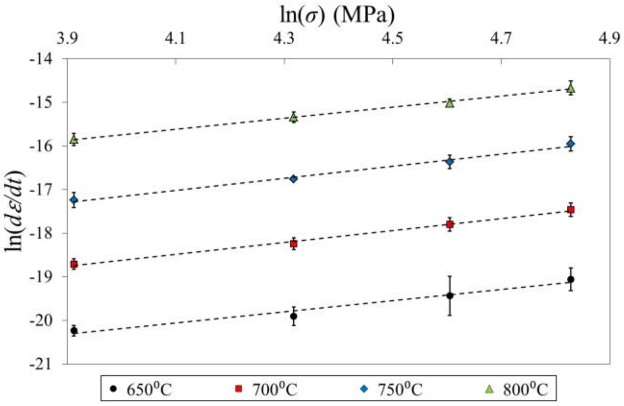

Figure 5.5. Plots of $\ln(\dot{\varepsilon})$ against $\ln(\sigma)$ for constant temperatures. Error bounds on each of the strain rate values have been included to demonstrate the 95% confidence intervals on these terms.

Figure 5.6 shows the estimates of stress rate exponent and associated 95% confidence intervals for each of the temperatures implemented in this study. As expected, the reduced creep rate at lower temperatures has resulted in larger 95% confidence limits at the lower temperatures. The four values are consistent to within the 95% confidence interval and the weighted average was found to be $\bar{n} = 1.32 \pm 0.08$. This confidence interval represents an 11.5% margin of error, a factor of 4.6 times greater than the error observed in the estimation of activation energy. This decreased certainty is a combination between the proximity of this exponent to 1 and the reduced stress range over which this study was performed.

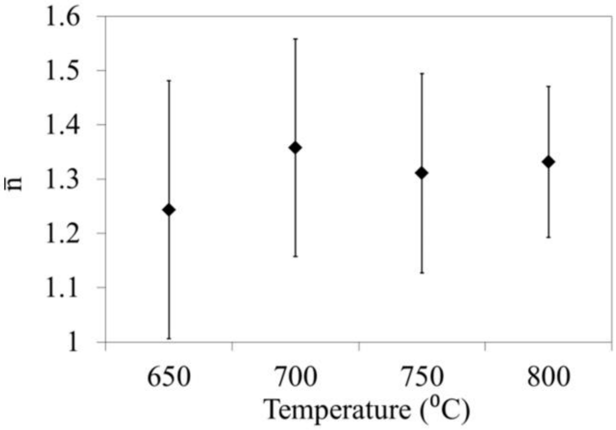

Figure 5.6. Estimates of $\bar{n}$ for each temperature. The 95 % confidence intervals are shown by the error bars and demonstrate that the four values are consistent to within this margin of error.

The reduced stress range variation is demonstrated more clearly in Figure 5.7, in which the relative deviation associated with each of the stress exponents is demonstrated. It can be seen that, within the stress range examined in this study, the relative variation of $\sigma^{\bar{n}}$ is approximately half an order of magnitude. If we compare this to the variation in thermally driven effects (using the average activation energy calculated) we find that over the temperature range considered, $e^{-Q/RT}$ varies by almost two orders of magnitude. This increased parameter variation ensures that an improved estimate of the activation energy is possible from the data collected.

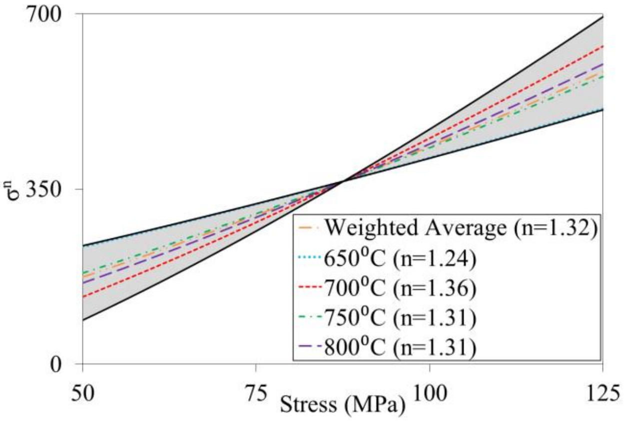

Figure 5.7. Schematic diagram showing the relative variation in $\boldsymbol{\sigma^{\bar{n}}}$ with respect to the weighted average distribution, in the stress range examined in this study. The vertical offset applied to each value has been selected to minimise displacement relative to the weighted average value of $\boldsymbol{\bar{n}}$. The 95% confidence region of the weighted average is highlighted by the grey region of the plot

Following the determination of average values of $\bar{n}$ and Q, analysis into the average value and relative variation of the creep rate (A) constant was performed. No clear trends could be observed in this parameter in terms of stress or temperature and the average value was found to be $490\ \mathrm{MPa}^{-1.32}\mathrm{s}^{-1}$ with a 95% confidence interval of $\pm\ 83.2\ \mathrm{MPa}^{-1.32}\mathrm{s}^{-1}$.

5.2.4.Discussion

The lack of comparable tensile creep rate data means that only approximate estimates of the stress exponent ($\bar{n}$) and activation energy (Q) can be provided by comparison with previous creep rate studies of compounds containing both silica and alumina. For example, Wereszczak et. al [57] focused on compressive creep of two silica core ceramics doped with alumina and other oxides. They presented estimates of activation energies of $130\ \mathrm{kJmol}^{-1}$ and $210\ \mathrm{kJmol}^{-1}$, and stress exponents of 1.4 and 1.3 for the two compounds examined. Four point bending creep has also been previously performed on porcelain containing silica and alumina by Ponraj et. al [204] which quantified the activation energy as $190\ \mathrm{kJmol}^{-1}$ and the stress exponent in the range of $1.54 - 2$.

Despite the large differences in elemental composition between these studies, a critical comparison between the present value of $Q\ =\ 243.0\ \pm 3.1\ \mathrm{kJmol}^{-1}$ and those previously quantified through creep rate analysis reveals that this value appears to be a realistic estimate of activation energy. Further comparison can be drawn against a diffusion kinetics study into the activation energy of the alumina silica ceramics by Davis and Pask [58]. In this study, a 22.3 wt % alumina ceramic was found to have an activation energy of $Q = 245 \pm 3$ kJmol^{-1}. The elemental composition of this compound is very similar to the $20 - 23$ wt % porcelain that was examined in this study and the similarity of these two figures demonstrates a consistent measure for activation energy in this material, despite the differing experimental techniques used to quantify this behaviour.

Quantification of the stress rate exponents in ceramics has previously highlighted that this parameter is typically found within the range of $\bar{n} = 1 - 2$ [212]. This insight, along with the values of exponent obtained through existing porcelain creep studies, suggests that the estimate of $\bar{n} = 1.32 \pm 0.08$ determined in the present study is likely to be a reliable measure of the behaviour of this material.

Creep damage has previously been observed in a wide range of structural ceramics both in the form of amorphous cavitation (originating at flaws) and where relevant, grain boundary induced cavitation [214]. Despite these effects, and as highlighted in these previous creep rate studies [57, 204], the impact of this behaviour cannot typically be observed with the application of the small strains. This insight, in combination with the small strains applied (0.4%) and the consistency of the creep rate fitting results obtained in this study, suggests that creep damage has had minimal effect on the behaviour recorded.

High Temperature Creep Analysis

The tensile creep rate experimental approach outlined in this experiment has been designed to overcome the limitations imposed by the maximum size of representative dental feldspathic porcelain samples which are available. This size constraint meant that there was insufficient material to machine the sample geometries necessary for many well-established creep rate tests [208, 209] and therefore a new approach was developed. Further to this effect, this limitation on sample size meant that difficulties were encountered when trying to hold or machine the sample using ‘conventional’ approaches. For this reason specially designed machining grips were produced to mount the sample on a lathe, thereby facilitating diamond grinding of a suitable tensile sample shape.

Despite these sample size constraints, the activation energy (Q) and stress exponent ($\bar{n}$) values calculated in this analysis appear to be consistent with literature and suggest that this methodology is suitable for creep testing of ceramic samples which are very limited in terms of specimen size. The optimisation steps performed in this study suggest that in order to minimise stress concentration in the sample, care must be taken to accurately machine and finish both the experimental samples and loading grips. High temperature materials and water cooling of the grips was also necessary to reduce grip deformation, which was found to lead to stress concentrations in the sample.

In this study the single sample creep rate approach, similar to that implemented by Post [210], has also been shown to be reliable under certain tightly controlled conditions. The area on which most effort was imparted was the minimisation of creep induced damage in the material through the application of small strains at each load and temperature. Tolerances on the signal to noise ratio during each hold period proved to be a useful guide to limit the applied strain whilst simultaneously ensuring that noise did not have a large impact on the data recorded. The decision to unload the sample during the long equilibrium dwell periods also helped to further reduce the strain applied to the sample. Further to this, the 1 MPas^{-1} loading rate applied was also chosen to be as large as practically possible (taking into account loading shock in the sample) in order to minimise the creep strain induced during loading.

5.3. Creep Induced Nanovoiding Analysis

Nano-scale cavitation, otherwise known as nanovoiding, has been observed in a wide range of materials and is known to be induced by several distinct processes ranging from the impact of irradiation and creep in ceramics [56, 215] to plastic deformation in metals and polymers [216, 217]. The presence of nanovoiding is known to influence the mechanical properties of materials including strength, stiffness and fracture toughness. At sufficient concentrations nanovoiding has also been shown to induce an early onset of component failure through brittle fracture [61].

As outlined in § 7.3, TEM analysis of the YPSZ-porcelain interface has confirmed the presence of porcelain nanovoiding in a band located a few microns from the YPSZ-porcelain interface. The motivation for this study was to improve the current limited understanding of the impact of creep on the nanostructure of dental porcelain, and thereby determine if this behaviour contributes to the failures observed at the YPSZ-porcelain interface in dental prostheses.

Three samples of identical elemental composition were examined in this study. Creep was applied to the first specimen (sample C) using the tensile creep loading arrangement outlined in § 5.2 at a temperature of $750℃$ and stress of 100 MPa. These conditions were selected in order to replicate the conditions present at the YPSZ-porcelain interface [35, 218]. In order to promote the formation of voids and their subsequent growth, a 96 hour hot dwell was applied. The specimen subjected to heat treatment (sample H) was exposed to the same thermal cycle as the crept sample (C), but without the application of force. A third specimen (sample A) was selected as a reference sample of the as-machined state.

SANS was used to collect diffraction spectra from each of the samples. This technique is known to be sensitive to length scales in the range $\approx 1 - 100$ nm [219] which corresponds closely to the length scale of voids observed at the YPSZ-porcelain interface. As a volume-averaging method, SANS provides important insight into the mean shape, number density, size and distribution of these artefacts. This averaging response is performed over much larger (mm length scale) gauge volumes than those examined using TEM analysis, and therefore is known to provide estimates which are representative of the bulk void statistics.

TEM lamellae were extracted from the core of each of the three samples in order to provide a more localised measure of the impact of creep at this location. This approach benefits from direct 2D visualisation of voids, such that image post-processing can provide insight into the shape, number density, interface characteristics and distribution. These results can also be directly compared with the TEM analysis performed at the YPSZ-porcelain interface in § 7. 3.

5.3.1.Materials and Methods

The three samples examined in this study were manufactured from a single batch of I14 Vitablocs Mark II for Cerec [49]. The samples were machined using the tensile specimen manufacturing procedure outlined in § 5.2. Multiple dog-bone samples were produced and the gauge diameters and lengths of each specimen were measured using a micrometer screw gauge. The reference sample in the as-machined state (sample A) was selected as one of these specimens.

High temperature creep was induced in sample C using the routine outlined in § 5.2 at a temperature of $750\ ℃$ and stress of 100 MPa. In order to provide a quantitative measure of the strain rate at these conditions, the estimates of A, $\bar{n}$ and Q determined in § 5.2 were used as inputs into Equation 1.1. This calculation revealed that under these conditions the corresponding strain rate is small ($8.24 \times 10^{-8}\mathrm{s}^{-1}$). Therefore, to ensure that the impact of creep on the microstructure could be clearly identified, the sample was subjected to creep loading for 96 hours to reach a nominal strain of 2.85 %.

At the end of the creep experiment, the loading rig strain reading was found to be 2.75 %. The sample was then carefully removed and a micrometer screw gauge was used to measure the length of the deformed specimen which was found to correspond to a strain of 2.67 %. Despite the fact that these three measurements show reasonable agreement (to their associated levels of precision), the localised necking which was observed in the centre of the gauge volume suggests that the local strain at this position may have been higher.

In order to replicate the thermal history of sample C, the remaining machined sample was placed into a Carbolite RHF 16-8 Chamber Furnace. The same ramp rate and 750 ℃ thermal dwell was then applied to this heat-treated specimen (sample H).

Small Angle Neutron Scattering

SANS was performed at beamline LOQ at the ISIS Pulsed Neutron Source, UK for which a comprehensive overview of the capabilities and experimental setup has previously been published elsewhere [220]. Specially manufactured mounts were produced to hold the samples in an orientation such that their axial direction was perpendicular to the beam as shown in Figure 5.8. The gauge volume studied within each of the samples was aligned with the incident beam to within ≈ 0.2 mm.

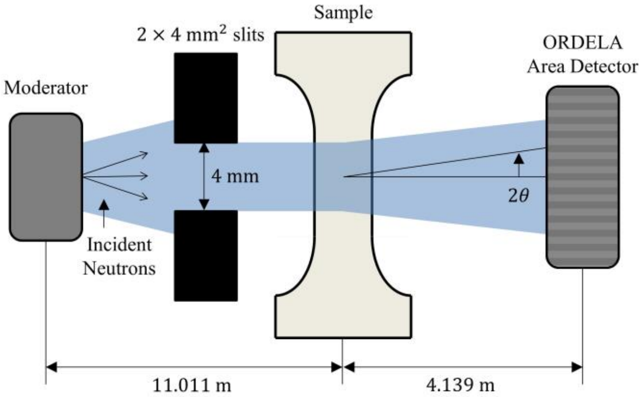

Figure 5.8. Schematic diagram of the SANS experiment.

Collimation of the incident beam was performed to define a 2×4 mm^2 cross sectional area. A sample to detector distance of 4.14 m, incident beam collimation length of 4.00 m and moderator to sample distance of 11.01 m were used in this study. The beam chopper was configured to define incident wavelengths between $2.2 < \lambda < 10.0$ Å at a repetition rate of 25 Hz. In order to collect sufficient statistics each sample was exposed for 6 hours corresponding to ≈ 0.5 mA-hours of flux incident on the target station. A 6 hour exposure of an empty holder was also collected to enable background correction.

Transmission Electron Microscopy

For TEM analysis, representative lamella samples were extracted from each of the three dog-bone specimens from the location from which SANS measurements were collected. A Beuhler Isomet low speed diamond saw was initially used to section the sample across the gauge volume at a position just below the point where minor necking had been observed in the crept sample (Figure 5.9). A slow cutting speed was selected to minimise the impact on the local microstructure and a multi-stage grinding and diamond grit polishing process was next applied to the sectioned surface to further reduce the impact of sectioning. Colloidal silica polishing was finally applied to leave a smooth, uniform surface which was minimally influenced by sample sectioning.

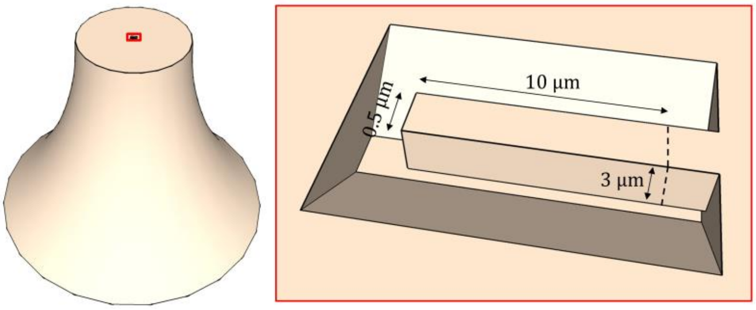

Figure 5.9. Schematic showing sample sectioning and location of TEM lamella.

The three samples were mounted onto Scanning Electron Microscopy (SEM) stubs using silver paint. A 5 nm layer of Au/Pd was sputtered onto the surface of the specimens in order to improve the conduction path and thereby minimise the impact of charging during lamella preparation. Initial SEM imaging of the polished surfaces revealed that micro-scale voids were present in all three samples as shown in Figure 5.10. These voids were many orders of magnitude larger than the nano-scale voiding typically induced by creep [56] and have previously been shown to be present in as-machined samples of dental porcelain [221]. SEM imaging of the entire cross section was performed in order to ascertain the impact of creep or heat treatment at these length scales. A working distance of 9 mm, voltage of 30 keV and pixel size of $150 \times 150\ \mathrm{nm}^2$ was used for imaging over the $\approx 9\ \mathrm{mm}^2$ cross sectional area.

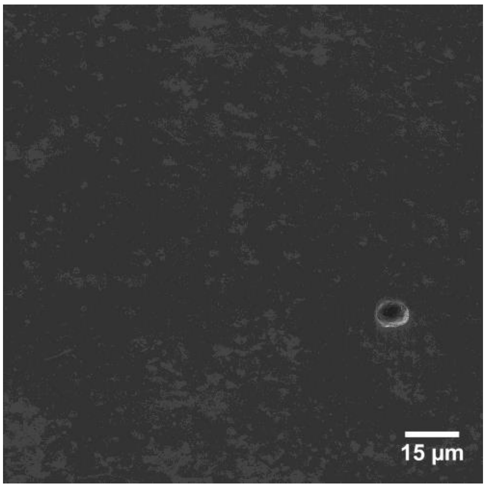

Figure 5.10. SEM image of cross sectional surface of sample A showing a single microscale void typical of those observed in the cross sectional surface of all three samples.

FIB milling was then used to extract TEM lamella from the centre of the polished cross-sections of each sample as shown in Figure 5.9. The automated 'AutoSlicer' routine [222] was used to extract small sections of material with nominal dimensions of $10 \times 3 \times 0.5\ \mu\mathrm{m}^3$ which were attached to a copper TEM grid. Gentle FIB polishing was then performed on each of the samples using a milling current of 100 pA. The thickness of the completed lamellas was found to be $0.1 - 0.05\ \mu\mathrm{m}$ however this process was found to reduce the visible cross sections of all samples.

TEM imaging was performed using an imaging current of $1.0\ \mu\mathrm{A}$ and accelerating voltage of 200 kV. These parameters produced a nominal spot size of 0.25 nm and 2056×2056 pixel images were captured at a resolution of 0.33 nm per pixel. Multiple TEM images were captured in order to interrogate total areas of $22.9\ \mu\mathrm{m}^2$, $11.6\ \mu\mathrm{m}^2$ and $18.3\ \mu\mathrm{m}^2$ for samples A, H and C, respectively. Example micrographs of each of the three samples are given in Figure 5.11.

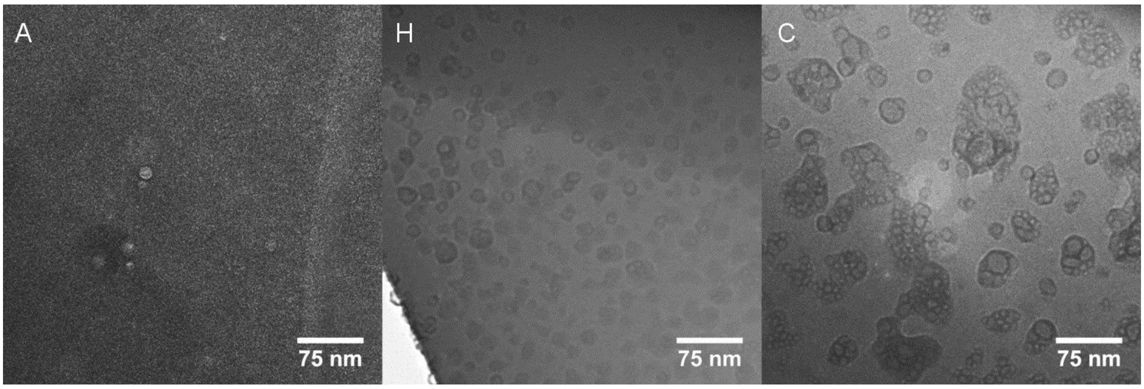

Figure 5.11. TEM images of the as-machined (A), heat-treated (H) and crept (C) samples.

5.3.2.Results

Neutron Scattering

In order to enable valid comparison between SANS results, care must initially be taken to determine the differences in the scattering volume between the specimens. For the three samples examined in this study the gauge volume is a $2 \times 4\ \mathrm{mm}^2$ section through the centre of a 6 mm tall cylinder which is ≈ 3.4 mm diameter. Taking into account any minor differences in diameter and the maximum offset, the expected maximum difference in gauge volume was determined to be 0.28 %. Therefore, results that show differences in the scattered intensity greater than this bound were assumed to be the consequence of the differing scattering response of the samples.

Inspection of the two dimensional SANS patterns showed no apparent anisotropy in the scattering response. Therefore the data was reduced to 1D profiles of scattered intensity versus the modulus of the scattered wavevector Q by radially averaging the two dimensional scattering patterns using Mantid, a neutron scattering data manipulation software package [223]. The data was then corrected for instrumental background, the measured transmission, sample volume and detector efficiency [224]. A perdeuterated /protonated polystyrene blend was used as a calibrant in order to determine measures of the absolute scattered intensity ($I(Q)$) to within $\pm$ 5 % [225] as shown in Figure 5.12. This procedure also gives an indirect check on the Q scale (through measurement of the polymer radius-of-gyration). In order to aid in the visualisation of the data, the distributions of samples H and C have been offset by factors of 5 and 25, respectively in Figure 5.12.

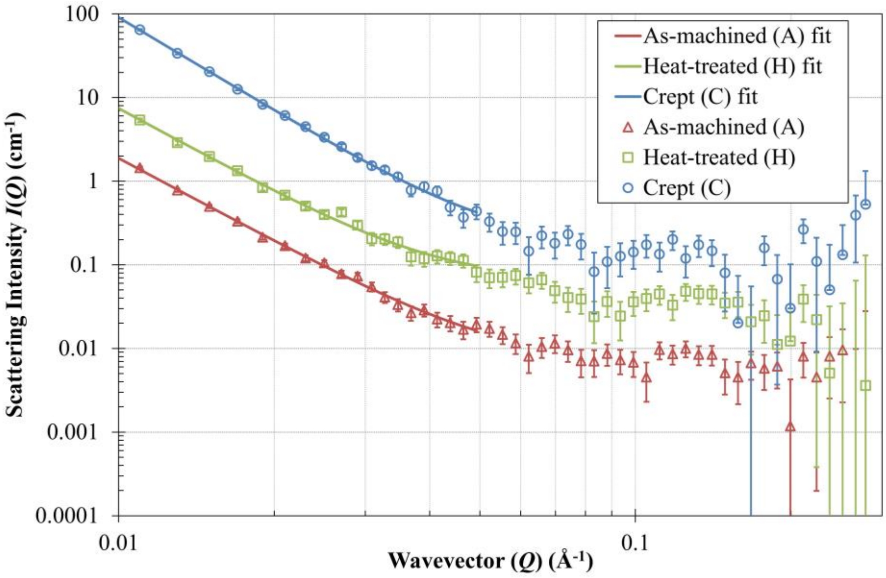

Figure 5.12. Intensity against wavevector for the three samples. In order to reduce the overlap between distributions samples H and C have been scaled by 5 and 25, respectively. The power law fitting is included and the error bars indicate the standard deviation of each point.

The three curves show broadly similar behaviour with a power law response at low Q (i.e. $I(Q) \propto Q^{-k}$) and fitting was performed on each of the three data sets in order to quantitatively describe the differences observed. The as-machined (A), heat-treated (H) and crept (C) samples were found to have power law exponents of 3.3, 3.2 and 3.7, respectively. Variations in the power law exponent can be indicative of differences in void shape, interface behaviour or larger (microscale) phenomena and are discussed in more detail in § 5.3.3 [226].

Examination of the three scattering profiles reveals a number of peak type features overlying the power law distributions. These may be indicative of the spherical shape of the voids [227], however close inspection reveal that the confidence bounds of the associated data points are typically larger than the offsets observed. The only exception to this behaviour is observed at intermediate wavevector values ($Q = 0.08 - 0.17$ Å^{-1}) within samples H and C as shown in Figures 5.12 and 5.13.

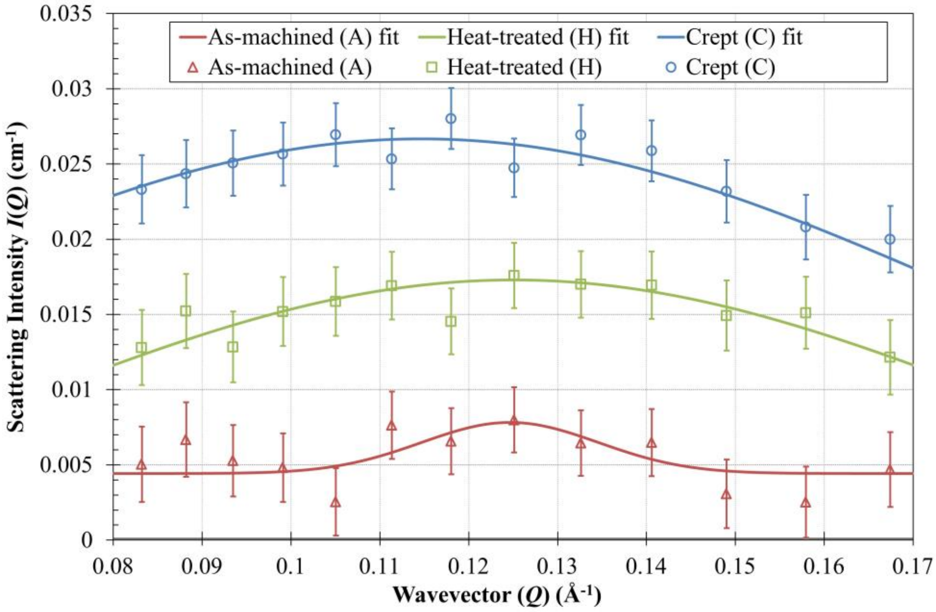

Figure 5.13. Intensity against wavevector in showing the peak fitting applied to the data sets. In order to reduce data overlap the heat-treated (H) and crept (C) data has been offset by $\mathbf{0.01}$ and $\mathbf{0.02}$, respectively. The error bars indicate the standard deviation of each data point.

In order to provide quantitative comparison between the three profiles at the location of interest, Gaussian peak least squares fitting was performed using Equation 2.2. The relationship between the real space and reciprocal space dimensions (Equation 2.11) was then used to convert these descriptors into the associated void dimensions and the results of this analysis are given in Table 5.1.

Table 5.1. Parameter descriptors of peak centres and widths observed in the intensity vs wavevector plots. The void diameter $(\boldsymbol{d})$ associated with each peak has also been included.

Sample	α	β (Å^{-1})	s (Å^{-1})	d (nm)
As-machined (A)	0.004	0.125	0.010	10.0
Heat-treated (H)	0.021	0.125	0.057	10.0
Crept (C)	0.027	0.111	0.063	11.3

Examination of the Gaussian fitting applied to sample (A) reveals that the peak intensity is the same order of magnitude as the standard deviation of each data point. This suggests that this peak is not statistically significant in comparison with the underlying background noise and therefore limited conclusions can be drawn from this fit.

The peak fitting analysis revealed that the average void diameter associated with the heat-treated sample (H) was smaller than in the crept sample (C) with the nominal sizes of 10.0 nm and 11.3 nm, respectively. The two peaks were also found to have different intensities, with the crept sample (C) demonstrating a peak height 28 % higher than the heat-treated sample (H). The width of the two peaks was also found to differ, with the crept sample (C) showing a broader distribution of void sizes (s values equal to 0.057 $\mathrm{Å}^{-1}$ and 0.063 $\mathrm{Å}^{-1}$ for H and C, respectively). Further explanation of the likely origins of these differences are provided in § 5.3.3.

Micrograph Analysis

Examination of the SEM images collected from the porcelain cross section revealed that relatively low numbers (< 50) of microscale voids were observed in all the samples. The average void diameter and standard deviations of these measurements were 4.0 ± 0.6 μm, 3.1 ± 0.5 μm, and 5.8 ± 1.3 μm for the as-machined (A), heat-treated (H) and crept (C) samples, respectively. It is interesting to note that heat treatment appears to lead to a reduction in average void size and that creep results in a moderate increase. However, the limited number of micro-voids that could be examined in this study limits any firm conclusions that can be reliably drawn on the impact of these processes on the void distribution at this length scale. The primary conclusion from this analysis is that a random distribution of voids is present prior to creep. These voids have a number density of ≈ 4.3 $\mu\mathrm{m}^{-2}$ and diameters covering the range from $1 - 20$ μm with an average of ≈ 4 μm.

In order to quantify the number and size of each of the particles within the TEM images, the 'analyse particles' subroutine within the image processing software ImageJ was used [228]. A minimum linear dimension threshold of 4 pixels (1.3 nm) was applied during processing. The outputs from this analysis include the area, perimeter, orientation and aspect ratio (maximum / minimum dimension) of each particle. The total number of particles identified was $37,\ 295$ and $1{,}805$ which corresponds to number densities of 1.61 $\mu\mathrm{m}^{-2}$, 25.4 $\mu\mathrm{m}^{-2}$ and 98.6 $\mu\mathrm{m}^{-2}$ for sample A, H and C, respectively.

The examination of the orientation distribution revealed that no clear preferred direction could be found. A broad range of particle aspect ratios were also observed in all samples, covering the range from $1 - 15$. The mean aspect ratio of all particles (1.77) was found to be influenced greatly by large values and therefore the median (1.366) and mode (1.094) were found to be more representative. This analysis suggests that most voids are close to spherical, with a few outliers.

In order to obtain a representative value for the diameter of each particle the nominal diameter d^n was determined based on the cross-sectional area A:

$$d^n = 2\sqrt{\frac{A}{\pi}}. \tag{5.5}$$

This data was next discretised into one hundred bins 1.3 nm-wide each and normalised by dividing each data set by the cross-sectional area over which imaging was successfully performed (22.9 $\mu\mathrm{m}^2$, 11.6 $\mu\mathrm{m}^2$ and 18.3 $\mu\mathrm{m}^2$ for samples A, H and C, respectively) to produce histograms of number per $\mu\mathrm{m}^2$ against d^n as shown in Figure 5.14. Examination of these distributions revealed that they follow approximately log-normal variation of the form:

$$L(d^n) = \frac{\kappa\xi}{d^n\varrho\sqrt{2\pi}} e^{-\frac{\left(\ln\left(\frac{d^n}{\xi}\right)-\mu\right)^2}{2\varrho^2}}, \tag{5.6}$$

where μ and ϱ are the location and variance parameters, respectively and κ and ξ are the vertical and horizontal scaling parameters respectively. The κ scaling parameter is necessary to accommodate for the fact that these profiles are not probability density functions and therefore the area under the curve does not sum to 1. The ξ scaling factor scales the data in the horizontal direction in order to account for the differences between the void mode sizes.

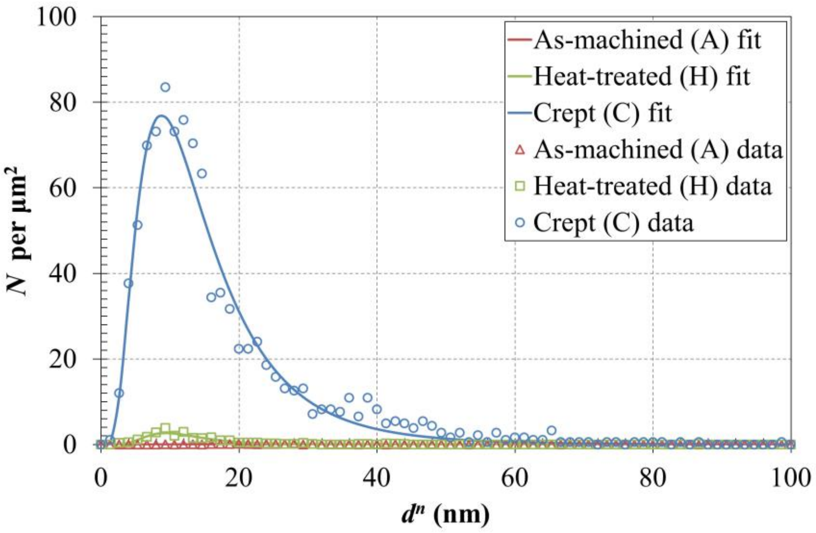

Figure 5.14. Histogram of void numbers per $\mu\mathrm{m}^2$ against nominal diameter. The least squares log-normal fits of each curve are also shown.

Least squares fitting of the log-normal distribution to the three data sets was performed in order to evaluate μ, ϱ, κ and ξ. These parameters can then be used to provide descriptors of the data set including the arithmetic mean $\bar{E}[d^n]$ and median $\mathrm{Med}[d^n]$:

$$\bar{E}[d^n] = \xi e^{\mu+\frac{\varrho^2}{2}}, \tag{5.7}$$

$$\mathrm{Med}[d^n] = \xi e^{\mu}. \tag{5.8}$$

These measures provide information on the average void diameter. To gain insight into the characteristics of the ‘tail’ of the distribution, the skewness of each data set can be obtained from:

$$Skew[d^n] = \left(e^{\varrho^2} + 2\right)\sqrt{e^{\varrho^2} - 1}. \tag{5.9}$$

Larger values of skew are indicative of void growth and therefore provide quantitative descriptors of this behaviour. The tabulated results of all statistical measures and fitted parameters are given in Table 5.2.

Table 5.2. Log-normal parameter descriptors and associated statistical measures of the void distribution histograms obtained from TEM analysis of samples A, H and C.

Sample	ϱ (μm)	μ (μm)	κ	ξ	$\bar{E}$ (nm)	Med (nm)	$Skew$
As-machined (A)	0.39	0.11	0.0940	0.022	27.1	24.8	1.27
Heat-treated (H)	0.43	0.15	2.90	0.008	10.2	9.3	1.43
Crept (C)	0.61	0.19	108	0.008	11.6	9.7	2.35

For the three data sets large variations were observed between the maximum values of the void number per μm^2, N_{max}. This effect is reflected in the relative values of κ, however also presents difficulties when visibly comparing the distributions obtained from the three samples as shown in Figure 5.14. In order to overcome this limitation, a normalised version of the data was replotted in which each dataset was divided by the corresponding value of N_{max} as shown in Figure 5.15. In this figure the peak centre and the characteristics of the distribution “tail” of the three data sets can be more clearly observed.

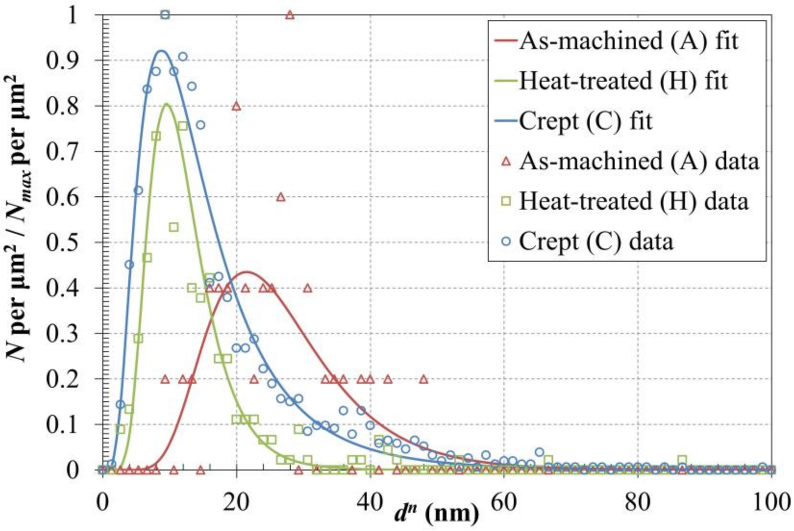

Figure 5.15. A histogram of normalised void numbers per μm^2 against nominal diameter.

5.3.3. Discussion

Examination of the body of characterisation data reveals that statistically significant differences have been detected between the as-machined (A), heat-treated (H) and crept (C) samples using both SANS and TEM analysis. It is important to reiterate at this stage that the gauge volumes of these two techniques were different, and therefore a degree of difference in the observation is to be expected. In the case of TEM analysis, the lamella was extracted from the centre of the sample at the exact location where creep-induced necking was observed. Neutron diffraction, on the other hand, was performed to provide insight into the bulk characteristics of the three samples, and therefore is a technique that delivers measurements with lower spatial resolution, but with increased statistical averaging. The presence of necking in the crept sample (C) indicates that the deformation response was induced within a subsection of the gauge volume and it is therefore perhaps unsurprising that after averaging over neighbouring regions, the changes detected in the neutron scattering data are more subtle.

Void Numbers

Examination of Figure 5.14 indicates that large variations in the number of voids were detected in the TEM study. The total number of voids per unit area was found to be $1.61\ \mu\text{m}^{-2}$, $25.4\ \mu\text{m}^{-2}$ and $98.6\ \mu\text{m}^{-2}$ for samples A, H and C, respectively.

The regions of increased intensity as a function of neutron scattering wavevector correspond to the length scales for which consistent periodic variation is observed in the number of scattering features, such as interfaces or regions of high gradient of density. The average void sizes observed in the TEM analysis ($10-30$ nm diameter) correspond to Q values in the range $0.08-0.12\ \text{Å}^{-1}$. Examination of this region in the three scattering profiles reveals that the two strongest scattering peaks are observed at this location in the heat-treated (H) and crept (C) samples. Peak fitting of these profiles has revealed that the crept data shows a 28% increase in the scattering response over that observed in the heat-treated sample (H). In the case of the as-machined sample (A), no clear peaks are observed in this region, suggesting that the number of voids in this sample cannot be detected by SANS. This trend in the increasing scattering response matches the relative void numbers obtained by TEM analysis, indicating consistency between both techniques.

The absence of grain boundaries in amorphous materials means that creep-induced void nucleation is primarily driven by vacancy condensation [229]. The thermodynamic origins of this phenomenon have been the focus of several studies, and a number of constitutive models have been proposed to describe this response observed [230-233]. Typically these models show a negative exponential dependence upon the inverse of temperature. Therefore at higher temperatures, void nucleation occurs at a faster rate. The void nucleation rate stress dependence in these models is either linear or proportional to the negative exponential of the inverse square of stress, demonstrating that larger numbers of voids are expected to initiate at higher stresses.

Although the limited number of samples examined in this study is insufficient to perform model matching or quantitative assessment of these relationships, the void numbers determined experimentally do match the relationships previously published. The largest number of voids was found in the crept sample (C) which was exposed to the highest temperature and stress combination, and the smallest number of voids was observed in the as-machined sample (A).

Void Size Distribution

The void size distributions obtained through TEM analysis are well matched by the log-normal fitting. This distribution is widely observed in particles sizes and other natural phenomena, and occurs as a result of Gibrat's law which indicates systems in which relative growth rates are independent of size [234]. This suggests that over the length scales examined in this TEM analysis, the proportional void growth rate in porcelain is close to being uniform irrespective of the current diameter. This result is perhaps surprising as below a certain threshold it is generally more energetically favourable for voids to reduce in size and ultimately annihilate [235]. However, it may simply be the case that for this system this threshold is below the length scale resolved by TEM analysis.

Examination of the mean and median void sizes obtained by TEM analysis reveals that these measures are similar for the heat-treated (H) ($\bar{E} = 10.2$ nm and $\mathrm{Med} = 9.3$ nm) and crept (C) ($\bar{E} = 11.6$ nm and $\mathrm{Med} = 9.7$ nm) samples. In contrast to this behaviour, the mean and median size of the as-machined sample (A) are approximately $2 - 3$ times larger ($\bar{E} = 27.1$ and $\mathrm{Med} = 24.8$). Despite the limited number of voids observed in the as-machined sample (A), this significant difference indicates that the thermal processing conditions applied during manufacture were distinct from those applied during this study. In the case of the heat-treated (H) and crept (C) samples, the similarities in response indicate that the average void size is dominated by the 750℃ hold and that a stress of 100 MPa has a limited impact on this aspect of behaviour.

In contrast to the average void size behaviour, the skewness of the as-machined (A) (1.27) and heat-treated (H) (1.43) void distributions are similar, while the skewness of the crept (C) sample is almost twice as large (2.35). This indicates that in the case of the crept sample (C), the 'tail' characteristics are more dominant than for the other two specimens. This behaviour is evident in the creep distribution shown in Figure 5.15 for which relatively large numbers of voids can still be seen at large values of d^n. This distinct difference in the void distribution profiles suggests that the application of stress increases larger diameter void growth in porcelain.

In terms of SANS behaviour, the average size of a particular phenomenon is indicated by the peak centre position on the intensity against wave vector plot. In the case of the as-machined (A) sample, there is a lack of clear peaks in the scattering data, and therefore no insight can be obtained into this measure. In contrast, peak fitting applied to the heat-treated (H) and crept (C) SANS results indicates the presence of voids of nominal diameters of 10.0 nm and 11.3 nm, respectively. Comparison of these diameters with the TEM analysis indicates similar behaviour in both the heat-treated (H) $(10.2\ \mathrm{nm})$ and crept (C) samples $(11.6\ \mathrm{nm})$.

Insight into the distributions of voids within the sample can either be derived from the presence of multiple peaks or through peak broadening, with wider peaks indicating a larger variation in the nominal size of scattering medium. The standard deviation measures obtained from the Gaussian peak fitting analysis reveals that the crept sample (C) shows a broader distribution $\left(0.063\ \text{Å}^{-1}\right)$ than the heat-treated sample (H) $\left(0.057\ \text{Å}^{-1}\right)$. This is consistent with the larger values of skew observed in the TEM analysis of the crept sample (C) data.

In order to provide a more rigorous understanding of the variations in void size and distribution observed, the underlying relationships which drive this behaviour can be considered. Thermodynamic analysis of the impact of temperature on creep reveals that higher temperatures induce larger diameter voids within a broad range of ductile materials [236], as well as in the primary constituent of porcelain, silica [237]. This suggests that the large average void size in sample A is indicative of a manufacturing temperature greater than the 750°C applied to samples H and C. Although the exact manufacturing conditions of Vitablocs are confidential, details have been published for similar dental porcelain ingots [17]. This method is based on melting the porcelain at temperatures above $1{,}000$°C (the exact temperature is not revealed) and then applying compressive pressure during cooling to reduce the build-up of pores. This high temperature process correlates well with the average pore size and low numbers of pores observed in sample A.

The wider distribution of void sizes observed in the crept sample (C) can also be explained through the underlying thermodynamics of optimal void sizes. As in the case of the heat-treated sample (H), the dominating influence on void size behaviour in the crept sample (C) is temperature. However the application of stress induces a small increase in growth rate which acts preferentially on larger pores. This generates a larger number of larger pores and results in a broader and more skewed void size distribution. As well as initially accommodating the increased strain energy applied to the crept sample (C), analysis has shown that broader void distributions of this type result in a more ductile material (for the same void volume fraction) which is better able to accommodate deformation induced by creep [238].

Void Shape and Interface Behaviour

In order to gain insight into the shape and interface behaviour of the nanoscale voiding, detailed examination of the TEM images collected from each of the samples can be performed (Figure 5.11). In sample A this visual study reveals that within the limited number of voids in the sample, most voids are close to spherical in shape, and there is no obvious void grouping. Examination of the edge of the voids reveals a lack of distinct boundary layer which suggests that the interface of the void is sharp.

Although the heat-treated sample (H) contains a larger number of voids, most of them remain close to spherical in shape, and limited void clustering is observed. The main difference between this void type and that observed in sample A is the presence of a distinct boundary layer at void edges. This suggests that the interface between the void and bulk material is thicker for this sample.

Examination of the TEM image collected from the crept sample (C) reveals that although the voids are larger in number, the average void shape remains close to spherical. Similar to the heat-treated sample (H), distinct boundary layers can be observed at the edge of the void, suggesting a thicker interface than that observed in sample A. The distinguishing feature of the crept sample (C) is the void clustering behaviour observed.

In the context of SANS, the impact of void shape and interface behaviour is indicated by the underlying distribution of intensity against wavevector. Typically power law fitting is used to give a numerical descriptor of this behaviour [80] and this approach has previously been successfully applied to study voiding behaviour in silica [239]. In the present study the power law exponents for the three samples were found to be 3.3, 3.2 and 3.7 for the as-machined (A), heat-treated (H) and crept (C) samples, respectively. These values suggest that the behaviour of the crept sample (C) is distinct from the other two specimens however care must be taken when interpreting these results, as multiple structural features are known to influence this parameter.

Variation in the average shape and connectivity of voids is known to influence the power law exponent, in the case of a dispersion of voids with limited connectivity, larger exponents indicate a more spherical void geometry [226]. However, as previously mentioned, visual examination of the TEM images reveals that the average void shape is very similar for the three samples. This conclusion is further validated by the average aspect ratios obtained from particle analysis which were found to be 1.08, 1.10 and 1.09 for the as-machined (A), heat-treated (H) and crept (C) samples, respectively. This suggests that the differences in power exponents observed are not a consequence of void shape changes.

A second variable which is known to affect the power law exponents is the sharpness of the void-to-bulk interface, with the more gradual/diffuse transitions being associated with smaller power law exponents in the range $3 - 4$ [226]. In TEM, images with sharper transitions correspond to more distinct interfaces between the void and the surrounding bulk material. Within the three porcelain samples it can be seen that the heat-treated (H) and crept (C) specimens have noticeably thicker diffuse interfaces and therefore that the power law exponent associated with these two samples (3.2 and 3.7) should be smaller than the as-machined (A) (3.3). This contradiction between the results of TEM and SANS analysis suggests that that there is another effect which dominates the SANS power law exponent response. One potential explanation is the microscale voiding observed using SEM analysis.

In order to consider the origins of the dark interfaces observed at the edges of the voids in the heat-treated (H) and crept (C) samples it is necessary to consider the fundamentals of TEM imaging [240]. A region containing a void has a reduced number of atoms interacting with the incident electron beam and therefore should appear lighter in a light field TEM image. In contrast to this, regions of increased disorder may interact more with the incident beam and therefore appear darker. In the case of a void surrounded by a region of increased disorder, a dark boundary layer is observed surrounding a lighter central region [241]. In some cases, after travelling through the two disordered layers (top and bottom of the void), the scattering is such that the overall greyscale value is darker than neighbouring regions [242]. These regions of high disorder have previously been observed at the void interfaces of other types of silica [56] and similar features were observed during TEM analysis of the YPSZ-porcelain interface as outlined in more detail in § 7.3.

Consideration must also be given to the void coalescence response which was observed only in the crept sample (C). Typically this clustering behaviour is considered to be energetically favourable at either a critical void growth rate or critical void volume fraction [243, 244]. The crept sample (C) has a higher volume fraction and growth rate than the other two samples, and therefore may have surpassed this threshold. The absence of clear void clustering or coalescing in dental porcelain which was exposed to similar stresses and temperatures but for a shorter time period (at the YPSZ-porcelain interface) suggests that the critical parameter may be void fraction rather than growth rate. One factor which remains unclear about the void clustering behaviour is why multiple voids are present rather than single large voids which typically have a lower surface energy penalty. The reason for this may simply be associated with the time taken for mass transport to remove these connections and similar arrangements have previously been observed in simulations of void coalescence [245].

5.4. Conclusions

5.4.1.Secondary Creep Rate Quantification

In order to facilitate tensile creep analysis of this feldspathic porcelain, a new tensile creep rate testing procedure has been developed which is capable of analysing very small samples of ceramic material. This approach was based on maximising the creep rate information obtained from a single sample and therefore necessitated very careful control over creep induced damage in the material. Despite these challenges, the reasonable confidence intervals and realistic estimates of strain rate parameters provided by this study suggest that this experimental approach is reliable and effective. This approach therefore has the potential for use in creep rate studies of small ceramic samples or those in which conventional machining approaches have proven difficult.

The tensile secondary creep rate parameters of a dental feldspathic porcelain have been quantified in the temperature range of $650 - 800^{0}\mathrm{C}$ and stress range of $50 - 125$ MPa. The values of activation energy at each of the stresses was found to be consistent to within the 95% confidence intervals of these parameters and the average value was determined to be $Q = 243.0 \pm 3.1$ kJmol^{-1}. Similar consistency was observed within the 95% confidence limits of the stress exponent at each temperature, and the average value was found to be $\bar{n} = 1.32 \pm 0.08$. These values were found to compare well with literature values quantified through compressive creep, and in tensile studies of similar materials.

5.4.2. Creep Induced Nanovoiding Analysis

Examination of the nanovoiding response has demonstrated clear distinctions between the as-machined, heat treated and crept samples. The results of SANS and TEM characterisation have been shown to be generally consistent in terms of nanoscale void numbers, distribution and average size. Furthermore, the outcomes of the limited microscale void analysis also indicate some variation at this length scale.

These results demonstrate that a thermal dwell is sufficient to induce nanovoiding in porcelain. This explains the limited sintering associated with porcelain veneers of maximum mechanical strength. The application of stress during heat treatment has also been shown to increase void nucleation rates and growth rates in porcelain. This would therefore suggest that the band of nanovoiding observed at the YPSZ-porcelain interface (where high magnitude residual stresses are known to be present) is likely to be associated with creep in this material. Based on this insight, the minimisation of near interface porcelain creep through modified heat treatment and control of residual stresses has the potential to improve near-interface mechanical properties of porcelain and thereby reduce prosthesis failure rates.

6. Microscale Residual Stress and Phase Analysis of the YPSZ-Porcelain Interface

6.1. Introduction and Motivation

Microscale variations in residual stress and YPSZ phase composition are known to affect the failure of the YPSZ-porcelain interface [29]. However, a very limited number of analytical studies have been performed to characterise this variation: nanoindentation has been used to assess the average in-plane variation of residual stress [33, 34] and more recently the ring-core FIB milling residual stress analysis technique has been applied at features of interest and at a spacing of ≈ 0.5 mm [35]. Raman spectroscopy has also been applied to analyse phase and stress within a microscale near-interface region [14]. Although providing local insight, these studies have failed to simultaneously characterise the variation in phase composition and stress state, in order to facilitate firm conclusions regarding the interaction between these effects. In this chapter, a comprehensive multi-technique assessment has been carried out across a representative cross-section in order to improve understanding of this behaviour.

In § 6.2, analysis of the residual strain variation within the amorphous porcelain veneer has been performed using a new technique based on PDF analysis of the diffuse X-ray diffraction patterns from a prosthesis cross-section. This approach is based on the strain induced PDF peak shifting behaviour recently identified by Huang et al. [87] and has provided unique insight into strain accommodation in amorphous substrates. A journal article has recently been submitted on this topic [246].

Insight into the crystallographic phase and lattice strain variation of the YPSZ was provided by transmission X-ray powder diffraction of a thin (115 μm) prosthesis cross section at an incremental step size of 2.8 μm in § 6.3. Raman spectroscopy was performed at the same location in order to provide cross-validation of the phase and mechanical state at a step size of 1 μm in § 6.4.

Residual stress analysis has been performed across both YPSZ and the porcelain veneer using both the sequential ring-core and parallel FIB milling and DIC techniques in § 6.5. This analysis provided insight into the principal stress orientations and magnitudes as a function of distance across the interface at an incremental step size of 50 μm, as well as high resolution (4 μm) insight into the residual stress variation in the near-interface (< 36 μm) YPSZ.

The results of this analysis have served as inputs for analytical modelling of the macroscale residual stresses induced by CTE mismatch during veneering and YPSZ sintering in §6.6. A boundary layer eigenstrain gradient transformation plasticity model of the YPSZ-porcelain interface is also presented in this section. A journal article combining all of these results is currently under review [247].

6.1.1.Sample Preparation

The incisal dental prosthesis examined in this study was produced by the Specialist Dental Group, Singapore, using the manufacturing routine outlined in § 1.1. In order to facilitate spatially resolved X-ray mapping, the completed prosthesis was mounted in a two part epoxy and sectioned such that at the location of interest the YPSZ-porcelain interface was perpendicular to the cross-section surface, as shown in Figure 6.1. In order to minimise the residual stresses induced during sample preparation, a Buehler Isomet Diamond Saw was used to perform gentle sectioning.

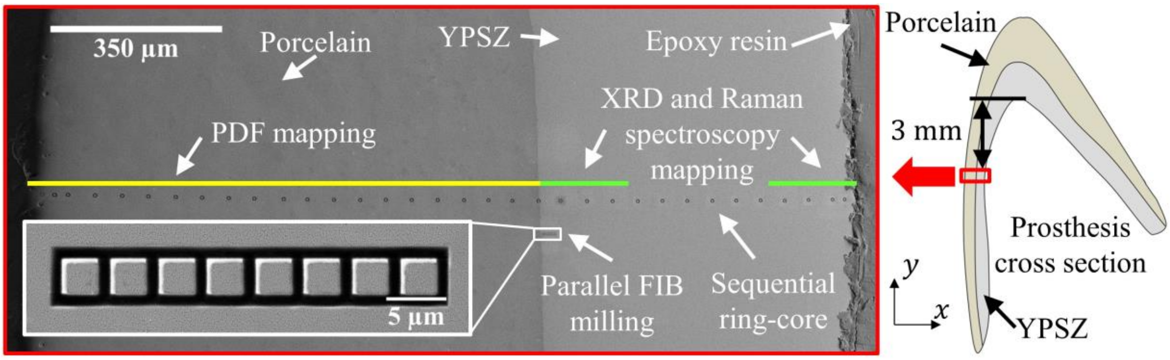

Figure 6.1. Schematic diagram of prosthesis cross section. The insert shows the relative positions of the PDF, XRD and Raman spectroscopy mapping regions, as well as that of the sequential and parallel ring-core FIB milling.

In the case of transmission X-ray diffraction analysis, the sample thickness needs to be carefully selected based on the material of interest (YPSZ or porcelain) and the energy of the incident X-ray radiation. This is a balance between minimising X-ray absorption from the sample, on the one hand, and maximising X-ray scattering behaviour, on the other. In the PDF analysis of porcelain (in § 6.2), the incident radiation was selected to have an energy of 76 keV and therefore the optimum sample thickness was determined to be 2 mm. In contrast, for the XRD experiment of YPSZ (in § 6.3) an incident beam energy of 17.9 keV was selected. The high absorption coefficient of zirconium resulted in an optimum sample thickness of 115 µm for this experiment.

Based on this analysis, the prosthesis sample was initially sectioned to a thickness of ≈ 2.5 mm. A multi-stage diamond grit and colloidal silica polishing routine was then applied to each side of the sample in order to minimise the zone affected by sample preparation to a sub-micron region and to thin the sample to 2 mm. X-ray mapping was then performed on porcelain veneer at the location shown in Figure 6.1. In order to facilitate XRD of the YPSZ, further diamond and colloidal silica polishing was next applied to reduce the sample thickness to 115 μm (as outlined in detail in § 6.3). Following this process, the sample was mounted onto an SEM stub using silver paint and Raman spectroscopy was performed at the same locations as the XRD. The sequential and parallel FIB milling and DIC approaches were then performed to cross-validate the residual stress variation in YPSZ and porcelain.

6.2. Pair Distribution Function Analysis for Strain Quantification

As outlined in detail in § 2.2, micro-focused synchrotron X-ray diffraction has become well established as one of the most suitable techniques for microscale structural analysis and residual strain quantification [248]. The regularly spaced structure of atomic planes within crystalline materials produces sharp X-ray diffraction patterns which form a convenient and precise basis for the XRD lattice strain quantification approach [249]. Amorphous materials such as porcelain produce diffraction patterns with broad and diffuse peaks which, despite containing large amounts of structural information, cannot be analysed for strain in the same manner [250]. In order to extract local structure information, diffraction data collected over a sufficient momentum transfer range can, after careful correction and background subtraction, be Fourier transformed to give the Pair Distribution Function (PDF) [251]. These representations of the probability of finding an atom at a particular interatomic radial distance characterise the average distribution of atoms within the amorphous material and recent studies have demonstrated that the application of macro-strain induces peak shifting within these profiles [86, 252]. Further, the relationship between peak centre and applied strain has recently been shown to be linear for some amorphous materials [87].

Using this insight as a formal basis, it can be seen that by characterising the influence of macroscopic strain on the PDF pattern of an amorphous material, the unknown residual strain can be determined at a particular point within a sample by PDF quantification. In the analysis which follows, 4-point bending was used to impose a well-characterised strain distribution within porcelain, and the impact on the resulting PDF strain distributions was assessed. This provided insight into the fundamental atomic scale response of porcelain, and hence facilitated residual strain profiling within a porcelain dental veneer of a YPSZ coping using X-ray scanning and PDF analysis.

6.2.1.Materials and Methods

As outlined in § 1.4, dental porcelain such as IPS e.max Ceram are supplied as powders which are then applied as aqueous slurry and fired to build up millimetre thick multiple layer veneers. It is therefore difficult to produce representative samples of this material which are of sufficient thickness to enable *in situ* 4-point loading. In a similar approach to that implemented in Chapter 5, the decision was therefore made to use Cerec Vitablocs Mark II ingots [49] to produce the mechanical test specimen for this study. As previously highlighted, the composition of Vitablocs is very similar to that of IPS e.max Ceram, and it was hoped that the impact of strain on the PDF distributions of both materials would be sufficiently similar as to enable direct comparison.

A cuboidal four-point bending specimen was manufactured from an I14 Vitabloc using a Buehler Isomet Diamond Saw. This process was followed by diamond polishing of the surfaces, in order to reduce the impact of any residual stresses induced during sectioning. The uniform crack-free surfaces resulting from this process also minimised any localised stress concentrations during loading. The dimensions of the completed sample were $2.00 \times 1.03 \times 15.8\ \mathrm{mm}^3$. For the X-ray scattering experiment the through-beam thickness was selected as $2\ \mathrm{mm}$ in order to match the prosthesis slice thickness and to maximise the intensity of the diffracted signal.

X-ray scattering data was collected at beamline I15 at Diamond Light Source, UK, using an X-ray energy of $76\ \mathrm{keV}$ and a collimated beam with a circular cross-section and diameter of $70\ \mu\mathrm{m}$. A Perkin Elmer flat panel 1621 EN area detector was placed $262\ \mathrm{mm}$ downstream from the sample in a transmission geometry. The high X-ray energy and the short sample-to-detector distance allowed scattering data to be collected up to the maximum momentum transfer, Q_{max}, of $25.1\ \text{Å}^{-1}$. Calibration of the sample to detector distance was performed for each type of sample using lanthanum hexaboride.

An optical microscope was used to align the sample region of interest with the incident beam and translation stages were used to raster the beam interaction point. The data collection routine consisted of a one minute dark field data collection, which was used to correct for the detector background noise level, followed by a one minute data collection exposure. This sequence was repeated 12 times at each point on the sample in order to collect the statistics necessary to produce reliable pair distribution profiles. Background X-ray scattering data in the absence of the sample (flat field) was collected using the same data collection routine.

In situ four-point bending was performed on the cuboidal porcelain sample as shown in Figure 6.2 using a Deben Microtest 200 N loading rig. The moment distribution for this arrangement can be determined as function of the total applied load (F) and the vertical spacing between nearest loading points (L) as shown in Figure 6.2. From this distribution the vertical stress component can also be determined as function of the distance from the centre of the beam (x) and the 2nd moment of area about the neutral axis in the bending direction (I). Diffraction patterns were collected at a vertical position midway between the loading half cylinders. Ten data points were collected at each of the three loading increments ($0, 10$ and 20 N), at x positions ranging from -0.45 mm to 0.45 mm in steps of 0.1 mm. This ensured that diffraction patterns corresponding to both nominal tensile and compressive strains (and the corresponding Poisson response) were collected at each loading increment.

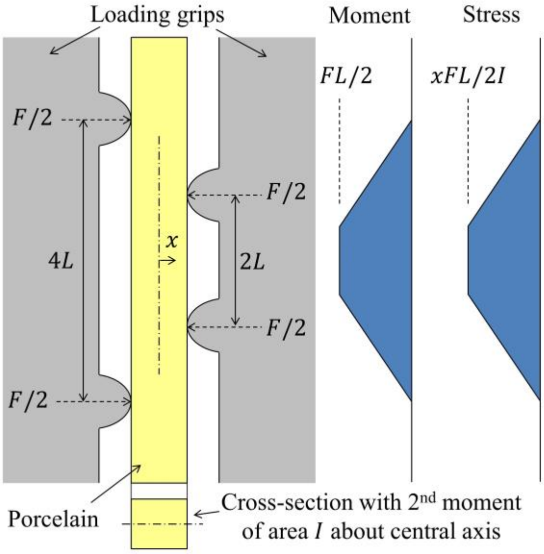

Figure 6.2. Schematic of *in situ* four-point loading of the cuboidal porcelain sample. The incident beam direction is into the page. The moment and stress distributions in the vertical direction are illustrated to the right of the diagram.

Transmission X-ray scattering data was collected across the porcelain veneer of the 2 mm prosthesis cross section shown at the location shown in Figure 6.1. The position of the line scan was selected to be within a region where the YPSZ-porcelain interface was uniform in the through-beam direction and also to be far from the boundaries of the prosthesis, to reduce the impact of curvature and surface relief effects in these areas. A line scan was then performed from the YPSZ-porcelain interface to the edge of the veneer in increments of 70 μm. Thirteen points, covering a total distance of 0.91 mm, were successfully collected from within this region. The full veneer thickness of the porcelain at this location was found to be 0.925 mm, as measured from Scanning Electron Microscopy (SEM) images.

However, surface effects and the reduced scattering intensity meant the diffraction patterns at either end of the line scan could not be reliably converted to PDF data of the quality necessary for further analysis.

6.2.2. Theory and Calculation

The 2D X-ray scattering data was initially processed using the software package DAWN [253] to give 1D scattering data. Small intense spots were observed, which was attributed to crystalline phases in both the porcelain veneer and 4-point bending specimen. Rietveld refinement was used to estimate the volume fraction of this material, which was determined to be $< 1\%$ for both porcelain types [254]. In order to reduce the impact of these phases on the resulting PDF data, these spots were masked using the tools available within DAWN. The twelve sets of data collected at each point were then averaged. The combination of masking and averaging was sufficient to ensure that contribution from the minority crystalline phases was minimised. In order to resolve the horizontal and vertical strain components obtained through amorphous diffraction, azimuthal integration of the resulting 2D data was performed over 30° sectors as shown in Figure 6.3. Averaging of the distributions around the horizontal direction ($-15°$ to $15°$ and $165°$ to $195°$) and the vertical direction ($75°$ to $105°$ and $255°$ to $285°$) was performed to give equivalent 1D distributions representative of each orientation.

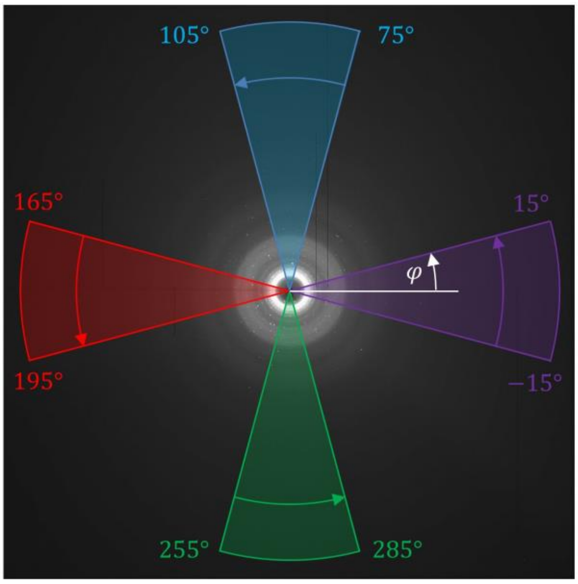

Figure 6.3 Schematic diagram indicating the ranges of angles over which azimuthal integration was performed.

The segmented 1D scattering data from DAWN was further processed using the computer program Gudrun [255]. The data was corrected for background, Compton and multiple scattering, as well as beam attenuation by the sample mounting arrangement to produce the normalised total scattering function, $S(Q)$. The total scattering function was then Fourier transformed to produce the PDF in the form of function $G(r)$ using Equation 2.13, as defined by Keen [256].

The pair distribution function, $G(r)$, is a quantitative histogram of interatomic distances between a pair of atoms, and the area of the peaks are related to the coordination of the atoms [84]. The PDF can therefore give structural information about the atomic bonding environment for both amorphous and crystalline substrates. Even in the absence of a complete structural model, deviations in the PDF peak positions and intensities provide quantitative indication of the alteration in the local structural lengths within the material. A typical PDF for this type of dental porcelain is shown in Figure 6.4a.

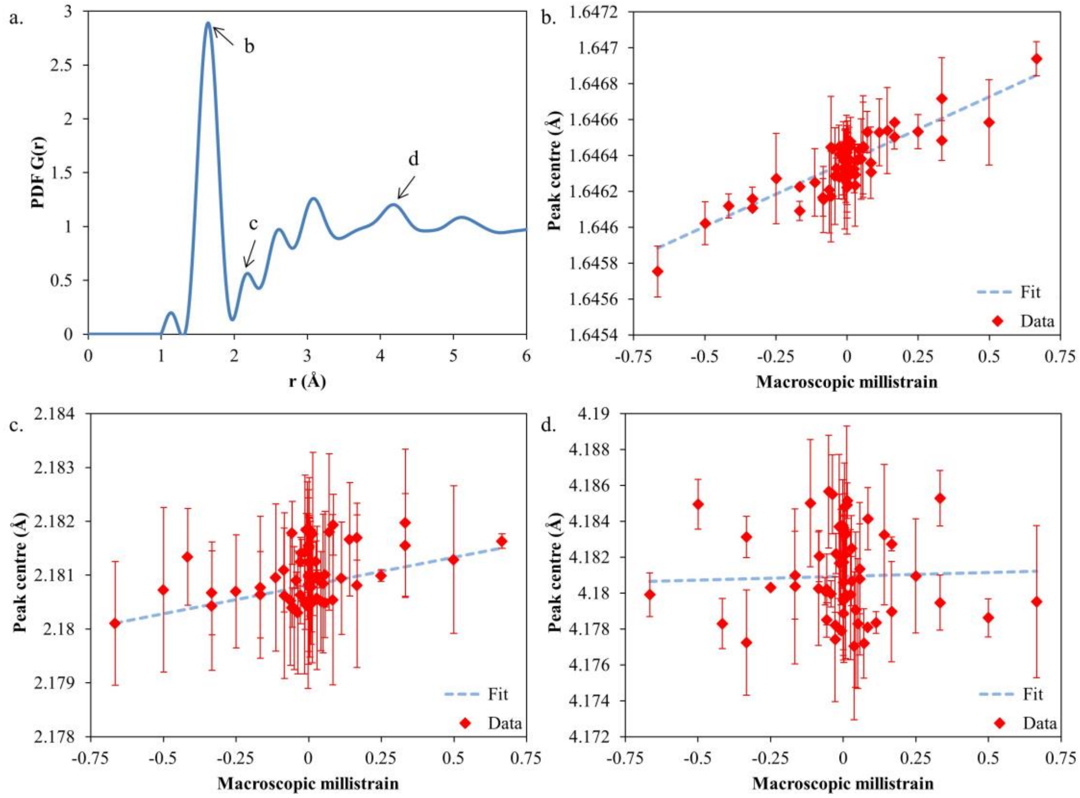

Figure 6.4. a) PDF distribution of porcelain. Peak centre positions are shown as functions of macroscopic strain for peaks with b) a strong correlation with applied strain ($R = 0.88$), c) an intermediate level of correlation ($R = 0.49$) and d) no correlation ($R = 0.03$).

Previous studies of the influence of strain on $G(r)$ have revealed that PDF peak shifts can be induced by external loading in amorphous materials [87]. This behaviour can be considered to be analogous to the Bragg peak shifting response observed in crystalline materials under applied strain [257]. In the case of Bragg diffraction, X-ray powder diffraction produces Debye-Scherrer rings that correspond to 1D profiles with sharp, clearly defined peaks after azimuthal integration. These peaks can be individually fitted to provide reliable estimates of peak centres and lattice parameters, and thereby lattice strain for crystallites with a given Miller index [258]. Alternatively, full refinement of the diffraction pattern can be performed to provide an overall estimate of the unit cell dimensions (lattice parameters) of the material. This is a global minimisation problem that takes into account the peak centres (and shape) of multiple peaks to derive the parameter descriptors of the crystalline lattice.

For PDF data, peak positions also change due to the local displacement of atoms under the application of macroscopic strain. However, not all peaks displace to the same extent: the amount of peak shift depends on the extension and rotation of the bonds that define the particular interatomic distance. The broad peak shape observed in PDF data of amorphous substances means that peak overlap, coupled with differences in the amount of shift between individual peaks, may reduce the certainty with which the centre of a single peak can be determined. Statistical noise in the collected diffraction pattern, particularly at high values of Q where the scattering signal is weak, may also induce aberrations in the peak centre position determination at lower radial distances. Typically this is not a problem as the peak shifts are small [259], and when matching structural models to entire patterns, this behaviour can be averaged out over multiple peaks This means that an approach equivalent to single PDF peak fitting and the associated identification of strain is imprecise and ultimately forms an unreliable measure of strain. However, in order to overcome this limitation, an approach based on multiple PDF peak fitting in order to identify a single average measure of strain is sufficiently precise as to provide a reliable measure. This fundamental approach forms the basis of strain quantification in the remainder of this subsection.

Strain Calibration

In order to provide estimates of the macroscopic strain distribution within the porcelain veneer, the impact of macroscopic strain (ε^M) on the PDF profile of porcelain needs to be determined. In order to describe this relationship most effectively, I will begin by introducing the concept of atomic strain (ε^A) within amorphous materials [87]. This descriptor can be considered the equivalent of lattice strain within crystalline materials and is given by the expression:

$$\varepsilon^A = \frac{r^{Cen} - r^0}{r^0}, \tag{6.1}$$

where r^{Cen} is the radial peak centre position and r^0 is the equivalent unstrained radial peak centre, i.e. when the applied macroscopic strain is zero. The value of r^0 for each peak is unknown prior to calibration and needs to be determined to enable comparison between macroscopic and atomic strains.

Macroscopic loading of crystalline materials will induce lattice strains dependent upon both the orientation within the crystal (Miller index) and the crystal stiffness in the corresponding direction. Lattice strains will be equal in all orientations under hydrostatic loading of an isotropic material, but will be different for an anisotropic crystal. The knowledge of different lattice strain responses to external loading can be used to provide insight into the single crystal stiffness of anisotropic materials [189].

In contrast to this behaviour, in the case of amorphous materials, it is unclear what relationships exist between macroscopic and atomic level strain. Conceptually this relationship must tend towards a 1:1 relationship at large interatomic positions, while at small length scales deviations may be observed due to the effect of stiffness of specific bonds. However, the distances over which these two effects dominate, and their relative magnitudes for a particular amorphous material depend on the number and strength of the bonds and the interatomic distances corresponding to a given peak. Pre-assessment of this behaviour is not possible in absence of a complete structural model.

Therefore, in order to establish the relationships between atomic and macroscopic strains required for strain quantification, the nature and magnitude of the relationship between peak centre and applied strain needs to be determined for each peak. It is clear that the broad spectrum of elements and amorphous nature of porcelain will result in not only peak shifting, but also changes in peak shape and interference between neighbouring peaks. Care therefore needs to be taken to identify those peaks which show the strongest correlation between applied load and peak centre position.

Least squares Gaussian peak fitting was applied to each of the 39 distinguishable peaks within the PDF radial distribution function (to a radial distance of ≈ 38 Å) in order to determine the peak centre and associated confidence interval at each position. Scatter plots were produced which showed the correlation between macroscopic strain and peak centre position for each of the peaks. Some peaks were found to give rise to the correlation coefficient (R) values close to 1 (a strong correlation, as shown in Figure 6.4b), while others showed intermediate levels of correlation (as shown in Figure 6.4c) or very little correlation (Figure 6.4d). Only those peaks with a strong level of correlation (correlation coefficient value greater than $\approx 2/3$) were selected for the remainder of the analysis. This gave 18 peaks within the data set, covering r values in the range $1.64 - 37.84$ Å.

In order to determine the relationship between the peak centre and macroscopic strain (ε^M) at each position, least squares fitting of the remaining data sets were performed using the expression:

$$r^{Cen} = \bar{\alpha}\varepsilon^{M} + r^{0}, \tag{6.2}$$

where $\bar{\alpha}$ is the coefficient relating the peak centre to the applied macroscopic strain, and the axis intercept r^0 corresponds to the peak centre at which there is no macroscopic strain. During this linear fitting process the relative uncertainty of each peak centre value was accommodated by applying a weighting factor equal to the inverse of the standard deviation obtained from peak fitting at each point. The standard deviations for $\bar{\alpha}$ and r^0, $\sigma_{\bar{\alpha}}$ and σ_{r^0} respectively, were also determined.

Rearrangement of Equation 2 and substitution into Equation 1 reveals that the relationship between atomic and macroscopic strain can be written as:

$$\varepsilon^{A} = \frac{\bar{\alpha}}{r^{0}}\varepsilon^{M} = \bar{\beta}\varepsilon^{M}. \tag{6.3}$$

Here $\bar{\beta}$ is the constant of proportionality between the two measures of strain. For peaks at large radial distances the value of atomic strain must tend towards that of macroscopic strain, and therefore it is expected that $\lim_{r\to\infty} \bar{\beta}(r) = 1$. In order to determine the confidence intervals of each value, estimates of the standard deviation of $\bar{\beta}$, $\sigma_{\bar{\beta}}$ were also obtained from the expression:

$$\sigma_{\bar{\beta}} = \frac{\bar{\alpha}}{r^{0}}\sqrt{\left(\frac{\sigma_{r^0}}{r^{0}}\right)^{2} + \left(\frac{\sigma_{\bar{\alpha}}}{\bar{\alpha}}\right)^{2}}. \tag{6.4}$$

Further analysis was performed to assess the relationship between macroscopic strain and the other two peak fitting parameters; Gaussian peak height and width. Low correlations were observed for these two measures for all of the peaks assessed.

Dental Prosthesis Analysis

Despite the similarities in elemental composition between Vitabloc Mark II and e.max Ceram, differences were observed within the PDF patterns of the two materials. These differences are likely to be associated with minor differences in elemental composition, microstructure and processing route applied to the two compositions. Examination of the PDF profiles obtained from the two porcelain types revealed however that for small values of r, strong similarities were observed. For this reason the remainder of the residual strain quantification analysis was focused on the range of interatomic distances $r \leq 5.5$ Å. Within this radial distance, seven distinct peaks were observed which correspond to the nearest 1st and 2nd neighbour distances, primarily between Si and O atoms. It was found that four of these peaks showed good correlation between macroscopic and atomic strains as shown in Table 6.1.

Table 6.1. Peak centre, correlation coefficient and macro-atomic strain proportionality coefficient for the four PDF peaks used in the porcelain veneer macroscopic strain quantification. The silica bonds corresponding to each peak have been identified.

Bond	$\boldsymbol{r^0}$ (Å)	$\boldsymbol{\sigma_{r^0}}$ (Å)	$\boldsymbol{\bar{\beta}}$	$\boldsymbol{\sigma_{\bar{\beta}}}$	$\boldsymbol{R}$
Si-O	1.65	9.31×10^{-6}	0.44	5.73×10^{-2}	0.88
O-O	2.64	3.64×10^{-5}	0.47	7.07×10^{-2}	0.76
Si-Si	3.10	4.44×10^{-5}	0.45	9.03×10^{-2}	0.79
Si-Si / O-O *	5.11	2.17×10^{-5}	0.43	8.17×10^{-2}	0.90

* The peak at $r = 5.11$ corresponds to a combination of the peaks of the 2nd nearest neighbours of silicon and oxygen

Gaussian peak fitting was performed on the data collected from the porcelain veneer in directions parallel and perpendicular to the YPSZ-porcelain interface. The peak centre r^{Cen} and confidence interval $\sigma_{r^{Cen}}$ were obtained for each of the four peak positions given in Table 6.1. A rearranged form of Equation 6.2 was used to convert the peak centre positions to macroscopic strain estimates for each peak:

$$\varepsilon^M = \frac{r^{Cen} - r^0}{\bar{\alpha}}. \tag{6.5}$$

The standard deviation of these macroscopic strain estimates were also obtained using the expression:

$$\sigma_{\varepsilon^M} = \sqrt{\frac{\bar{\alpha}^2\left(\sigma^2_{r^{Cen}} + \sigma^2_{r^0}\right) + (r^{Cen} - r^0)^2\sigma^2_{\bar{\alpha}}}{\bar{\alpha}^4}} \tag{6.6}$$

In order to determine a single parallel and perpendicular strain estimate at each position, a weighted average of the two vertical and the two horizontal strain values (Figure 6.3) was obtained using the standard deviation of each estimate.

Initial examination of the macroscopic strain estimates obtained by this analysis revealed that although the variation between terms seemed realistic, the magnitude of the estimates was far beyond the yield strain of porcelain. Similar unrealistic strain magnitude offsets of this type can be found during lattice strain quantification of crystalline substrates due to incorrect value of the material-dependent unstrained lattice parameter d^0_{hkl} [75]. As highlighted in § 2.2.1 one approach applied to overcome this problem has been to compare the lattice strain variation with distributions obtained by other independent experimental techniques, for example the ring-core FIB milling and DIC approach. Adopting this approach, Equation 6.5 was modified to include a correction factor $(\mathcal{B})$ on r^0:

$$\varepsilon^M = \frac{r^{Cen} - \mathcal{B}r^0}{\bar{\alpha}}. \tag{6.7}$$

Optimisation of this scaling factor was performed by comparison with the strain estimates obtained in § 6.5 in order to give a single value of $\mathcal{B} = 0.9927$ for the entire data set. This parameter may be indicative of the minor elemental and microstructural differences between the two porcelain types examined in this study, or alternatively may indicate a small (1.9 mm) offset in the sample to detector distance used in the two diffraction experiments.

6.2.3. Results

The variation of $\bar{\beta}$ obtained from the porcelain *in situ* loading experiment and corresponding 95% confidence intervals are shown as a function of the radial distance in Figure 6.5. Thresholding has been applied to the data set to leave only those peaks which show a strong correlation between macroscopic and atomic strain. In this plot the correlation coefficient has also been indicated by the marker colour.

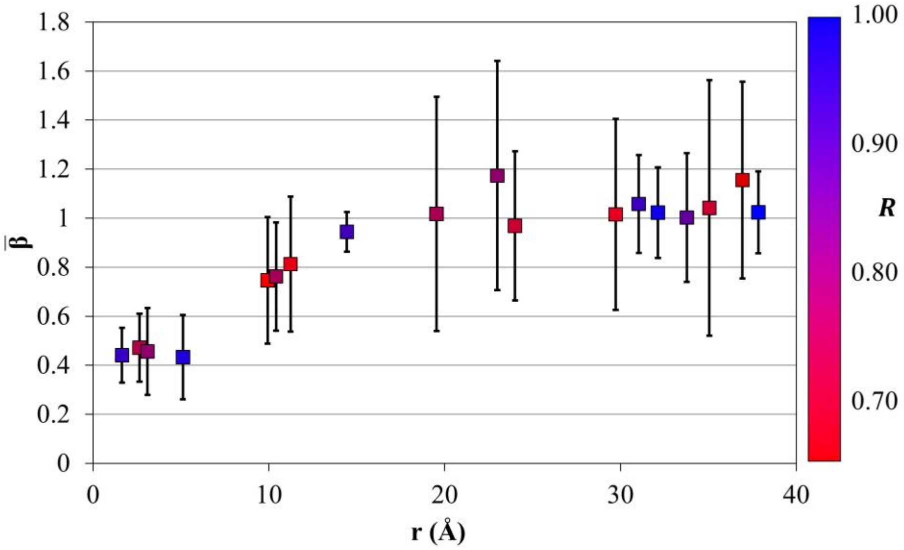

Figure 6.5. Constant of proportionality between atomic and macroscopic strain $(\bar{\beta})$ against interatomic distance. The correlation coefficient between atomic and macroscopic strain at each point (R) is indicated by marker colour and error bars indicate the 95% confidence interval.

Examination of Figure 6.5 reveals that at small radial distances $(r < 5.5 \text{ Å})$ the atomic strain amounts to less than half the associated macroscopic strain, i.e. $\bar{\beta} \approx 0.4$. At larger radial distances $\bar{\beta}$ demonstrates a gradual increasing trend towards a value of 1. This means that the atomic strain measure tends towards the macroscopic equivalent beyond $\approx 20 \text{ Å}$.

The 95% confidence intervals associated with each of the data points also appear to show a general increasing trend at larger radii. This decreasing certainty is likely to be associated with the reduced peak heights within the PDF distribution at larger values of r. It can be seen that peaks with larger uncertainties typically have lower levels of atomic to macroscopic strain correlation and that $\bar{\beta}$ estimates greater than unity are only observed at data points with high uncertainties

Strain Variation in the Porcelain Veneer

The estimates of strain variation within the porcelain veneer obtained using PDF analysis and the sequential FIB milling and DIC approach (from § 6.5) are shown as a function of distance from the YPSZ-porcelain interface in Figure 6.6. Strains in directions parallel and perpendicular to the interface have been plotted separately and are shown in Figures 6.6a and 6.6b, respectively.

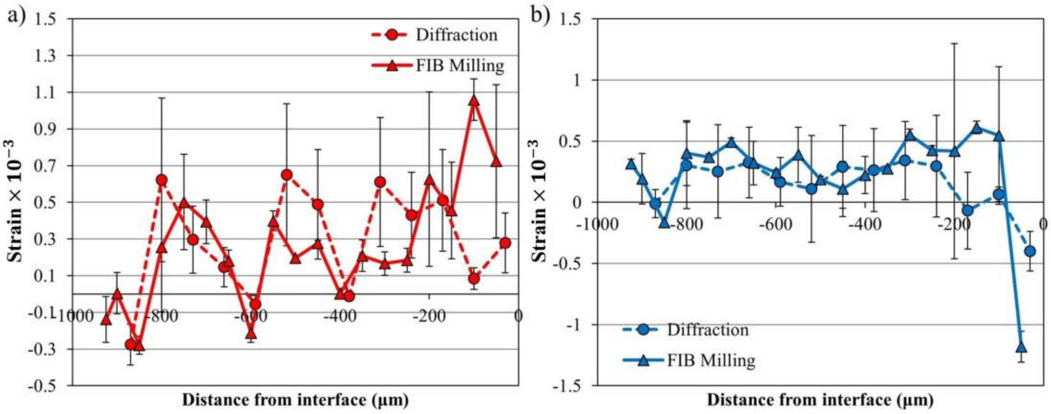

Figure 6.6. Strain variation within the porcelain veneer as a function of distance from the interface. The results from PDF analysis and sequential FIB milling and DIC are shown in directions a) parallel and b) perpendicular to the YPSZ-porcelain interface. The distance measurement from the interface is negative in order to be consistent with the remainder of this chapter and the error bars indicate the 95% confidence intervals of each data point.

In order to draw reliable comparisons between the strain measurements obtained, consideration of the gauge volumes and stress states associated with the two techniques is required. The ring-core milling geometry has a well-defined gauge volume which is contained within the 5 μm diameter core. This technique is surface based and therefore can be well approximated by plane stress conditions.

In the case of the PDF analysis study, the gauge volume has a cross section equal to the size of the incident beam ($\varnothing = 70$ μm) and is representative of an average through the thickness of the sample (2 mm). Therefore, the sampled volume contains both the near-surface region (which can be approximated by plane stress conditions) and the region far from the sample surface (close to plane strain conditions). The difference between the near-surface and through-thickness average stress states has been outlined in detail in the derivation of the FIST ring-core milling analysis. A good approximation for the difference between plane stress and plane strain (under initially equivalent eigenstrain) is given by the square of Poisson's ratio (Appendix A). This means that the maximum difference between the stress states measured using the two techniques is expected to be $\approx 4\%$ [260].

In the case of strains in a direction parallel to the interface (Figure 6.6a), it can be seen that despite the differing gauge volumes, the distributions show several similar trends. The porcelain is on average in a state of mild tension within the first ≈ 0.4 mm from the YPSZ-porcelain interface. A periodic distribution with a spacing of $0.2 - 0.3$ mm is then observed. This repeating pattern has maximum tensile strain of approximately 0.5×10^{-3} and a maximum compressive strain of $\approx 0.25 \times 10^{-3}$. Mild compressive strains of $\approx 0.1 \times 10^{-3}$ are also present within $50 - 70$ μm of the edge of the sample.

Examination of the strain distributions obtained in a direction perpendicular to the interface (Figure 6.6b) reveals that the porcelain is predominately in a constant state of mild tension of $\approx 0.4 \times 10^{-3}$. At the YPSZ-porcelain interface, a single point of compressive strain is observed and at the free edge a region of low magnitude compressive and tensile strains are present.

For both strain orientations it can be seen that the strain estimates obtained through PDF analysis are less precise than those obtained using the FIB milling and DIC approach. Despite this, the majority of PDF strain estimates show 95% confidence interval overlap with neighbouring FIB milling and DIC strain estimates, suggesting that realistic approximations of the strain state have been identified.

6.2.4.Discussion

Previous diffraction studies of *in situ* loading of amorphous materials have noted that peak shifting is induced in the resulting PDF data by the application of macroscopic strain [86, 87, 252]. In these studies the trend of increasing $\bar{\beta}$ values as a function of radial distance have previously been noted. However, limited explanation for the differing response between atomic and macroscopic strain has been presented beyond the fact that strain at small length scales is influenced by "interatomic rearrangements" [86]. While consideration of the disordered atomic structure of amorphous materials immediately rules out the average uniform lattice stretching response observed in crystalline materials, further investigation is required to improve current understanding.

The continuum mechanics response of porcelain dictates that the macroscopic strain must be accommodated locally at all points within the material. Taken on its own, this material requirement is incompatible with the atomic strain response of porcelain at very small radii where the bond length extension or nearest neighbour distance demonstrate a strain of approximately $\frac{2}{5}$ of the macroscopic response. I therefore put forward the hypothesis that at small length scales the atomic level response is dominated by the only other atomic level response available, namely, bond rotation.

Molecular Dynamic Simulations

In order to improve the understanding of the interaction between bond extension and rotation at small length scales, the outstanding modelling capability of MD simulations can be exploited. In the following discussion, Atomistix ToolKit–Virtual NanoLab [261] has been used to model amorphous silica, the primary constituent of porcelain (> 65 wt. %), in order to improve understanding of the $\bar{\beta} < 1$ values observed at small radial distances ($r < 20$ Å).

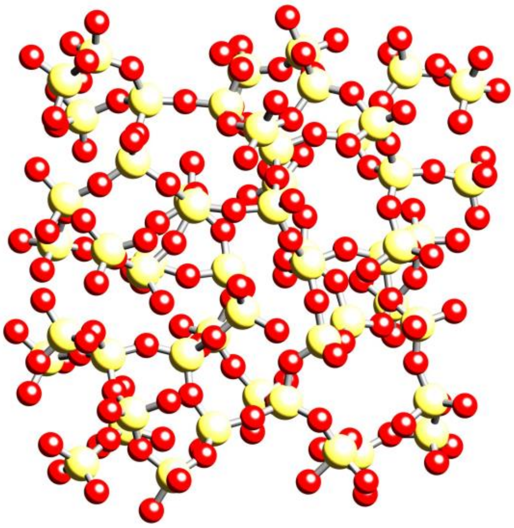

Figure 6.7. Subsection of amorphous silica MD simulation showing a random arrangement of the characteristic silica tetrahedral structure. Silicon atoms are indicated in yellow and oxygen atoms are indicated in red.

Prior to loading simulations, an atomic arrangement representative of amorphous silica was required. In order to create a model for this ensemble, a large (1,728 silicon atoms and 3,456 oxygen atoms) unit cell of cristobalite was initially generated from the atomistic library and melted to 5000 K using the ATK classical calculator and the silica potential developed by Pedone et al. [262]. The initial velocity of the atoms was based on a 5000 K Maxwell-Boltzmann distribution and 20,000 steps were used in the simulation. Next, the results of this high temperature simulation were used as an input into a 20 step incremental cooling regime using the same simulation parameters as the melting stage. During this cooling cycle the density of the amorphous material was monitored closely to ensure that the final density of the amorphous material obtained in the simulation ($2.72\ \mathrm{gcm}^{-3}$) was suitably representative of silica at room temperature ($2.65\ \mathrm{gcm}^{-3}$ [263]). A tight bonding and annealing procedure was also implemented in order to minimise any residual stresses within the sample [264] and to reduce the amount of defects within the amorphous material to realistic levels [265]. Examination of the resulting amorphous atomic structure revealed a random distribution of silicon surrounded by 4 oxygen atoms in the characteristic tetrahedral arrangement illustrated in Figure 6.7.

In order to simulate macroscopic straining of amorphous silica, an NPT Melchionna type simulation was used to apply an external pressure to the amorphous material. A bulk modulus of 37 GPa [266], and thermostat timescale of 20 fs was implemented in the simulation which was performed over 20,000 steps. To simulate the case of an unloaded sample, the first simulation was run at an applied pressure of 1 Pa. Pressures covering the range from 25 to 500 MPa were then incrementally applied in steps of 25 MPa to simulate residual strains from 6.75×10^{-4} to 1.35×10^{-2}. At each load the position of each atom was recorded, and a simulated PDF was generated.

An identical PDF peak fitting procedure to that outlined in § 6.2.2 was next applied to determine the peak centres, atomic to macroscopic strain ratio $\bar{\beta}$, and the correlation coefficient for each peak. Despite having a reduced number of peaks in this data set, some peak centres showed little correlation with the applied strain. Critical examination of the peaks within this region revealed that the origin of this behaviour was neighbouring peaks demonstrating small differences in macroscopic strain response. This appears as a change in peak shape in the complete PDF distribution which results in ineffective peak centre tracking. In total three peaks were found to have reasonable correlation coefficient values and these are shown in Table 6.2.

Table 6.2. Peak centre, correlation coefficient and macro-atomic strain proportionality coefficient for the three PDF peaks, showing strong correlations between peak shift and macroscopic strain. The silica bonds corresponding to each peak have also been included.

Bond	$\boldsymbol{r^0}$ (Å)	$\boldsymbol{\sigma_{r^0}}$ (Å)	$\boldsymbol{\bar{\beta}}$	$\boldsymbol{\sigma_{\bar{\beta}}}$	$\boldsymbol{R}$
Si-O	1.61	2.31×10^{-6}	0.19	1.03×10^{-2}	0.97
Si-Si	3.15	7.39×10^{-6}	0.47	5.03×10^{-2}	0.91
O-O *	7.26	5.00×10^{-6}	0.66	3.84×10^{-2}	0.87

* The peak at $r = 7.26$ corresponds to the 3rd nearest neighbours of oxygen

One of the first conclusions that can be drawn from the results presented in Table 6.2 is that the MD results show stronger levels of correlation and higher precision on the estimates of r^0 and $\bar{\beta}$. This is likely to be associated with the reduced noise associated with the MD simulations as well as the reduced number of other interfering peaks within these PDF distributions (due to the absence of the alloying elements which are present in porcelain).

Comparison between the r^0 values for the Si-O and Si-Si bonds obtained experimentally (1.65 Å and 3.10 Å) and those obtained using MD (1.61 Å and 3.15 Å) reveals reasonable matching. This suggests that despite the superposition of PDF contribution of other alloying elements in the porcelain, the peak fitting process was able to capture the peak centre positions of the silica within the porcelain.

Examination of the $\bar{\beta}$ values in Table 6.2 reveals that for the Si-O peak the experimentally derived value (0.44) is over twice as large as that obtained using MD simulations (0.19). In contrast to this the Si-Si bond shows a good match between the experimental (0.45) and MD (0.47) $\bar{\beta}$ estimates. No comparable experimental results were available for the O-O 3rd nearest neighbour peak. However, a $\bar{\beta}$ value of 0.66 at the radial distance of 7.26 Å falls within the general trend of this parameter shown in Figure 6.5. Despite minor differences in the magnitude of $\bar{\beta}$ it can be seen that the same general trend of $\bar{\beta}$ increasing towards 1 at larger radial distances is observed within both the MD and experimental data.

Following the PDF peak analysis, examination of the atomic arrangement within the loaded MD simulations was performed. It was found that variations in atomic position were dominated by thermal vibrations and examination of the strain or angle between two individual bonds was found to be unrepresentative of the global response. Statistical measures were therefore applied in order to gain insight into the average behaviour of all simulated atoms.

Examination of the average nearest neighbour distances for Si-O, O-O and Si-Si revealed that the average strain variation was linear with applied load and had maximum values of 2.7×10^{-3}, 6.0×10^{-3} and 6.1×10^{-3} (corresponding to $\bar{\beta}$ values of $0.20, 0.44$ and 0.45) for the three bonds respectively. In the case of the O-O and Si-Si bonds these values match very closely the $\bar{\beta}$ values of 0.47 and 0.45 obtained experimentally. This would suggest that the MD simulation is capable of capturing the bond strains observed experimentally within the porcelain for these two nearest neighbours.

As previously hypothesised, in the case where macroscopic strain is larger than the equivalent atomic strain, local atomic level strain has to be accommodated by bond rotation. In order to assess the magnitude of this rotational response, critical examination of average bond angles in the Si-O-Si and O-Si-O linkages was performed. The O-Si-O bond represents the angle within the tetrahedral unit cell of silica which has previously been shown to deform little under the application of load [267]. The maximum angular variation of this bond within the MD simulation was $0.015°$. In contrast to this, examination of the Si-O-Si bond at the joining vertex of the rigid tetrahedra revealed an average bond rotation of $0.3°$ at 500 MPa, and a maximum change of $15°$ was recorded. This suggests that bond angle change between the SiO_4 tetrahedra plays a crucial role in the atomic level deformation of silica and is likely to be the origin of the reduced $\bar{\beta}$ values observed at small atomic radii.

In order to facilitate direct comparison with the stress analysis performed in the remainder of this chapter, the residual strain estimates outlined in this study were used to provide estimates of the residual stress in the porcelain veneer. The results of this conversion and further discussion of the potential origins of the cyclic variations in residual stress are outlined § 6.7.2.

6.3. X-ray Powder Diffraction

Synchrotron micro-focus X-ray powder diffraction of the YPSZ-porcelain dental prosthesis was performed on Beamline B16 at Diamond Light Source, Harwell, UK. In order to minimise sample absorption, a monochromatic 17.9 keV incident beam (just below the 18.0 keV K-edge of Zr) was selected using a double crystal monochromator. A transmission setup identical to that previously outlined in § 3.9 was used for this study. The sample was mounted onto two crossed Newport 25 mm linear translation stages in order to facilitate 2D translation in a direction perpendicular to the beam at a precision better than ± 0.1 μm. KB mirrors were used to focus the incident beam to a spot size of $2.8 \times 3\ \mu m^2$ and a Zeiss Stereo Optical Microscope was used to place the sample in the focal plane. A Photonic Science X-ray Image Star 9000 detector was placed 169 mm downstream of the sample to record 2D cross-sections of the Debye-Sherrer diffraction cones at this position and calibration of this sample to detector distance was performed using Si powder. Radiographs of the sample were captured using a Photonic Science MiniFDI X-ray eye in order to align the sample to the focused beam.

In order to generate the smooth, high intensity diffraction peaks necessary for strain quantification, an XRD exposure time of 480 seconds at each point was required. A 60 point 2.8 μm incremental line scan was performed from the near interface porcelain into the YPSZ at the position shown in Figure 6.1. A similar 60 point scan was then performed from the free surface of the YPSZ.

6.3.1. Micro-focus X-ray Diffraction Phase Mapping

Monoclinic volume fraction analysis of the diffraction data was performed by $360°$ radial integration of the 2D diffraction patterns about the beam centre. This approach reduces all of the scattering data into a single 1D distribution of intensity against scattering angle (2θ) (Figure 6.8), and thereby maximises the precision with which volume fraction can be determined.

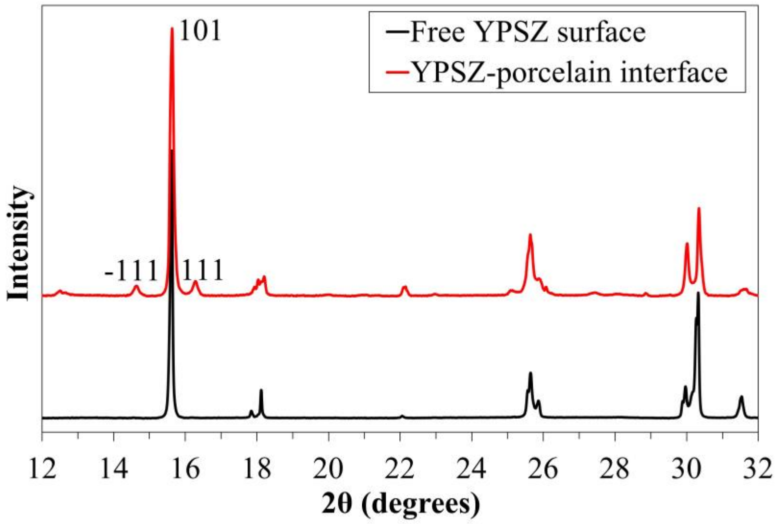

Figure 6.8. XRD intensity against scattering angle for the free YPSZ surface and the YPSZ-porcelain interface. The 101 tetragonal and the -111 and 111 monoclinic peaks are indicated.

In order to provide reliable estimates of the integrated intensity of the diffraction peaks, least square fitting of Gaussian peaks was performed using Equation 2.2. Equation 2.3 was then used to determine estimates of the integrated intensity for the tetragonal 101 (I^t_{101}), monoclinic -111 (I^m_{-111}), and monoclinic 111 (I^m_{111}) diffraction peaks. These three intensities were then used as inputs into Equation 2.4 & 2.5 in order to provide an estimate of the monoclinic volume fraction as a function of position.

The main benefit of using the Gaussian peak fitting approach, rather than the simple summation of data points on the curve, is that least squares fitting provides standard deviation estimates of the fitted parameters α and s. These in turn can be used to quantify the standard deviations of the integrated areas, the amount of monoclinic phase present and the monoclinic volume fraction. Importantly, this enables the computation of the confidence intervals of the volume fraction estimates, as shown in Figure 6.9. These estimates become particularly important at the edge of the YPSZ, where the scattering intensity is reduced, yet the steepest variation in the phase composition is observed.

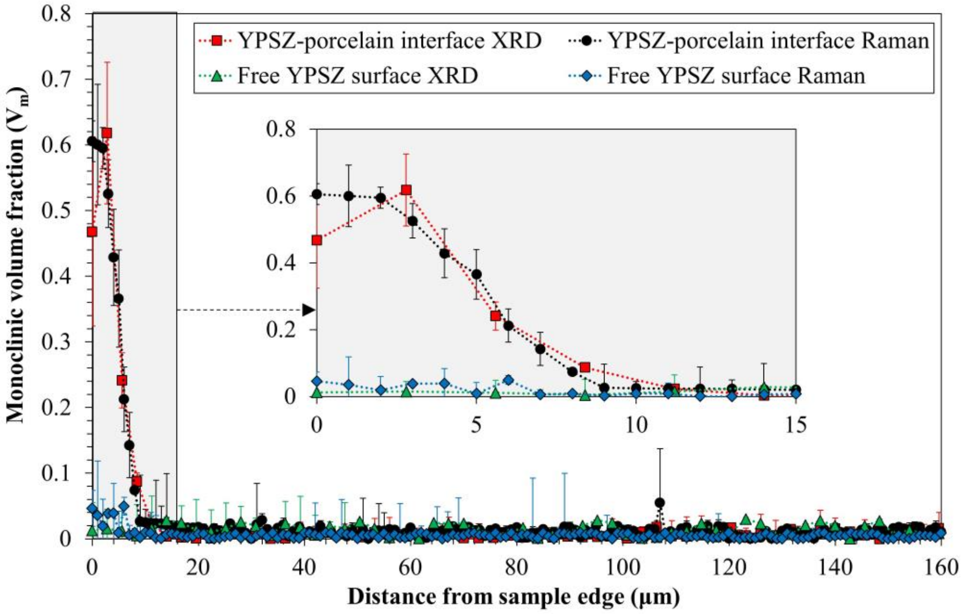

Figure 6.9. Monoclinic volume fraction as a function of distance from the YPSZ-porcelain interface and YPSZ free edge. The results of both XRD and Raman spectroscopy analysis are shown, along with the 95% confidence intervals of each data point. Graph inset shows region $0 - 15$ μm from the edge in more detail.

6.3.2. Tetragonal Lattice Strain and Stress

In recent decades, strain tensor quantification using powder XRD has become a well-established technique. It exploits the strain-induced changes in the diffraction peak positions to gain insight into lattice strain variation with the azimuthal angle (φ) [77, 155, 156], that corresponds to the in-plane strain direction. To give precise estimates of the lattice strain, this approach requires sharp, clearly defined diffraction peaks with high signal-to-noise ratios. In the case of YPSZ, the highest intensity peak is associated with the tetragonal phase, and corresponds to the reflection from the family of lattice planes with the Miller index 101, as shown in Figure 6.8. This property, in combination with the prevalence of tetragonal YPSZ at both the YPSZ-porcelain interface and the YPSZ surface, makes this the optimal choice for in-plane strain tensor analysis in this study.

A complete discussion of the in-plane strain tensor analysis previously performed on this YPSZ prosthesis has been outlined in § 3.4. Azimuthal integration of the 2D diffraction data was performed over $10°$ sectors to provide 1D profiles of average intensity against 2θ scattering angle for 36 orientations within the sample plane (normal to the incident beam). For example, the equivalent 1D profile for $0°$ orientation was obtained by integrating from $\varphi = -5°$ to $\varphi = 5°$. Gaussian peak fitting of the form shown in Equation 2.2 was next applied to determine the tetragonal 101 peak centre position as a function of azimuthal angle, $\beta^{101}(\varphi)$. Bragg's law can then be used to convert this to estimates of the tetragonal 101 lattice spacing $d^{101}(\varphi)$ which in turn can be used to estimate the tetragonal 101 lattice strain $\varepsilon^{101}(\varphi)$ through Equation 2.7. The unstrained lattice parameter used in this calculation was $d_0^{101} = 2.9586$ as outlined in § 3.4. In order to determine the principal strains (ε_1 and ε_2) and principal direction with respect to the laboratory coordinate frame (ϕ), the azimuthal variation of the 101 tetragonal lattice strain was fitted with Mohr's strain circle formulation (Equation 2.8). A weighted least square approach was used for fitting, and the standard deviation values of the azimuthal lattice strain estimates were obtained by propagation of the peak centre uncertainties through Bragg's law and Equation 2.7. This analysis provided estimates of the standard deviation of ε_1, ε_2 and ϕ.

The magnitudes of the principal in-plane residual stresses (σ_1 and σ_2) were then obtained using Hooke's law for plane stress conditions (Equations 3.20 & 3.21) and the bulk Young's modulus (210 GPa) and Poisson's ratio (0.3) for YPSZ [11].

The YPSZ-porcelain interface introduces a key geometric orientation within the system, and therefore the shear (τ) and direct stresses were resolved in directions parallel (σ_{Pa}) and perpendicular (σ_{Pe}) to the interface:

$$\sigma_{Pa,Pe} = \frac{\sigma_1 + \sigma_2}{2} \pm \frac{\sigma_1 - \sigma_2}{2} \cos 2\phi \tag{6.8}$$

$$\tau = \frac{\sigma_1 - \sigma_2}{2} \, sin\, 2\phi. \tag{6.9}$$

This analysis was performed on the XRD data collected at both the YPSZ-porcelain interface and at the YPSZ free surface as shown in Figure 6.10. Estimates of the confidence intervals of each of these stresses were obtained by propagation of the standard deviations of ε_1, ε_2 and ϕ through the analytical steps used to determine these parameters.

At this stage in the analysis it is important to recall that the residual stress estimates obtained from XRD analysis are representative of a subset of the grains within the YPSZ that have a tetragonal crystal structure. Almost everywhere within YPSZ this phase forms the majority. However, comparative analysis against other independent methods is necessary to determine if the variation obtained in this way is representative of the polycrystal average, particularly at the near interface location where the tetragonal phase forms a smaller percentage of the total composition.

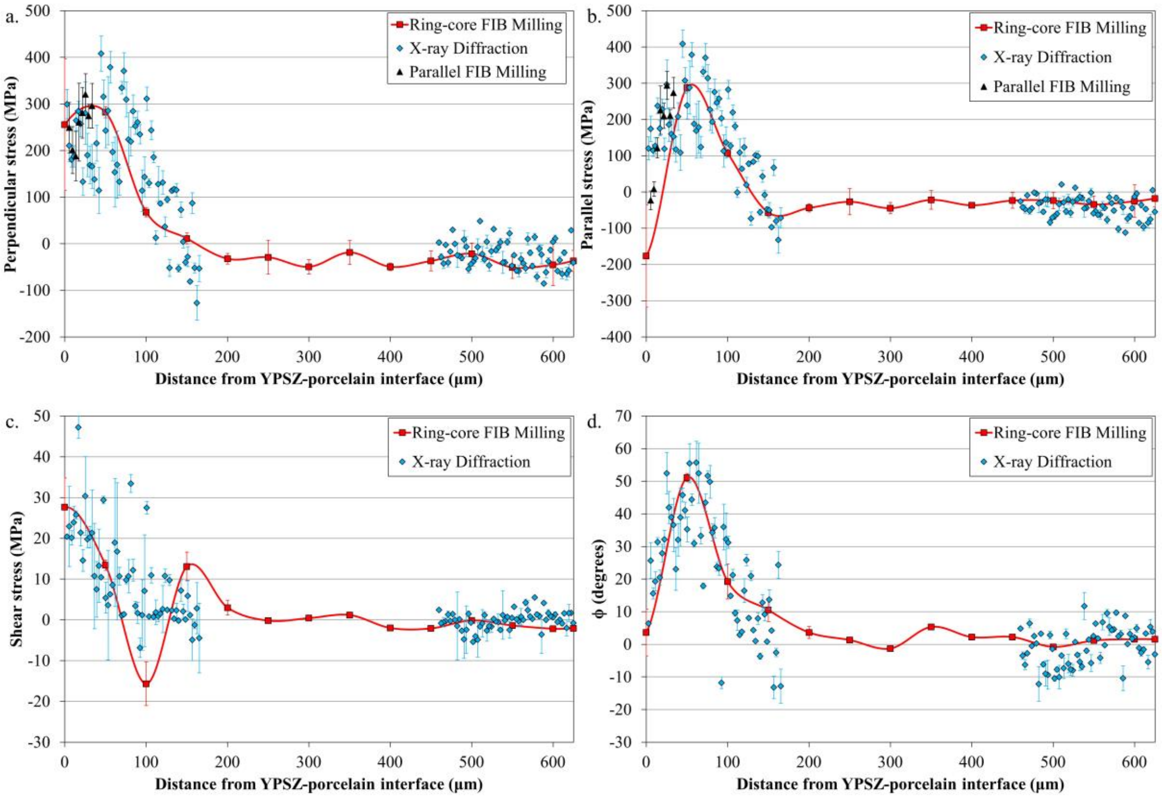

Figure 6.10. Residual stress in YPSZ as a function of distance from the YPSZ-porcelain interface. The free YPSZ edge of the sample is located at ≈ 625 μm. The results obtained from XRD, sequential ring-core FIB milling and parallel milling are included to show stresses a) perpendicular and b) parallel to the interface, as well as c) shear stresses and d) the angular offset ϕ from the principal coordinates. The 95% confidence intervals are indicated by the error bars.

6.4. Raman Spectroscopy

Raman spectroscopy was performed using the Renishaw inVia Raman confocal microscope at the Research Complex at Harwell, UK. A laser power of 15 mW, excitation frequency of 514 nm and non-polarised × 100 objective lens was used. Taking into account the magnification, the incident wavelength and any scattering phenomena, the spot size was expected to be ≈ 1 μm in diameter.

In order to align the sample to the same position within the YPSZ-porcelain cross section, the apex of the YPSZ free surface was located optically and stage translation was used to offset the sample by 3 mm. An exposure time of 120 seconds was required to produce a clear spectrum with low levels of background noise at each point. Two incremental line scans with a 1 μm step were performed on the prosthesis cross-section in order to provide direct comparison with the XRD results as shown in Figure 6.1. The first was a 170 point line scan which performed from the near interface porcelain towards the bulk YPSZ and the second was a 170 point line scan from the free surface of the YPSZ into the bulk.

6.4.1.Raman Phase Mapping

Typical Raman spectra from the free YPSZ surface and from the YPSZ-porcelain interface are shown in Figure 6.11, in which the peaks corresponding to the different phases have been indicated. As outlined in detail in § 2.2.5, the peaks appearing in Raman spectroscopy profiles are known to display a combination of Gaussian and Lorentzian character, however a Gaussian distribution is known to give a good approximation for the spectra obtained from the solid materials [92]. In the context of Raman spectroscopy, peak intensity is defined as the number of counts recorded at the peak apex [268] which is equivalent to Gaussian peak height (α) in Equation 2.2. Peak fitting was applied to determine the Raman peak intensities monoclinic peaks at $178\ \mathrm{cm}^{-1}$ and $189\ \mathrm{cm}^{-1}$, and the tetragonal peaks at $145\ \mathrm{cm}^{-1}$ and $260\ \mathrm{cm}^{-1}$. These intensities were then used as inputs into Equation 2.15 in order to determine estimates of the monoclinic volume fraction [93].

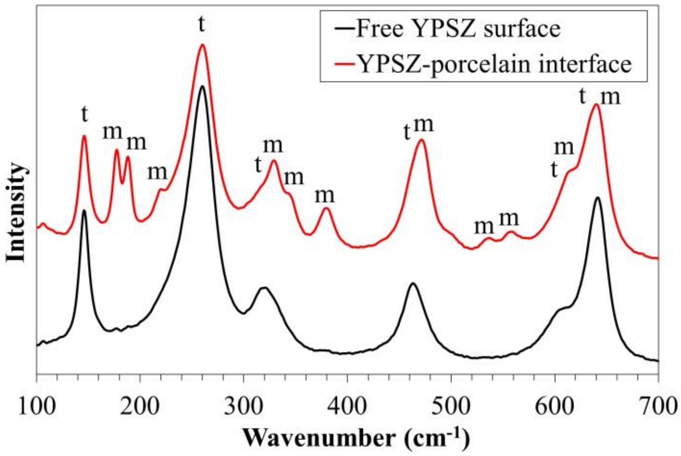

Figure 6.11. Raman wavenumber against intensity at the free YPSZ surface and the YPSZ-porcelain interface. The monoclinic and tetragonal peaks have been indicated.

Similar to the results of XRD analysis, reductions in the Raman spectrum intensity were observed at the YPSZ edge, where the largest monoclinic volume fractions were observed and reliable confidence intervals were most needed. The standard deviation of the peak heights were combined in accordance with Equation 2.15 to provide estimates of the 95% confidence intervals for V_m, as shown in Figure 6.9.

6.4.2.Raman Peak Shift Analysis

As outlined in § 2.2.5, the relationship between Raman peak centre position and residual stress is well-established and has been the focus of several dedicated research articles [94, 268]. In the case of YPSZ it has recently been shown that the trace of the stress tensor demonstrates the strongest correlation with Raman peak centre positions [94]. The relationships between peak centre position and the sum of the three principal stress values can therefore be used as method of validating the stress estimates obtained from the tetragonal lattice 101 reflection analysis. Importantly, this approach is independent of the crystal orientation and is representative of the average behaviour within the entire family of tetragonal grains. The absence of monoclinic peaks in the majority of the spectra prevented reliable stress quantification from being performed in this phase.

In order to determine the most suitable peaks for peak centre analysis, the distribution of peaks in Figure 6.11 was used. Five distinct peaks can be observed within the tetragonal spectrum corresponding to wavenumbers of $145\ \mathrm{cm}^{-1}, 260\ \mathrm{cm}^{-1}, 318\ \mathrm{cm}^{-1}, 461\ \mathrm{cm}^{-1}$ and $\approx 630\ \mathrm{cm}^{-1}$. This latter peak is a convolution of three peaks at $605\ \mathrm{cm}^{-1}, 635\ \mathrm{cm}^{-1}$ and $641\ \mathrm{cm}^{-1}$ which were found to have different peak shift responses under stress application [268]. This presents difficulties in reliable peak fitting, and therefore the peak cluster around $\approx 630\ \mathrm{cm}^{-1}$ was not analysed further. The former four peaks were found to yield effective measures of peak centre shift under stress within bulk YPSZ. However, the presence of monoclinic phase in the near-interface region resulted in peak overlap and led to difficulties in reliable peak fitting for the $318\ \mathrm{cm}^{-1}$ and $461\ \mathrm{cm}^{-1}$ tetragonal peaks (due to the $304\ \mathrm{cm}^{-1}$ and $479\ \mathrm{cm}^{-1}$ monoclinic peaks, respectively). Gaussian peak fitting was therefore performed only for the tetragonal peaks at $145\ \mathrm{cm}^{-1}$ and $260\ \mathrm{cm}^{-1}$ to obtain estimates of the peak centre position and the associated confidence interval at each position.

In order to provide approximate estimates of the first stress invariant, the in-plane principal stresses obtained by XRD at each location were used. This approach intrinsically assumes that within the Raman spectroscopy gauge volume, the out of plane stress component is much smaller than the in-plane stresses. Linear interpolation was next applied to the sum of the principal XRD stress values in order to derive estimates of this value at each of the Raman measurement locations (since XRD and Raman spectroscopy were performed at different distinct points).

The relationship between peak centre position and XRD first stress invariant was found to be approximately linear for both the $145\ \mathrm{cm}^{-1}$ and $260\ \mathrm{cm}^{-1}$ peaks. Total least squares fitting was applied to determine the gradient (Π) and axis intercept (ω) of this data as shown in Figure 6.12. The uncertainties associated with both measurements were accommodated by using the inverse standard deviation as a weighting factor. The results of this analysis are shown in Table 6.3, along with equivalent literature values obtained for a similar composition of YPSZ [268].

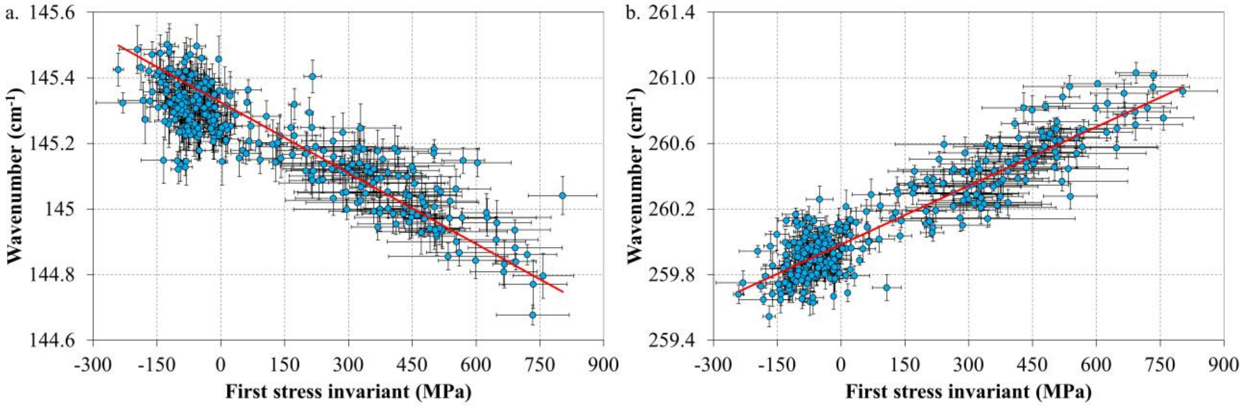

Figure 6.12. Raman peak centre vs interpolated XRD first stress invariant for the tetragonal Raman peaks with nominal peak centres of a) $145\ \mathrm{cm}^{-1}$ and b) $260\ \mathrm{cm}^{-1}$. The 95% confidence intervals of each data point are indicated by the error bars and the results of total linear least squares fitting are shown in red.

Table 6.3. Axis intercept (ω), gradient (Π) and correlation coefficient (R^2) of the relationship between Raman peak centre and first stress invariant for the tetragonal Raman peaks at nominal peak centres of $145\ \mathrm{cm}^{-1}$ and $260\ \mathrm{cm}^{-1}$. Independent literature values obtained by Pezzotti et al. [268] have been included for comparison.

Source	ω (cm^{-1})	Π $(\mathrm{cm}^{-1}/\ \mathrm{GPa})$	R^2
This study	145.28 ± 0.01	-0.58 ± 0.01	0.77
	259.98 ± 0.01	1.19 ± 0.02	0.84
Pezzotti et al. [268]	144.68	−0.6	0.95
	259.57	1.1	0.76

6.5. Sequential and Parallel FIB Milling and DIC

FIB milling for comparative residual stress analysis was performed using the Tescan Lyra 3XM FIB-SEM at MBLEM, Oxford, UK. In order to reduce the impact of charging during SEM imaging and FIB milling, a 5 nm coat of Au/Pd was sputtered onto the prosthesis cross section. A working distance of 9 mm, SEM beam voltage of 5 keV, FIB beam energy of 30 keV and ion current of 750 pA was used for both the sequential and parallel FIB milling. In order to improve the surface contrast and thereby facilitate improved DIC, a single pass of the FIB was applied to the sample surface prior to milling. Tilt corrected SEM imaging was used in this study using the same approach that has been successfully employed in other investigations [106, 269].

The location of the sequential FIB milling was determined by placing the sample in the orientation shown in Figure 6.1, locating the apex of YPSZ free surface and then shifting the sample. The parallel FIB milling approach was then implemented at an offset of 75 μm from the sequential analysis as shown in Figure 6.1. This distance was selected as a balance between reducing the effect of stress relief induced by previous milling, and measuring residual stress states which were directly comparable.

6.5.1.Sequential Ring-core FIST Analysis

The analysis stages necessary to perform FIST ring-core FIB milling and DIC full strain tensor analysis are outlined in detail in § 3.4. This approach is based on determining the angular variation of strain relief in the core by repeated implementation of the strain quantification routine originally pioneered by Korsunsky et al. [64]. In the analysis presented here, correlation coefficient thresholding was performed at 0.5, standard deviation thresholding was performed for markers with this parameter greater than 1.5 times the average, and the removal of outliers to the expected displacement field was performed for offsets greater than 1.5 times the average.

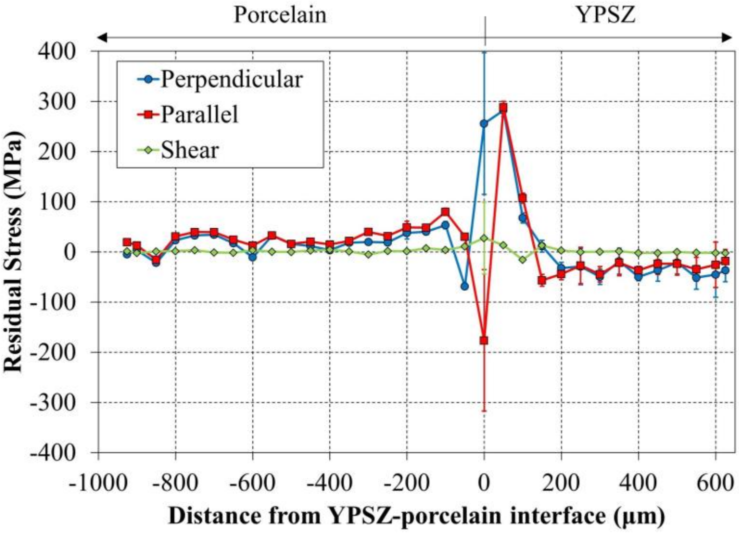

Figure 6.13. Sequential ring-core residual stress variation across YPSZ and porcelain. Stresses have been resolved in directions parallel and perpendicular to the YPSZ-porcelain interface and the error bars indicate 95% confidence intervals.

The profiles of strain relief against milling depth (or image number) resulting from this strain quantification routine were then used to provide estimates of the average residual strain (in a given direction) which was originally present within the core. This analysis was repeated in order to determine the residual strain variation as a function of angle within the plane of the sample (in increments of 10°). These distributions were then fitted with the $\cos 2\varphi$ variation given in Equation 2.8 in order to determine the principal residual strains and orientations. Hooke's law was then used to determine the principal stresses using plane stress approximations and the appropriate Young's modulus and Poisson's ratios. In order to extract comparable results, these stresses were then resolved in the directions parallel and perpendicular to the interface to determine the direct and shear stress components in each case (Equations 6.8 and 6.9), as shown in Figures 6.10 & 6.13.

To provide reliable confidence interval estimates for the residual stress and orientation estimates obtained from this analysis, careful error propagation was performed throughout the entire analytical procedure using the approach outlined in § 3.3. The only variables taken as absolute measures were Young's modulus and Poisson's ratio for both materials, since no confidence intervals were known for these parameters.

Some difficulties were encountered in the analysis of the bi-material ring-core marker milled directly at the YPSZ-porcelain interface. The FIB milling rates of YPSZ and porcelain are known to differ, which resulted in a non-uniform trench depth around the central core. This effect, combined with the differences in mechanical properties and the stress states within the two materials induced relief which was not fully represented by the single value strain tensor analysis outlined above. Despite these differences, the use of an average Young's modulus and Poisson's ratio (of YPSZ and porcelain) appears to give reasonable results, albeit with large uncertainty intervals, as shown in Figures 6.10 & 6.13.

6.5.2. Parallel FIB Milling

Parallel FIB milling analysis was carried out in a region lying 75 μm along the interface relative to the sequential milling area in order to reduce the impact of any relaxation from previous milling, as shown in Figure 6.1. The location of milling relative to the YPSZ-porcelain interface was intended to capture the response of the near interface region, where XRD stress analysis was thought to be least reliable. However, in order to prevent the problems encountered during the analysis of the bi-material ring-core milling data point, the parallel milling geometry was offset by 3 μm from the interface.

The close proximity, bloc type milling performed during the parallel FIB milling approach presents challenges in applying full in-plane strain tensor analysis routines. It is also worth noting that the islands, associated with this technique no longer possess the circular symmetry that is necessary for this analysis. Therefore, residual stress analysis was only performed in directions parallel and perpendicular to the YPSZ-porcelain interface during this study. Analysis of each of the cores was performed incrementally by digitally positioning markers and running automated DIC analysis of the sequence of SEM images collected [110]. The same outlier removal parameters were used as those implemented in the sequential analysis in order to leave only well tracked markers in the least squares fitting of strain relief.

The presence of neighbouring markers was found to influence the strain relief against milling depth curves obtained during this analysis in a similar manner that had previously been observed during other studies (Figure 3.24) [112, 121]. Clear plateaus were observed in all strain relief distributions, indicating that milling had been performed to a depth sufficient to induce full strain relief. Therefore, least squares fitting of the finite element ‘master curve’ published by Korsunsky [137] was used to determine $\Delta\varepsilon_{\infty}$.

This analysis was performed on all eight measurement points in order to obtain residual stress estimates in directions parallel and perpendicular to the interface at each location. The results of both XRD and sequential ring-core milling indicate that the principal strain orientations are not aligned with these directions. However, in order to provide comparable measures, this approximation was used to determine estimates of residual stress in directions parallel and perpendicular to the interface using Hooke’s law for plane stress conditions. The results of this analysis are shown in Figures 6.10 & 6.14.

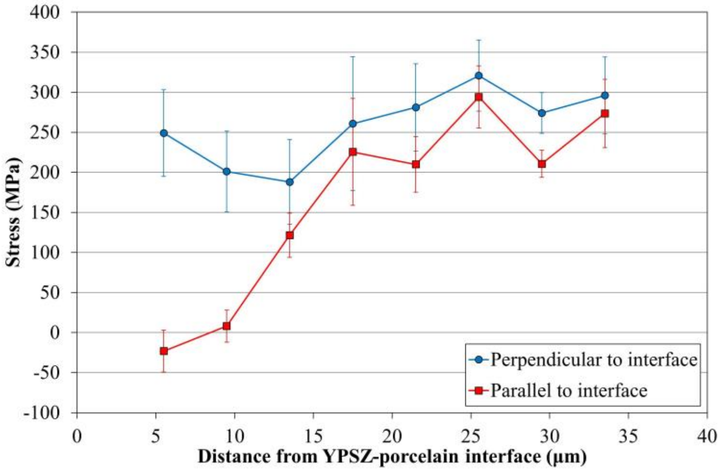

Figure 6.14. Residual stress variation against distance from the interface obtained using parallel FIB milling and DIC analysis.

The same error quantification and propagation procedures as those outlined in § 6.5.1 were performed during the parallel FIB milling analysis. However, the increased presence of noise generally led to increased uncertainty in the values obtained, as shown in Figure 6.14.

6.6. Residual Stress Modelling

FE modelling offers an effective and efficient approach to simulate various loading conditions and deformation characteristics, provided that reliable estimates of the mechanical properties of a component or system are known. Despite the many benefits associated with this approach, strength analysis using simulations of this kind presents a greater challenge, since these parameters depend greatly the on the microstructure and residual stress state induced by the processing routes applied. One approach which has previously been used to overcome this difficulty has been the integration of analytical residual stress distributions into FE simulations using an eigenstrain (equivalent plastic strain) distribution approach [270]. In order to facilitate future integration of these profiles into existing prosthesis simulations, in this section I present simple analytical solutions that aim to capture key aspects of the residual stress state at the YPSZ-porcelain interface.

The analysis presented in this section is focused on the residual stress component within YPSZ in the direction parallel to the interface and at two distinct length scales. Firstly, the global ('macro-scale') stress distribution across the entire coping has been decomposed into two key effects: CTE mismatch between YPSZ and porcelain that arises as a consequence of veneering (in § 6.6.1), and the residual stress induced by the temperature variation across the coping during YPSZ sintering (in § 6.6.2). The micro-scale residual stresses induced by the phase transformation at the YPSZ-porcelain interface are then modelled using eigenstrain gradient transformation plasticity (in § 6.6.3). Reassembly of these effects provides a satisfactory match to the experimental distribution observed, and facilitates quantitative assessment of the parameters associated with these different sources of residual stress.

6.6.1. Coefficient of Thermal Expansion Mismatch

Analytical modelling of the residual stress distribution at the YPSZ-porcelain interface has previously been performed by approximating the system by a bi-material strip [271-273]. This analysis can capture the linear variation of strain induced in both YPSZ and porcelain by the CTE mismatch which results in tensile near-interface stress in YPSZ and compressive in porcelain.

In the analysis that follows a simple bending model [274] has been used to determine the residual stress distribution in both materials as a function of the normal distance from the interface (x). Complete expressions for the stress profiles have previously been presented in the literature [275] and demonstrate that these are dependent upon the thickness of YPSZ ($L_Z = 625$ µm) and porcelain ($L_P = 925$ µm), the CTE's of the two materials (as outlined in § 1.2) and the post sintering temperature change $(750℃ \rightarrow 25℃)$. The required estimates of the elastic modulus of YPSZ $\left(E_Z^{Eff}\right)$ and porcelain $\left(E_P^{Eff}\right)$ can be represented well by the plane strain expressions:

$$E_Z^{Eff} = \frac{E_Z}{(1+\nu_Z)(1-2\nu_Z)} = 404\ \text{GPa}, \tag{6.10}$$

$$E_P^{Eff} = \frac{E_P}{(1+\nu_P)(1-2\nu_P)} = 96\ \text{GPa}. \tag{6.11}$$

The linearly varying residual stress distributions resulting from this analysis are shown in Figure 6.15 in which the near interface YPSZ is in tension (of ≈ 110 MPa) and the near interface porcelain is in a state of mild compression (of ≈ -30 MPa). These distributions do not match those observed experimentally (Figure 6.10b) and suggest that other factors are influencing the residual stress state at the interface. In the case of YPSZ, sintering is known to induce macro-scale variations in residual stress that are present in addition to the CTE mismatch. In porcelain, this is associated with the layering routine applied to the YPSZ coping which will not be considered in more detail here.

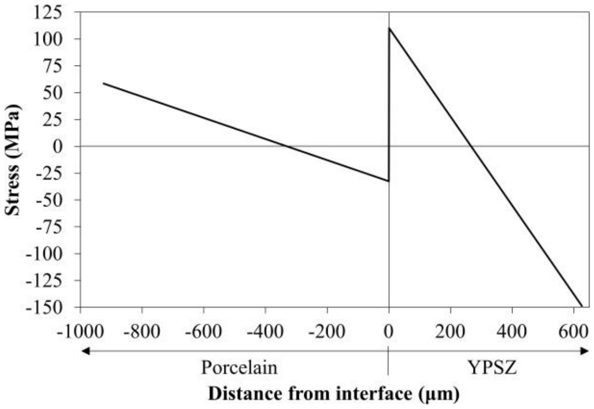

Figure 6.15. Stress variation across the YPSZ-porcelain interface predicted by CTE mismatch.

6.6.2. YPSZ Sintering Stresses

As outlined in § 1.1, during the manufacture of the coping, the machined YPSZ lightly pre-sintered green body is placed into a furnace and heated to $1600°\text{C}$ to sinter the component. This process is associated with a $\approx 20\%$ shrinkage (densification) of the YPSZ at a critical densification temperature T_D which is dependent upon the YPSZ grain size and elemental composition [276, 277]. This structural change is associated with a large increase in strength and fracture toughness [41].

Although sintering is typically performed using a slow heating rate, the extremely low thermal diffusivity of YPSZ ($D = 2.2 \times 10^{-7}\text{m}^2\text{s}^{-1}$ [278]) results in temperature gradients between the surface of the coping and the core. Consequently complete sintering and shrinkage do not occur uniformly across the YPSZ. This results in strain mismatch and induces a residual stress that varies with time and temperature according to the solution of the transient thermal conduction equation. Previous studies have demonstrated that the residual stress distribution that arises in this kind of sintering operation is near parabolic in profile [279], with compressive stresses in the core, and tensile stresses in the near-surface region. The magnitude of this residual stress distribution in YPSZ is particularly sensitive to the cooling rate applied, and sintering fracture can be induced by high heating or cooling rates [280].

In order to understand the distribution of residual stress within the coping, consideration must first be given to the temperature distribution within the cross section, $T(x,t)$, as a function of position (x) and time (t). This variation can be determined from the solution of the 1D heat conduction equation:

$$\frac{\partial T(x,t)}{\partial T} = D\frac{\partial^2 T(x,t)}{\partial x^2}. \tag{6.12}$$

Separation of variables and Fourier series representation can be used to solve this equation using the appropriate boundary conditions. This approach has been covered in detail in the literature [281].

In order to gain insight into the likely temperature distribution induced within the coping cross section during sintering, one of the simplest solutions that can be exploited is based on an instantaneous temperature rise. This analysis starts by holding the prosthesis at $25°\text{C}$ and then imposing boundary conditions at $1600°\text{C}$ at either surface (i.e. $\Delta T = 1575°\text{C}$) and has the solution:

$$T(x,t) = 1600 - \sum_{m=1}^{\infty} \frac{4\Delta T}{(2m-1)\pi} e^{-tD\left(\frac{(2m-1)\pi}{L_Z}\right)^2} \sin(2m-1)\frac{\pi x}{L_Z}. \tag{6.13}$$

The temperature profiles at different time intervals are shown in Figure 6.16. This plot demonstrates that after a short time period (≈ 5 s), the temperature distribution is well approximated by a sine curve with a magnitude equal to the difference between the external temperature and the central temperature. In the case of a reduced heating rate, a similar sinusoidal distribution is expected but with a magnitude dependent upon the heating rate applied.

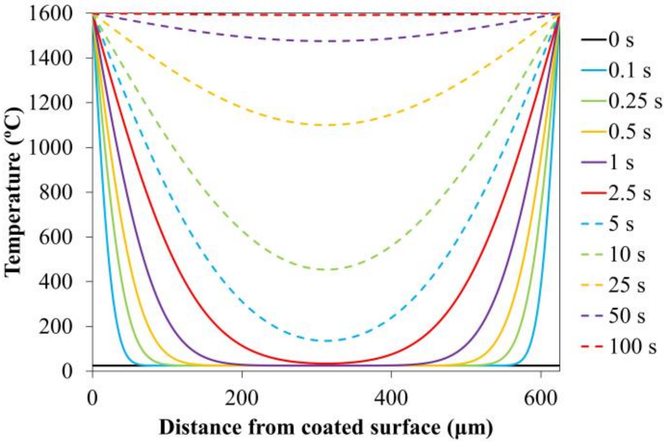

Figure 6.16. Temperature distributions within the YPSZ coping as a function of time after an instantaneous temperature increase at the boundaries to $1600°\text{C}$.

Having established the nominal sintering temperature distribution profile within the coping, the relationship between residual stress (or rather, the underlying eigenstrain) and this distribution needs to be established. In materials with a distinct mechanical property transition temperature, one of the simplest and most effective approaches which can be exploited to determine this relationship is the *instant freeze model* pioneered by Indenbom [282]. This approach is based on separating the total strain $\varepsilon^T(x)$ into three additive components, elastic strain $\varepsilon^E(x)$, viscous train $\varepsilon^V(x)$ and thermal strain $\varepsilon^H(x)$:

$$\varepsilon^T(x) = \varepsilon^E(x) + \varepsilon^V(x) + \varepsilon^H(x). \tag{6.14}$$

It is presumed that on one side of the transition temperature (below in the case of sintering) the material does not sustain any elastic strain (and therefore that stress is zero). At the critical densification temperature T_D the strain component within the green body is 'frozen in' permanently. This effective viscous strain is subsequently referred to as eigenstrain $\varepsilon^*(x)$, and is the source of residual stress within the component. Since heating continues in the component, densification proceeds from either surface until this front reaches the centre of the body and the entire component is at a temperature above T_D. The eigenstrain distribution is then fixed and the final residual stress state at room temperature arises from the interplay between this distribution and the changing thermal and elastic strains.

One study which has recently used this approach to great effect has been an analysis of thermal tempering of bulk metallic glass plates [283] in which similar trigonometric temperature distributions are observed. The principal difference between the results of this approach and those presented here, is that an increase in strength and stiffness is observed during cooling below the glass transition temperature in that study, whereas in the situation considered in this thesis an increase in strength observed when heating above T_D. With this distinction accounted for, the analysis presented in this study can be used by simply changing the sign of the eigenstrain distribution. The resulting stress distribution has the form:

$$\sigma(x) = \alpha_Z E_Z^{Eff} T(x, t_D) + \sigma_{Bal}, \tag{6.15}$$

where σ_{Bal} is the term required to ensure that stress distribution is in equilibrium across the plate cross section i.e. $\int_0^{L_Z} \sigma(x)dx = 0$ and t_D is the time at which full densification occurs, i.e. when the minimum temperature in the cross section is equal to T_D. Since both T_D and the external temperature at a time t_D are unknown, a trigonometric approximation of the form:

$$\sigma(x) = -\alpha_Z E_Z^{Eff} \Lambda \sin\frac{\pi x}{L_Z} + \sigma_{Bal}, \tag{6.16}$$

can instead be used, where Λ is the difference between the external temperature and T_D at a time t_D. In order to determine a numerical estimate of this parameter, comparison between the experimental and analytical residual stress profiles can be used. This process requires the addition of the linear residual stress distribution resulting from CTE mismatch to provide estimates of the total macroscopic stress distribution as shown in Figure 6.17.

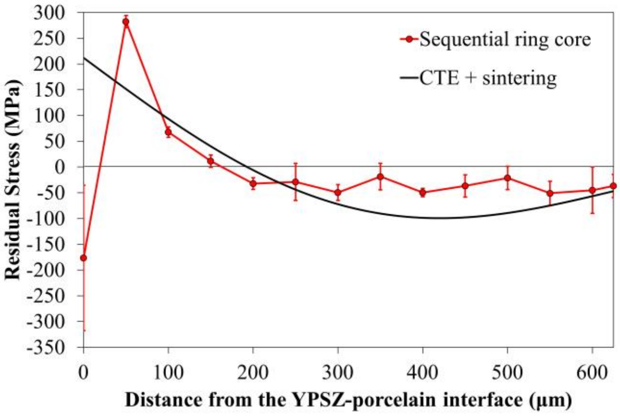

Figure 6.17. Residual stress as a function of distance from the YPSZ-porcelain interface. The experimental results obtained through sequential ring-core milling (markers) and the predicted analytical distribution based on the combination of CTE mismatch and sintering are shown.

The fitted value of Λ was found to be 38 K, and the resulting stress profile was found to show a satisfactory match with the experimental results for most of the coping cross section. The largest deviation between these two profiles is observed at the YPSZ-porcelain interface, at the location where the tetragonal to monoclinic phase transformation is known to have been induced. This suggests that the volume expansion associated with the phase transformation has influenced the residual stress state at this location. Due to the importance of this effect for understanding the root cause of chipping failure, further modelling of this behaviour is presented in § 6.6.3. Some discrepancy is also observed at the points 50 µm and $350 - 500$ µm from the interface, indicating that the profile sharpness has not been fully captured by the two residual stress sources considered in this analysis.

6.6.3. Transformation Boundary Layer Modelling

The limited experimental insight available into the location and extent of the tetragonal to monoclinic phase transformation has previously prevented this effect from being included in the analysis of residual stress at the YPSZ-porcelain interface. The principal difficulty has been the fact that the related phenomena play out at extremely short length scales. I believe that the refined experimental approaches for system characterisation that I developed and applied to the YPSZ-porcelain system were necessary to elucidate this behaviour. The present subsection is devoted to the derivation of the boundary layer model for the transformation-induced inelastic strain (eigenstrain) that allows comparison with the V_m distributions obtained experimentally. These results can then be combined with those presented in § 6.6.1 and § 6.6.2 to provide a model prediction for complete residual stress state in YPSZ.

As shown in Figure 6.17, the CTE mismatch and sintering residual stress generation approach fails to predict the very steep stress gradients observed at the YPSZ-porcelain interface. In fact, these high magnitude localised stresses are similar to those observed at crack tips [4], which have previously been shown to be sufficient to induce the tetragonal to monoclinic phase transformation. The atomic rearrangement associated with the phase change is diffusionless and is therefore equivalent to inelastic stress-free straining, which can be simulated through the use of eigenstrain [284]. The magnitude of the eigenstrain distribution can be considered to be equivalent to the extent of transformation at a given position and can therefore be used to link the phase transformation to the mechanical state.

In this section I present the boundary layer solution for the 1D distribution of stress and strain component parallel to the YPSZ-porcelain interface that is described as a function of normal distance (x) within the narrow band of material where the steep stress gradient is present. An estimate of the total strain (here meaning the sum of elastic strain and eigenstrain) within YPSZ at the interface (ε_0^T) based on the CTE mismatch cooling from $750\ ℃ \rightarrow 25℃$ is given as:

$$\varepsilon_0^T = \varepsilon^T(0) = (\alpha_{Zir} - \alpha_{Por})(750 - 25) = 1.09\ \times 10^{-3}. \qquad (6.17)$$

Critical examination of Figure 6.17 indicates that the analytical macroscale residual stress estimate at the interface is ≈ 210 MPa. However, due to the activation of phase transformation the actual residual stress measured at this location is compressive and, due to scatter, has a magnitude in the range $25 - 175$ MPa. The average value of this stress is ≈ -100 MPa. Therefore the stress change induced by the tetragonal to monoclinic phase transformation at the interface can be approximated as 310 MPa. By way of estimate, this corresponds to an eigenstrain value of $\varepsilon^*(0) \approx 7.7\ \times 10^{-4}$.

Using the approximations outlined above, the form of the expected eigenstrain $\varepsilon^*(x)$ profile can be determined from energy considerations and variational calculus. In this analysis, total strain is equal to the sum of elastic strain and eigenstrain. The elastic strain energy is therefore given as:

$$U^E = \frac{1}{2}E_{eff}\int_0^L [\varepsilon^E(x)]^2 dx = \frac{1}{2}E_{eff}\int_0^L [\varepsilon^T(x) - \varepsilon^*(x)]^2 dx, \qquad (6.18)$$

where L is the width of the region of interest (boundary layer). In addition to this elastic expression, two further energy terms need to be considered. The first is associated with the energy reduction induced by strain gradient plasticity [285] given by:

$$U^{SG} = \frac{1}{2} E_{eff} \int_0^L \left[\frac{d\varepsilon^*}{dx}\right]^2 \ell^2 dx = \frac{1}{2} E_{eff} \int_0^L \varepsilon_{,x}^{*}{}^2 \ell^2 dx, \tag{6.19}$$

where ℓ is the strain gradient material length scale [286] and $\varepsilon_{,x}^*(x)$ is the rate of change of eigenstrain as a function of position x. The origin of this energy penalty lies in the fact that the deformation of solid material volumes that are closely neighbouring at the micron-scale cannot be entirely independent: sharp transitions become ‘blurred’ into local gradients. The total energy of the system is therefore not simply the sum of contributions from sub-volumes, but also depends upon the steepness of transition (strain gradient) between them. In the present treatment, eigenstrain gradient plays a role similar to the plastic strain gradient in the Fleck and Hutchinson strain gradient plasticity theory [286].

The second energy term is the Gibbs free energy reduction due to the phase transformation:

$$U^{Tr} = \frac{1}{2} E_{eff} \int_0^L [\varepsilon^*(x)]^2 \Gamma dx, \tag{6.20}$$

where Γ is the coefficient which relates the square of the eigenstrain to the amount of energy required to induce the phase transformation per unit volume.

These expressions can be combined to give an expression for the total energy:

$$U^T = U^E - U^{SG} - U^{Tr} = \frac{E_{eff}}{2} \int_0^L \left[\left(\varepsilon^T(x) - \varepsilon^*(x)\right)^2 - \ell^2\left(\varepsilon_{,x}^*(x)\right)^2 - (\varepsilon^*(x))^2\Gamma\right] dx. \tag{6.21}$$

Rearrangement gives:

$$U^T = E_{eff} \int_0^L \left[\frac{1}{2}\left(\varepsilon^T(x)\right)^2 - \varepsilon^*(x)\varepsilon^T(x) + \frac{1}{2}(1-\Gamma)(\varepsilon^*(x))^2 - \frac{1}{2}\ell^2\left(\varepsilon_{,x}^*(x)\right)^2\right] dx. \tag{6.22}$$

In order to minimise the total energy, the derivative of U^T must be set equal to zero, such that:

$$\delta U^T = \frac{dU^T}{d\varepsilon^*}\delta\varepsilon^* = 0. \tag{6.23}$$

Therefore:

$$\delta U^T = 0 = E_{eff} \int_0^L [-\varepsilon^T(x) + (1-\Gamma)\varepsilon^*(x)]\delta\varepsilon^* dx - E_{eff} \int_0^L \ell^2 \varepsilon_{,x}^*(x)\delta\varepsilon_{,x}^* dx. \tag{6.24}$$

In order to remove $\delta\varepsilon_{,x}^*$ from this expression, integration by parts can be applied to the 2nd integral:

$$\int_0^L \ell^2 \varepsilon_{,x}^*(x)\delta\varepsilon_{,x}^* dx = \left[\varepsilon_{,x}^*(x)\delta\varepsilon_{,x}^*\right]_0^L - \int_0^L \ell^2 \varepsilon_{,xx}^*(x)\delta\varepsilon^* dx, \tag{6.25}$$

where $\varepsilon^*_{,xx}(x)$ is the second derivative of eigenstrain with respect to x. In order to ensure that U^T is a minimum for any value of $\delta\varepsilon^*$, the term associated with limit substitution must equal zero. This results in the so-called ‘natural’ boundary conditions of $\varepsilon^*_{,x}(L) = \varepsilon^*_{,x}(0) = 0$. Back substitution then gives:

$$0 = E_{eff} \int_0^L \left[-\varepsilon^T(x) + (1 - \Gamma)\varepsilon^*(x) + \ell^2 \varepsilon^*_{,xx}(x)\right] d\varepsilon^* dx. \tag{6.26}$$

Since $\delta\varepsilon^*$ can take any value, this expression is only guaranteed to be true when the expression in the square brackets is equal to zero. This results in the Euler differential equation for this system:

$$\varepsilon^*_{,xx}(x) + \frac{(1 - \Gamma)}{\ell^2} \varepsilon^*(x) = \frac{1}{\ell^2} \varepsilon^T(x). \tag{6.27}$$

This equation has the complementary function solution:

$$\varepsilon^*_{CF}(x) = Ae^{-\omega x} + Be^{\omega x}, \tag{6.28}$$

where A and B are constants to be found, and $\omega^2 = (\Gamma - 1)/\ell^2$.

In order to determine the particular integral for the Euler equation, the form of the total strain distribution needs to be considered. Within the thin (≈ 10 µm) boundary layer the total strain variation can be approximated as linear, with the interface strain equal to that derived in Equation 6.17. Therefore it is possible to write:

$$\varepsilon^*_{PI}(x) = \frac{\varepsilon^T_0 + Cx}{1 - \Gamma}, \tag{6.29}$$

where C is another unknown constant to be found. In order to determine the expressions for A, B and C, the ‘natural’ boundary conditions can be used, along with the fact that the phase transformation at L is expected to be zero, i.e. $\varepsilon^*(L) = 0$. The resulting eigenstrain distribution is given by:

$$\varepsilon^*(x) = \frac{\varepsilon^T_0}{1 - \Gamma}\left[1 + \frac{\left(1 - e^{\omega L}\right)e^{-\omega x} + \left(1 - e^{-\omega L}\right)e^{\omega x} + \omega x\left(e^{-\omega L} - e^{\omega L}\right)}{2 - e^{-\omega L} - e^{\omega L} - \omega L(e^{-\omega L} - e^{\omega L})}\right]. \tag{6.30}$$

This expression can then be simplified using the hyperbolic functions $\sinh(x)$ and $\cosh(x)$:

$$\varepsilon^*(x) = \frac{\varepsilon^T_0}{1 - \Gamma}\left[1 - \frac{\sinh \omega\left(\frac{L}{2} - x\right) + \omega x \cosh\frac{\omega L}{2}}{\omega L \cosh\frac{\omega L}{2} - \sinh\frac{\omega L}{2}}\right]. \tag{6.31}$$

In order to obtain estimates of L, Γ and ℓ, this expression can then be compared to the monoclinic phase variation determined experimentally as shown in Figure 6.18. This fitting process also requires the estimate of the interface eigenstrain to be incorporated, $\varepsilon^*(0) \approx 7.7 \times 10^{-4}$. The optimum values of the system parameters were found to be $L = 10.7 \pm 0.3$ µm, $\Gamma = 1.55 \pm 0.06$ and $\ell = 2.88 \pm 0.15$ µm.

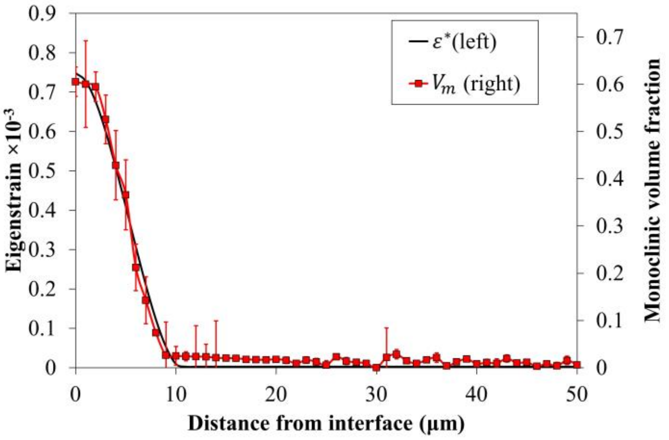

Figure 6.18. Comparison between the analytical eigenstrain distribution (left) and monoclinic volume fraction determined using Raman spectroscopy (right).

The similarity observed between the shape of the analytically derived eigenstrain distribution and Raman spectroscopy experimental results suggests that the present energy minimisation approach for the description of eigenstrain gradient transformation plasticity boundary layer appears to capture some of the features of the near-interface region. Despite this encouraging resemblance, this analysis represents a first attempt to understand this behaviour and there remains uncertainty over whether the material response is correctly captured by this approach. One further comparison can be drawn by combining the eigenstrain variation with the macro-scale formulation of the stress state within the prosthesis to match the overall state in the coping as shown in Figure 6.19.

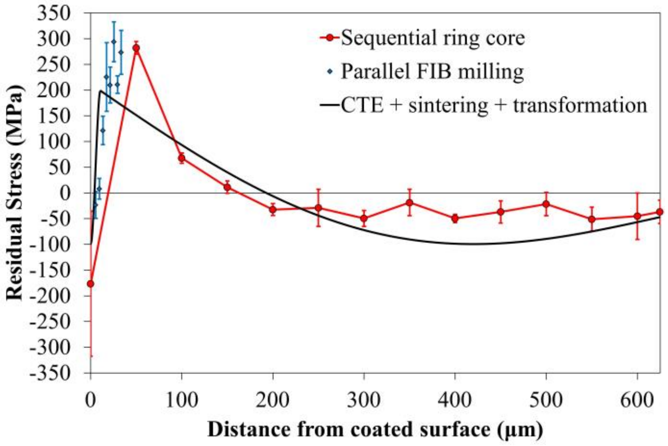

Figure 6.19. Residual stress as a function of distance from the YPSZ-porcelain interface. The experimental results obtained through FIB milling are shown with the complete analytical solution.

6.7. Discussion

6.7.1. Monoclinic YPSZ Phase Distribution

The results of XRD phase mapping near the YPSZ-porcelain interface reveals a high concentration ($\approx 40 - 60\%$) of monoclinic YPSZ within the first 2.8 μm of the interface. At further distances from the interface, the monoclinic volume fraction reduces until purely tetragonal YPSZ is observed at distances greater than ≈ 11 μm.

Within this study, the position of the YPSZ-porcelain interface was defined by the first diffraction pattern in which the YPSZ XRD peaks could be reliably fitted. Some evidence for very weak diffraction peaks was observed in the porcelain diffraction pattern collected at a nominal position of -2.8 μm from the interface, indicating that the precision of this alignment is only accurate to this step size.

It is important to note that there was no evidence for tetragonal YPSZ at the free surface of YPSZ. The transition from epoxy to YPSZ was also more distinct than that observed at the YPSZ-porcelain interface (with a single increment between no YPSZ diffraction and clear peaks), indicating that this interface was either sharper or more closely aligned to the incoming beam.

Raman spectroscopy phase analysis of the YPSZ-porcelain interface demonstrates a monoclinic volume fraction distribution which is very similar to the results obtained through XRD. Three points with approximately 60% monoclinic phase were observed within the first 3 μm of the interface followed by a reduction in concentration over the next 7 μm towards a purely tetragonal phase state. Increased noise was identified within the data points closest to the interface (which is most likely associated with incident beam scatter onto the porcelain) increasing the 95% confidence intervals at these locations.

At both the YPSZ free edge, and at distances beyond 10 μm from the YPSZ-porcelain interface, no clear evidence for monoclinic YPSZ was obtained in the Raman spectroscopy study. This matches the results of the XRD analysis. Moreover, similar minor variations in the monoclinic volume fraction were observed. The largest outlier was observed at 108 μm from the interface, which was found to have relatively large amounts of noise at $178\ \mathrm{cm}^{-1}$ and $189\ \mathrm{cm}^{-1}$.

Examination of the literature reveals that the tetragonal to monoclinic phase transformation has previously been identified at the YPSZ-porcelain interface of specially manufactured test samples in which the YPSZ had been sandblasted prior to the application of the porcelain veneer [14]. However, no such studies have examined this behaviour in representative dental prosthesis suitable for implantation.

The absence of monoclinic YPSZ at the free surface of YPSZ indicates that porcelain is necessary to induce the phase transformation. The driving force for this phase change could therefore be potentially associated with several factors:

1. Elemental composition exerts a strong influence on the transformability of YPSZ [287]. Diffusion across the interface between porcelain and YPSZ could provide a basis for explaining the transformation observed. However, the EDXS analysis outlined in § 7.2 demonstrates maximal diffusional distances of less than 5 μm into the YPSZ region. Therefore, the 10 μm width of transformed region cannot be fully explained by this effect.
2. Thermal history is also known to play a critical role in the phase transformation of YPSZ [288]. The sintering process associated with the application of porcelain veneer to the YPSZ-porcelain interface creates different thermal histories at the YPSZ free surface and in the near-interface region. However, despite these differences, this explanation is insufficient to explain why the phase transformation is only induced within a narrow band at the YPSZ-porcelain interface and does not extend further into the YPSZ bulk (where the thermal history is almost identical).
3. The tetragonal to monoclinic phase transformation is known to be induced by both applied and residual stresses [72, 289, 290]. Therefore the high magnitude tensile residual stress observed at the YPSZ-porcelain interface is the most likely origin of the phase transformation. This response has previously been observed in microscale near-interface regions of surfaces of dental YPSZ in which tensile stresses have been induced by fracture or cutting [32, 291].

6.7.2. XRD Residual Stress Variation

Within this chapter, estimates of the in-plane residual stress state have been obtained from the YPSZ lattice strain calculated on the basis of the tetragonal 101 peak. This measure of strain is representative of a subset of the polycrystalline material both in terms of phase and orientation, and therefore validation using independent FIB milling was crucial for confident interpretation.

In the transmission XRD experiment a through-thickness sample volume is illuminated, and an average measurement is obtained over both the near surface regions (close to plane stress) and bulk (well approximated by plane strain). Therefore in order to facilitate direct comparison between the results of FIB milling and XRD analysis, refinement of d_{101}^{0} has been required as outlined in § 3.4. The in-plane variation of residual strain was found to correspond well with the $\cos 2\varphi$ variation for almost all data points collected. In a few locations, high noise level resulted in low quality fitting, as indicated by the large 95% confidence intervals at these points.

Examination of the stress and orientation distributions (Figure 6.10) reveals that the residual stress estimates obtained through XRD match closely the results of FIB milling, both in terms of magnitude and distribution. The scatter associated with the XRD measurements is far larger than that observed in the FIB milling approach. This variation may be associated with the underlying noise within the diffraction patterns, and its impact on the peak centre quantification. Also, the nanocrystalline nature of YPSZ and microscale probe size used in this study may be sufficient to capture the region to region variation in residual stress which is indicated by the scatter about the underlying distribution [121].

Examination of the underlying trends in the near-interface XRD analysis reveals high tensile stresses in the order of $\approx 150 - 300$ MPa within the first ≈ 100 μm of the interface. A decreasing trend is then observed towards a moderately compressive stress (≈ -50 MPa) at a distance of ≈ 150 μm from the interface. In the parallel direction a response similar to the perpendicular direction is observed, with the exception that within the first ≈ 30 μm from the interface the stress is approximately 200 MPa. The shear variation within this region shows a maximum of approximately 30 MPa at the boundary between YPSZ and porcelain which decreases linearly to a constant near zero stress at distances $\gtrsim 70$ μm from the interface. The variation in the principal orientation angle, ϕ, indicates that at the near interface location and at approximately 150 μm from the interface, close alignment is observed between principal directions and the interface normals. Between these two points there is a peak in the principal orientation rotation angle with the maximum value of $\approx 50°$ at a distance of ≈ 50 μm from the interface.

The XRD residual stress analysis of the free surface shows no variation in the parallel, perpendicular or shear stress response. Low magnitude compressive stresses were observed in both the parallel direction (≈ -25 MPa) and perpendicular direction (≈ -35 MPa), and the shear stress average value was found to be close to zero. In terms of angular orientation, the principal directions were closely aligned with the YPSZ free edge and its normal, with minor scatter about this direction.

6.7.3.Raman Spectroscopy Stress Tensor Analysis

In this study Raman spectroscopy analysis was performed using unpolarised incident radiation, which has no directional sensitivity. Therefore the most representative measure of stress was the first invariant of the stress tensor (trace) as described in § 2.2.5. In order to provide representative estimates of this stress measure, interpolation of the XRD results has been performed. Examination of Figure 6.12 reveals that this approach, in combination with the high levels of noise in the XRD data results in relatively high levels of uncertainty in the first stress invariant estimates. However, despite these relatively large errors, the large number of data points sampled in this study (particularly with the values of the first invariant in the range $0 \rightarrow -150\ \mathrm{MPa}$) are sufficient to reveal the underlying trend.

The total least squares fitting performed on this data set reveals a similar response to that previously published by Pezzotti et al. [268]. The fitted peak centres at $145.28 \pm 0.01\ \mathrm{cm}^{-1}$ and $259.98 \pm 0.01\ \mathrm{cm}^{-1}$ show a reasonable match to the literature values of $144.68\ \mathrm{cm}^{-1}$ and $259.57\ \mathrm{cm}^{-1}$, respectively. Raman peak centres are known to be highly sensitive to variations in the elemental composition and thermal processing conditions in YPSZ [292]. The most likely explanation for the minor differences in the peak centre trends are therefore associated with the differences in the chemical makeup and thermal history of the YPSZ examined in this study.

The plots of peak shift vs first stress invariant were found to have gradients (Π) equal to $-0.58 \pm 0.01\ \mathrm{cm}^{-1}/\ \mathrm{GPa}$ and $1.19 \pm 0.02\ \mathrm{cm}^{-1}/\ \mathrm{GPa}$ for the peaks with the nominal centres $145\ \mathrm{cm}^{-1}$ and $260\ \mathrm{cm}^{-1}$, respectively. This corresponds well to the literature values of $-0.6\ \mathrm{cm}^{-1}/\ \mathrm{GPa}$ and $1.1\ \mathrm{cm}^{-1}/\ \mathrm{GPa}$ [268]. These minor differences in Π may be indicative of the different elemental compositions and thermal histories of the two types of YPSZ or alternatively may indicate that the first invariant stress values obtained from the 101 tetragonal lattice strain may not be fully representative of the average stress within the tetragonal phase. The large amount of noise within the data set prevents any firm conclusions from being drawn on this suggestion.

Overall the Raman spectroscopy peak centre strain invariant analysis shows good agreement with the values previously published in the literature. This indicates that, despite the large amount of scatter, the results of the XRD 101 tetragonal lattice strain analysis are most likely to be a reasonable estimate of the average stress within the tetragonal regions.

6.7.4. YPSZ Sequential Ring-core FIB Milling and DIC Analysis

Comparison between the results of the ring-core FIB milling and the XRD residual stress analysis reveals similar values both in terms of magnitude and distribution. The $\cos 2\varphi$ fitting performed as part of the FIST analysis was successful, and tight confidence intervals were observed at all data points except for the marker milled at the YPSZ-porcelain interface. This measurement point also has the largest difference between the results of XRD and the ring-core milling approach; with estimates of $\approx 100\ \mathrm{MPa}$ and $\approx -180\ \mathrm{MPa}$ in directions perpendicular and parallel to the interface, respectively. These differences may be indicative of the bi-material composition of the milled island, and the associated errors in the ring-core measurement. Alternatively, it may highlight the different stress states in the monoclinic and tetragonal phases at this location, as discussed in more detail in § 6.7.5.

The remaining sequential FIB milling and residual stress estimates show a good match to the XRD data with the exception of the shear stress estimate at 100 μm from the interface where the two techniques are similar in magnitude ($\approx 10 - 15$ MPa) but are acting in opposing directions. Between the two regions of XRD analysis, in the centre of the YPSZ coping, near uniform stresses are observed in the perpendicular (≈ -30 MPa) and parallel (≈ -20 MPa) directions. The shear component in this region is also constant and near zero.

6.7.5.Parallel FIB Milling and DIC Analysis

The parallel FIB milling residual stress analysis technique was used to provide comparative analysis with the XRD results at the location where monoclinic volume fraction was largest, and the least agreement was found with the results obtained through the sequential ring-core milling approach. During residual stress quantification, the implicit assumption was made that principal axes were aligned with the YPSZ-porcelain interface, i.e. $\phi \approx 0°$. Examination of the distribution of ϕ reveals that, while this is a good approximation for the near-interface region, this approximation is not valid at larger distances. Inaccuracy in this approximation would lead to an error in the stress estimate of the order of shear stress at this location ($\approx \pm 20$ MPa). This potential error must therefore be taken into consideration when discussing the results of this analysis.

The magnitude and variation of residual stress determined using the parallel FIB milling approach are generally comparable to the results of XRD and sequential ring-core milling. In the direction perpendicular to the interface, stresses of magnitude $180 - 320$ MPa were observed, broadly correlating with the magnitude of neighbouring stress estimates. Similarly, at distances greater than 13.5 μm from the interface, tensile stresses increasing from $120 - 320$ MPa are observed which closely match the results of XRD analysis.

The main discrepancy between the parallel ring-core approach and the XRD analysis is observed in a direction parallel to the interface at the two measurement points closest to the interface (5.5 μm and 9.5 μm). At this location the XRD residual stress estimate is ≈ 100 MPa, whereas the results of parallel FIB milling indicate a nearly stress-free state. This location corresponds closely to the discrepancy observed between the XRD analysis and sequential ring-core milling analysis (at the YPSZ-porcelain interface), and is the location where the greatest amount of tetragonal to monoclinic phase transformation is observed. XRD results are representative of the stress state within the tetragonal YPSZ, whereas the FIB milling residual stress analysis provides a measure of the *overall* average stress across both the monoclinic and tetragonal phases (weighted according to the volume fraction of each phase). The difference in the stress estimates obtained using the two techniques suggests that the monoclinic and tetragonal phases may therefore find themselves in different states of residual stress. Similar behaviour has recently been observed using Raman spectroscopy of YPSZ [14]. The exact distribution of stresses and the interaction between these grain groups remain unclear, but the magnitude of stresses may indicate that the volume expansion associated with the tetragonal to monoclinic transformation has relieved the tensile stresses in these grains. This is consistent with the strain energy relaxation in the thermodynamic constructs used to describe this phase transformation response [73].

Examination of the literature reveals that very few publications have been dedicated to analysing residual stress within YPSZ copings. Despite this, a number of similarities between previous studies and the results obtained during this analysis can be observed: the near-constant compressive stresses across the bulk of the YPSZ coping has previously been observed by Zhang et al. [33] with the magnitude of this stress plateau being shown to be dependent upon both the cooling rate and veneer thickness of the prosthesis [293]. Similar large variations between tensile and compressive stress within the first few microns of the YPSZ-porcelain interface have also been recently identified by Inokoshi et al. [14].

6.7.6. Residual Stress Variation within the Porcelain Veneer

In order to provide direct comparison between the porcelain residual stress estimates obtained through the FIST sequential ring-core milling, the PDF strain values were converted to nominal residual stress estimates using Equations 3.29 & 3.30. This analysis was performed using the bulk elastic modulus and Poisson’s ratio of porcelain [17] and was based on the implicit approximation that the orientation of the principal stresses were closely aligned in directions parallel and perpendicular to the interface. The low magnitude shear stresses in Figure 6.13 indicate that this approach is valid at distances beyond 50 μm from the interface and the results of this analysis are shown in Figure 6.20.

Examination of the residual stress profiles obtained through diffraction and the sequential FIB milling and DIC approach reveals that in general both approaches give results that are comparable both in terms of magnitude and in terms of spatial variation (Figure 6.20). As described in § 6.2.3, the maximum error associated with the difference between the plane strain and plane stress approximations is expected to be in the order of 4%, which is significantly lower than the average 95% confidence intervals associated with the two methods. However, this calculation is based on the approximation that a uniform residual strain state exists as a function of distance from the interface throughout the sample cross-section. Significant deviations between the results obtained by the two techniques would indicate that this assumption was invalid; however, this appears not to be the case.

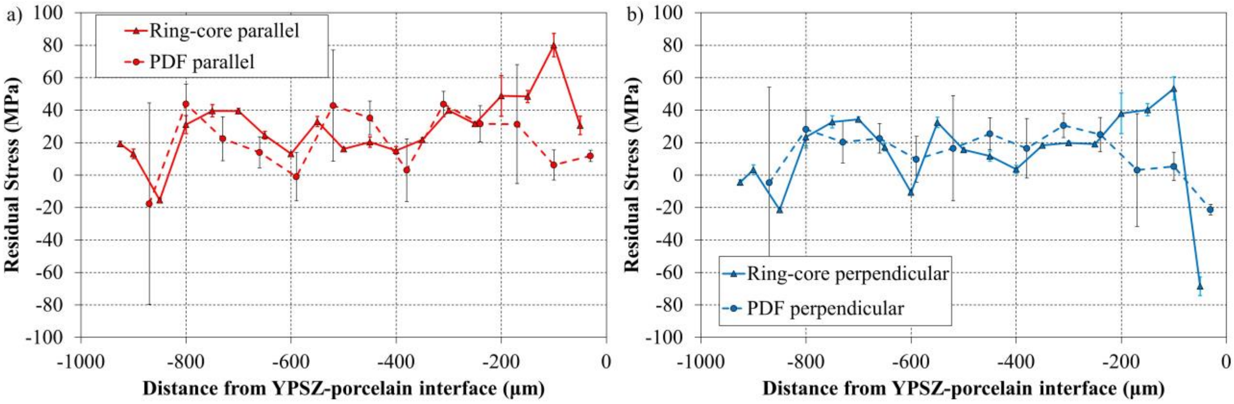

Figure 6.20. Residual Stress Variation within the porcelain veneer in directions a) parallel and b) perpendicular to the YPSZ-porcelain interface. The results of FIST ring-core milling and the converted PDF strain analysis are included.

The region which appears to show maximum difference between the two stress profiles is contained within the first 0.2 mm of the YPSZ-porcelain interface. This region is known to be the most influenced by CTE mismatch between the two materials [34] and contains the point at which failure of the system is most likely to occur [42]. The large gradients in residual stress expected at this location ensure that the approximation of uniform stress through thickness is least reliable.

In order to understand the likely origins of the residual strain state of the porcelain the manufacturing route of the veneer needs to be considered. To build up the required shape, multiple layers of porcelain slurry are applied and heated to 750°C for a relatively short time period. Furnace cooling is then used to return the coping to room temperature over a period of several tens of minutes. The spatial period of the tensile and compressive stresses observed within the veneer corresponds closely to the typical thickness of these porcelain layers, and suggests that this is the origin of the stress variation.

As outlined in §6.6, characteristic tensile and compressive stress distributions similar to those observed in the multi-layer veneer are known to be induced in quenched components [294]. This stress state is induced by the surface cooling at a faster rate than the bulk material and the associated solidification which occurs before that of the underlying bulk material. Continual cooling leads to shrinkage of the bulk and the induction of compressive stresses in the surface layer. Stress equilibrium then ensures that tensile stresses are induced in these sub-surface regions upon full solidification.

In the case of the multi-layered porcelain veneer, this process occurs multiple times during the manufacture of the prosthesis, and therefore a characteristic alternating pattern of tension and compression is induced in the porcelain. Similar tensile and compressive stress variations have previously been observed in veneers of the same overall thickness, with the period of the cyclic behaviour showing a strong dependence upon the thickness of the applied layers [33]. Another important consideration in this manufacturing process is the impact of repeated exposure to sintering temperatures of the underlying veneer layers. It can be seen that the layers nearest the YPSZ are exposed to larger number of thermal cycles, which may facilitate relaxation of the stress state within the veneer through porcelain creep [206, 295]. This would result in lower magnitude, smoother stress variation similar to that identified between 0.2 and 0.4 mm from the interface.

Examination of the residual stresses in the direction perpendicular to the interface indicates tensile residual stress acting in this orientation. Uniform tensile residual stresses within porcelain veneers have been widely reported in the literature [33, 34, 296]. This response is believed to be associated with the combined effects of thermal expansion mismatch and the geometry produced during veneer manufacture.

The final stage of prosthesis manufacture involves manual polishing with diamond grit papers in order to produce an aesthetically pleasing and lustrous finish. Polishing of this type is known to induce near-surface compressive stresses in prosthesis materials [297] and therefore may explain the compressive stresses observed at the surface in both orientations.

6.8. Conclusions

6.8.1.PDF Analysis for Strain Quantification

In § 6.2 a new technique for residual strain evaluation in amorphous materials based on PDF analysis has been introduced and applied. This approach is based on determining the effect of applied strain, in this case by 4-point bending, on the material’s PDF, and using this insight to determine the unknown residual strains at the location of interest. This method offers a new tool for improved characterisation of strain distributions within a broad range of amorphous materials, including bulk metallic glasses and polymers. Despite the many benefits of this approach, this study has highlighted that in order to produce reliable strain estimates, careful calibration is required.

In the course of the development of this technique, new insights into the reduced atomic strain response (compared to the macroscopic strain applied) of porcelain at small interatomic distances ($r < 20$ Å) were also obtained. This analysis suggests that at small length scales the bond stiffness prevents nearest neighbour atoms from moving closer or apart from each other, and that strain is instead accommodated primarily by relative bond rotation. MD simulations of silica, the primary constituent of porcelain, were used to demonstrate that atomic level strain accommodation by bond stretching and bond rotation corresponded well to that observed experimentally. This approach offers a new technique for studying the atomic level strain response of amorphous materials under macroscopic loading.

6.8.2.Monoclinic YPSZ Phase Distribution

Comparison between the monoclinic volume fraction distributions obtained from XRD and Raman spectroscopy indicates that the results obtained from the two techniques show a high degree of similarity. Both techniques indicate a maximum monoclinic volume fraction of $\approx 60\%$ which is localised within the first 3 μm of the YPSZ-porcelain interface. The concentration of the monoclinic phase then reduces up until ≈ 11 μm from the interface, beyond which purely tetragonal phase is observed. Both data sets demonstrate low levels of noise in the remaining volume fraction data, along a few low certainty outliers.

The similarity between the two distributions indicates that despite having differing gauge volumes (through sample average for XRD, and near-surface for Raman spectroscopy), consistent amounts of transformed material are present. This serves to validate the implicit approximation of much of the analysis performed in this chapter, that near-surface measurements are representative of cross-sectional characteristics of the interface and can be approximated as a 1D distribution which is dependent purely upon distance from the interface.

Critical assessment of the origins of the phase transformation suggests that residual stress is the most likely driving factor for this change. These high magnitude residual stresses are highly localised to the interface location and an overview of the potential interaction between phase and stress is outlined in Chapter 8.

6.8.3. Residual Stress Experimental Results

In this chapter the variation of residual stress within the cross section of YPSZ dental coping has been evaluated using PDF analysis, XRD, FIB milling and Raman spectroscopy. Overall, in the YPSZ region, the following consistent picture emerges. Tensile stresses are present within the first 100 μm from the YPSZ-porcelain interface with a peak value of ≈ 300 MPa at a distance of 50 μm from the interface. These moderate tensile stresses, in combination with the discrepancies observed between the tetragonal and monoclinic stress state, indicate that stress relief may have been induced by the near-interface phase transformation. The distribution of shear stress within the coping demonstrates a maximum value of ≈ 30 MPa at the YPSZ-porcelain interface which may be associated with the twinning induced at this location by the introduction of the monoclinic phase. Moderate compressive stresses ≈ 30 MPa are observed over the remainder of the prosthesis which are most likely associated with stress equilibration within the YPSZ coping. The principal stress orientations are predominantly parallel to the YPSZ-porcelain boundary close to the interface and the bulk of the YPSZ, with reorientation of up to ≈ 50° being observed at the location of maximum tensile stress. Further explanation of the potential origins of this residual stress distribution based on the combination with microstructural, micro-mechanical and phase analysis of this region is presented in Chapter 8.

The residual stress within the YPSZ-porcelain veneer has been shown to correspond primarily to the state of tension, with the highest magnitude strains being located where failure has previously been found to occur. In the direction parallel to the interface, the multi-stage veneering process used to manufacture the prosthesis induces oscillatory tensile and compressive strains, while a purely tensile residual strain was observed in the perpendicular direction. These insights can be used to suggest new prosthesis manufacturing routes, e.g. in terms of the choice of veneer layer thickness or sintering temperatures as outlined in more detail in Chapter 8.

6.8.4. Residual Stress Modelling Conclusions

In § 6.6, conceptual analytical modelling of the residual stress component in YPSZ in the direction parallel to the YPSZ-porcelain interface have been presented. This distribution has been decomposed into the macroscale effects of CTE mismatch and residual stresses induced during YPSZ sintering, as well as the phase transformation characteristics induced within a few microns of the interface. Figure 6.19 demonstrates that there is a satisfactory match between the experimental results and the analytical distribution over much of the distribution. The main deviation between these two profiles is observed at $\approx 20 - 70$ μm from the interface, where higher experimental stresses are observed. The origins of this deviation are unclear but may be associated with the influence of thermal tempering, or the multi-layering porcelain manufacture approach which have not been considered. Despite these differences, the general trends in residual stress have been captured effectively by the three sources of residual stress outlined in § 6.6 to provide the simple and flexible analytical approach required for later integration and refinement within existing FE models of YPSZ-porcelain dental prostheses.

One aspect of the approach that is worth remarking on is the successful use of eigenstrain as the order parameter that describes the diffusionless phase transformation in partially stabilised zirconia, *combined* with the strain gradient plasticity formulation. This opens up interesting possibilities for modelling many other processes and phenomena related to martensitic transformation, including quenching of carbon steels, shape memory alloys and polymers, and other effects.

7. Microscale Mechanical and Structural Analysis of the YPSZ-Porcelain Interface

7.1. Introduction and Motivation

Residual stress, phase composition and creep are known to influence the microstructure and mechanical characteristics of both YPSZ and porcelain. High resolution (micro-to-nanoscale) assessment of the variation of these parameters therefore offers an alternative route to determine the impact of these processes on the near-interface YPSZ and porcelain. This chapter outlines several characterisation techniques which have been applied to improve understanding of this near-interface region, and which have formed the basis of two recent publications [295, 298].

Elemental composition is known to be influential in both the mechanical and structural characteristics of both YPSZ and porcelain [36]. Previous studies have indicated that elemental diffusion can occur during bonding of zirconia [299] and therefore insight into the elemental distribution across the YPSZ-porcelain interface is required in order to determine if this behaviour influences near-interface failure. High resolution EDXS mapping has been performed across the YPSZ-porcelain interface in order to determine the diffusional distances of the constituent elements of YPSZ and porcelain in § 7.2.

The highly localised nature of monoclinic phase variation and the close proximity of near-interface porcelain chipping [300] indicates that high resolution imaging of the YPSZ-porcelain interface has the potential to provide insight into the microstructural characteristics at this location. TEM analysis was performed on a lamella extracted from across the interface, in order to provide insight into the characteristics of near interface YPSZ and porcelain at nanoscale resolution in § 7.3.

Quantitative insight into the spatial variation of elastic modulus, yield strength and toughness is critical in understanding the mechanical response within the near-interface region. Recent technique development has facilitated microscale quantification of these parameters through nano-manipulation of FIB milled micropillars. Arrays of pillars were therefore milled within the first 100 µm of the YPSZ-porcelain interface in order to perform spatially resolved analysis within this region. Micropillar compression was performed to determine the variation in Young's modulus and yield strength in § 7.4 [301], and micropillar splitting was used to provide insight into the fracture toughness in § 7.5 [63].

7.1.1. Sample Preparation

In order to be as consistent as possible with the experimental analysis outlined in Chapter 6, microscale mechanical and structural analysis were performed on a prosthesis selected from the same batch. An identical sample sectioning and polishing routine to that outlined in § 6.1.1 was used to generate a 2 mm thick cross section of the prosthesis which was mounted onto an SEM stub using silver paint as shown in Figure 7.1. The interface region selected for further examination was chosen to be the location at which the interface was most straight in order to reduce the effects of interface curvature on the analysis. EDXS was initially performed on this sample, and the remaining three procedures were then performed as close as possible (< 100 μm) to each other whilst ensuring that there was no interference between the techniques.

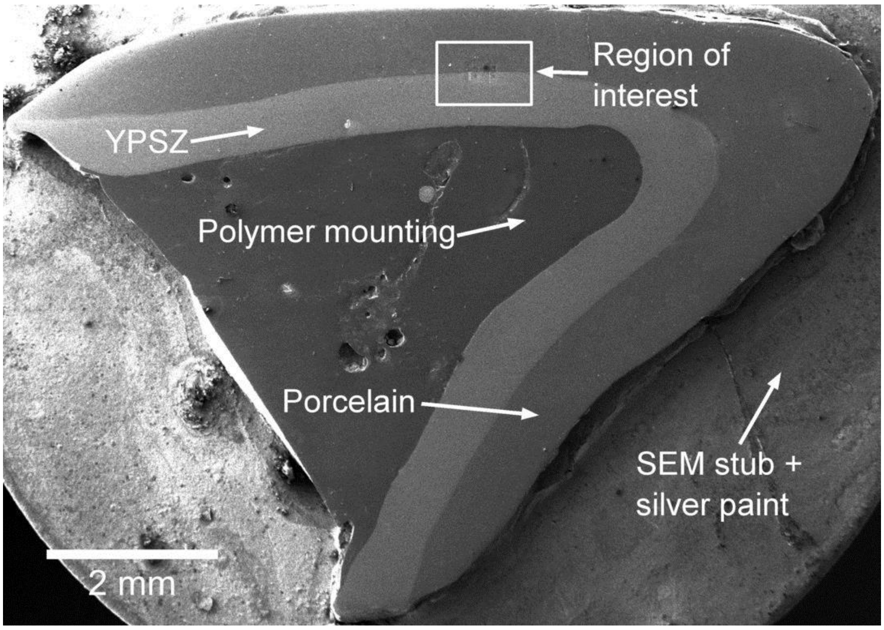

Figure 7.1. SEM image of the prosthesis cross section mounted on an SEM stub using silver paint.

7.2. Energy Dispersive X-ray Spectroscopy

As outlined in § 1.2, EDXS analysis at the YPSZ – porcelain interface has previously been performed in disc samples to determine the impact of different thermal processing routes on zirconium and silicon concentrations within the first few microns of the interface [27]. This study determined that the typical diffusional distances of these two materials were $5 - 10$ μm however no other elements were examined. Therefore, in the analysis that follows, examination of all detectible elements has been performed at two differing length scales ($\pm$ 5 μm and $\pm$ 100 μm) in order to improve insight into this behaviour.

7.2.1.Materials and Methods

EDXS was performed across the YPSZ-porcelain interface using an Oxford Instruments X-max silicon drift detector mounted on the chamber of the Tescan Lyra-3 XM FIB-SEM at MBLEM, Oxford, UK. Calibration of the EDXS software AZtecEnergy, was performed using Au, Si and Cu standards immediately prior to the EDXS mapping. Optimisation of the beam intensity and dwell time was performed in order to minimise the detector 'dead time' and to reduce noise at the 30 kV accelerating voltage selected, with the final values being selected as $12\ \mathrm{a.u.}$ and $850\ \mathrm{ms}$ per pixel, respectively. Mapping at two different magnifications (with image sizes of 2048×2048 pixels) was performed across this region. The first corresponded to a $200\ \times 200\ \mathrm{\mu m}^2$ viewfield (nominal pixel size 97 nm) and the second to a $10\ \times 10\ \mathrm{\mu m}^2$ viewfield (with a nominal pixel size of 2.5 nm) in order to examine elemental distributions at these two length scales.

7.2.2.Results and Discussion

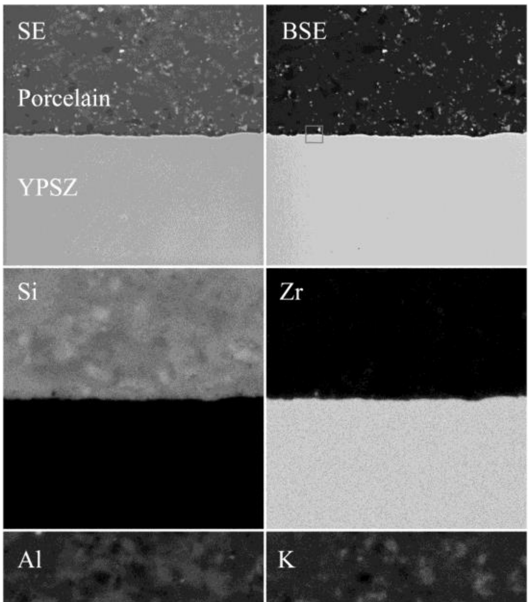

Figure 7.2. Montage of Si, Zr, Al and K elemental distributions within a $200 \times 200\ \mathrm{\mu m}^2$ region. The location of the high magnification EDXS is shown on the BSE image.

In the lower magnification EDXS map, fifteen elements were identified as present in the examined region, and eight elements were found to be present in only trace amounts ($< 0.1\%$): C, Mg, Fe, Ni, Rb, Sb, Ce and W. The EDXS maps of the 4 elements showing greatest variation, Al, Si, K and Zr, are shown in Figure 7.2. SE and BSE SEM images of the same region have been included to in order to facilitate comparison between the EDXS results and the local microstructure. The BSE and SE images clearly show variations in contrast across the surface and careful examination of these regions demonstrates that these particles are embedded in the surface. Further, comparison between the location of this electron contrast and the EDXS analysis demonstrates that these regions are distinct in terms of concentration of Al, Si or K, compared to the surrounding area.

Initial examination of Figure 7.2 clearly demonstrates that the elemental distribution within YPSZ is more consistent than in porcelain. Correlations between the porcelain elemental maps reveal quartz (high Si, low Al and K content) and fluorapatite (high Ca, F and P, reduced Si) regions of size $\sim 1 - 15$ μm as expected in dental porcelains of this type [302].

Figure 7.3 shows the variation in average elemental composition across the interface calculated from the low magnification EDXS maps in which a large change in elemental composition at the interface region can clearly be observed. The elemental diffusion zone obtained from this low magnification imaging appears to be of the order of $\pm\sim 10$ μm. However, since the surface roughness is ± 5 μm, the resulting convolution of interface roughness and diffusion makes it difficult to comment on the exact depth to which this behaviour extends.

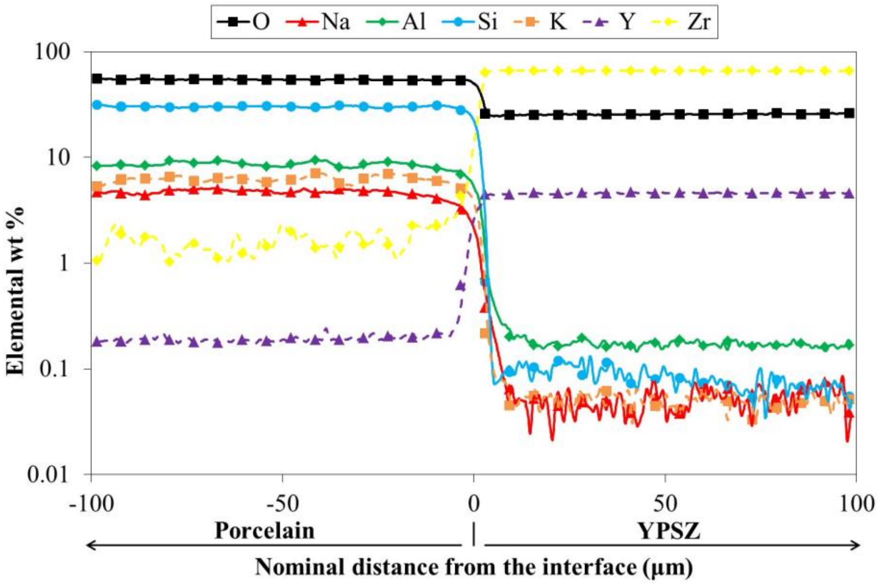

Figure 7.3. Logarithmic plot of average elemental weight % within the first 100 μm from the YPSZ – porcelain interface.

To overcome this limitation, a second EDXS map at a higher magnification was obtained (Figure 7.4) from a region embedded within the low magnification EDXS region previously analysed, as shown in the BSE image in Figure 7.2. Thirteen elements were recorded in this analysis, in which trace amounts ($< 0.2\%$) of six elements were identified: Mg, Fe, Ni, Sb, Ce and W. Figure 7.4 shows a montage of the Al, Si, Zr and K, the elements which most clearly show variation in this region, along with the SE and BSE SEM images of the region investigated.

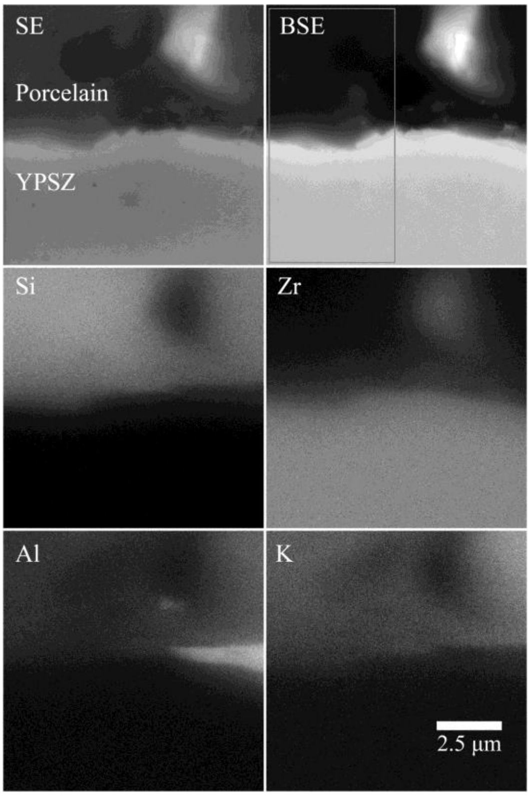

Figure 7.4. Montage of Si, Zr, Al and K elemental distributions within a 10×10 µm^2 region of the YPSZ – porcelain interface. The reduced area over which elemental diffusional analysis was performed is highlighted in the BSE image.

Several grains of differing electron contrast (sized in the range $\sim 0.2 - 2$ µm) can clearly be seen embedded in the near-interface porcelain. Examination of the corresponding regions in the EDXS maps reveals that these locations have lower levels of Si and K than the neighbouring porcelain, but contain high amounts of Al or Zr. Although the Al rich grain is typical of the grain like structure of porcelain, the Zr rich grain suggests that YPSZ particles have detached from the YSPZ surface and become embedded in the porcelain during manufacture. The loose bonding of near interface YPSZ grains highlighted in the TEM study (in § 7.3) may be a demonstration of a similar effect to that observed here, however the grain sizes observed in EDXS are approximately a factor of 1,000 times larger than those observed in TEM. Despite this size difference, previous studies have also have highlighted similar $1 - 5$ µm diameter Zr rich grains embedded in the near interface porcelain of similar dental coping systems [90].

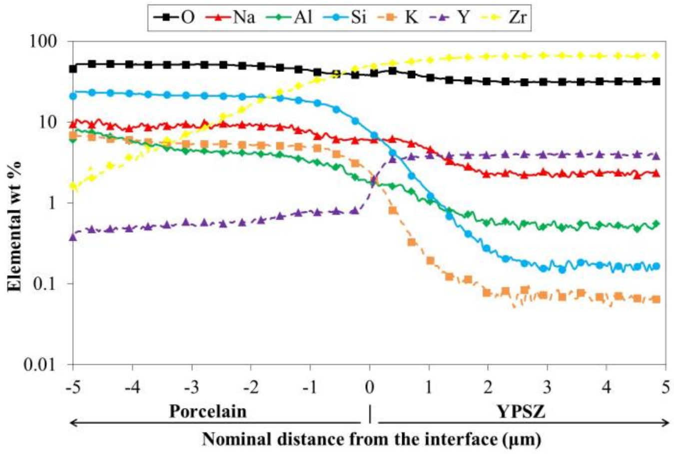

Figure 7.5. Logarithmic plot of average elemental weight % within the first 5 µm from the YPSZ – porcelain interface.

In order to remove the influence of the embedded YPSZ grains, the 1D elemental distribution plots (in weight %, Figure 7.5) were obtained from a reduced region of the higher magnification EDXS map as shown in the BSE image in Figure 7.4. The average roughness of the interface was determined from the higher magnification SEM imaging and was found to have a maximum amplitude of 330 nm. Although this variation is much smaller than the $\pm\sim 5$ µm observed over the 200 µm region, this will act to blur the effective diffusional distances by a length scale approximately equal to this distance. Careful consideration of the size of the interaction volume is also necessary in order to determine the nominal area from which X-rays will be emitted at each location. Monte Carlo simulations of these processes have previously been used to study the size of this behaviour [88] and empirical relationships for the average distance between the entrance point and its final resting place (R_{av}) have been determined. Based on the manufacturer's published elemental compositions [17], these distances have been determined as 1.5 µm and 1.2 µm for porcelain and YPSZ respectively. The teardrop shape interaction volume associated with EDXS ensures that most emission is emitted from a region parallel with the incident beam and a distance of approximately R_{av} into the material. Further simulations, beyond the scope of this investigation, would be necessary to precisely quantify the cross sectional area of the interaction volume. A critical examination of the EDXS mapping performed, particularly of the Al rich grain, reveals that the cross-sectional resolution of technique is far greater than $\mathrm{R_{av}}$, however here I propose to use this value as an upper bound. This will result in apparent elemental diffusion over a maximum distance approximately equal to $\mathrm{R_{av}}$ and therefore this will act as a limit to the effective diffusional limits which can be determined by EDXS.

The average diffusional zones of $\pm\sim 3$ μm observed in this figure are smaller than the $\pm\sim 10$ μm calculated from low magnification analysis and clearly demonstrate that diffusion has occurred between YPSZ and porcelain. Si and Zr appear to show the largest diffusional distances ($6 - 7$ μm) and the greatest changes in composition across the interface is present in Si (~ 400 fold reduction). Characteristic slope changes can be seen at the 0.5 μm position in Al and Na, suggesting that this location may be indicative of an elemental barrier after which diffusion was greatly reduced. This point can therefore be considered as the nominal elemental interface position. Previous studies have found diffusion zones of approximately similar sizes ($8 - 10$ μm) in fractured tensile specimens of the YPSZ – porcelain interface [303] suggesting that diffusion is typically limited to these very small length scales in this system.

At the nominal 0.5 μm position, a peak in the elemental weight % of O can also be seen. Previous studies have highlighted this oxygen-rich interface band at the YPSZ – porcelain interface [304], although the exact origin of this behaviour is unknown. Potential explanations for the increased oxygen content include variations in stoichiometry in the near-interface oxides, or this may alternatively be indicative of oxygen trapped in voids during the manufacturing process. The positioning of this zone in relation to the “knees” observed in the elemental weight % distributions of the Al and Na oxides does however suggest that these two responses are directly related.

In contrast to the O weight % peak at the interface, a plateau in concentration can be observed in Y at its transition, which again may be indicative of a limiting diffusional distance characteristic of the interface region. Changes in YPSZ doping composition are known to impact a whole range of properties, from elastic behaviour [189] to grain size [12] and fracture toughness [305].

As a final check on the reliability of my EDXS results, analysis was performed to compare the average compositions of the YPSZ and porcelain with those provided by their respective manufacturers. The areas over which the averaging was performed were selected as $20 - 100$ μm from the interface for the low magnification imaging and $2 - 5$ μm for the higher magnification imaging (in the region highlighted in the BSE image in Figure 7.4).

In the case of YPSZ, the oxide weight percent tolerances published for Zenotec Zr Bridge [11] were used to calculate the weight % bounds for the five main elements present within this material; Al, Hf, O, Y and Zr. These manufacturer’s tolerances, along with the results of both low and high magnification elemental composition averaging are shown in Figure 7.6. It can be seen that the averages are representative of the composition found in Zenotec Zr Bridge for all elements except for the high magnification Al and O.

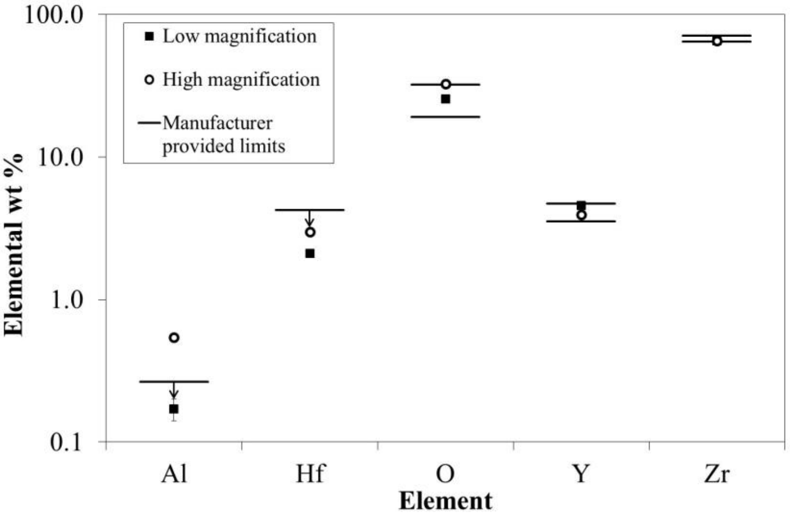

Figure 7.6. Average elemental weight % of the 5 main elements in YPSZ near-interface region; Al, Hf, O, Y and Zr. 95% confidence intervals from EDXS peak fitting intervals are included.

A similar elemental weight % composition calculation was performed for the porcelain using the oxide content tolerances provided Ivoclar Vivadent [17]. The bounds calculated for the nine principal elements (Al, Ca, F, K, Na, O, P, Si and Zn) were then plotted with the results of the high and low magnification averaging, as shown in Figure 7.7.

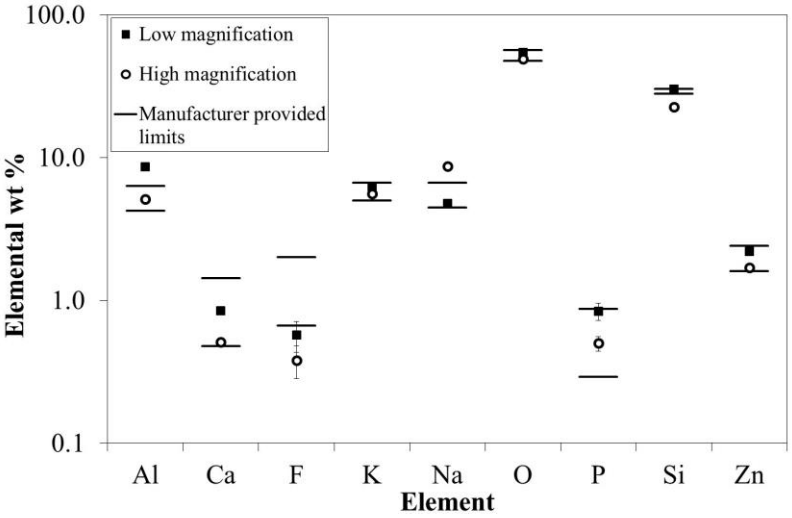

Figure 7.7. Average elemental weight % of the 9 main elements in porcelain near-interface region; Al, Ca, F, K, Na, O, P, Si and Zn. 95% confidence intervals from EDXS peak fitting intervals have also been included

Both materials generally showed good correlation, with 21 out of 28 elemental weight % values being found to be within tolerance. The issue of representative averaging in terms of porcelain regional variation as well as the impact of the interface diffusion mean that some variation is expected. Added to this effect, the known decreased sensitivity of EDXS to lighter molar mass elements [306] may explain why outliers are only present in elements with molar masses less than or equal to that of Al.

7.3. Transmission Electron Microscopy

Examination of the literature reveals that one TEM study focusing on the impact of different YPSZ surface treatments on the YPSZ – porcelain interface in disc samples has previously been published by Grigore et. al [307]. This study revealed distinct differences in the near-interface YPSZ microstructure of these specially prepared samples and therefore that YPSZ surface preparation is highly influential in the YPSZ-porcelain bonding characteristics. In contrast to this study, in the present TEM analysis my focus was instead placed on mapping both the YPSZ and porcelain near-interface regions. Importantly, the study was carried out over much larger distances than previously considered, and on a sample representative of clinically relevant copings.

7.3.1. Materials and Methods

Lamellae for TEM observation were fabricated using the software module ‘AutoSlicer’ and the Tescan Lyra-3 XM FIB SEM at MBLEM. A 20×5 μm^2 area lamella containing the YPSZ-porcelain interface with an average thickness in the range of $100 - 150$ nm, was milled out for TEM analysis. A very low magnitude polishing current (100 pA) and beam energy (5 keV) was used to carefully control the sample thickness while minimising the impact of gallium ion implantation.

7.3.2. Results and Discussion

Figure 7.8 shows a bright field TEM image of the interface between porcelain and YPSZ. The interfacial region exhibits a markedly different microstructure in comparison to the bulk. A band of spherical structures can be clearly observed in porcelain at a distance between 0.4 μm and 1.5 μm from the interface. These spheres have sizes in the range $\sim 5 - 50$ nm and are present at the location at which tensile residual stress has previously been shown to be induced during manufacture [33]. As highlighted in Chapter 5, the combination of stresses and sintering temperatures applied to this interface region can induce creep in dental porcelain compositions. The resulting nanovoiding size distribution is very similar to that observed in TEM of the crept samples and offers a likely explanation of the origin of spherical type features observed in this region. Further, the appearance of these voids is very similar to the amorphous shell / empty voids observed in the creep based study.

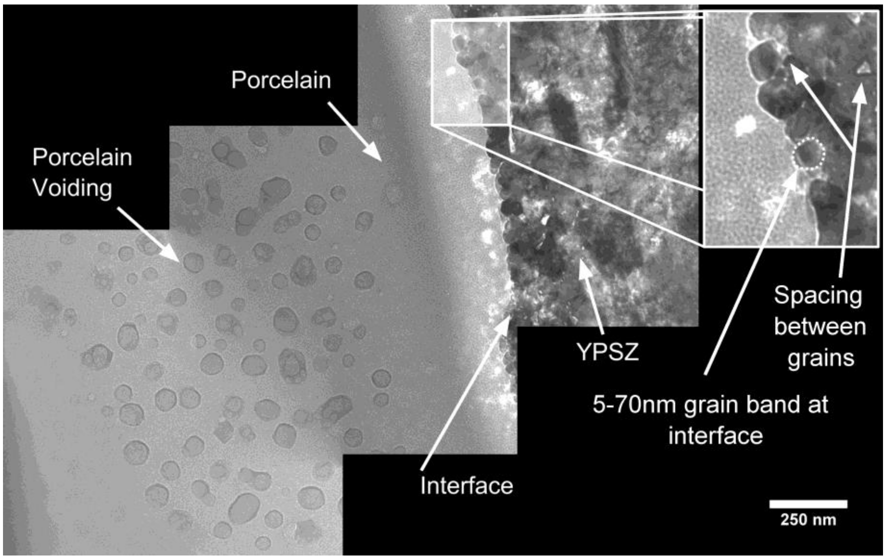

Figure 7.8. Composite TEM image of the YPSZ – porcelain interface. The insert shows a higher magnification image of the band of small YPSZ grains at the interface.

On the YPSZ side, a band of small grains (ranging in size from $\sim 5-70$ nm) was observed in the first 200 nm of YPSZ closest to the interface (as shown in the insert in Figure 7.8). This band was found to be present along the entire length of the ~ 5 μm interface which was imaged using TEM. The grains in this region appear to be loosely bound in comparison to the bulk material and are much smaller than the bulk grain size of YPSZ copings. This suggests that the parameters affecting grain growth behaviour in this region are different to those of the bulk material.

Another composite TEM image of the first 6 μm of the near-interface YPSZ is shown in Figure 7.9. Following the 200 nm grain refined zone, a $\sim 1-2$ μm high contrast region can be observed in YPSZ showing no clear facets or grain boundaries. One explanation may be the presence of amorphous zirconia which has previously been observed at the interface between two dissimilar materials [308]. However, the relatively large length scales over which this zone extends ($\sim 1-2$ μm) makes it unlikely that this is in fact the case. An alternative and more likely explanation is that this high contrast YPSZ region contains a large number of twinning domains and stacking faults which are associated with the tetragonal to monoclinic phase transformation. This location corresponds to the exact position where high (60%) monoclinic volume fractions were observed through XRD (in § 6.3) and Raman spectroscopy (in § 6.4). Multiple layers of twinned material can provide the appearance of multi-directional facets and similar high contrast features have previously been observed at the interfaces of zirconia-based thermal barrier coatings which have undergone phase transformation [309, 310]. These microstructural changes are speculated to be the result of the residual stresses and thermal histories present at such interfaces, and suggest that similar transformational responses are induced at the YPSZ–porcelain interface. Following this high contrast zone, grain sizes consistent with those reported in literature are observed [11].

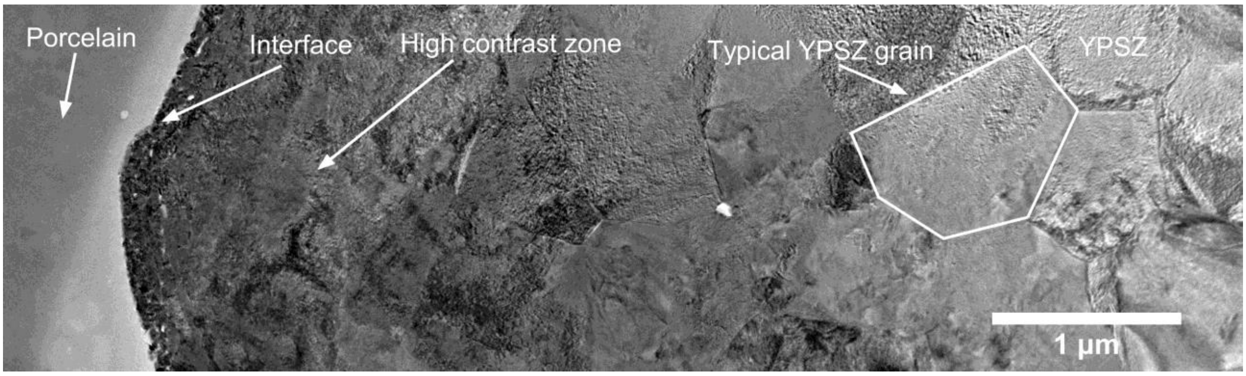

Figure 7.9. Composite TEM image of the YPSZ – porcelain interface and neighbouring YPSZ.

Examination of the composite TEM images in Figures 7.8 and 7.9 clearly demonstrates that the local microstructure in both the porcelain and YPSZ interface are different from the nominal bulk structures of amorphous porcelain and polycrystalline YPSZ. The result of this varying grain size has previously been shown to impact the fracture toughness of interfaces between materials of differing mechanical behaviour [311] and therefore may partially explain the failures observed.

7.4. Micropillar Compression for Stiffness and Yield Strength Variation

As outlined in § 2.3.2, micropillar compression can be used to provide insight into the loading modulus and yield strength behaviour within a microscale gauge volume. In the analysis which follows, an array of FIB milled micropillars have been used to determine the variation of these two properties within 100 μm of the YPSZ-porcelain interface. Although this technique has not previously been applied to study this interface, or dental porcelain, a number of previous micro-compression studies on various forms of zirconia have also been reported [62, 312], which revealed clearly the length scale dependence of the behaviour of this material.

7.4.1. Materials and Methods

Arrays of micropillars were FIB-milled across the YPSZ-porcelain interface using a two-step milling process: coarse milling using 2.5 nA milling current followed by fine milling at 0.75 nA. The average pillar diameter and height were ∼1.9 μm and ∼5 μm respectively, and an aspect ratio of ~2.5 (Figure 7.10) was selected to reduce the impact of pillar buckling during compression, as successfully implemented in previous studies [313].

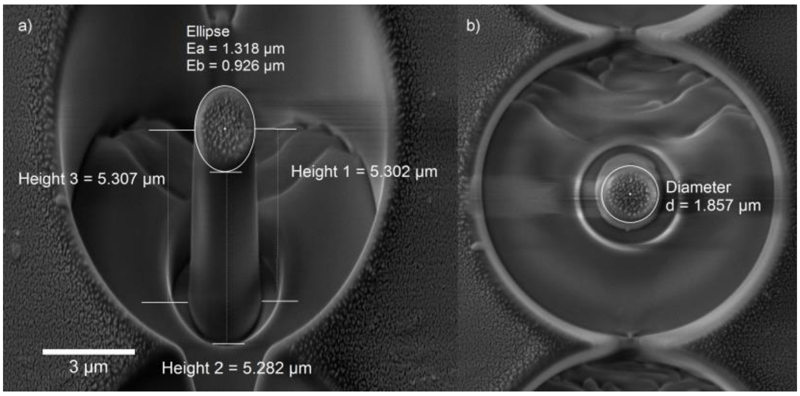

Figure 7.10. SEM images of a completed porcelain micropillar at a distance of 33 μm from the interface. a) Sample tilted at 55^0 (tilt correction of 35^0). b) Sample normal to the electron column.

The pillars were separated from each other by ∼10 μm and two arrays of 20 pillars each, offset by ∼7 μm, were milled in order to attain the overall spatial resolution of ∼5 μm in terms of the distance from the interface, as shown in Figure 7.11. The relative variation in mechanical properties parallel to the interface is believed to be such that an offset of this size should not significantly influence the properties calculated. This is further demonstrated by the consistent trends observed as shown in § 7.4.2.

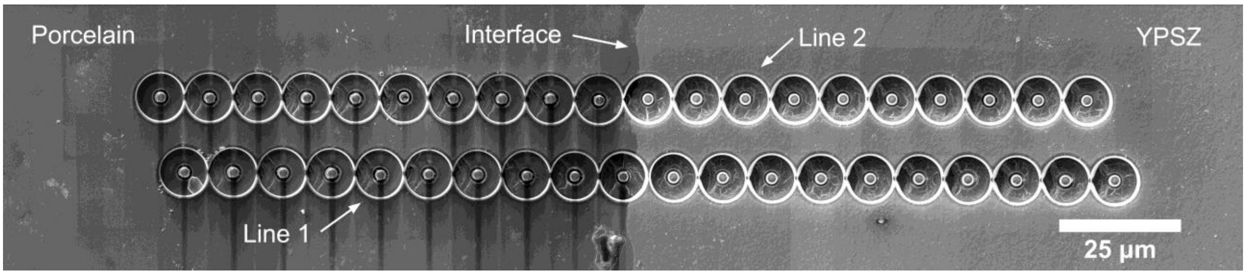

Figure 7.11. SEM image of milled micropillars showing the location relative to the YPSZ – porcelain interface and the offset between Line 1 and Line 2.

7.4.2.Results and Discussion

Microcompression offers the possibility of uniaxial compression testing at small length scales [314] with high spatial resolution. It has been successfully used to study the deformation behaviour of wide range of materials including metals, ceramics, polymers, glasses and biological materials [315-317]. Typical microcompression stress-strain responses for porcelain and YPSZ micropillars are shown in Figure 7.12. Both of these materials exhibit a drop in stress beyond elastic limit due to crack nucleation and propagation. The average loading modulus, calculated from the elastic linear stress-strain regime, of YPSZ (∼214 GPa) was higher than that of porcelain (∼72 GPa). Although the accuracy of the extracted loading modulus from microcompression data depends on a more rigorous data analysis than that considered here [318], these results are in reasonable agreement with those provided by the manufacturer for YPSZ (210 GPa) and for e.max Ceram (60 GPa). Post compression imaging of the deformed pillars showed evidence of brittle fracture and therefore the unloading modulus was not analysed.

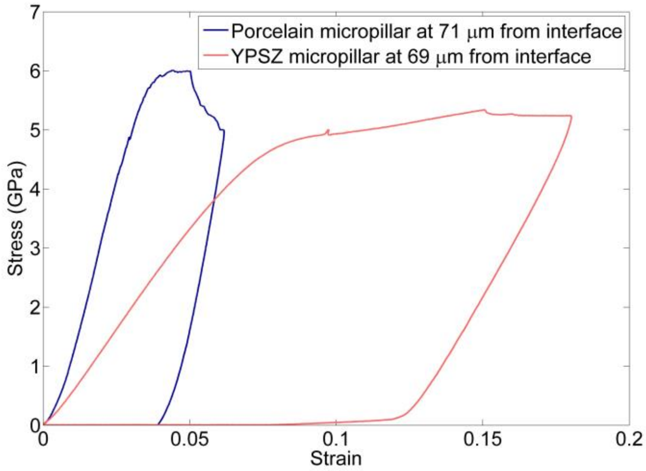

Figure 7.12. Nominal stress-strain plot of a porcelain and a YPSZ micropillar.

A plot of loading modulus and 2% yield strength of the pillars as a function of distance from the YPSZ-porcelain interface for both Line 1 and 2 is shown in Figure 7.13. In the context of this study, the 2% yield strength has been defined as the intersection point between the stress-strain curve and a line subtended from 2% strain with a slope equal to the calculated loading modulus. Although this approach was consistently applied to the data set, the impact of random brittle failure was observed to influence this measure, particularly in the YPSZ region. The modulus and yield strength 95% confidence intervals were calculated based on the standard deviations of micropillar height and diameter measurements, along with the fit quality associated with each measure.

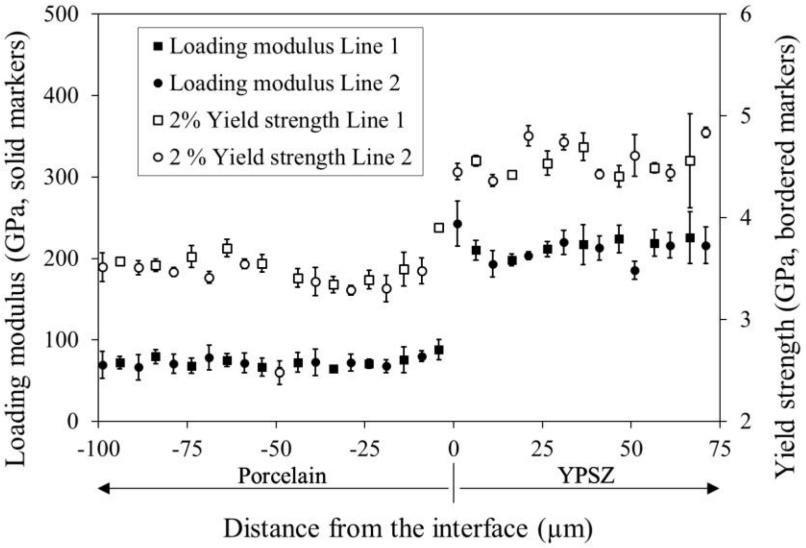

Figure 7.13. Loading modulus (solid markers, left) and 2% yield strength (bordered markers, right) for the YPSZ and porcelain micropillars as a function of distance from the interface. The 95 % confidence intervals are shown by the error bars

A number of outliers were observed in the data set, most notably in the 2 % yield strength in porcelain at a distance of 49 μm from the interface and the loading modulus in YPSZ at a distance of 51 μm from the interface. The singular nature of these variations in an otherwise relatively consistent data set suggests that these are unrepresentative.

A critical examination of the trends in YPSZ loading modulus reveals that this value is approximately constant (within experimental scatter) at a value of 216 GPa for distances greater than 10 μm from the interface. At the near interface location an increase in modulus, up to a maximum of 242 GPa, is observed. The limited diffusion zones (< 5 μm) outlined by EDXS suggest that elemental variation cannot explain the origins of this behaviour, however this distance corresponds closely with the length scale of the tetragonal to monoclinic phase change observed through XRD (in § 6.3) and Raman spectroscopy (in § 6.4).

The average value of the YPSZ 2 % yield strength in this study was found to be 4.5 GPa. To the best of my knowledge, the yield strength of YPSZ has not been reported in literature. However, the maximum compressive strength of this material (Zenotec Zr bridge) has been reported to be 2.0 GPa by the manufacturer [11]. This difference between bulk and microscale behaviour suggests that length scale effects are present in YPSZ, as previously outlined in the literature [319]. The relatively low ductility of this ceramic ensures that this parameter is highly influenced by the statistical likelihood of brittle failure in the micropillar. For this reason, the yield strength values show relatively large levels of scatter and no clear trends in spatially resolved behaviour could be identified.

In contrast, more consistent 2 % yield strength values were observed in the porcelain, with an average magnitude of 3.44 GPa. A moderate reduction in yield strength (of up to $\approx 10\%$) can also be observed within the first 50 μm of the interface. To the best of my knowledge, this study is the first to perform micropillar testing on porcelain of any type. Previous micropillar studies have however been performed on amorphous silica, the primary constituent of porcelain, which showed a uniaxial compressive yield strength of 5.22 GPa [320].

In terms of macro-scale yield strength comparisons, no compressive testing data was available for IPS e.max Ceram. However, macroscopic compression studies performed on similar powder-based dental porcelains have reported compressive strengths of 340 MPa [321]. Despite the lack of any evidence for microstructural features of this size (for example, grain size, etc.) this indicates different responses between the bulk and microscale. This is most likely to be associated with the statistical likelihood of failure at these different length scales.

An increased yield strength value of 3.91 GPa was observed in the porcelain at a distance of 4 μm from the interface. Critical examination of Figure 7.11 suggests that this pillar is composed of both porcelain and YPSZ. Therefore, the intermediate value of this strength (between the results of YPSZ and porcelain) appears to be realistic in magnitude.

7.5. Micropillar Splitting for Toughness Variation

As outlined in more detail in § 1.2, the spatial variation of fracture toughness, is critical in understanding the origins of the brittle failure observed at the YPSZ-porcelain interface. Quantification of the fracture toughness of both bulk YPSZ [43] and bulk porcelain [300] has previously been reported. However, no microscale spatially resolved analysis has been performed to determine the variation in the vicinity of the interface. Therefore, in order to improve understanding of this behaviour, a modified version of the micropillar indentation and splitting routine established by Sebastiani et al. [63] has been implemented.

7.5.1.Materials and Methods

FIB milling was used to generate an array of micropillars which were aligned in a direction perpendicular to the interface as shown in Figure 7.14a. This pattern was selected to maximize the number of pillars within the first 15 μm of the interface in order to enable improved statistics to be captured in the location where most variation was expected. A nominal pillar diameter and depth of 5 μm was selected in order to provide the required resolution while simultaneously minimizing the impact of ion beam damage on the fracture toughness recorded. This size was also consistent with the successful experiments previously performed by Sebastiani et al [63]. A trench width of 3 μm was selected as a compromise between maximizing the spatial resolution of the data collected and ensuring that there was no interaction between the indenter and the surrounding material. In order to aid in aligning the indenter to the centre of each pillar, a 25 nm deep cross was milled into the surface as shown in Figure 7.14b. High resolution imaging was performed on each pillar using SEM stage tilt angles of 0° and 35° in order to measure the radius (R) and height of each pillar as outlined in detail in § 7.4.1. Measurement of the distance from the interface to the centre of each pillar was also performed during this process.

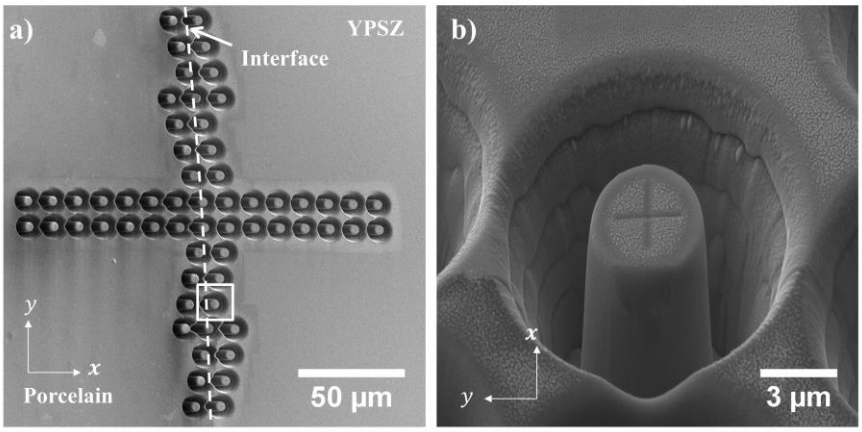

Figure 7.14. a) Positions of FIB milled micropillars across the YPSZ-Porcelain interface. b) A high magnification image of one pillar. Both images were captured at tilt of $55°$ in the x direction. Figure 7.14a has been rotated to be orientationally consistent with other techniques in this chapter.

Micropillar indentation splitting was performed using an Alemnis SEM Indenter inside the TESCAN Lyra 3 FIB-SEM at Empa, Thun, Switzerland. Prior to the start of the experiment, compliance calibration was performed by indenting fused silica which has a well characterized indentation response. Before each indentation, the tip was cleaned by indenting the polymer substrate in which the prosthesis was embedded. A displacement control mode was used during the analysis in order to prevent the large displacements typically observed during fracture under load control. The purpose of this approach is to enable the failure mode of the pillars to be examined in more detail through SEM imaging of the fractured pillars. Videos of the indentation were also recorded to provide further insight into the pillar failure behavior and stills from two example indentations are shown in Figure 7.15.

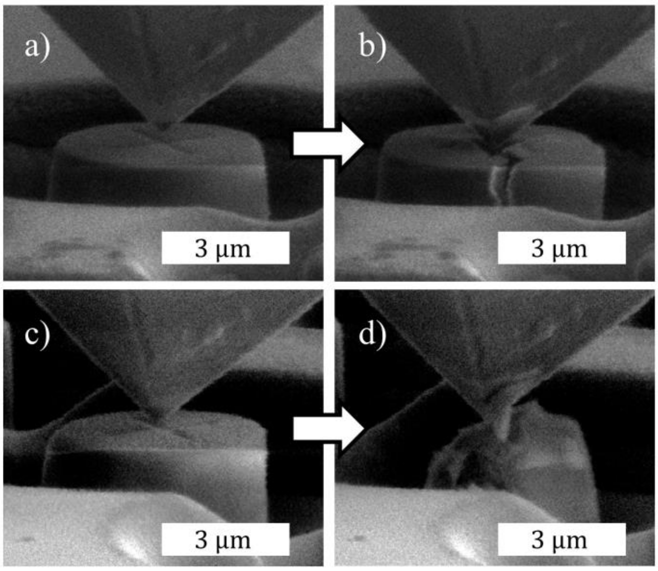

Figure 7.15. Stills from videos of cube corner nanoindentation splitting before and after indentation in YPSZ 9 µm from interface (a and b) and porcelain 11 µm from interface (c and d).

Preliminary micropillar indentation splitting was performed using the approach pioneered by Sebastiani et al. [63]. A diamond Berkovich tip, with a total included angle of 142.3° was used to perform this analysis. This facilitated the use of the Berkovich indentation load pre-multiplier (γ_B) values which have previously been published for this technique. The relationship between the Berkovich fracture toughness (K_B), critical failure load (P_C) and pillar radius (R) is given in Equation 2.16.

The large included angle associated with the Berkovich tip is known to reduce the sliding between the indenter and pillar surfaces. This ensures that the fracture load is less dependent upon the frictional coefficient between these two surfaces (a parameter which is typically unknown). In spite of this, the shallow viewing angle imposed by the tip presents difficulties in aligning the indenter tip to the center of the pillar. In total 9 indents were performed in the YPSZ using this approach and 3 indents were performed in porcelain, taking an average time of 40 minutes per point. All of these points were selected to be far from the interface where the variation in fracture toughness was expected to be small.

In order to increase the precision of the alignment between the indenter tip and the center of the pillar and reduce the time required to indent the remaining 48 pillars, the decision was made to change to a diamond cube corner indenter tip. The reduced included angle of $90°$ associated with this tip geometry increases the sensitivity of the technique to the friction between diamond and the substrate material and means that the value of γ_B previously published by Sebastiani et al. [63] is no longer valid. Despite this, direct comparison between the fracture toughness results obtained using Berkovich and cube corner indentation tips can be used to provide an estimate of the cube corner indentation load pre-multiplier (γ_C) for a given material as outlined in § 7.5.2. Indentation was then performed on all of the remaining pillars in an average time of 11 minutes per point. Imaging of the fractured pillars was implemented using the Hitachi S-4800 (CFE) SEM at EMPA, Thun, Switzerland with an imaging direction which was normal to the surface of the substrate.

7.5.2. Results

In order to perform fracture toughness evaluation through micropillar splitting, insight into the Young's modulus (E) and hardness (H) within the region of interest is required. The ratio between these parameters can then be used to calculate the load pre-multiplier γ_B through Finite Element (FE) simulations. A plot of the relationship between E/H and γ_B was recently published by Sebastiani et al

[104] which demonstrates that for E/H values ranging from 5 to 22 this relationship is approximately linear and can be fitted to give the following relationship:

$$\gamma_B = 0.0149\frac{E}{H} + 0.057. \tag{7.1}$$

Although nanoindentation has previously been successfully performed across the YPSZ-porcelain interface [33, 35], the influence of residual stress and brittle fracture (inelastic behavior) is known to greatly influence this experimental approach [322]. Therefore, in order to gain insight into the likely trends in hardness across the interface, the approximately constant relationship that exists between yield strength (σ_y) and hardness for a given material can be exploited. Although the exact relationship between these two parameters is highly dependent upon the specific substrate, a good approximation for the relationship is that hardness is three times the yield strength [323]. Comparison between the average yield strength obtained through microcompression [295] and those provided in the literature, demonstrate that this is a good approximation for YPSZ (13.5 GPa compared to 12.75 GPa provided by the manufacturer [11]) but not for porcelain (10.3 GPa compared to 5.4 GPa published in the literature [17]). These differences are likely associated with size effects and the microstructures of the two materials.

Therefore, in order to provide insight into the likely variation of the ratio between Young's modulus and hardness across the YPSZ – porcelain interface, the yield strength and Young's modulus results obtained through micropillar compression (in § 7.4) were used in the following approximation:

$$\frac{E(x)}{H(x)} \approx \frac{E(x)}{3\sigma_y(x)}, \tag{7.2}$$

where x is the distance from the interface. The standard deviations of E and σ_y were also used to calculated the 95% confidence intervals of E/H.

The variation of E/H is shown in Figure 7.16 which reveals that within each material the scatter of E/H is generally equal to or smaller than the 95% confidence intervals of each value. This means that, within the scatter of the results obtained experimentally, the value of E/H can be considered to be approximately constant in both YPSZ and porcelain. Further, as highlighted in Equation 7.1, it can be seen that moderate changes in the value of E/H result in very small changes in γ_B, i.e. the fracture toughness estimate is robust to minor deviations in E/H. This approximation of constant material mechanical parameters in both YPSZ and porcelain was therefore used in the remainder of the analysis.

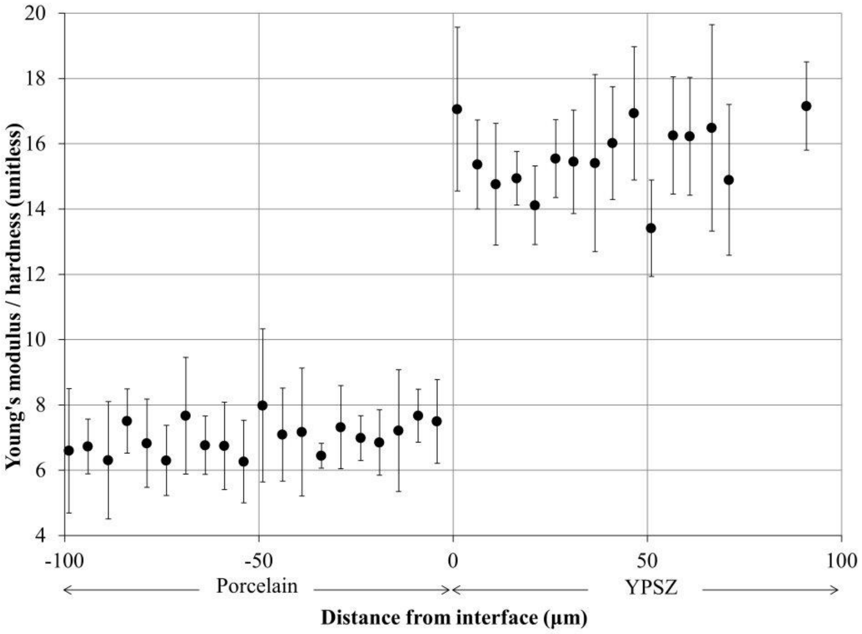

Figure 7.16. Variation of E/H as a function of distance from the YPSZ-porcelain interface. The error bars indicate the 95% confidence intervals of each value.

It was decided that the literature values of Young's modulus and hardness would be used to calculate the E/H ratio for both YPSZ and porcelain as shown in Table 7.1. The magnitude of these bulk estimates are typically more reliable than the results of micro-mechanical testing and the use of these values is also consistent with the approach implemented by Sebastiani et al. [63].

Table 7.1. Mechanical properties and indentation load pre-multipliers for YPSZ and porcelain. The fracture toughness estimate obtained from Berkovich indentation is included for comparison.

Material	E **(GPa)**	H **(GPa)**	K **(MPam$^{0.5}$)**	γ_B	γ_C	K_B **(MPam$^{0.5}$)**
YPSZ	210 [11]	12.75 ± 1.96 [11]	5.00 [11]	0.31 ± 0.02	1.10 ± 0.05	4.79 ± 0.24
Porcelain	60 [17]	5.40 ± 0.20 [17]	2.75 ± 0.25 [17]	0.22 ± 0.01	0.41 ± 0.04	2.65 ± 0.27

Micropillar Splitting

After successfully fracturing each of the 60 FIB milled pillars, analysis was performed on the load-displacement curves obtained from the analysis. Distinct differences were observed between the fracture of the YPSZ and porcelain micropillars, examples of which are shown in Figure 7.17. In the case of porcelain, brittle failure occurred without the onset of plasticity. However in the case of YPSZ, a gradient decrease in the load-displacement plot was observed prior to failure. Despite these differences, consistent estimates of the critical instability load (P_C) were obtained from each of the pillars from the point where large drops in the load were observed.

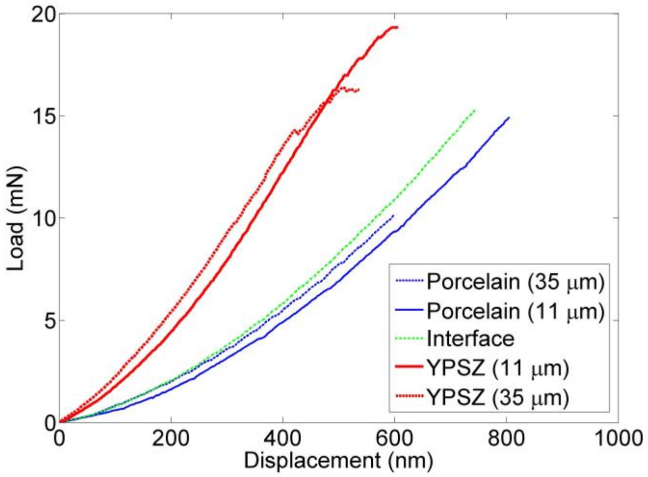

Figure 7.17. Typical load-displacement plots for YPSZ, porcelain and the interface up to the point of brittle failure. The distance from the interface to the pillar center is given in the plot legend.

In order to obtain estimates of the fracture toughness of each of the pillars, quantification of the Berkovich indentation load pre-multiplier γ_B for each material were next obtained. These were based on the bulk values of Young's modulus and hardness for YPSZ and porcelain outlined in Table 7.1 as well as Equation 7.1. Estimates of the Berkovich fracture toughness were then determined using Equation 2.16. In order to provide comparisons with the cube corner indentations, the average value of K_B was determined at positions where both techniques had been applied; at $60, 70$ and 80 μm from the interface for porcelain and at $35, 50$ and 60 μm from the interface for YPSZ. The averages and standard deviations of K_B acquired from these three points are given in Table 7.1. These estimates were then treated as absolute measures of fracture toughness in order to optimize γ_C, the cube corner indentation load pre-multiplier for each material. This parameter relates the cube corner fracture toughness K_C to the critical instability load, through the expression:

$$K_C = \gamma_C \frac{P_C}{R^{3/2}}. \tag{7.3}$$

The magnitude and standard deviation of γ_C for YPSZ and porcelain determined in this analysis are given in Table 7.1. These estimates were then used in combination with the critical fracture toughness values to obtain estimates of the K_C in the YPSZ and porcelain near-interface regions. At the locations where both YPSZ and porcelain were contained within the pillar an average value of $\gamma_C = 0.5 \times \left(\gamma_C^{Zir} + \gamma_C^{Por}\right)$ was used to determine K_C. The standard deviations of the fracture toughness values were acquired from the combined uncertainties of each of the parameters used in their calculation and the results of this analysis are shown in Figure 7.18.

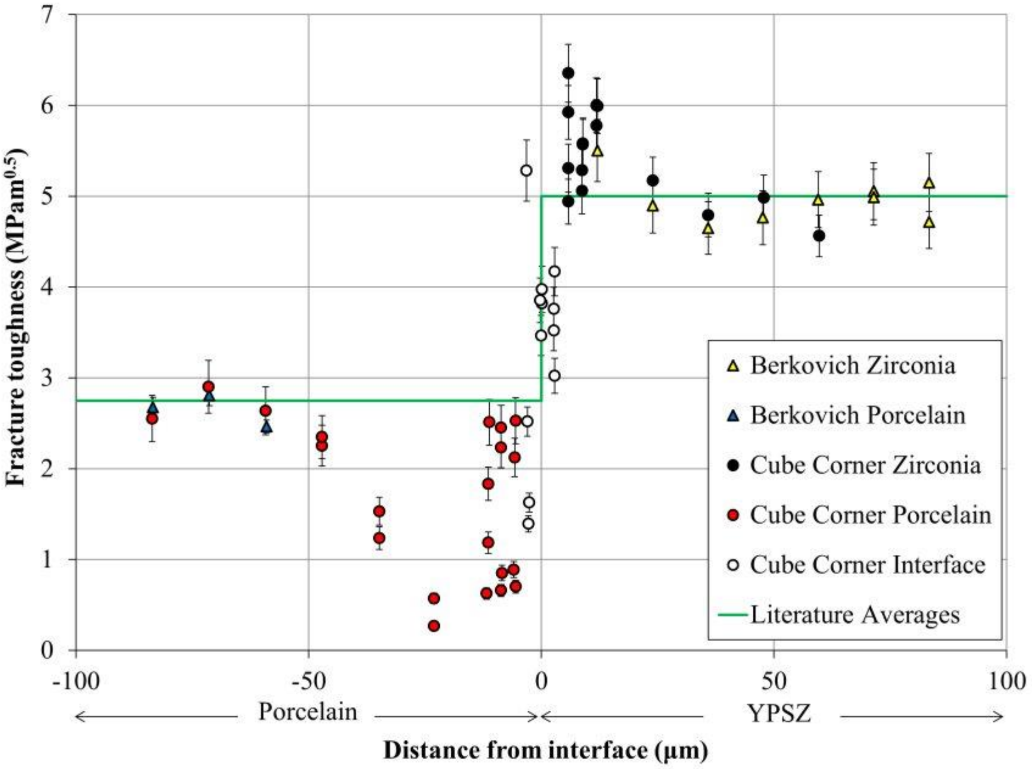

Figure 7.18. Fracture toughness variation across the YPSZ – porcelain interface. The results from both Berkovich and cube corner indentation are shown along with the average values obtained from the literature [11, 17]. The error bars indicate the 95% confidence intervals.

Examination of the SEM images of the fractured pillars revealed that the average offset between the center of the pillar and the indenter tip was less than 100 nm for the cube corner indentations, compared with $100 - 300$ nm for the Berkovich tip. Four main failure modes were observed in the pillars depending upon the substrate material, location and indenter tip geometry as shown in Figure 7.19.

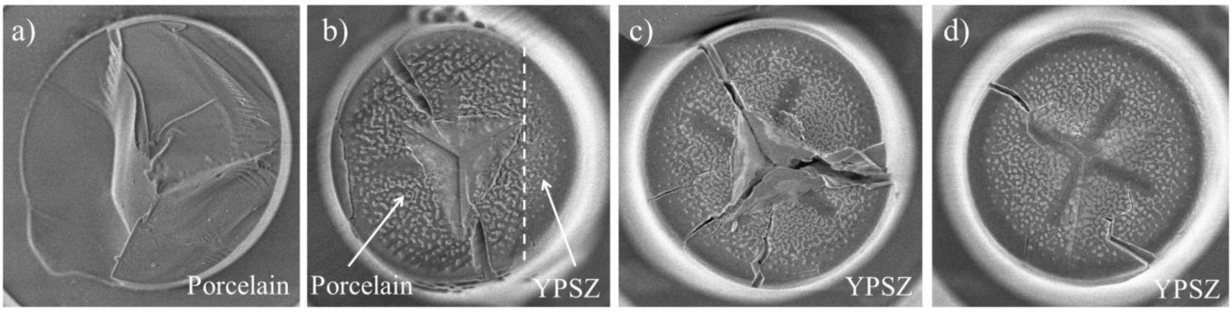

Figure 7.19. SEM images of fractured pillars. a) Complete brittle failure of a porcelain micropillar. b) Typical near-interface cube corner micropillar failure showing pillar splitting. Examination of multiple interface fractures revealed that the fracture direction was often closely aligned to the interface. c) Typical YPSZ cube corner tip fracture showing multiple cracks. d) Berkovich tip indentation of a YPSZ micropillar.

Examination of the porcelain micropillars revealed that for many of the tested positions, the indentation had been sufficient to fully fracture the stub, leaving only the base or a small section of the pillar (Figure 7.19a). The smooth, sharp facets of the remaining surfaces suggested that porcelain failure was brittle, in contrast to the gradual failure in YPSZ. In near-interface pillars, which contained both YPSZ and porcelain within a single pillar (Figure 7.19b), a different failure mode was widely observed. Typically the pillar was found to fracture into two pieces, with the direction of fracture being closely aligned to the interface direction. The fracture of these pillars was sharp suggesting a single failure event, and the crack was typically induced within the porcelain at a distance of between $1-2$ μm from the interface. Cube corner indentation of YPSZ resulted in pillar splitting along the sharp edges of the indent as shown in Figure 7.19c. The surface of these fractures was highly faceted suggesting failure increased gradually through the continued application of load. In contrast to this behavior, Berkovich indentation cracks were localized to pillar edges in YPSZ, this was believed to be associated sub-surface cracking which propagated to the pillar surface as shown in Figure 7.19d.

7.5.3.Discussion

Examination of the fracture toughness variation across the interface in Figure 7.18 reveals that beyond 50 μm from the interface in porcelain and beyond 25 μm in YPSZ, the fracture toughness is approximately constant and equal to the average values published in the literature [11, 17]. This suggests that the results obtained though the of Berkovich pillar splitting approach developed by Sebastiani et al [63, 104] are reliable in both YPSZ and porcelain. Further, the minimal variation in fracture toughness ensures that the calibration of γ_C implemented based on constant K values is valid.

The values of γ_C for YPSZ and porcelain were determined to be 1.10 and 0.41 respectively. Pillar splitting using a cube corner indentation tip has not previously been published in the literature and therefore no comparative results are available The magnitude of these pre-multipliers are several times larger than the equivalent γ_B values for each material and are known to be associated with the sharper indentation and increased surface sliding associated with a cube corner indent. This induces a different type of pillar failure but also increases the sensitivity of the technique to the friction coefficient between the diamond tip and the substrate material. Despite these differences, the variation in fracture toughness obtained through cube corner indentation appears to be realistic and can begin to explain the high failure rates of this system.

In order to gain insight into the scatter within the very near interface region (< 15 μm) a systematic examination was performed to assess factors which may have influenced these values. No correlation could be observed between the fracture toughness and the magnitude of misalignment between the pillar centre and the indentation position. In contrast, the analysis instead revealed that the pillar splitting approach is robust to minor errors in indenter positioning. Analysis was also performed to assess the impact of spatial positioning (along the interface direction), pillar diameter and pillar height on the fracture toughness values obtained. No trends could be identified in any of these parameters, suggesting that the scatter in the near-interface region is instead more likely to be representative of the random fracture toughness variation at this location.

As previously highlighted, there were distinct differences between the YPSZ, porcelain and interface failures. Figures 7.15b and 7.19c both demonstrate that the failure of YPSZ is gradual and occurs by crack propagation and slow growth under increasing load. This results in a reduction in gradient on the load-displacement curve which is indicative of energy absorption and a ‘plastic’ type failure. The multi-faceted crack surfaces of the fractured pillars provide further evidence that YPSZ failure is associated with gradual crack growth. In contrast to this behaviour, Figures 17.15d and 7.19a highlight the brittle failure mode induced in porcelain. There is no change in gradient on the load-displacement curve and complete pillar fracture occurs at a point at which there were no visible cracks in the pillar surface.

In the near interface region, a distinct failure mode is observed which is believed to be a combination of both the YPSZ and porcelain failure mechanisms and preferential pillar splitting along the direction of the YPSZ-porcelain interface. Planar interfaces are implicitly associated with orientational dependence and therefore it is perhaps unsurprising that the half pillar splitting in the interface region is preferentially aligned to the interface. What is however more surprising is that failure was not induced at the interface location, where a step change in mechanical properties is expected, or at the pillar centre. Failure was found to be more likely within the near-interface porcelain at a distance of between $1 - 2$ μm from the interface. This length scale correlates well with the position of nanoscale voiding determined in the TEM study, suggesting that there may be an implicit weakness in the porcelain at this location. The random nature of void type features may also explain the large scatter in the fracture toughness of the near-interface porcelain pillars.

Clear differences can be observed between the literature average values of fracture toughness and those obtained micropillar splitting for both YPSZ and porcelain in the near-interface region (Figure 7.18). There is a reduction in fracture toughness of porcelain (by up to $\approx 90\%$) starting at a distance of approximately $50\ \mu\mathrm{m}$ from the interface and extending to the near interface location. This variation is highly self-consistent, suggesting that this weakness may be associated with a gradual variation in mechanical properties. For example, through localised creep rate behaviour which is known to reduce the fracture toughness of porcelain [324]. In contrast, at distances less than $15\ \mu\mathrm{m}$ from the interface, the data shows a large amount of scatter suggesting more statistically driven weaknesses than those seen at larger distances.

The variation of fracture toughness within the interface pillars (containing both YPSZ and porcelain) demonstrates relatively high levels of scatter with an average value of $3.8\ \mathrm{MPam}^{0.5}$. This corresponds well with the average literature fracture toughness values of YPSZ and porcelain of $3.9\ \mathrm{MPam}^{0.5}$. Despite this consistency, the fracture toughness in pillars containing mostly porcelain shows high levels of scatter. Of the four pillars measured, three are within the scatter observed in the neighbouring porcelain however one high toughness pillar ($5.3\ \mathrm{MPam}^{0.5}$) was present at this location, this may be an outlier or perhaps is more representative of failure within YPSZ.

In YPSZ the fracture toughness is approximately constant and equal to the literature value of $5\ \mathrm{MPam}^{0.5}$ up a distance of $15\ \mu\mathrm{m}$ from the interface. In the near-interface region there is an $\approx 10\%$ increase in fracture toughness and an increase in scatter, with values between $4.9 - 6.4\ \mathrm{MPam}^{0.5}$ being observed. This scatter suggests that this behaviour is statistically driven, rather than a gradual transition and therefore is likely to be associated with local features. One explanation may be high elemental composition sensitivity of YPSZ fracture toughness [325, 326]. However, the grain size dependence of YPSZ fracture toughness is perhaps more likely [327]. Larger grains of YPSZ are more likely to transform from a tetragonal to a monoclinic phase during stress application, increasing the amount of energy absorbed by the material during fracture. The TEM analysis outlined in § 7.2 previously highlighted YPSZ grain size variations at this location, including the presence of relatively large grains ($1 - 2\ \mu\mathrm{m}^2$) within the first $10\ \mu\mathrm{m}$ of the interface. This scatter may therefore be dependent upon the presence, or lack of, a large grain within the gauge volume under consideration.

7.6. Conclusions

In this chapter, four complimentary micro-scale experimental techniques were applied across the YPSZ – porcelain near-interface region of a cross section of a dental prosthesis. All four studies represent ‘first insight’ into the characteristic behaviour at the YPSZ-porcelain interface in a representative dental sample. In the case of EDXS, the broad range of elemental species assessed, and high resolution analysis performed, provides critical insight into the elemental diffusional distances and associated mechanical and microstructural variations induced by this effect. The TEM analysis has provided much improved insight into the near-interface characteristics of both YPSZ and porcelain, in terms of the nanovoiding and grain size variation in these regions. Both the micropillar compression and micropillar splitting studies represent the first published work in which spatially resolved mechanical analysis has been performed. Further, cube corner indentation (which can be aligned more quickly and precisely to pillar centers) has been shown to provide realistic estimates of fracture toughness by making use of a new critical failure load pre-multiplier γ_C.

At distances greater than $10 - 15$ μm from the interface YPSZ was found to be highly uniform and consistent with published values both in terms of elemental composition and mechanical behaviour. In this region YPSZ has been shown to fail through a gradual, ‘plastic’ type fracture mode in which cracks incrementally propagate, until a critical load is reached and the load drops in magnitude.

Mechanical variations in the near-interface YPSZ were observed within the first ≈ 10 μm of the interface. Within this region a 10% increase in fracture toughness was identified, along with a $5 - 15\%$ increase in loading modulus. This may be associated with grain size variation or perhaps more likely is associated with the tetragonal to monoclinic phase transformation. Within the first 3 μm of the interface TEM analysis demonstrated clear variations in grain morphology within YPSZ. This length scale closely matches the limits on elemental diffusion of Si, K, Zn and Al and suggests that these two effects are likely to be directly related. This position also corresponds to a peak in loading modulus (242 GPa at 5 μm from the interface).

TEM imaging of the near interface porcelain demonstrates creep induced nano-scale voiding within the first few microns of the interface. In this region, EDXS analysis has revealed elemental diffusion of Zn and Y along with the presence of YPSZ particles which have detached from the YPSZ surface and become embedded in the porcelain. Across the interface a distinctive half pillar splitting type failure was also observed during fracture toughness testing. This failure was typically aligned with the interface and was at a distance of $1 - 2$ μm from the interface. Variations in loading modulus and yield strength were also seen, suggesting that the combined effects of nanovoiding and elemental variation in the near-interface porcelain were sufficient to severely alter the mechanical characteristics at this location.

Scatter was also observed in the fracture toughness values of porcelain within the first 15 μm of the interface, which was followed by a gradual and consistent reduction in toughness within the first 50 μm of the interface (of up to $\sim 90\%$). This large reduction in fracture toughness corresponded to a region of decreased yield strength and has the potential to explain the high failure rates at this location.

At distances greater than 50 μm from the interface the mechanical properties of YPSZ and porcelain were reasonably constant. Any minor variations are most likely associated with the slight variations in local elemental composition.

Overall, these four studies indicate that there are distinct variations in the microstructure, mechanical properties and elemental composition across the YPSZ-porcelain interface. These variations arise through a complex interplay between diffusion, thermal treatment, grain growth kinetics, residual stress, creep behaviour and grain cohesion in this region. Further discussion on the potential origins and interaction between these effects are outlined in Chapter 8.

8. Discussion and Conclusions

This chapter draws together the conclusions from each of the studies outlined in this thesis in order to provide critical assessment of the results obtained. The integration of these results can provide potential explanations for the failures observed, as well as possible interpretations for the impact of the parameters which are known to influence prosthesis failure rates, as outlined in § 8.1. A brief overview of the achievements outlined in this thesis are then provided in § 8.2, along with potential future studies arising from the results in § 8.3. The main conclusions of the thesis are then summarised in § 8.4

8.1. Compendium of Mechanical Microscopy of the YPSZ-porcelain Interface

In order to improve the understanding of the underlying processes responsible for the near-interface residual stresses and phase transformations identified in this thesis, consideration of the mechanical properties and microstructure at this location is necessary. In this regard, Figure 8.1 has been produced as a compendium of the results of the high resolution property profiling across the YPSZ-porcelain interface. Figure 8.1a shows the variation of residual stress across the entire YPSZ-porcelain interface which has been determined using FIST sequential ring core residual stress analysis (in § 6.5.1). In Figure 8.1b the Young's modulus and yield strength results obtained using micropillar compression (from § 7.4), and the fracture toughness variation from micropillar splitting (in § 7.5) are shown. The results of EDXS have also been included in Figure 8.1c.

The variations in phase composition, in combination with mechanical property assessment and the results of TEM provide a comprehensive overview of the near-interface YPSZ. Within the first 200 nm of the interface a band of small ($5 - 70$ nm diameter) YPSZ grains are present. Immediately adjacent to this band lies a ~2 µm thick region which shows no obvious grain boundaries, but the presence of high contrast features similar to those observed in monoclinic YPSZ [309, 310]. The location and thickness of this phase change correspond closely with the results of Raman spectroscopy and XRD which revealed a region containing up to 60% YPSZ monoclinic phase within the first 3 µm of the interface. In these studies, monoclinic YPSZ was observed up to ≈ 10 µm from the interface, agreeing closely with the 12 µm length scale over which increased fracture toughness (by $\approx 10\%$) was seen within the YPSZ. Previous studies have indicated that increased amounts of monoclinic phase as well as the larger grain features at this location affect fracture toughness through an increased propensity to transform [327].

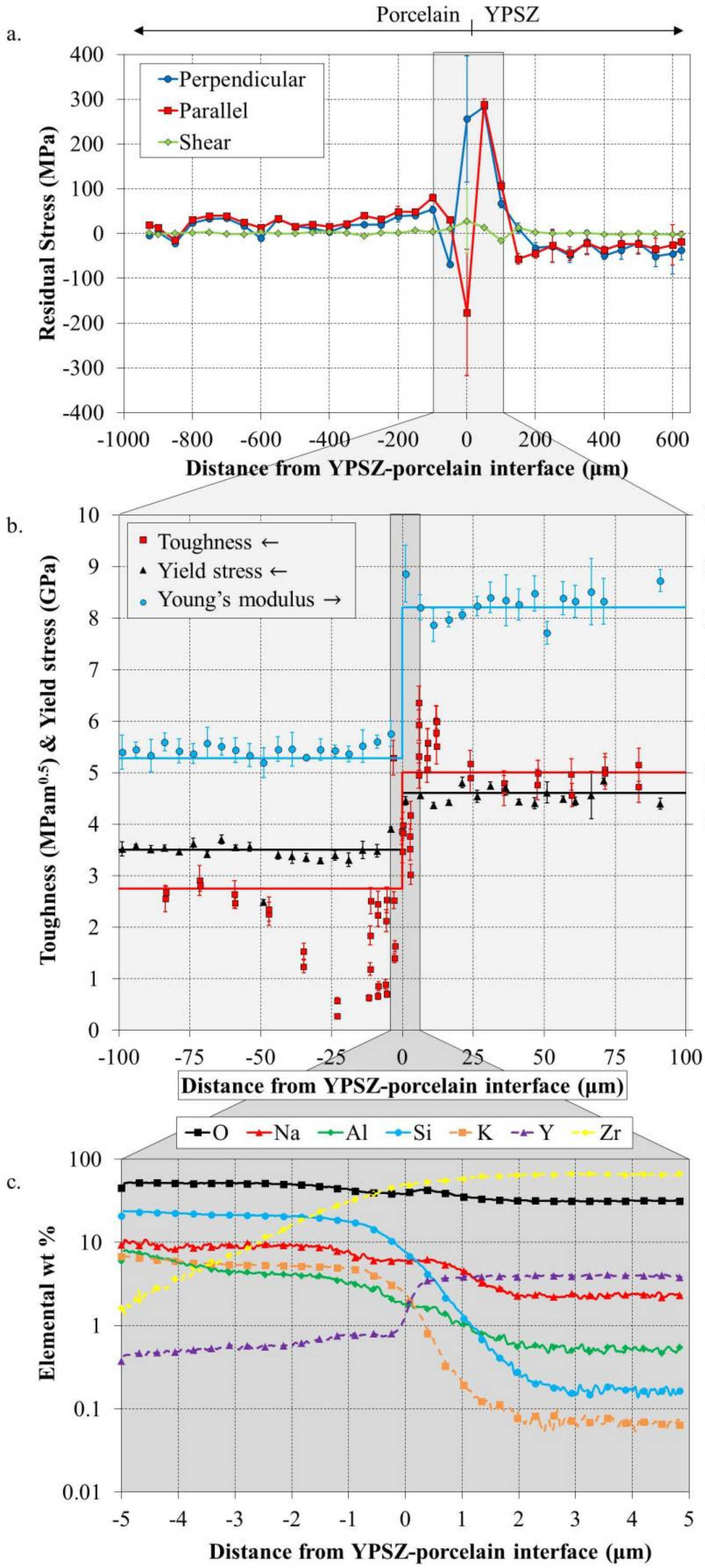

Figure 8.1. Compendium of property profiling across the YPSZ-porcelain interface. Error bars indicate 95% confidence intervals and solid lines indicate bulk averages. a) Sequential ring-core FIB milling. b) K, E and σ_y from micropillar analysis. c) EDXS results.

A distinct variation in Young’s modulus has also been characterised within the first $10\ \mu\mathrm{m}$ of the interface, with an increasing trend stiffness found in the three measurements closest to the interface. Monoclinic YPSZ is known to have a different elastic response than tetragonal YPSZ, and this may be the origin of this behaviour [189]. The impact of elemental diffusion may also be influencing the near-interface YPSZ state and mechanical response, with typical diffusional distances of $2 - 3\ \mu\mathrm{m}$ being observed in YPSZ.

The near-interface porcelain also has characteristic structural features that have also been observed using the different analytical techniques applied. Nanoscale voids with the average diameter $\approx 10\ \mathrm{nm}$ were identified at distances in the range $0.4 - 1.5\ \mu\mathrm{m}$ from the interface which closely match nanovoiding induced by high temperature tensile creep by in Chapter 5. Although no nanoscale structural evidence for creep was identified at distances $> 2\ \mu\mathrm{m}$ from the interface, the larger distances over which moderate tensile residual stresses have been characterised ($\approx 100\ \mu\mathrm{m}$) indicate that creep is likely to also occur within this region (Figure 8.1a). Further evidence for this behavioural response is given by the large (up to $\approx 90\%$) decrease in the fracture toughness of porcelain within the first $50\ \mu\mathrm{m}$ of the interface (Figure 8.1b). Tensile creep damage of similar silica based ceramics have been shown to influence both the fracture toughness and yield strength of these materials [56] and a smaller reduction in yield strength (of up to $\approx 10\%$) has also been identified within the first $10 - 50\ \mu\mathrm{m}$ of the interface. Elemental diffusion may also be influencing the mechanical response of the very near-interface region, with the depth of diffusion of zirconium into porcelain found to be $\approx 5\ \mu\mathrm{m}$. The increased stiffness and yield strength of zirconia may explain the minor increase in these two parameters at the measurement point at $4\ \mu\mathrm{m}$ from the interface.

The conventional design approach which is used in the manufacture of YPSZ-porcelain dental prosthesis is to ensure that the CTE of porcelain is moderately lower than that of YPSZ, thereby generating low magnitude compressive residual stress in the veneer and exploiting the higher magnitude compressive strength of this material (relative to the tensile behaviour) [29]. Despite using this design principle in this study, the average residual stress state within the porcelain has been found to be mildly tensile. This agrees with the results of similar studies within the literature [33, 34, 296] and suggests that the phase transformation at the YPSZ-porcelain interface is influencing the residual stress in the veneer.

Another factor to highlight at this stage is that the analytical decomposition of the residual stress state within YPSZ (in § 6.6) reveals that a parabolic residual stress state is likely to be present within the coping before the veneer is applied. This state is associated with the high temperature sintering used in the manufacture of the YPSZ and is associated with tensile stresses at the coping surface, and compressive stresses in the core.

The combination of microstructural, micromechanical and residual stress analysis obtained in this study and presented in the above discussion leads to the following explanation for of the origins of the observed behaviour. During manufacture, the porcelain slurry is initially applied to the surface of the already sintered YPSZ coping at room temperature. This component is then heated to $750℃$ in a vacuum furnace in order to fire the veneer. During cooling, the CTE mismatch between the YPSZ and porcelain drives the boundary layer of near-interface porcelain into compression, and increases the magnitude of the tensile stress in the near-interface YPSZ. This tensile region is contained within ≈ 200 μm of the interface and has a peak stress which is located at the YPSZ-porcelain interface.

During further cooling, the peak tensile stresses at this near-interface location reach a sufficient magnitude to induce the tetragonal to monoclinic phase transformation in YPSZ [29]. This is associated with a 4% volume expansion in the monoclinic grains (as shown by the eigenstrain gradient transformation plasticity model in § 6.6.3) which act to greatly reduce the average tensile stress within this region of YPSZ. Importantly, the relaxation of the neighbouring tetragonal grains may not be as large as that of their monoclinic counterparts. This explains the discrepancy between the XRD (exclusively tetragonal phase) and ring-core (overall average) stress evaluation results at this location. The 60% volume fraction of transformed material within YPSZ leads to a strain expansion which is sufficient to replace the compressive stresses within the near-interface porcelain veneer with residual tension. It is this locked-in residual stress state at the YPSZ-porcelain interface that acts as the driving force for the porcelain chipping failure.

The next stage of veneer fabrication involves the application of another layer of slurry and reheating the system to $750℃$ in order to sinter the new material. This temperature is insufficient to melt the proceeding layer of porcelain, but has shown to be sufficient to induce creep at tensile stresses in Chapter 5. Tensile creep is activated within the porcelain in the first 50 μm from the interface. This process reduces the residual tensile stresses within this region, but leads to a reduction of fracture toughness and yield stress at the YPSZ-porcelain interface. The application of further veneering layers leads to further reduction of the tensile stresses in the near-interface region, but at the expense of degrading the mechanical integrity of porcelain in this area.

The interaction outlined above provides an explanation for several observations of the YPSZ-porcelain system that have been reported previously:

1. The primary failure mode of these prostheses (through porcelain chipping) originates almost entirely from the very near-interface region [6, 300]. This is the location of porcelain creep, moderate tensile stresses and the region of greatly reduced mechanical strength.
2. Thicker veneers are known to result in higher failure rates in YPSZ prostheses [18]. Force equilibrium of the CTE mismatch of thicker veneers will result in larger tensile stresses at the YPSZ-porcelain interface, increasing the amount of transformed YPSZ and thereby inducing more damage in the near-interface porcelain. It is worth noting that other effects such as the amount of strain energy induced by thermal expansion mismatch, and the associated energy release rate also increase with the thickness of the applied veneer.
3. Heat treatment of the prosthesis may lead to either increased or reduced integrity, depending upon the conditions and number of cycles applied [328]. This behaviour arises as a consequence of interplay between tensile stress relaxation of the near-interface region and the increased creep damage associated with this process. An optimum thermal cycle may exist that minimises the induced residual stresses without excessive reduction in mechanical properties.
4. Abrasive surface treatment of the YPSZ surface leads to increased reliability of the prosthesis [329]. Sand or air blasting of the YPSZ surface is known to induce the YPSZ tetragonal to monoclinic phase change within a micro-scale near-interface region [14]. This approach reduces the extent of any further transformation during the sintering cycle, thereby minimising tensile residual stress build up and creep effects in the porcelain veneer.
5. Smaller differences in thermal expansion mismatch lead to increased prosthesis reliability [330]. By reducing the strain mismatch induced between the YPSZ and porcelain during cooling, this approach minimises residual stress build up and creep induced damage in the near-interface porcelain.

6. Slower heating and cooling rates during YPSZ coping sintering reduce the likelihood of porcelain chipping [280]. This process minimises the magnitude of the tensile stresses induced in the near-surface regions of the coping and reduces the propensity of this region to transform. In turn, the magnitude of the tensile residual stresses in the near surface porcelain are minimised.

8.2. Main Achievements and Current State-of-the-art

This section provides a brief overview of the main conclusions and new techniques outlined in this thesis, along with the connections between each of the studies presented. In Chapters 1 and 2, an introduction to existing experimental methods and the current state of the literature was presented as a starting point on which this analysis has been based.

Chapter 3 presents the work I performed to refine and expand upon the ring-core FIB milling and DIC residual stress analysis technique. A fully automated outlier removal and error propagation analytical routine has been developed and is presented. This methodology has been critical in facilitating efficient, reliable and operator independent results, as well as providing precise estimates of the confidence bounds on stress estimates. A new approach for ring-core FIB milling and DIC full in-plane strain tensor analysis has also been established along with two new spatially resolved residual stress analysis techniques; the sequential ring-core approach for incremental measurements between mm and tens of microns, and the parallel approach for between $1 - 10$ μm. All of these techniques have been validated using XRD and have proven to be effective in determining estimates of unstrained lattice parameters. These refinements have greatly increased the capabilities of the ring-core FIB milling approach, and have provided the tools necessary to investigate the YPSZ-porcelain interface, as outlined in Chapter 7.

Quantification of the single crystal stiffness of YPSZ is known to be particularly challenging using traditional wave based techniques and Chapter 4 presents a new approach using polycrystalline neutron diffraction. This technique is based on FE simulations and model matching of *in situ* compressive loading of YPSZ to refine estimates of the single crystal parameters. These improved estimates are necessary to enhance existing models of the YPSZ-porcelain interface, which have the potential to reduce prosthesis failures rates through process parameter optimisation as outlined in § 8.3.

The combination of high magnitude stresses identified in Chapter 6, and porcelain nanovoiding observed at the interface in Chapter 7 suggested that creep may be induced in the near-interface porcelain. In order to improve understanding of this behaviour, in Chapter 5 a new high temperature tensile creep approach has been established which can be implemented on the small ceramic sample sizes used in the dental industry. This approach quantified the tensile secondary creep rate behaviour of dental porcelain for the first time, and was used to generate crept samples for nanostructural characterisation. A comparative TEM and SANS study was then performed to gain insight into the nanoscale characteristics of crept porcelain. This creep induced nanovoiding shows strong similarities with those identified at the YPSZ-porcelain interface and suggests that this may be associated with porcelain chipping.

In Chapter 6, the refined ring-core FIB milling and DIC techniques (FIST, sequential and parallel) have been applied to assess the residual stress variation in a YPSZ-porcelain cross-section. High resolution ($1\ \mu\text{m}$) cross-validation has been performed in YPSZ using XRD and Raman spectroscopy, which indicated high magnitude ($200 - 300\ \text{MPa}$) tensile stresses within the first $100\ \mu\text{m}$ of the interface. These two approaches were also used to study the phase composition of YPSZ, which was found to have transformed within the first $10\ \mu\text{m}$ of the interface. In order to provide cross-validation of the stress state within the amorphous porcelain, a new experimental approach has been established based on peak shifting of the PDF distributions obtained from XRD. As well as presenting a brand new amorphous strain characterisation tool, the results of this analysis demonstrate that the layering approach used to manufacture the veneer induces cyclic tensile and compressive stresses, and that bond rotation is critical in atomic scale strain accommodation in this material. This chapter provides insight into the residual stress variation across the YPSZ-porcelain interface at a resolution far surpassing any previous analysis and has therefore been able to capture the stress induced YPSZ phase transformation at the interface for the first time. Importantly, analytical modelling of the impact of CTE mismatch and the residual stress induced by YPSZ sintering could be used to match the stress distribution observed at the macroscale. Eigenstrain gradient transformation plasticity was also able to capture the behaviour of the near interface region, which is critical in understanding failure at this location, as outlined in § 8.1.

In order to understand the impact of the highly localised (microscale) phase transformation and residual stress state on near-interface characteristics, high resolution microstructural and mechanical analysis has been performed, as outlined in Chapter 7. EDXS revealed characteristic elemental diffusion in both YPSZ and porcelain at micrometer length-scales, at the exact location that failure occurs. TEM analysis revealed a complex microstructure within the first few microns of the interface, including porcelain nanovoiding as well as YPSZ transformation induced twinning. A new approach, based on using micropillar arrays to assess spatially resolved mechanical properties was then carried out using both micropillar compression and the first ever implementation of cube corner pillar splitting. This analysis revealed distinct loading modulus, yield strength and fracture toughness behaviour within the first few microns of the interface in both YPSZ and porcelain, which arise as a result of phase transformation and creep induced damage, respectively.

The integration of the results obtained in this study can begin to provide an explanation for the high failure rates observed in YPSZ dental prosthesis, as outlined in § 8.1. The origins of this behaviour are closely related to thermal expansion mismatch between YPSZ and porcelain, the stress induced YPSZ phase transformation and resulting porcelain creep. This improved understanding also provides explanations for several of the parameters known to influence prosthesis failure rates.

8.3. Future Work

In this thesis conscious and focused effort has been directed towards characterising the mechanical and structural state of the YPSZ-porcelain interface, in order improve understanding the relatively high failure rates at this location. In contrast to previous analysis based on incremental improvement of manufacturing routines through trial and error, the insight gained through this analysis facilitates directed optimisation of the prosthesis design and processing routes in order to minimise failure rates.

Prior to the establishment of new optimised designs, it is important to highlight that it has been necessary to direct the focus of this study towards a few representative samples. This focused approach has not facilitated investigation into the scatter / variation of the mechanical properties within a batch of samples or even within a single specimen. Therefore assessment of this variation forms a critical next step in the study of the YPSZ-porcelain interface. Initially, I believe that focus should be directed towards conventional prosthesis design in order to fully characterise the behaviour of these components. As previously highlighted, assessment of alternative manufacturing routes has previously provided varying and contradictory results, and therefore complete understanding of the fundamentals of this mechanical system are initially required in order to understand the impact of process changes.

The most effective approach which can be used to combine the insights and results obtained from this thesis is the use of mechanical modelling. This methodology can build on analytical routines outlined in § 6.6, along with the polycrystalline interactions and the single crystal stiffnesses outlined in Chapter 4. The creep rate characteristics and associated reductions in mechanical strength outlined in Chapter 5 also need to be integrated into this simulation. Finally, the mechanical and structural variations observed across the interface also need to be included in order to fully capture the prosthesis behaviour.

Several potential types of model could be used to perform the necessary simulations across the YPSZ-porcelain interface, however one of the most promising approaches appears to be based on phase field analysis [331, 332]. This approach would be particularly effective at capturing the stress induced phase transformation characteristics of the near-interface region and the associated interaction between monoclinic and tetragonal grains. Alternatively, simulations based on FE models could be established in order to fully accommodate the interface behaviour, thermal characteristics, creep response and variations in mechanical properties observed at the interface [333].

As outlined in § 8.2, there are a number of different parameters which are known to influence the failure rates of YPSZ-porcelain prosthesis. Modelling provides a versatile, efficient and effective optimisation tool which can be used to investigate the response of the YPSZ-porcelain interface to these differing variables. Potential investigations can be grouped into three main categories:

1. *Thermal processing routes.* The veneer sintering regime applied to the YPSZ-porcelain prosthesis can be assessed to determine the impact of differing dwell times, sintering temperatures as well as the heating and cooling rates implemented. As outlined in § 8.1, the impact of applying multiple veneers (and repeated thermal sintering) is particularly influential on the microstructure of the YPSZ-porcelain interface and can be assessed through modelling. Post processing of the prosthesis through temperature dwells also has the potential to relieve residual stresses within the veneer, at the expense of increased porcelain creep and the interaction between these two processes can be evaluated and optimised.
2. *Material optimisation and selection.* Many differing types of dental YPSZ and porcelain are commercially available, however the complex interaction between these two materials presents severe difficulties in materials selection. The establishment of an effective and representative model would facilitate material optimisation in terms of CTE, porcelain creep characteristics,

the transformability of YPSZ and the mechanical parameters of each material. For example, a higher concentration of yttria increases the stabilisation of YPSZ and reduces the likelihood of transformation at the interface at the expense of a more brittle coping material.

3. *YPSZ coping treatment.* The manufacture of the YPSZ coping is dependent upon several parameters which have the potential to be optimised in order to minimise chipping of the porcelain veneer. Of particular importance is the residual stress state and phase composition of the near interface region prior to veneering. Thermal or surface treatment could potentially be used to alter these parameters and thereby reduce chipping rates.

Although modelling offers an effective approach which can be used to suggest improved manufacturing routes, further mechanical testing of these optimised designs is necessary. The next stage of analysis would therefore be to manufacture prosthesis based on the newly optimised parameter design and to use the suite of refined analytical tools presented in this thesis in order to assess the impact of this new approach. As highlighted above, this approach would likely involve assessment of the variability between multiple components, and would also require clinical testing.

The overall aim of all of this analysis would be to use the improved insight offered by the results presented in this thesis, in combination with the new experimental techniques which have been established, to reduce the likelihood of near-interface chipping in commercially manufactured YPSZ-porcelain dental prostheses.

8.4. Conclusions

In this thesis a focused and critical assessment of the mechanical state and microstructure within the first few hundred microns of the YPSZ-porcelain interface in dental prostheses has been presented. This analysis has involved the first reported application of several well-established techniques including Raman spectroscopy, TEM, SANS, XRD and EDXS analysis. Several recently proposed experimental techniques were also modified and refined to furnish the insight required, namely, the ring-core FIB milling and DIC residual stress analysis technique, and micropillar compression and splitting. The development of several new experimental techniques has been necessary to capture fully the interface characteristics, including amorphous strain quantification through X-ray PDF analysis, a new tensile creep loading methodology, and a method for single crystal stiffness quantification from powder diffraction data.

The results of this analysis reveal complex chemical, microstructural and mechanical interactions at the interface that locally (within $\approx 50 - 100\ \mu m$) modify the elemental composition, phase composition, defect population and grain morphology, residual stress state and fracture response in this region. This behaviour is a direct consequence of the manufacturing process used to produce YPSZ-porcelain dental prostheses and results in a localised band of weakness in the near interface porcelain. The combination of mastication loading and this strength reduction is sufficient to induce early onset of failure through porcelain chipping, and can explain the relatively high failure rates reported during clinical trials.

9. References

[1] F. Zarone, et al. From porcelain-fused-to-metal to zirconia: Clinical and experimental considerations, Dent Mater, 27 (2011) 83-96.

[2] C. Piconi, G. Maccauro. Zirconia as a ceramic biomaterial, Biomaterials, 20 (1999) 1-25.

[3] R.C. Garvie, et al. Ceramic steel?, Nature, 258 (1975) 703-704.

[4] R.M. McMeeking, A.G. Evans. Mechanics of Transformation-Toughening in Brittle Materials, J Am Ceram Soc, 65 (1982) 242-246.

[5] M.J. Kim, et al. Wear evaluation of the human enamel opposing different Y-TZP dental ceramics and other porcelains, J Dent, 40 (2012) 979-988.

[6] J. Schmitt, et al. Zirconia Posterior Fixed Partial Dentures: A Prospective Clinical 3-year Follow-up, Int J Prosthodont, 22 (2009) 597-603.

[7] C.E. Misch. Dental Implant Prosthetics, Elsevier Health Sciences, 2014.

[8] Cemented Implant.http://www.hertfordshireimplants.co.uk/wp-content/uploads/2012/06/cemented-implant.jpg. 09/02/2016.

[9] P.K. Moy, et al. Dental implant failure rates and associated risk factors, Int J Oral Max Impl, 20 (2005).

[10] Dental cast.http://www.infodentis.com/fixed-prosthodontics/dental-cast.html. 09/02/2016.

[11] Zenotec Zr Bridge.http://www.wieland-dental.de/en/products/zenotec/materials/zenotec-zr-bridge/. 10/09/15.

[12] J.R. Kelly, I. Denry. Stabilized zirconia as a structural ceramic: An overview, Dent Mater, 24 (2008) 289-298.

[13] R.K. Chintapalli, et al. Phase transformation and subsurface damage in 3Y-TZP after sandblasting, Dent Mater, 29 (2013) 566-572.

[14] M. Inokoshi, et al. Structural and Chemical Analysis of the Zirconia–Veneering Ceramic Interface, J Dent Res, 95 (2016) 102-109.

[15] K.J. Anusavice, et al. Phillips' Science of Dental Materials, Elsevier Health Sciences, 2014.

[16] A.J.G. Lunt, et al. An Electron Microscopy Study of Sintering in Three Dental Porcelains, Proc WCE, 2 (2015).

[17] IPS e.max® Ceram Scientific Documentation www.roedentallab.com/downloads/emaxceramicdata.pdf. 19/02/15.

[18] M. Guazzato, et al. Influence of thickness and cooling rate on development of spontaneous cracks in porcelain/zirconia structures, Aust Dent J, 55 (2010) 306-310.

[19] B. Al-Amleh, et al. Clinical trials in zirconia: a systematic review, J Oral Rehabil, 37 (2010) 641-652.

[20] A.J. Raigrodski, et al. Survival and complications of zirconia-based fixed dental prostheses: A systematic review, J Prosthet Dent, 107 (2012) 170-177.

[21] Y. Zhang, et al. Chipping resistance of graded zirconia ceramics for dental crowns, J Dent Res, 91 (2012) 311-315.

[22] X. Tang, et al. Effects of multiple firings on the mechanical properties and microstructure of veneering ceramics for zirconia frameworks, J Dent, 40 (2012) 372-380.

[23] M. Ferraris, et al. Coatings on zirconia for medical applications, Biomaterials, 21 (2000) 765-773.

[24] N. Wakabayashi, K. Anusavice. Crack initiation modes in bilayered alumina/porcelain disks as a function of core/veneer thickness ratio and supporting substrate stiffness, J Dent Res, 79 (2000) 1398-1404.

[25] V. Preis, et al. In vitro failure and fracture resistance of veneered and full-contour zirconia restorations, J Dent, 40 (2012) 921-928.

[26] A.O. Rueda, et al. Tomography of indentation cracks in feldspathic dental porcelain on zirconia, Dent Mater, 29 (2013) 348-356.

[27] Y. Kawai, et al. Microstructure evaluation of the interface between dental zirconia ceramics and veneering porcelain, Nano Biomed, 2 (2010) 31-36.

[28] B. Gökçe, et al. A study of compressive strength between zirconia framework and veneering ceramic as a function of thermal expansion coefficient using Shell–Nielsen test method, J Adhes Sci Technol, 29 (2015) 1924-1936.

[29] A.K. Mainjot, et al. Influence of zirconia framework thickness on residual stress profile in veneering ceramic: Measurement by hole-drilling, Dent Mater, 28 (2012) 378-384.

[30] E.C. Subbarao, et al. Martensitic transformation in zirconia, Physica Status Solidi (a), 21 (1974) 9-40.

[31] M. Allahkarami, J.C. Hanan. Mapping the tetragonal to monoclinic phase transformation in zirconia core dental crowns, Dent Mater, 27 (2011) 1279-1284.

[32] C. Mochales, et al. Monoclinic phase transformations of zirconia-based dental prostheses, induced by clinically practised surface manipulations, Acta Biomater, 7 (2011) 2994-3002.

[33] Y. Zhang, et al. Measuring residual stress in ceramic zirconia–porcelain dental crowns by nanoindentation, J Mech Behav Biomed Mater, 6 (2012) 120-127.

[34] M. Baldassarri, et al. Residual stresses in porcelain-veneered zirconia prostheses, Dent Mater, 28 (2012) 873-879.

[35] M. Sebastiani, et al. Residual micro-stress distributions in heat-pressed ceramic on zirconia and porcelain-fused to metal systems: Analysis by FIB–DIC ring-core method and correlation with fracture toughness, Dent Mater, (2015).

[36] I. Denry, J.A. Holloway. Ceramics for Dental Applications: A Review, Materials, 3 (2010) 351-368.

[37] J. Chevalier. What future for zirconia as a biomaterial?, Biomaterials, 27 (2006) 535-543.

[38] R.H. Hannink, et al. Transformation toughening in zirconia-containing ceramics, J Am Ceram Soc, 83 (2000) 461-487.

[39] A.G. Evans, et al. Martensitic Transformations in Zirconia - Particle-Size Effects and Toughening, Acta Metall Mater, 29 (1981) 447-456.

[40] C. Mercer, et al. On a ferroelastic mechanism governing the toughness of metastable tetragonal-prime (t ') yttria-stabilized zirconia, P R Soc A, 463 (2007) 1393-1408.

[41] T. Sato, et al. Effects of surface-finishing condition and annealing on transformation sensitivity of a 3mol% Y2O3 stabilized tetragonal zirconia surface under interaction of lubricant, Wear, 194 (1996) 204-211.

[42] M. Oishi, et al. Evaluation of Tensile-Strength and Fracture-Toughness of Yttria-Stabilized Zirconia Polycrystals with Fracture Surface-Analysis, J Am Ceram Soc, 78 (1995) 1212-1216.

[43] A. Selçuk, A. Atkinson. Strength and Toughness of Tape-Cast Yttria-Stabilized Zirconia, J Am Ceram Soc, 83 (2000) 2029-2035.

[44] S.R. Choi, N.P. Bansal. Mechanical behavior of zirconia/alumina composites, Ceram Int, 31 (2005) 39-46.

[45] R.P. Ingel, D. Lewis. Elastic-Anisotropy in Zirconia Single-Crystals, J Am Ceram Soc, 71 (1988) 265-271.

[46] G. Fadda, et al. First-principles study of the structural and elastic properties of zirconia, Phys Rev B, 79 (2009).

[47] W.J. O'Brien. Dental materials and their selection, Quintessence Publ., 1997.

[48] E. Zúñiga-Márquez, et al. Nanoindentation analysis within the elastic regime of zirconia-based materials for advanced gas turbines, Proc SBOMat, C (2008).

[49] Vitablocs for Cerec / inLab Working Instructions.https://www.vita-zahnfabrik.com/en/VITABLOCS-Mark-II-25030,27568.html. 10/03/2015.

[50] E.A. McLaren, P.T. Cao. Ceramics in dentistry—part I: classes of materials, Inside dentistry, 5 (2009) 94-103.

[51] A. Shenoy, N. Shenoy. Dental ceramics: An update, J Cons Dent, 13 (2010) 195.

[52] M. Santos, et al. Current all-ceramic systems in dentistry: a review, Compend Contin Educ Dent, 36 (2015) 31-37.

[53] M. Manda, et al. Probing the mechanical properties of dental porcelain through nanoindentation, J Mech Behav Mater, 21 (2012) 41-46.

[54] R. Seghi, et al. Relative fracture toughness and hardness of new dental ceramics, J Pros Dent, 74 (1995) 145-150.

[55] R. Pickup. Effect of porosity on Young's modulus of a porcelain, Brit Ceram T, 96 (1997) 96-98.

[56] F. Lofaj, et al. Creep Damage in an Advanced Self-Reinforced Silicon Nitride: Part I, Cavitation in the Amorphous Boundary Phase, J Am Ceram Soc, 82 (1999) 1009-1019.

[57] A.A. Wereszczak, et al. Dimensional changes and creep of silica core ceramics used in investment casting of superalloys, J Mater Sci, 37 (2002) 4235-4245.

[58] R.F. Davis, J.A. Pask. Diffusion and Reaction Studies in the System Al2O3-SiO2, J Am Ceram Soc, 55 (1972) 525-531.

[59] Y.S. Na, J.H. Lee. Interpretation of viscous deformation of bulk metallic glasses based on the Nabarro–Herring creep model, J Mater Process Tech, 187–188 (2007) 786-790.

[60] M. Tane, et al. Nanovoid formation by change in amorphous structure through the annealing of amorphous Al 2 O 3 thin films, Acta Mater, 59 (2011) 4631-4640.

[61] T. Neeraj, et al. Hydrogen embrittlement of ferritic steels: Observations on deformation microstructure, nanoscale dimples and failure by nanovoiding, Acta Mater, 60 (2012) 5160-5171.

[62] E. Camposilvan, M.J. Anglada Gomila. Micropillar compression inside zirconia degraded layer, J Eur Ceram Soc, 35 (2015) 4051-4058.

[63] M. Sebastiani, et al. A novel pillar indentation splitting test for measuring fracture toughness of thin ceramic coatings, Philos Mag, (2014) 1-17.

[64] A.M. Korsunsky, et al. Focused ion beam ring drilling for residual stress evaluation, Mater Lett, 63 (2009) 1961-1963.

[65] Y.J. Lin, et al. Microstructural and Chemical Influences of Silicate Grain-Boundary Phases in Yttria-Stabilized Zirconia, J Am Ceram Soc, 73 (1990) 2728-2735.

[66] P. Willmott. An Introduction to Synchrotron Radiation: Techniques and Applications, Wiley, 2011.

[67] W.H. Bragg, W.L. Bragg. The reflection of X-rays by crystals, P Roy Soc Lond A-Mat, 88 (1913) 428-438.

[68] P. Barnes, et al. Powder Diffraction.http://pd.chem.ucl.ac.uk/pdnn/diff2/kinemat2.htm. 14/02/2016.

[69] M. Marciszko, et al. Stress Measurements in Polished Al-Mg Alloy and CrN Coating Using Multireflection Grazing Incidence Method, Mater Sci Forum, 783 (2014) 2091-2096.

[70] A. Hammersley. FIT2D: an introduction and overview, European Synchrotron Radiation Facility Internal Report ESRF97HA02T, 68 (1997).

[71] M. Winterer, et al. X-ray diffraction, neutron scattering and EXAFS spectroscopy of monoclinic zirconia: analysis by Rietveld refinement and reverse Monte Carlo simulations, J Appl Crystallogr, 35 (2002) 434-442.

[72] O. Roberts, et al. A Study of Phase Transformation at the Surface of a Zirconia Ceramic, Proc WCE, 2 (2014).

[73] R.C. Garvie, P.S. Nicholson. Phase analysis in zirconia systems, J Am Ceram Soc, 55 (1972) 303-305.

[74] H. Toraya, et al. Calibration Curve for Quantitative-Analysis of the Monoclinic-Tetragonal Zro2 System by X-Ray-Diffraction, J Am Ceram Soc, 67 (1984) C119-C121.

[75] P. Withers, et al. Methods for obtaining the strain-free lattice parameter when using diffraction to determine residual stress, J Appl Crystallogr, 40 (2007) 891-904.

[76] N. Baimpas, et al. Stress evaluation in thin films: Micro-focus synchrotron X-ray diffraction combined with focused ion beam patterning for d0 evaluation, Thin Solid Films, 549 (2013) 245-250.

[77] Y. Saito, S. Tanaka. Residual Stress Tensor Distributions in Cracked Austenitic Stainless Steel Measured by Two-Dimensional X-Ray Diffraction Method, Adv Mat Res, 996 (2014) 128-134.

[78] S.R. MacEwen, et al. The use of time-of-flight neutron diffraction to study grain interaction stresses, Acta Metall Mater, 31 (1983) 657-676.

[79] S.M. King. Small angle neutron scattering. vol. 171: John Wiley & Sons New York, 1999.

[80] G. Beaucage. Approximations leading to a unified exponential/power-law approach to small-angle scattering, J Appl Crystallogr, 28 (1995) 717-728.

[81] L. Rubatat, et al. Structural study of proton-conducting fluorous block copolymer membranes, Macromolecules, 39 (2006) 720-730.

[82] I.-J. Kuo, et al. Cellulose-to-HMF conversion using crystalline mesoporous titania and zirconia nanocatalysts in ionic liquid systems, RSC Advances, 3 (2013) 2028-2034.

[83] T. Egami, S.J.L. Billinge. Underneath the Bragg Peaks: Structural Analysis of Complex Materials, Pergamon, 2003.

[84] T. Proffen, et al. Atomic pair distribution function analysis of materials containing crystalline and amorphous phases, Zeitschrift für Kristallographie, 220 (2005) 1002-1008.

[85] V. Petkov, et al. Structure of V2O5 n H2O Xerogel Solved by the Atomic Pair Distribution Function Technique, J Am Chem Soc, 124 (2002) 10157-10162.

[86] H.F. Poulsen, et al. Measuring strain distributions in amorphous materials, Nature Mat, 4 (2005) 33-36.

[87] Y. Huang, et al. In situ study of the evolution of atomic strain of bulk metallic glass and its effects on shear band formation, Scripta Mater, 69 (2013) 207-210.

[88] K. Kanaya, S. Okayama. Penetration and energy-loss theory of electrons in solid targets, J Phys D, 5 (1972) 43-58.

[89] EDXS Software - AZtecEnergy.http://www.oxford-instruments.com/products/microanalysis/energy-dispersive-x-ray-systems-eds-edx/eds-for-sem/eds-software-aztec. 16/02/2016.

[90] F. Massimi, et al. FIB/SEM and SEM/EDS microstructural analysis of metal-ceramic and zirconia-ceramic interfaces, Bull Group Int Rech Sci Stomatol, 50 (2012) 1-10.

[91] G. Pezzotti, A.A. Porporati. Raman spectroscopic analysis of phase-transformation and stress patterns in zirconia hip joints, J Biomed Opt, 9 (2004) 372-384.

[92] M. Bradley. Curve fitting in Raman and IR spectroscopy: basic theory of line shapes and applications, Thermo Fisher Scientific, Madison, USA, Application Note, 50733 (2007).

[93] D.R. Clarke, F. Adar. Measurement of the Crystallographically Transformed Zone Produced by Fracture in Ceramics Containing Tetragonal Zirconia, J Am Ceram Soc, 65 (1982) 284-288.

[94] W.H. Müller, G. Pezzotti. Micromechanics of fracture in Partially Stabilized Zirconia (PSZ) studiedby in-situ Raman spectroscopy, PAMM, 5 (2005) 349-350.

[95] P. Withers. Residual stress and its role in failure, Rep Prog Phys, 70 (2007) 2211.

[96] D. Di Maio, S. Roberts. Measuring fracture toughness of coatings using focused-ion-beam-machined microbeams, J Mater Res, 20 (2005) 299-302.

[97] J. McCarthy, et al. FIB micromachined submicron thickness cantilevers for the study of thin film properties, Thin Solid Films, 358 (2000) 146-151.

[98] D. Kiener, et al. A further step towards an understanding of size-dependent crystal plasticity: In situ tension experiments of miniaturized single-crystal copper samples, Acta Mater, 56 (2008) 580-592.

[99] L.A. Giannuzzi, N.C.S. University. Introduction to Focused Ion Beams: Instrumentation, Theory, Techniques and Practice, Springer US, 2006.

[100] M. Kappl. Focused Ion Beam.http://www.mpip-mainz.mpg.de/62502/Focused_Ion_Beam. 17/02/2016.

[101] B. Song, et al. Nano-structural changes in Li-ion battery cathodes during cycling revealed by FIB-SEM serial sectioning tomography, J Mat Chem A, 3 (2015) 18171-18179.

[102] S. Khan. Tiny Beauties at the UCLA.http://blog.engineeringstudents.org/?p=3723. 17/02/2016.

[103] W. Mook, et al. Hysitron Application Note: In-Situ Micropillar Compression.https://www.hysitron.com/media/1660/pico03an-r1f.pdf. 04/03/2016.

[104] M. Sebastiani, et al. Measurement of fracture toughness by nanoindentation methods: Recent advances and future challenges, Curr Opin Solid St M, (2015).

[105] G. Schajer, et al. Hole-drilling residual stress measurement with artifact correction using full-field DIC. Experimental and Applied Mechanics, Volume 4. Springer, 2013. pp. 403-414.

[106] A.J.G. Lunt, A.M. Korsunsky. A Review of Micro-scale Focused Ion Beam Milling and Digital Image Correlation Analysis for Residual Stress Evaluation and Error Estimation, Thin Solid Films, 283 (2015) 373-388.

[107] E. Bemporad, et al. A critical comparison between XRD and FIB residual stress measurement techniques in thin films, Thin Solid Films, 572 (2014) 224-231.

[108] A.J.G. Lunt, A.M. Korsunsky. Intragranular Residual Stress Evaluation Using the Semi-Destructive FIB-DIC Ring-Core Drilling Method. vol. 996. Adv Mat Res, 2014. p.8-13.

[109] DaVis - The Complete Software for Intelligent Imaging Applications http://www.lavision.de/en/products/davis.php. 18/02/2016.

[110] C. Eberl, et al. Digital image correlation and tracking, MatLabCentral, Mathworks file exchange server, FileID - 12413 (2006).

[111] E. Salvati, et al. Uncertainty Quantification of Residual Stress Evaluation by the FIB-DIC Ring-Core Method due to Elastic Anisotropy Effects, Int J Solids Struct, (2016).

[112] N. Baimpas, et al. Nano-scale mapping of lattice strain and orientation inside carbon core SiC fibres by synchrotron X-ray diffraction, Carbon, 79 (2014) 85-92.

[113] B. Winiarski, et al. Mapping Residual-Stress Distributions in a Laser-Peened Vit-105 Bulk-Metallic Glass Using the Focused-Ion-Beam Micro-Slitting Method. MRS Proceedings, vol. 1300: Cambridge Univ Press, 2011. p.1300-1310.

[114] Y. Oka, et al. Measurement of residual stress in DLC films prepared by plasma-based ion implantation and deposition, Surf Coat Tech, 186 (2004) 141-145.

[115] K.J. Kang, et al. A method for in situ measurement of the residual stress in thin films by using the focused ion beam, Thin Solid Films, 443 (2003) 71-77.

[116] N. Sabate, et al. Measurement of residual stress by slot milling with focused ion-beam equipment, J Micromech Microeng, 16 (2006) 254-259.

[117] M. Krottenthaler, et al. A simple method for residual stress measurements in thin films by means of focused ion beam milling and digital image correlation, Surf Coat Tech, 215 (2013) 247-252.

[118] G. Schajer, E. Altus. Stress calculation error analysis for incremental hole-drilling residual stress measurements, J Eng Mater Tech, 118 (1996) 120-126.

[119] B. Winiarski, P.J. Withers. Mapping residual stress profiles at the micron scale using FIB micro-hole drilling. Appl Mech Mater, vol. 24: Trans Tech Publ, 2010. p.267-272.

[120] E. Salvati, et al. An Investigation of Residual Stress Gradient Effects in FIB-DIC Micro-Ring-Core Analysis, Proc IMCECS, 2 (2015).

[121] A.J.G. Lunt, et al. A state-of-the-art review of micron-scale spatially resolved residual stress analysis by FIB-DIC ring-core milling and other techniques, J Strain Anal Eng, (2015) 0309324715596700.

[122] X. Song, et al. Residual stress measurement in thin films using the semi-destructive ring-core drilling method using Focused Ion Beam, Procedia Engineering, 10 (2011) 2190-2195.

[123] M. Sebastiani, et al. Focused ion beam four-slot milling for Poisson's ratio and residual stress evaluation at the micron scale, Surf Coat Tech, 251 (2014) 151-161.

[124] A.J.G. Lunt, et al. Full In-plane Strain Tensor Analysis using the Microscale Ring-core FIB milling and DIC Approach, J Mech Phys Solids, In Press (2016).

[125] X. Song, et al. Residual stress measurement in thin films at sub-micron scale using Focused Ion Beam milling and imaging, Thin Solid Films, 520 (2012) 2073-2076.

[126] F. Hild, S. Roux. Digital image correlation, Wiley-VCH, Weinheim, 2012.

[127] N. McCormick, J. Lord. Digital image correlation, Mater Today, 13 (2010) 52-54.

[128] J. Blaber, et al. Ncorr: Open-source 2D digital image correlation Matlab software, Exp Mech, (2015) 1-18.

[129] T. Chu, et al. Applications of digital-image-correlation techniques to experimental mechanics, Exp Mech, 25 (1985) 232-244.

[130] M.A. Sutton, et al. Image correlation for shape, motion and deformation measurements: basic concepts, theory and applications, Springer Science & Business Media, 2009.

[131] B. Pan, et al. Full-field strain measurement using a two-dimensional Savitzky-Golay digital differentiator in digital image correlation, Opt Eng, 46 (2007) 033601-033601-033610.

[132] Y. Wang, A.M. Cuitiño. Full-field measurements of heterogeneous deformation patterns on polymeric foams using digital image correlation, Int J Solids Struct, 39 (2002) 3777-3796.

[133] B. Pan, et al. Study on subset size selection in digital image correlation for speckle patterns, Opti express, 16 (2008) 7037-7048.

[134] S. Yaofeng, J.H. Pang. Study of optimal subset size in digital image correlation of speckle pattern images, Opt Lasers Eng, 45 (2007) 967-974.

[135] J. Lewis. Fast normalized cross-correlation. Vision Interface, vol. 10, 1995. p.120-123.

[136] B. Winiarski, P.J. Withers. Micron-Scale Residual Stress Measurement by Micro-Hole Drilling and Digital Image Correlation, Exp Mech, 52 (2012) 417-428.

[137] A.M. Korsunsky, et al. Residual stress evaluation at the micrometer scale: Analysis of thin coatings by FIB milling and digital image correlation, Surf Coat Tech, 205 (2010) 2393-2403.

[138] R.W. Farebrother. Linear Least Squares Computations, Taylor & Francis, 1988.

[139] H. Huang, et al. On errors of digital particle image velocimetry, Meas Sci Technol, 8 (1997) 1427.

[140] E. Salvati, et al. On the Accuracy of Residual Stress Evaluation from Focused Ion Beam DIC (FIB-DIC) Ring-core Milling Experiments, Proc ICNFA'15 265 (2014).

[141] G.H. Golub, C.F. Van Loan. An analysis of the total least squares problem, SIAM J Numer Anal, 17 (1980) 883-893.

[142] E. Wachtel, I. Lubomirsky. The elastic modulus of pure and doped ceria, Scripta Mater, 65 (2011) 112-117.

[143] K.S. Suresh, et al. Microstructure dependent elastic modulus variation in NiTi shape memory alloy, J Alloy Compd, 633 (2015) 71-74.

[144] R. Nava. Evaluation of the high-temperature pressure derivative of the grüneisen constant from the temperature variation of the elastic moduli, J Phys Chem Solids, 59 (1998) 1537-1539.

[145] H.Y. Yu. Variation of elastic modulus during plastic deformation and its influence on springback, Mater Design, 30 (2009) 846-850.

[146] J.M. Chaves, et al. Influence of phase transformations on dynamical elastic modulus and anelasticity of beta Ti–Nb–Fe alloys for biomedical applications, J Mech Behav Biomed Mater, 46 (2015) 184-196.

[147] A.B. Antunes, et al. Magnetic domains and anisotropy in single crystals of Er(Co,Mn)O3, J Magn Magn Mater, 320 (2008) 69-72.

[148] S. Qiu, et al. On elastic moduli and elastic anisotropy in polycrystalline martensitic NiTi, Acta Mater, 59 (2011) 5055-5066.

[149] S. Mortazavian, A. Fatemi. Effects of fiber orientation and anisotropy on tensile strength and elastic modulus of short fiber reinforced polymer composites, Compos Part B: Eng, 72 (2015) 116-129.

[150] Y. Calahorra, et al. Young's Modulus, Residual Stress, and Crystal Orientation of Doubly Clamped Silicon Nanowire Beams, Nano Lett, 15 (2015) 2945-2950.

[151] S. Schorr, et al. The complex material properties of chalcopyrite and kesterite thin-film solar cell absorbers tackled by synchrotron-based analytics, Prog Photovoltaics, 20 (2012) 557-567.

[152] M.E. Kartal, et al. Determination of the complete microscale residual stress tensor at a subsurface carbide particle in a single-crystal superalloy from free-surface EBSD, Acta Mater, 60 (2012) 5300-5310.

[153] F. Hosseinzadeh, P. Bouchard. Mapping multiple components of the residual stress tensor in a large P91 steel pipe girth weld using a single contour cut, Exp Mech, 53 (2013) 171-181.

[154] Y. Traore, et al. Measurement of the residual stress tensor in a compact tension weld specimen, Exp Mech, 53 (2013) 605-618.

[155] N. Tamura, et al. High spatial resolution grain orientation and strain mapping in thin films using polychromatic submicron x-ray diffraction, Appl Phys Lett, 80 (2002) 3724-3726.

[156] N. Tamura, et al. Scanning X-ray microdiffraction with submicrometer white beam for strain/stress and orientation mapping in thin films, J Sync Rad, 10 (2003) 137-143.

[157] N. Tamura, et al. Submicron x-ray diffraction and its applications to problems in materials and environmental science, Rev Sci Instrum, 73 (2002) 1369-1372.

[158] J. Lachambre, et al. Extraction of stress intensity factors for 3D small fatigue cracks using digital volume correlation and X-ray tomography, Int J Fatigue, 71 (2015) 3-10.

[159] M. Kim, et al. Effects of the sintering conditions of dental zirconia ceramics on the grain size and translucency, J Adv Prosthod, 5 (2013) 161-166.

[160] S. Deshpande, et al. Size dependency variation in lattice parameter and valency states in nanocrystalline cerium oxide, Appl Phys Lett, 87 (2005) 133113-133113.

[161] A.M. Korsunsky, et al. Multi-Beam Engineering Microscopy - A Versatile Tool for Optimal Materials Design, Proc IMCECS, 2 (2015).

[162] K. Shah, et al. Effect of coloring with various metal oxides on the microstructure, color, and flexural strength of 3Y-TZP, J Biomed Mater Res-A, 87 (2008) 329-337.

[163] A. Della Bona, et al. Characterization and surface treatment effects on topography of a glass-infiltrated alumina/zirconia-reinforced ceramic, Dent Mater, 23 (2007) 769-775.

[164] A.M. Korsunsky, et al. Fast residual stress mapping using energy-dispersive synchrotron X-ray diffraction on station 16.3 at the SRS, J Sync Rad, 9 (2002) 77-81.

[165] P.J. Withers, et al. Recent advances in residual stress measurement, Int J Pres Ves Pip, 85 (2008) 118-127.

[166] P. Ballard, A. Constantinescu. On the inversion of subsurface residual stresses from surface stress measurements, J Mech Phys Solids, 42 (1994) 1767-1787.

[167] M. Moore, W. Evans. Mathematical correction for stress in removed layers in X-ray diffraction residual stress analysis. SAE Technical Paper, 1958.

[168] C. Howard, et al. Structures of ZrO2 polymorphs at room temperature by high-resolution neutron powder diffraction, Acta Crystallogr B, 44 (1988) 116-120.

[169] D.G. Lamas, N.E. Walsöe De Reca. X-ray diffraction study of compositionally homogeneous, nanocrystalline yttria-doped zirconia powders, J Mater Sci, 35 (2000) 5563-5567.

[170] R.V. Martins, et al. Full 3D spatially resolved mapping of residual strain in a 316L austenitic stainless steel weld specimen, Mat Sci Eng A, 527 (2010) 4779-4787.

[171] W.L. Zhu, et al. Spatially resolved Raman spectroscopy evaluation of residual stresses in 3C-SiC layer deposited on Si substrates with different crystallographic orientations, Appl Surf Sci, 252 (2006) 2346-2354.

[172] B.L. Boyce, et al. The residual stress state due to a spherical hard-body impact, Mech Mater, 33 (2001) 441-454.

[173] W. Zhao, et al. On Thick-Walled Cylinder Under Internal Pressure, J Pres Ves Tech, 125 (2003) 267-273.

[174] B. Sahoo, et al. Effect of Shot Peening on Low Cycle Fatigue Life of Compressor Disc of a Typical Fighter Class Aero-Engine, Procedia Eng, 55 (2013) 144-148.

[175] X. Sheng, et al. Residual stress field induced by shot peening based on random-shots for 7075 aluminum alloy, T Nonferr Metal Soc, 22, Supplement 2 (2012) 261-267.

[176] X. Song, et al. An eigenstrain-based finite element model and the evolution of shot peening residual stresses during fatigue of GW103 magnesium alloy, Int J Fatigue, 42 (2012) 284-295.

[177] M.A.S. Torres, H.J.C. Voorwald. An evaluation of shot peening, residual stress and stress relaxation on the fatigue life of AISI 4340 steel, Int J Fatigue, 24 (2002) 877-886.

[178] Y. Watanabe, et al. Simulation of residual stress distribution on shot peening, JSMS, 44 (1995) 110-116.

[179] C. Slama, M. Abdellaoui. Structural characterization of the aged Inconel 718, J Alloy Compd, 306 (2000) 277-284.

[180] D. Mukherji, et al. Lattice misfit measurement in Inconel 706 containing coherent γ' and γ'' precipitates, Scr Mater, 48 (2003) 333-339.

[181] A. King, et al. Observations of intergranular stress corrosion cracking in a grain-mapped polycrystal, Science, 321 (2008) 382-385.

[182] G.L. Harris. Properties of Silicon Carbide, INSPEC, IET, Stevenage, UK, 1995.

[183] R.W. Henson, W.N. Reynolds. Lattice parameter changes in irradiated graphite, Carbon, 3 (1965) 277-287.

[184] M.C. Thompson, et al. The all-ceramic, inlay supported fixed partial denture. Part 2. Fixed partial denture design: a finite element analysis, Aust Dent J, 56 (2011) 302-311.

[185] M.V. Nevitt, et al. The Elastic Properties of Monoclinic ZrO2, Physica B & C, 150 (1988) 230-233.

[186] S.K. Chan, et al. Temperature-Dependence of the Elastic-Moduli of Monoclinic Zirconia, J Am Ceram Soc, 74 (1991) 1742-1744.

[187] E.H. Kisi, C.J. Howard. Elastic constants of tetragonal zirconia measured by a new powder diffraction technique, J Am Ceram Soc, 81 (1998) 1682-1684.

[188] G.Q. Tong, et al. The grain size dependency of compressive deformation of a superplastic 3 mol% yttria stabilized tetragonal zirconia, Mat Sci Eng A, 336 (2002) 263-269.

[189] A.J.G. Lunt, et al. Calculations of single crystal elastic constants for yttria partially stabilised zirconia from powder diffraction data, J Appl Phys, 116 (2014) 053509.

[190] M.R. Daymond, H.G. Priesmeyer. Elastoplastic deformation of ferritic steel and cementite studied by neutron diffraction and self-consistent modelling, Acta Mater, 50 (2002) 1613-1626.

[191] Y.X. Ma, et al. Neutron diffraction study of ferroelasticity in a 3 mol% Y2O3-ZrO2, J Am Ceram Soc, 84 (2001) 399-405.

[192] D. Dierickx, et al. Statistical extreme value modeling of particle size distributions: experimental grain size distribution type estimation and parameterization of sintered zirconia, Mater Charact, 45 (2000) 61-70.

[193] X. Song, et al. Finite element modelling and diffraction measurement of elastic strains during tensile deformation of HCP polycrystals, Comp Mater Sci, 44 (2008) 131-137.

[194] Z.Y. Ren, Q.S. Zheng. Effects of grain sizes, shapes, and distribution on minimum sizes of representative volume elements of cubic polycrystals, Mech Mater, 36 (2004) 1217-1229.

[195] H.M. Kandil, et al. Single-Crystal Elastic-Constants of Yttria-Stabilized Zirconia in the Range 20-Degrees to 700-Degrees-C, J Am Ceram Soc, 67 (1984) 341-346.

[196] N.G. Pace, et al. The elastic constants and interatomic binding in yttria-stabilised zirconia, J Mater Sci, 4 (1969) 1106-1110.

[197] C.J. Howard, E.H. Kisi. Measurement of single-crystal elastic constants by neutron diffraction from polycrystals, J Appl Crystallogr, 33 (2000) 418-418.

[198] X.S. Zhao, et al. Elastic properties of cubic, tetragonal and monoclinic ZrO2 from first-principles calculations, J Nucl Mater, 415 (2011) 13-17.

[199] S. Fabris, et al. Relative energetics and structural properties of zirconia using a self-consistent tight-binding model, Phys Rev B, 61 (2000) 6617-6630.
[200] U.F. Kocks, et al. Texture and Anisotropy: Preferred Orientations in Polycrystals and their Effect on Materials Properties. 1 ed., Cambridge University Press, 1998.
[201] M.R. Winter, D.R. Clarke. Thermal conductivity of yttria-stabilized zirconia-hafnia solid solutions, Acta Mater, 54 (2006) 5051-5059.
[202] A. Marmier, et al. ElAM: A computer program for the analysis and representation of anisotropic elastic properties, Comput Phys Commun, 181 (2010) 2102-2115.
[203] G.N. Greaves, et al. Poisson's ratio and modern materials, Nature Mat, 10 (2011) 986-986.
[204] R. Ponraj, et al. Creep of porcelain-containing silica and alumina, J Mater Sci, 29 (1994) 4385-4392.
[205] "Standard Test Method for Elevated Temperature Tensile Creep Strain, Creep Strain Rate, and Creep Time-to-Failure for Advanced Monolithic Ceramics". West Conshohocken, PA: ASTM International, 2010.
[206] A.J.G. Lunt, et al. Tensile Secondary Creep Rate Analysis of a Dental Veneering Porcelain, Thin Solid Films, 596 (2015) 269-276.
[207] A.J.G. Lunt, et al. Characterisation of nanovoiding in dental porcelain using small angle neutron scattering and transmission electron microscopy, Acta Mater, Under review (2016).
[208] D.F. Carroll, et al. Technique for Tensile Creep Testing of Ceramics, J Am Ceram Soc, 72 (1989) 1610-1614.
[209] K.C. Liu. Self-aligning hydraulic piston assembly for tensile testing of ceramic. vol. US4686860 A. United States of America, 1987.
[210] R.L. Post Jr. High-temperature creep of Mt. Burnet Dunite, Tectonophysics, 42 (1977) 75-110.
[211] Instron: Series Load Cells.http://www.instron.com/~/media/literature-library/products/2003/08/2530-400-series-load-cells.pdf?la=en. 04/05/2015.
[212] W.R. Cannon, T.G. Langdon. Creep of ceramics, J Mater Sci, 18 (1983) 1-50.
[213] F.R.N. Nabarro, F. de Villiers. Physics Of Creep And Creep-Resistant Alloys. 1st ed., Taylor & Francis, London, 1995.
[214] K.S. Chan, R.A. Page. Creep damage development in structural ceramics, J Am Ceram Soc, 76 (1993) 803-826.
[215] S. Kanehira, et al. Periodic Nanovoid Structure in Glass via Femtosecond Laser Irradiation, Ceram Trans, 190 181-189.
[216] C. Ruestes, et al. Plasticity mechanisms in nanovoided bcc metals under high strain rate compression. APS Shock Compression of Condensed Matter Meeting Abstracts, vol. 1, 2013. p.4006.
[217] L. Li, A.F. Yee. Effect of the scale of local segmental motion on nanovoid growth in polyester copolymer glasses, Macromolecules, 36 (2003) 2793-2801.
[218] K.C. Cheung, B.W. Darvell. Sintering of dental porcelain: effect of time and temperature on appearance and porosity, Dent Mater, 18 (2002) 163-173.
[219] R. Lapovok, et al. Evolution of nanoscale porosity during equal-channel angular pressing of titanium, Acta Mater, 57 (2009) 2909-2918.
[220] R. Heenan, et al. SANS at pulsed neutron sources: present and future prospects, J Appl Crystallogr, 30 (1997) 1140-1147.
[221] K. Anusavice, B. Hojjatie. Tensile stress in glass-ceramic crowns: effect of flaws and cement voids, Int J Prost, 5 (1991) 351-358.
[222] AutoSlicer - Sample Preparation Tool.http://www.tescan.com/en/other-products/software/autoslicer-sample-preparation-tool. 19/02/15.
[223] O. Arnold, et al. Mantid—Data analysis and visualization package for neutron scattering and μ SR experiments, Nucl Instrum Meth A, 764 (2014) 156-166.
[224] R. Heenan, S. King. Development of small-angle diffractometer LQD at the ISIS pulsed neutron source, Proc Int Sem Struct, (1993).
[225] B. Hammouda, et al. Small angle neutron scattering from deuterated polystyrene/poly (vinylmethyl ether)/protonated polystyrene ternary polymer blends, Polymer, 33 (1992) 1785-1787.
[226] J.M. Carpenter, C.K. Loong. Elements of Slow-Neutron Scattering: Basics, Techniques, and Applications, Cambridge University Press, 2015.
[227] L.A. Feigin, D.I. Svergun. Structure Analysis by Small-Angle X-Ray and Neutron Scattering, Springer US, 2013.

[228] M.D. Abràmoff, et al. Image processing with ImageJ, Biophoton Int, 11 (2004) 36-43.
[229] K. Weinberg. Void nucleation by vacancy condensation, PAMM, 8 (2008) 10249-10250.
[230] J.W. Christian. The theory of transformations in metals and alloys, Newnes, 2002.
[231] R. Raj, M.F. Ashby. Intergranular fracture at elevated temperature, Acta Metall Mater, 23 (1975) 653-666.
[232] J.P. Hirth, W.D. Nix. Analysis of cavity nucleation in solids subjected to external and internal stresses, Acta Metall Mater, 33 (1985) 359-368.
[233] R.L. De Orio, et al. Physically based models of electromigration: From Black's equation to modern TCAD models, Microelect Rel, 50 (2010) 775-789.
[234] H.D. Rozenfeld, et al. Laws of population growth, Proce Nat Aca Sci, 105 (2008) 18702-18707.
[235] F.D. Fischer, J. Svoboda. Void growth due to vacancy supersaturation – A non-equilibrium thermodynamics study, Scripta Mater, 58 (2008) 93-95.
[236] M. Horstemeyer, S. Ramaswamy. On factors affecting localization and void growth in ductile metals: a parametric study, Inter J Dam Mech, 9 (2000) 5-28.
[237] M. Liehr, et al. Kinetics of high-temperature thermal decomposition of SiO2 on Si (100), J Vac Sci Tech A, 5 (1987) 1559-1562.
[238] A. Melander, U. Ståhlberg. The effect of void size and distribution on ductile fracture, Int J Fract, 16 (1980) 431-440.
[239] S. Sinha, et al. Observation of power-law correlations in silica-particle aggregates by small angle neutron scattering, Kinet Aggreg Gela, 19842 (1984) 87-90.
[240] D.B. Williams, C.B. Carter. The transmission electron microscope, Springer, 1996.
[241] A. Mahapatra, et al. Oxidation mechanism in metal nanoclusters: Zn nanoclusters to ZnO hollow nanoclusters, J Phys D, 45 (2012) 415303.
[242] G. Krishnan, et al. Thermal stability of gas phase magnesium nanoparticles, J Appl Phys, 107 (2010) 053504.
[243] T. Pardoen, et al. Experimental and numerical comparison of void growth models and void coalescence criteria for the prediction of ductile fracture in copper bars, Acta Mater, 46 (1998) 541-552.
[244] Y. Gao. Improvement of fatigue property in 7050–T7451 aluminum alloy by laser peening and shot peening, Mat Sci Eng A, 528 (2011) 3823-3828.
[245] E. Seppälä, et al. Onset of void coalescence during dynamic fracture of ductile metals, Phys Rev Lett, 93 (2004) 245503.
[246] A.J.G. Lunt, et al. Residual Strain Mapping Using Atomic Pair Distribution Function Analysis of Porcelain in Dental Prostheses, Biomaterials, Under review (2016).
[247] A.J.G. Lunt, et al. Microscale residual stress and phase quantification at the yttria-partially stabilised-zirconia-porcelain interface in dental prostheses, Biomaterials, Under review (2016).
[248] E. Lifshin. X-ray Characterization of Materials, John Wiley & Sons, 2008.
[249] J. Hastings, et al. Synchrotron X-ray powder diffraction, J Appl Crystallogr, 17 (1984) 85-95.
[250] S. Bates, et al. Analysis of amorphous and nanocrystalline solids from their X-ray diffraction patterns, Pharma Res, 23 (2006) 2333-2349.
[251] R. Feng. Modelling Atomic Structure in Amorphous Solids and X-Ray Diffraction: Experiments and Simulations, Lap Lambert Academic Publishing GmbH KG, 2012.
[252] G. Ice. Amorphous materials: Characterizing amorphous strain, Nat Mater, 4 (2005) 17-18.
[253] M. Basham, et al. Data Analysis WorkbeNch (DAWN), J Sync Rad, 22 (2015) 853-858.
[254] S. Kemethmüller, et al. Quantitative analysis of crystalline and amorphous phases in glass–ceramic composites like LTCC by the Rietveld method, J Am Ceram Soc, 89 (2006) 2632-2637.
[255] A.K. Soper, E.R. Barney. Extracting the pair distribution function from white-beam X-ray total scattering data, J Appl Crystallogr, 44 (2011) 714-726.
[256] D.A. Keen. A comparison of various commonly used correlation functions for describing total scattering, J Appl Crystallogr, 34 (2001) 172-177.
[257] R.E. Dinnebier, S.J.L. Billinge. Powder Diffraction: Theory and Practice, Royal Society of Chemistry, 2008.
[258] C. Suryanarayana, M.G. Norton. X-Ray Diffraction: A Practical Approach, Springer US, 2013.
[259] K. Mullen, I. Levin. Mitigation of errors in pair distribution function analysis of nanoparticles, J Appl Crystallogr, 44 (2011) 788-797.
[260] A. Rizkalla, D. Jones. Mechanical properties of commercial high strength ceramic core materials, Dent Mater, 20 (2004) 207-212.

[261] Atomistix ToolKit (ATK). http://www.quantumwise.com. 31/12/2015.

[262] A. Pedone, et al. A New Self-Consistent Empirical Interatomic Potential Model for Oxides, Silicates, and Silica-Based Glasses, J Phys Chem B, 110 (2006) 11780-11795.

[263] J.E. Shelby. Density of vitreous silica, J Non-Cryst Solids, 349 (2004) 331-336.

[264] E. Chagarov, A.C. Kummel. Generation of Realistic Amorphous Al2O3 And ZrO2 Samples By Hybrid Classical and First-Principle Molecular Dynamics Simulations, ECS Transactions, 16 (2008) 773-785.

[265] D.J. Cole, et al. Development of a classical force field for the oxidized Si surface: Application to hydrophilic wafer bonding, J Chem Phys, 127 (2007) 204704.

[266] C. Wong, R.S. Bollampally. Thermal conductivity, elastic modulus, and coefficient of thermal expansion of polymer composites filled with ceramic particles for electronic packaging, J Appl Poly Sci, 74 (1999) 3396-3403.

[267] T. Chu, et al. Geometric and electronic structures of silicon oxide clusters, J Phys Chem B, 105 (2001) 1705-1709.

[268] G. Pezzotti. Raman piezo-spectroscopic analysis of natural and synthetic biomaterials, Anal Bioanal Chem, 381 (2005) 577-590.

[269] T. Sui, et al. Understanding Nature's residual strain engineering at the human dentine-enamel junction interface, Acta Biomater, (2016).

[270] M. Achintha, et al. Eigenstrain modelling of residual stress generated by arrays of laser shock peening shots and determination of the complete stress field using limited strain measurements, Surf Coat Tech, 216 (2013) 68-77.

[271] M.V. Swain. Unstable cracking (chipping) of veneering porcelain on all-ceramic dental crowns and fixed partial dentures, Acta Biomater, 5 (2009) 1668-1677.

[272] K. Asaoka, J. Tesk. Transient and residual stress in a porcelain-metal strip, J Dent Res, 69 (1990) 463-469.

[273] P. Dehoff, K. Anusavice. Tempering stresses in feldspathic porcelain, J Dent Res, 68 (1989) 134-138.

[274] S. Timoshenko. Analysis of bi-metal thermostats, JOSA, 11 (1925) 233-255.

[275] J. Eischen, et al. Realistic modeling of edge effect stresses in bimaterial elements, J Electron Packaging, 112 (1990) 16-23.

[276] B. Stawarczyk, et al. The effect of zirconia sintering temperature on flexural strength, grain size, and contrast ratio, Clin Oral Investi, 17 (2013) 269-274.

[277] C.H. Hsueh, et al. Influence of multiple heterogeneities on sintering rates, J Am Ceram Soc, 69 (1986).

[278] B. Basu. Toughening of yttria-stabilised tetragonal zirconia ceramics, Inter Mat Revs, 50 (2005) 239-256.

[279] L. Grabner. Spectroscopic technique for the measurement of residual stress in sintered Al2O3, J Appl Phys, 49 (1978) 580-583.

[280] G. Magnani, A. Brillante. Effect of the composition and sintering process on mechanical properties and residual stresses in zirconia–alumina composites, J Eur Ceram Soc, 25 (2005) 3383-3392.

[281] E. Kreyszig. Advanced Engineering Mathematics, Wiley India Pvt. Limited, 2011.

[282] V. Indenbom. Theory of Tempering Glass, Zh. Tekh. Fiz, 24 (1954) 925-928.

[283] C. Aydiner, J. Hanan. Thermal-tempering analysis of bulk metallic glass plates using an instant-freezing model, Metall and Mat Trans A, 32 (2001) 2709-2715.

[284] A.M. Korsunsky. Eigenstrain analysis of residual strains and stresses, J Strain Anal Eng, 44 (2009) 29-43.

[285] T. Mura, T. Koya. Variational Methods in Mechanics, Oxford University Press, 1992.

[286] N. Fleck, J. Hutchinson. Strain gradient plasticity, Adv Appl Mech, 33 (1997) 296-361.

[287] J. Chevalier, et al. The Tetragonal-Monoclinic Transformation in Zirconia: Lessons Learned and Future Trends, J Am Ceram Soc, 92 (2009) 1901-1920.

[288] T. Gupta, et al. Stabilization of tetragonal phase in polycrystalline zirconia, J Mater Sci, 12 (1977) 2421-2426.

[289] P.G. Charalambides, R.M. McMeeking. Near-Tip Mechanics of Stress-Induced Microcracking in Brittle Materials, J Am Ceram Soc, 71 (1988) 465-472.

[290] T.K. Gupta, et al. Effect of stress-induced phase transformation on the properties of polycrystalline zirconia containing metastable tetragonal phase, J Mater Sci, 13 (1978) 1464-1470.

[291] M. De Kler, et al. Influence of thermal expansion mismatch and fatigue loading on phase changes in porcelain veneered Y-TZP zirconia discs, J Oral Rehabil, 34 (2007) 841-847.

[292] F. Yang, et al. In Situ Measurement of Stresses and Phase Compositions of the Zirconia Scale During Oxidation of Zirconium by Raman Spectroscopy, Oxidation Meta, 81 (2014) 331-343.

[293] B. Al-Amleh, et al. Influence of veneering porcelain thickness and cooling rate on residual stresses in zirconia molar crowns, Dent Mater, 30 (2014) 271-280.

[294] M. Imam, C. Gilmore. Fatigue and microstructural properties of quenched Ti-6Al-4V, Metallurgical Trans A, 14 (1983) 233-240.

[295] A.J.G. Lunt, et al. A Comparative Transmission Electron Microscopy, Energy Dispersive X-ray Spectroscopy and Spatially Resolved Micropillar Compression Study of the Yttria Partially Stabilised Zirconia–Porcelain Interface in Dental Prosthesis, Thin Solid Films, 596 (2015) 222-232.

[296] R. Belli, et al. A photoelastic assessment of residual stresses in zirconia-veneer crowns, J Dent Res, 91 (2012) 316-320.

[297] S. Deville, et al. Influence of surface finish and residual stresses on the ageing sensitivity of biomedical grade zirconia, Biomaterials, 27 (2006) 2186-2192.

[298] A.J.G. Lunt, et al. Microscale resolution fracture toughness profiling at the zirconia-porcelain interface in dental prostheses, SPIE Micro+ Nano, (2015) 96685S-96685S-96611.

[299] S. Aravindan, R. Krishnamurthy. Joining of ceramic composites by microwave heating, Mater Lett, 38 (1999) 245-249.

[300] S. Scherrer, et al. Fracture toughness (K IC) of a dental porcelain determined by fractographic analysis, Dent Mater, 15 (1999) 342-348.

[301] E. Camposilvan, M. Anglada. Micropillar compression inside zirconia degraded layer, J Eur Ceram Soc.

[302] R. Van Noort. Introduction to Dental Materials, Elsevier Health Sciences UK, London, (2014).

[303] M.N. Aboushelib, et al. Microtensile bond strength of different components of core veneered all-ceramic restorations: Part II: Zirconia veneering ceramics, Dent Mater, 22 (2006) 857-863.

[304] D. Liu, et al. Insights into porcelain to zirconia bonding, J Adhes Sci Technol, 26 (2012) 1249-1265.

[305] A. Bravo-Leon, et al. Fracture toughness of nanocrystalline tetragonal zirconia with low yttria content, Acta Mater, 50 (2002) 4555-4562.

[306] D. Bell, A. Garratt-Reed. Energy Dispersive X-ray Analysis in the Electron Microscope, Taylor & Francis UK, London, (2003).

[307] A. Grigore, et al. Microstructure of veneered zirconia after surface treatments: A TEM study, Dent Mater, 29 (2013) 1098-1107.

[308] Y. Wang, et al. A transmission electron microscopy study of the microstructure and interface of zirconia-based thermal barrier coatings, J Alloys Compd, 619 (2015) 820-825.

[309] H. Ibegazene, et al. Microstructure of yttria stabilized zirconia-hafnia plasma sprayed thermal barrier coatings, J Phys IV, 3 (1993) 1013-1016.

[310] L. Lelait, S. Alperine. TEM investigations of high toughness non-equilibrium phases in the ZrO2-Y2O3 system, Scripta Metall Mater, 25 (1991) 1815-1820.

[311] R. Goswami, N. Bernstein. Effect of interfaces of grain boundary Al2CuLi plates on fracture behavior of Al–3Cu–2Li, Acta Mater, 87 (2015) 399-410.

[312] A. Lai, et al. Shape memory and superelastic ceramics at small scales, Science, 341 (2013) 1505-1508.

[313] G. Mohanty, et al. Elevated temperature, strain rate jump microcompression of nanocrystalline nickel, Philos Mag, (2014) 1-18.

[314] M.D. Uchic, D.M. Dimiduk. A methodology to investigate size scale effects in crystalline plasticity using uniaxial compression testing, Mater Sci Eng A, 400 (2005) 268-278.

[315] R.-B. Adusumalli, et al. Deformation and failure mechanism of secondary cell wall in Spruce late wood, Appl Phys A-Mater, 100 (2010) 447-452.

[316] J. Schwiedrzik, et al. In situ micropillar compression reveals superior strength and ductility but an absence of damage in lamellar bone, Nature Mater, 13 (2014) 740-747.

[317] D. Ziskind, et al. A novel experimental method for the local mechanical testing of human coronal dentin, Dent Mater, 26 (2010) 179-184.

[318] Y. Yang, et al. Effects of specimen geometry and base material on the mechanical behavior of focused-ion-beam-fabricated metallic-glass micropillars, Acta Mater, 57 (2009) 1613-1623.

[319] E. Camposilvan, et al. Small-scale mechanical behavior of zirconia, Acta Mater, 80 (2014) 239-249.
[320] R. Lacroix, et al. Plastic deformation and residual stresses in amorphous silica pillars under uniaxial loading, Acta Mater, 60 (2012) 5555-5566.
[321] J. McLean, T. Hughes. The reinforcement of dental porcelain with ceramic oxides, Br Dent J, 119 (1965) 251.
[322] W.C. Oliver, G.M. Pharr. An improved technique for determining hardness and elastic modulus using load and displacement sensing indentation experiments, J Mat Res, 7 (1992) 1564-1583.
[323] P. Zhang, et al. General relationship between strength and hardness, Mat Sci Eng A, 529 (2011) 62-73.
[324] J. Quinn, et al. Influence of microstructure and chemistry on the fracture toughness of dental ceramics, Dent Mater, 19 (2003) 603-611.
[325] O. Vasylkiv, et al. Hardness and fracture toughness of alumina-doped tetragonal zirconia with different yttria contents, Mater Trans, 44 (2003) 2235-2238.
[326] K. Tsukuma, et al. Strength and Fracture Toughness of Isostatically Hot-Pressed Composites of Al2O3 and Y2O3-Partially-Stabilized ZrO2, J Am Ceram Soc, 68 (1985) C-4-C-5.
[327] M. Trunec, Z. Chlup. Higher fracture toughness of tetragonal zirconia ceramics through nanocrystalline structure, Scripta Mater, 61 (2009) 56-59.
[328] G. Isgrò, et al. The influence of multiple firing on thermal contraction of ceramic materials used for the fabrication of layered all-ceramic dental restorations, Dent Mater, 21 (2005) 557-564.
[329] M. Wolfart, et al. Durability of the resin bond strength to zirconia ceramic after using different surface conditioning methods, Dent Mater, 23 (2007) 45-50.
[330] A. Saito, et al. A comparison of bond strength of layered veneering porcelains to zirconia and metal, J Pros Dent, 104 (2010) 247-257.
[331] M. Mamivand, et al. Phase field modeling of the tetragonal-to-monoclinic phase transformation in zirconia, Acta Mater, 61 (2013) 5223-5235.
[332] S.C. Hwang, R.M. McMeeking. A finite element model of ferroelastic polycrystals, Int J Solids Struct, 36 (1999) 1541-1556.
[333] M. Kamlah, et al. Finite element simulation of a polycrystalline ferroelectric based on a multidomain single crystal switching model, Int J Solids Struct, 42 (2005) 2949-2964.

10. Appendix A – The Relationship between Plane Stress and Plane Strain Conditions

10.1. Stress State Decomposition Approach

In the analysis that follows, the connection between the plane strain state originally present in the YPSZ-porcelain system (which can be approximated as an infinite body) and the modified plane stress state induced during sample sectioning will be derived. This analysis is based on decomposing the stress state into its constituent parts and establishing the relationship between these two planar states.

A schematic showing both plane strain and plane stress conditions is shown in Figure A.1 in which the out of plane direction is parallel to the z axis and the principal stress orientations are aligned to the x, y coordinate system axes. In the unsectioned YPSZ body conditions of plane strain are present, the stresses in this system are given by $\tilde{\sigma}_x, \tilde{\sigma}_y$ and $\tilde{\sigma}_z$ and the in-plane strains by $\tilde{\varepsilon}_x$ and $\tilde{\varepsilon}_y$. Under the conditions of plane strain the out-of-plane strain component $(\tilde{\varepsilon}_z)$ must vanish at locations where the corresponding eigenstrain component is zero, i.e. $\tilde{\varepsilon}_z = 0$. If the out-of-plane eigenstrain component is present at the corresponding location, for example due to volumetric phase transformation, then it is necessary to set $\tilde{\varepsilon}_z = -\varepsilon_z^*$, where ε_z^* is the z direction eigenstrain component [284].

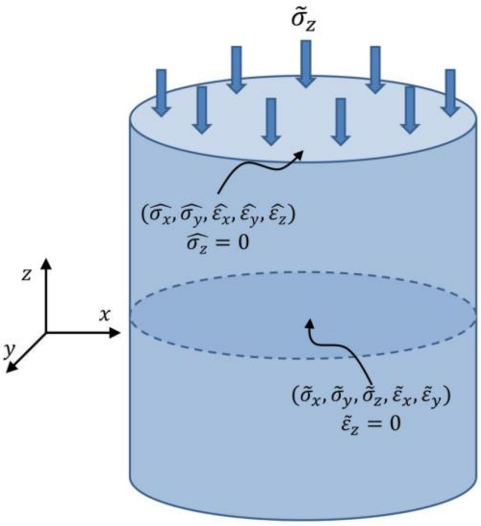

Figure A.1. Schematic showing plane strain state present in YPSZ prosthesis prior to sectioning $(\tilde{\sigma}_x, \tilde{\sigma}_y, \tilde{\sigma}_z, \tilde{\varepsilon}_x, \tilde{\varepsilon}_y, \tilde{\varepsilon}_z = 0)$ and the plane stress conditions induced during sample sectioning $(\widehat{\sigma_x}, \widehat{\sigma_y}, \widehat{\varepsilon_x}, \widehat{\varepsilon_y}, \widehat{\varepsilon_z}, \widehat{\sigma_z} = 0)$. The relationship between these two conditions can be determined by applying a uniform stress of magnitude $\tilde{\sigma}_z$ in a direction opposing the stress originally present.

Hooke's law can then be used to define the plane strain relationship between $\tilde{\sigma}_x, \tilde{\sigma}_y$ and $\tilde{\sigma}_z$:

$$\tilde{\varepsilon}_z = 0 = \frac{1}{E}\left[\tilde{\sigma}_z - \nu\left(\tilde{\sigma}_x + \tilde{\sigma}_y\right)\right], \tag{A.1}$$

$$\tilde{\sigma}_z = \nu\left(\tilde{\sigma}_x + \tilde{\sigma}_y\right). \tag{A.2}$$

The full stress and strain state of the plane strain state can then be written solely in terms of $\tilde{\sigma}_x$ and $\tilde{\sigma}_y$ as shown in Figure A.2, stress state 1.

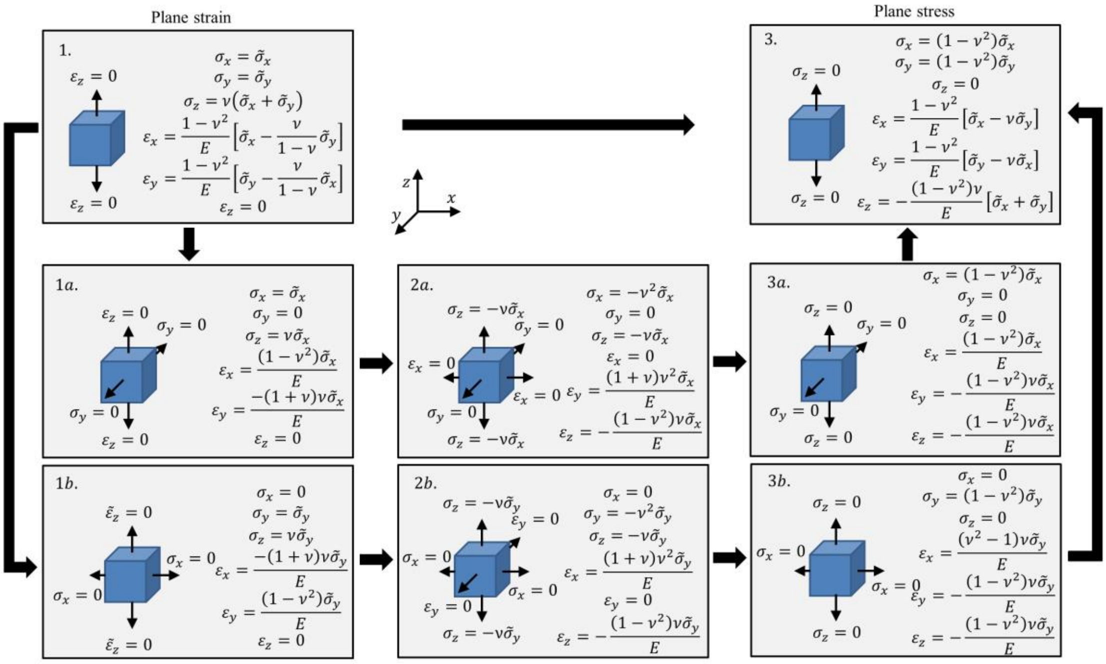

Figure A.2. Schematic showing the relationship between original plane strain conditions and the plane stress state induced by sample sectioning. All relationships are written in terms of the in-plane stresses originally present ($\tilde{\sigma}_x$ and $\tilde{\sigma}_y$). The systematic decoupling of the x and y in plane strains, and the associated stress changes are shown in a and b.

In order to establish a relationship between the plane stress and plane strain states, the influence of the two in-plane residual stresses need to be uncoupled. By considering the two cases where $\tilde{\sigma}_y = 0$ and $\tilde{\sigma}_x = 0$ these two states can be determined as shown in Figure A.2 (states $1a$ and $1b$).

The application of stress equal and opposite to $\tilde{\sigma}_z$ can be used to simulate the introduction of a traction-free surface as shown in Figure A.2. This will result in a surface stress value equal to zero in the z direction ($\sigma_z' = 0$), but will also modify the other stress and strain values. In the uncoupled stress states this is equivalent of applying stresses of $\sigma_z = -\nu\tilde{\sigma}_x$ and $\sigma_z = -\nu\tilde{\sigma}_y$ to the $1a$ and $1b$ states respectively.

Examination of stress state a reveals that the stress in the y direction is equal to zero and therefore that this orientation can be considered as having no displacement constraints. Equivalently stress state b

can be considered as having no constraints in the x direction. These two conditions can be used to decompose the stress change induced by the application of $-\tilde{\sigma}_z$ into two compatible tensor fields. In the case of state $2a$ the stress change in the y direction is zero and the strain change in the x direction is zero. Conversely, for state $2b$ the stress change in the x direction is zero and the strain change in the y direction is zero. The addition of stress states of these two types can be used to generate any arbitrary stress distribution.

In case $2a$ the stress state in the y and z directions are known. Using these values, the plane strain conditions in the x direction and Hooke's law, the stress in the x direction can be determined:

$$\varepsilon_x = 0 = \frac{1}{E}\left(\sigma_x - \nu\sigma_y - \nu\sigma_z\right) = \frac{1}{E}(\sigma_x - 0 + \nu^2\tilde{\sigma}_x), \tag{A.3}$$

$$\sigma_x = -\nu^2\tilde{\sigma}_x. \tag{A.4}$$

Equivalent analysis can be performed for $2b$ to determine that $\sigma_y = -\nu^2\tilde{\sigma}_y$ for this case. Hooke's law can then be used to determine the strains in the other two principal directions (Figure A.2).

To determine the impact of introducing the traction-free surface on the resultant stress and strain tensors, the decoupled intermediate states are added to give the plane stress states: $1a + 2a = 3a$ and $1b + 2b = 3b$. These two stress states are in conditions of plane stress in the z direction but also in one of the other principal directions (the y direction for case a and the x direction for case b). Summation of states $3a$ and $3b$ provides expressions for the plane stress tensors in terms of the in-plane plain strain stresses ($\tilde{\sigma}_x$ and $\tilde{\sigma}_y$) which are given in Equations 3.24-3.28. These expressions demonstrate the $(1 - \nu^2)$ factor which relates the existing in-plane plane strain stresses to those modified by the introduction of the free surface (plane stress). These expressions will only hold in the case of zero out of plane eigenstrain ($\tilde{\varepsilon}_z = 0$) and under conditions where the in plane strains ($\tilde{\varepsilon}_x$ and $\tilde{\varepsilon}_y$) do not change during sectioning.

10.2. Finite Element Analysis

FE simulations can be used as a fast and reliable tool for numerical validation of the analytical relationships between two stress states (for example, plane strain and plane stress) that arise in the body due to the presence of plane eigenstrain. Unconstrained 2D simulations of a rectangular region of YPSZ under plane stress and plane strain conditions were carried out for the case of a plane eigenstrain problem ($\varepsilon_z^* = 0$). The results of this analysis are shown in Figure A.3.

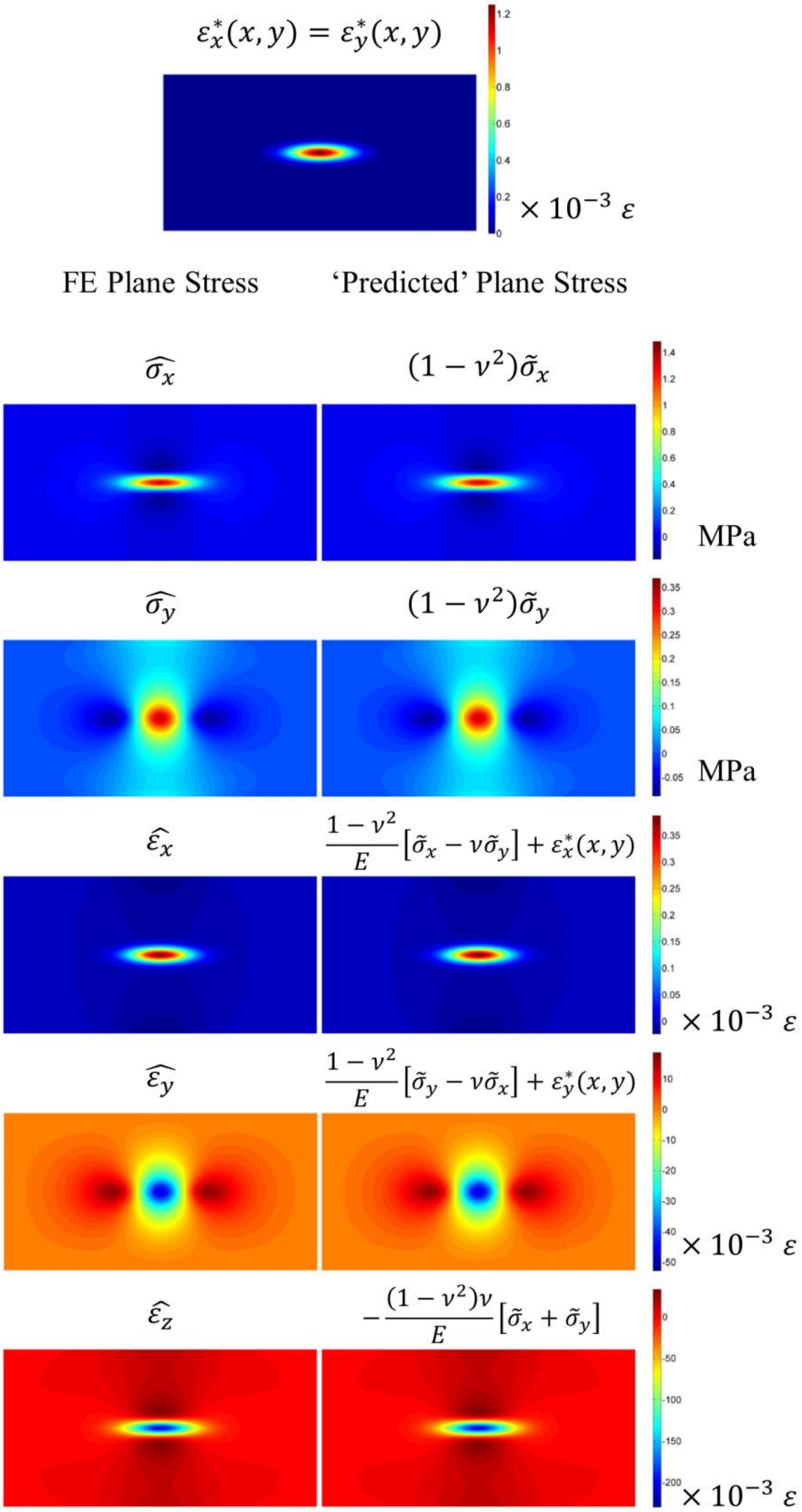

Figure A.3. Result of 2D YPSZ FE simulations of residual stresses and strains induced by the application of 2D Gaussian eigenstrain distributions ($\varepsilon_x^*(x,y)$ and $\varepsilon_y^*(x,y)$). The results of the FE plane stress analysis are shown on the left of the figure and the comparable 'predicted' plane stress results obtained from the plane strain simulations are shown on the right. The expressions used to calculate these distributions are given next to each plot.

The in-plane eigenstrains were given by an identical anisotropic 2D Gaussian distribution:

$$\varepsilon_x^*(x,y) = \varepsilon_y^*(x,y) = 1.25 \times 10^{-3} e^{-\left(\frac{x}{2}\right)^2} e^{-\left(\frac{y}{8}\right)^2}, \qquad \text{(A.5)}$$

where x and y are the coordinate positions. This localised peak of eigenstrain can be thought of as a basic constituent term in a wavelet transform or similar decomposition of an arbitrary eigenstrain field. In other words, if the transformation between plane strain and plane stress solutions is shown to be correct for this case, it is possible to assert with some justification that the result will also hold in the most generic cases that can be decomposed into superposition of such basic terms.

Following the eigenstrain modelling, the consequence of post-processing (transformation) of the plane strain solution was then compared with the full plane stress FE results (Figure A.3). The numerical discrepancy between the two approaches was found to be less than 0.5%, i.e. within the simulation error bounds. This provides numerical validation of the relations in Equations 3.24-3.28.